1

Nanomaterials

Synthesis Methods and Characterization Techniques

Ajit Khosla[1], Irshad A. Wani[2], and Mohammad N. Lone[3]

[1] *School of Advanced Materials and Nanotechnology, Xidian University, Xian, Shaanxi, China*
[2] *Department of Chemistry, Govt. Degree College Anantnag, Anantnag, University of Kashmir, Jammu and Kashmir, India*
[3] *Department of Chemistry, Central University of Kashmir, Ganderbal, Jammu and Kashmir, India*

1.1 Nanoscience and Nanotechnology: An Outline of Terms and Concepts

The definition of nanotechnology remains a central concern in the scientific community, prompting questions about its precise scope and boundaries. Nanotechnology generally pertains to the study and manipulation of materials and phenomena at the nanoscale, typically below 100 nm, where size-dependent quantum mechanical effects become prominent [1]. While this range captures the essence of nanotechnology and its unique properties, some experts caution against strictly adhering to the 100 nm boundary, as certain devices and materials in the pharmaceutical domain may be excluded [2].

An additional crucial aspect in defining nanotechnology is to consider whether the materials involved are natural, synthetic, or manufactured [3]. Naturally occurring biomolecules in living cells often exist at the nanoscale, which could redefine disciplines like biochemistry and molecular biology as integral parts of nanotechnology.

The following definition of nanotechnology is provided by the U.S. National Nanotechnology Initiative (NNI) [3]: "The understanding & control of matter at dimensions between approximately 1 & 100 nanometers, where unique phenomena enable novel nanotechnology applications." Other noteworthy definitions of nanotechnology encompass its broad scope and applications [2]. For example, it can be described as "The design, characterization, production, and utilization of structures, devices, and systems attained through deliberate manipulation of size and shape at the nanometer scale (atomic, molecular, and macromolecular scale) that demonstrate at least one unique or enhanced characteristic or property." Nanotechnology can also be viewed as "Developing objects and surfaces with unique functionalities stemming directly from nanoscale dimensions and/or arrangement." These unique properties may manifest in mechanical, electrical, or photochemical attributes not observed in bulk materials.

The term "nanotechnology" originates from the ancient Greek word "νᾶνος" and the Latin word "nanus," both meaning "dwarf" or "very small." Within the International System of Units (SI), "nano" represents a reduction factor of 10–9 times, indicating manipulation of matter at a scale one billionth of a meter (10–9 m) [4].

Nanotechnology represents more of an engineering approach than a standalone science, drawing extensively from fields such as biology, physics, chemistry, and materials science [5]. Its potential

Metallic, Magnetic and Carbon-Based Nanomaterials: Synthesis and Biomedical Applications, First Edition.
Ajit Khosla, Irshad A. Wani, and Mohammad N. Lone.

impact on these sciences is expected to be transformative. The term "nanotechnology" was initially coined by Eric Drexler in his publication "Engines of Creation" (1986). It refers to the manipulation of individual atoms and molecules to create structures characterized by exact atomic specifications [6]. It is observed that the concept of nanotechnology has its roots in physicist Richard Feynman's seminal lecture from 1959, titled "There's Plenty of Room at the Bottom" [7, 8]. In 1974, Norio Taniguichi of Tokyo Science University coined the term "nanotechnology" in reference to semiconductor processes involving control on the order of nanometers, which continues to serve as the foundational statement [9]: "Nanotechnology primarily involves the manipulation of materials through processes such as separation, consolidation, and deformation at the level of individual atoms or molecules." Nanoscience encompasses the examination of phenomena and the control of materials at atomic, molecular, and macromolecular levels, where properties exhibit notable deviations from those observed at larger scales. Nanotechnologies, on the other hand, entail the design, characterization, manufacturing, and utilization of structures, devices, and systems through precise control of shape and size at the nanometer scale [10].

Nanotechnology pertains to the manipulation and study of materials and phenomena at the nanoscale, corresponding to one-billionth of a meter or one-millionth of a millimeter [1, 4]. The nanoscale, defined by the order of magnitude 10^{-9} in the metric system, encompasses volumes, weights, and units of time. To illustrate, a nanometer bears a similar relation to a meter as the diameter of a hazelnut does to the diameter of the Earth. For instance, a water molecule spans approximately 0.3 nm, a single gold atom's diameter is about a third of a nanometer, a red blood cell is roughly 7000 nm wide, and a sheet of paper is about 100,000 nm thick.

At the nanoscale, materials exhibit unique physical, chemical, and biological properties at the nanoscale often exhibit substantial disparities from their bulk counterparts and individual atoms or molecules [11]. These distinctive properties have captured scientific interest due to the emergence of unusual phenomena and behaviors in nanomaterials. The term "nanoparticle" derives from "nanos" (Greek for dwarf) and "particulum" (Latin for a particle) [12]. In the context of nanotechnology, "nano" predominantly refers to particle length. Nanoparticles encompass objects ranging from 1 to several hundred nanometers in size [12–14]. On the other hand, nanocrystals represent crystalline clusters consisting of a few hundred to a few thousand atoms typically possess dimensions within the nanoscale range. Their properties are influenced primarily by their surfaces rather than their bulk volumes due to their small size. Nanoparticles can be composed of materials, including metals, metal oxides, micelles, biomolecules, and synthetic polymers [15]. The quality of colloidal inorganic nanocrystals depends on factors such as their crystalline nature, narrow size distribution, unique shape, and dispersion stability. "Nanocluster" refers to small aggregates of atoms and molecules with diameters typically in the nanoscale, ranging from a few units to several thousand [16]. Although there is not a strict demarcation between clusters and nanoparticles, the behavior of nanoparticles is significantly influenced by their nanometer dimensions. As such, characterizing nanoparticles involves investigating size, shape, surface charge, and porosity to comprehend and predict their behavior.

Nanoscience and nanotechnology are not entirely novel concepts. For instance, polymers composed of nanoscale monomers have been studied by chemists for over two decades [17]. However, recent advancements in fabrication tools have allowed direct probing and examination of atoms and molecules with great precision, further advancing nanoscience and nanotechnology [18]. Incorporating nanomaterials into bulk materials can drastically alter their properties, resulting in materials with enhanced strength and unique characteristics due to quantum confinement effects and increased surface area-to-volume ratios at the nanoscale.

In summary, nanotechnology explores and manipulates materials and phenomena at the nanoscale, where distinctive properties emerge. Nanoparticles and nanoclusters play vital roles in

this domain, offering unique attributes with potential applications across various fields, promising transformative advancements in science and technology.

1.1.1 Nanomaterials: Properties and Classification

Nanomaterials are materials wherein 50% or more of the constituent particles possess external dimensions falling within the size range of 1–100 nm [19]. Determining whether a material qualifies as a nanomaterial can be done through specific conditions, one of which is the volume-specific surface area (VSSA) or surface area-to-volume ratio. A VSSA greater than 60 m^2/cm^3 serves as a reliable indicator of nanomaterials; however, certain nanomaterials, such as metal nanoparticles, may have a VSSA below this threshold. Thus, the VSSA criterion confirms nanomaterial classification but is not applicable in the reverse direction [20].

Nanoparticles boast significantly larger surface areas per unit mass compared to larger particles [21, 22]. To illustrate the impact of particle size on surface area, let us consider an American Silver Eagle coin weighing 31 g and possessing a total surface area of approximately 3000 mm^2. If this coin were to be subdivided into spherical nanoparticles of, for instance, 10 nm size, the total surface area of all the resulting nanoparticles would amount to around 7000 m^2. This remarkable increase in surface area is equivalent to nearly the size of a soccer field. In essence, the total surface area of all nanoparticles with a size of 10 nm is over two million times greater than the surface area of the silver dollar coin.

As materials are reduced to the nanoscale, quantum effects and surface phenomena begin to exert significant dominance over their properties [23]. When approaching the lower end of the nanoscale, various characteristics of the material, such as optical, electrical, and magnetic behavior, undergo alterations. These effects are particularly pronounced in materials like QDs and quantum well lasers, which find applications in optoelectronics. For crystalline solids and other materials, diminishing their size to the nano range results in a substantial increase in interfacial area. This phenomenon profoundly impacts both the mechanical and electrical properties of these solids [24]. For instance, in materials like metals, the boundaries between grains play a vital role in slowing down or arresting the propagation of defects under stress, thereby providing strength to the material. When the grain size is reduced to the nanoscale, the interfacial area within the material significantly rises, leading to a remarkable enhancement in strength. This is precisely why nanocrystalline materials exhibit much greater strength compared to their bulk counterparts. An exemplary illustration of this phenomenon is nanocrystalline nickel, which demonstrates a strength comparable to that of hardened steel.

Two key factors that markedly differentiate nanomaterials from conventional materials are the enhanced relative surface area and the manifestation of quantum effects [25, 26]. These factors have the potential to modify or enhance properties like strength, reactivity, and electrical characteristics. A key characteristic that makes nanoparticles intriguing from a technical perspective is their surface-to-volume ratio, which grows as their particle diameter decreases. Consequently, nanoparticles consist of a few to several thousand atoms, with a considerable portion of these atoms located on the particle surface. As the particle size diminishes, a higher proportion of atoms occupies the surface in comparison to the interior. For instance, in a 30 nm particle, 5% of its atoms are on the surface, whereas a 10 nm particle has 20% of approximately 30,000 atoms positioned on its surface. This trend continues, with a 5 nm particle containing 40% of approximately 4000 atoms on its surface, and a 1 nm diameter particle having almost all 30 atoms on the surface. The surface atoms, distinct from those inside the material, possess unsaturated bonds, which contribute to the heightened reactivity of the particle surface.

Nanomaterials showcase heightened reactivity, serving as a cornerstone for their diverse range of applications [27]. Precise manipulation of particle size enables the creation of a new generation of exceptionally selective catalysts, capable of expediting specific chemical processes and generating targeted products from raw materials [28]. The increased reactivity of nanomaterials also accounts for their lower melting point, facilitating the reduction of firing temperatures in ceramics through the incorporation of nanoparticulate raw materials. Moreover, these composite materials exhibit minimized shrinkage during the hardening process, making them highly valuable for dental prosthetics. Nanoporous materials, with their expansive pore-specific surface area, find utility in efficient substance filtration, offering an ideal platform for the deposition of filtered substances [29]. These materials also function as potent catalytic agents and promoters of adsorption due to their heightened reactivity [30]. Additionally, nanomaterials possess remarkable optical attributes, such as transparency, absorption, luminescence, and scattering, opening up new possibilities for their utilization.

Given that nanoparticles possess sizes well below the visible light wavelength range (380–780 nm), they have a propensity to absorb light of specific wavelengths [14, 31]. Understanding this light absorption by nanoparticles requires a quantum mechanics-level comprehension. Semiconductor nanoparticles, commonly known as QDs, offer a means to tailor fluorescence wavelength [32]. These optical properties make nanoparticles particularly intriguing candidates for applications in optoelectronics, medical diagnostics, and cosmetics [33, 34]. Furthermore, magnetic materials in the nanometer range can be magnetized as permanent magnets in one direction only [35]. As a result, magnetic nanoparticles (MNPs) contribute to increased storage capacity in magnetic data storage devices. Additionally, the magnetic characteristics of nanomaterials display a relatively low sensitivity to temperature fluctuations.

Nanomaterials are categorized based on the number of dimensions that fall within the nanoscale range (<100 nm) [36, 37]. These classifications are as follows:

1. ***Zero-dimensional (0D) nanomaterials***. These materials have all three dimensions measured within the nanoscale, and none of the dimensions exceed 100 nm. 0D nanomaterials are commonly known as nanoparticles and include examples such as metal nanoparticles and QDs.
2. ***One-dimensional (1D) nanomaterials***. This category comprises materials in which one of the three dimensions extends beyond the nanoscale, while the other two dimensions are confined within the nanorange. Examples of 1D nanomaterials include nanotubes, nanorods, and nanowires.
3. ***Two-dimensional (2D) nanomaterials***. In this type, two dimensions are outside the nanoscale range, while the material is limited to the nanorange in the third dimension. Such nanomaterials exhibit plate-like shapes, and notable examples include graphene, nanofilms, nanolayers, and nanocoatings.
4. ***Three-dimensional (3D) nanomaterials***. These materials are not confined to the nanoscale in any dimension. The 3D nanomaterials category encompasses bulk powders, bundles of nanowires and nanotubes, as well as multi nanolayers.

1.1.2 Forms of Nanoparticles

Nanoparticles can exhibit diverse chemical compositions, encompassing inorganic materials like metals, metal oxides, and semiconductor materials, as well as organic materials such as carbon-based compounds, including fullerenes and carbon nanotubes [27]. Engineered or synthetic nanoparticles can be categorized into specific types based on their distinct chemical and physical attributes.

Carbon-based nanoparticles can be synthesized in various forms, such as spherical nanoparticles like fullerenes or cylindrical nanotubes like carbon nanotubes [38]. Carbon black, an industrially produced soot, is a precisely defined material, purposefully synthesized under controlled conditions with a carbon content exceeding 96%. On the other hand, soot resulting from chimney and diesel combustion contains organic and inorganic contaminations to varying degrees, making them less well-defined combustion by-products of hydrocarbons or coal.

Metal nanoparticles are submicron-scale entities composed of pure metals like gold, platinum, silver, titanium, zinc, cerium, iron, and thallium. They find extensive applications, particularly in catalysis and the biomedical field [39].

Metal oxide-based nanoparticles are formed from metal oxides like zinc oxide (ZnO) or titanium dioxide (TiO_2) [40]. Certain oxide nanoparticles are widely used in consumer goods, such as paints, cosmetics, and varnish [41, 42]. Others, such as aluminum oxide (Al_2O_3) and Zircon (ZrO_2) nanopowders, are employed in technical ceramics components to enhance hardness and breaking strength [43, 44].

Semiconductor nanoparticles originate from diverse compounds [45]. Depending on the elements they are derived from and their placement in the periodic table, they are classified as II–VI, III–V, or IV–VI semiconductors [46]. For instance, silicon and germanium fall under group IV, while GaN, GaP, GaAs, InP, and InAs are categorized as III–V semiconductors. II–VI semiconductors include ZnO, ZnS, CdS, CdSe, and CdTe. These semiconductor nanocrystals, with their distinctive optical properties, find applications in laboratory and medical diagnostics.

Composites, wherein the matrix is often composed of polymers, offer a remarkable approach to combine the unique characteristics of nanoparticles with those of the composite matrix.

1.2 Special Effects of Nanosystems

Nanosystems, often involving structures and materials at the nanometer scale, exhibit an array of exceptional and unique effects that transcend the boundaries of conventional science and engineering. These special effects manifest in various ways, influencing the behavior of materials, biological systems, and devices.

1.2.1 Quantum Confinement Effect

Inorganic nanosystems refer to chemical entities composed solely of inorganic materials. They demonstrate novel behaviors stemming from quantum size effects and the presence of significant surface areas and interfaces at the nanoscale, leading to unique phenomena. Indeed, individual molecules showcase characteristics governed by quantum mechanical principles, whereas the chemical and physical attributes of bulk materials adhere to quantum mechanics laws. Nanosystems exhibit electronic, electrochemical, photochemical, magnetic, optical, mechanical, or catalytic properties that deviate notably not only from individual molecular units but also from macroscopic systems.

Quantum-size effects manifest in nanosized entities due to their overall dimensions being on the same scale as the characteristic wavelength for fundamental excitations in materials [47, 48]. These excitations, which encompass the wavelengths of electrons, photons, and similar particles, transport energy quanta within materials, thereby dictating the dynamics of their transmission and transformation from one state to another. Yet, when the size of structures aligns with the order of magnitude of these characteristic wave functions, the transmission and behavior of quanta undergo significant perturbation. Consequently, quantum mechanical selection rules, typically

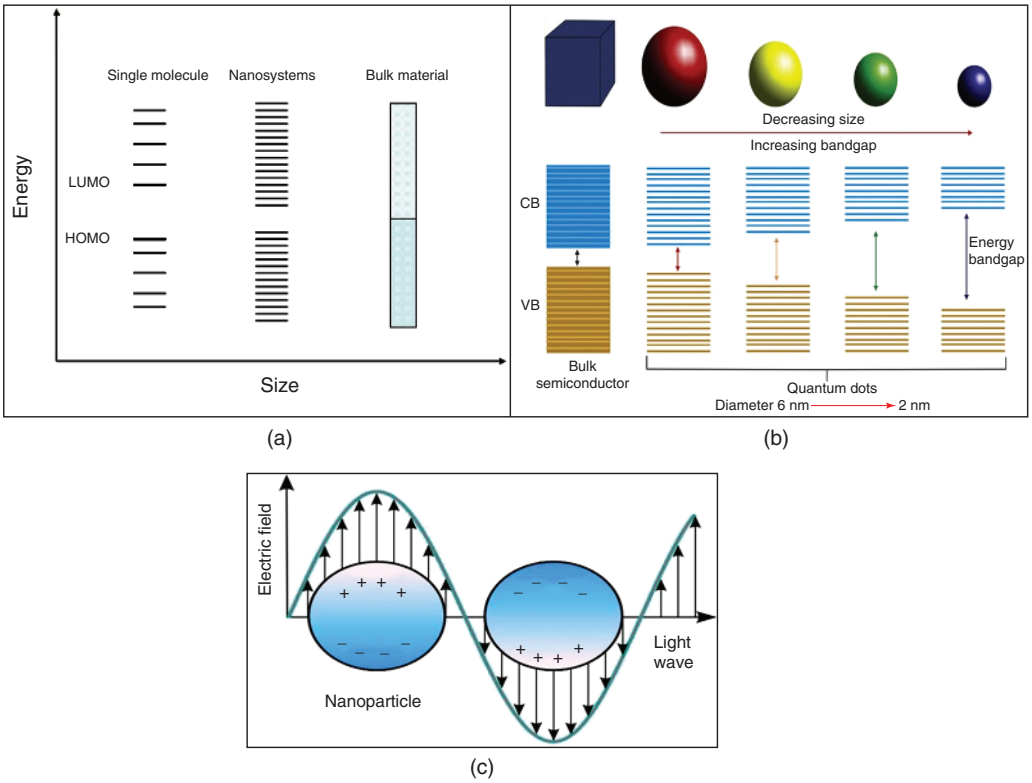

Figure 1.1 Variation of bandgap energy with size of (a) metals and (b) semiconductors. (c) Illustrations of plasmon oscillations in a spherical object, demonstrating the movement of the conduction electron charge distribution concerning the atomic nuclei. Source: (a, b) Reproduced with permission from Sumanth Kumar et al. [49]/Elsevier, (c) Unser et al. [50]/MDPI/CC BY 4.0.

imperceptible on a larger scale, become apparent. Take metals as an example; their conventional "metallic" attributes, such as conductivity, diminish as their size decreases as the number of atoms comprising the sample significantly reduces. In fact, the electronic conduction band of a metal transitions from continuous levels in bulk infinite materials to discrete states as size diminishes, leading to a rise in bandgap energy (Figure 1.1a).

Likewise, QDs possess electronic characteristics that fall between those of bulk semiconductors and isolated molecules [31]. Their optoelectronic attributes are influenced by their dimensions and shapes, and these attributes change depending on these factors. For instance, when QDs are stimulated by a photon with energy represented as $h\nu$ (where ν signifies the frequency of the incoming photon), larger QDs, typically around 5–6 nm in size, emit light in the orange or red wavelength range [49]. Smaller QDs emit shorter wavelengths, falling within the blue or green spectrum. Consequently, one can intentionally adjust these features by modifying the size and shape of the QDs to attain the desired results. Figure 1.1b provides a visual representation of how the bandgap of QDs changes with varying sizes. These QDs can be produced from single-element materials like silicon or germanium, or from compound semiconductors such as CdSe, PbSe, CdTe, and PbS [51–56]. Sometimes, QDs are referred to as "artificial atoms" since they exhibit discrete electronic states, akin to what is observed in atoms and molecules.

1.2.2 Concept of Surface Plasmon Resonance (SPR)

"How light interacts with matter" has been a subject of inquiry, notably pursued by Michael Faraday in his investigation of metal colloids. Faraday's pioneering work revealed that even when metal particles are substantially smaller than the wavelength of light, they exhibit substantial light scattering and absorption, resulting in vivid colors, even in dilute solutions [57, 58]. Notably, Faraday's exploration led to the understanding that the collective oscillation of conduction electrons within metal particles is accountable for the scattering and absorption of light at specific frequencies, giving rise to distinct colors, particularly in the cases of silver and gold. This occurrence, now known as SPR, derives its name from the polarization of surface charges generated by collective electron oscillations (surface) and the analogy to electron oscillations in gaseous plasma (plasmon) [59].

Localized surface plasmons (LSPs) refer to charge density oscillations constrained within metallic nanoparticles, often referred to as metal clusters, and metallic nanostructures (Figure 1.1c) [59]. The excitation of LSPs by an incident electric field, at wavelengths corresponding to resonance, results in robust light scattering, the emergence of intense surface plasmon (SP) absorption bands, and an augmentation of local electromagnetic fields. The frequency (absorption maxima or color) and intensity of these SP absorption bands are intrinsic to the material type, typically gold, silver, or platinum, and are remarkably sensitive to factors like size, size distribution, shape of nanostructures, and the surrounding environment [50]. These specific characteristics have spurred considerable interest in LSPs, leading to the development of a wide array of LSP-based sensors and devices.

The striking red color observed in aqueous colloidal gold dispersions is a direct manifestation of localized SPR. Throughout history, colloidal gold has intrigued many, having been used to provide color in medieval cathedral windows and believed, until the eighteenth century, to possess life-prolonging and rejuvenating properties when ingested as *aurum potabilis* [60, 61]. In contemporary times, colloidal gold has witnessed exponential growth in its utilization as a biological label, marker, and stain in various microscopic applications [62]. More recently, metallic nanoparticles and nanostructures have found successful use as molecular recognition elements and amplifiers in sensors and biosensors, as well as integral components in nanoscale optical devices [63–65]. Notably, surface plasmons are distributed unevenly around nonspherical metallic nanoparticles and nanostructures, resulting in shape-dependent LSPR absorption spectra [66]. For instance, in metallic nanorods, the plasmon resonance splits into low and high-energy absorption bands, with the high-energy band corresponding to electron oscillations perpendicular to the major axis and the low-energy band arising from electron oscillations along the major axis. This separation becomes more pronounced with increasing aspect ratio of the nanorods [67–69]. Triangular particles exhibit multiple plasmon resonances, including a longitudinal (bulk) plasmon mode and a highly localized enhancement at their sharp tips [70, 71].

Mie theory has been extended to cylindrical and needle-like nanoparticles, and optical properties, including absorption, extinction, and scattering efficiencies, have been calculated using discrete dipole approximations for metallic nanoparticles with arbitrary shapes [72–74]. The analysis of scattering spectra from differently shaped individual nanoparticles (e.g., spherical, rod-like, triangular, pentagonal, and tetrahedral) of silver, gold, and nickel through total internal reflection spectroscopy has obviated the necessity for producing highly monodisperse nanoparticle populations in specific shapes and provided valuable insights into the correlations between shape, environment, and spectra.

It is worth noting that Mie theory is only applicable to noninteracting nanoparticles that are well separated in their solid state or present at low concentrations in dispersions. For interacting

particles, the plasmon resonance red-shifts, followed by the emergence of a lower-energy absorption band, similar to the longitudinal absorption band observed in nanorods. Two main types of interactions occur between arrayed metallic nanoparticles: near-field coupling, which involves particles in close proximity, and far-field dipolar interactions [75]. Dipolar interactions are electrodynamic in nature, with dipole fields from a plasmon oscillation in one particle inducing surface plasmon oscillation in adjacent particles [76].

1.3 Aspects of Synthesis of Nanomaterials

Atoms and molecules serve as the fundamental constituents of all matter, shaping its properties and interactions. Understanding how these basic units assemble is crucial for comprehending material behavior. Precise control over synthetic pathways becomes imperative in crafting nanoscale building blocks of varied sizes and shapes, which in turn can facilitate the development of advanced devices and technologies with enhanced capabilities. To achieve this, two complementary approaches are pursued: a top-down strategy focusing on miniaturizing existing components and materials, and a bottom-up approach involving the construction of increasingly intricate molecular structures at the atomic or molecular level [77]. These divergent methods underscore the organizational complexity of nanosystems, situated at the intersection between molecular entities and bulk materials (Figure 1.2). Richard Feynman famously advocated for the top-down approach in his seminal 1959 lecture, emphasizing the ample opportunities for exploration at the nanoscale [79]. This method excels in achieving structures with long-range order and bridging connections with the macroscopic world. Conversely, Jean-Marie Lehn championed the bottom-up approach, recognizing the vast potential at the nanoscale and the ability to establish short-range order through assembly [80]. Integrating these two techniques promises to offer the most comprehensive toolkit for nanofabrication, theoretically enabling a wide array of possibilities.

1.3.1 Top-Down Approach

The top-down approach utilizes techniques such as machining, templating, or lithography to achieve miniaturization. Typically, this method starts with patterns created at larger scales, often in the microscale, which are then scaled down to the nanoscale [81]. An important advantage of this strategy is that components are both patterned and constructed in situ, obviating the need for additional assembly steps.

Various nanostructures can be crafted through methods like electronic, ionic, or X-ray lithography [27, 82]. Initially, a quantum well, characterized by two finite dimensions, is fashioned, followed by the creation of a quantum wire with one finite dimension. Ultimately, a quantum dot, a zero-dimensional structure with all dimensions in the nanoscale, is produced. While current short-wavelength optical lithography techniques can achieve dimensions of at least 100 nm, which traditionally mark the nanoscale threshold, efforts are ongoing to develop extreme ultraviolet and X-ray sources to extend lithographic printing capabilities to dimensions ranging from 10–100 nm. However, challenges persist, particularly related to beam focalization. Furthermore, scanning beam techniques like electron-beam lithography can generate patterns down to approximately 20 nm, with even smaller features attainable using scanning probes for depositing or removing thin layers.

Mechanical printing techniques usually start with the creation of a high-resolution master "stamp" using lithographic methods, as previously described [83]. This stamp, or its copies, is then

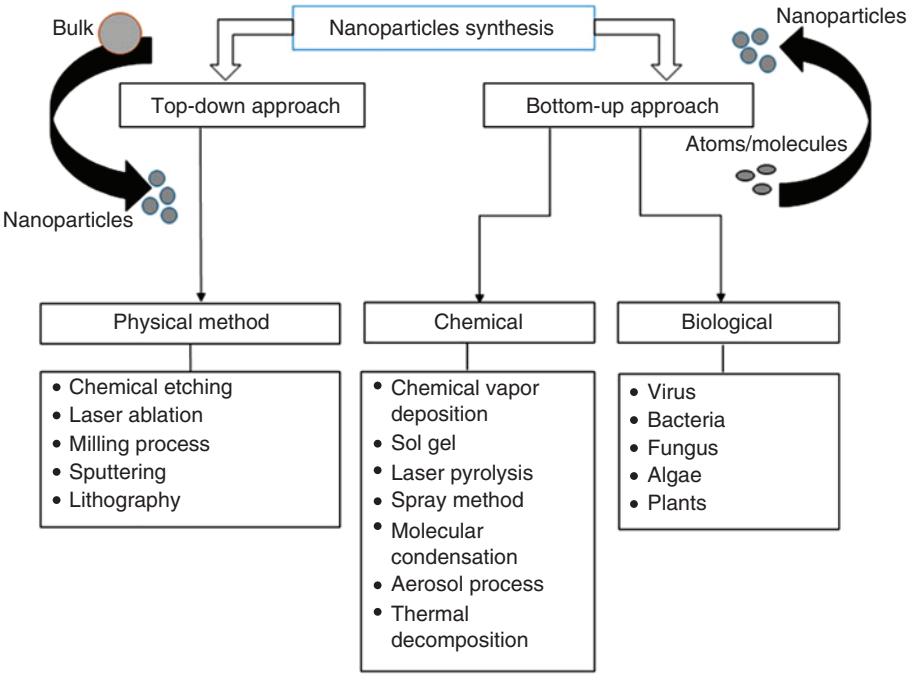

Figure 1.2 Various methods used for the synthesis of nanoparticles. Source: Bloch et al. [78]/Frontiers Media S.A./CC BY 4.0.

used to transfer the pattern onto a surface. Finally, the thin layer of masking material under the stamped regions is removed. These nanoscale printing methods provide several benefits, including the capability to work with various materials on curved surfaces.

These techniques are generally expensive and involve complex manufacturing processes. Despite their success at the microscale, top-down methods encounter difficulties when working at nanoscale dimensions. Moreover, they often yield two-dimensional structures, limiting the production of arbitrary three-dimensional objects due to their reliance on layer-by-layer patterning. Notably, the progress of top-down methodology has been mainly propelled by disciplines like materials engineering and physics, with limited input from inorganic chemists in leveraging these approaches.

1.3.2 Bottom-Up Approach

Bottom-up techniques in nanofabrication involve the step-by-step accumulation of atoms or clusters, utilizing either chemical or physical forces at the nanoscale to guide the assembly of basic units into more extensive structures [77]. Typically, this method entails the chemical synthesis of nanoscale materials within colloidal or supramolecular setups, often undergoing phase changes like sonochemical surface deposition or solid-phase precipitation from solutions. These strategies draw inspiration from biological systems, where chemical interactions drive the formation of diverse vital structures. Researchers seek to emulate nature's ability to produce precise atom clusters, enabling their spontaneous arrangement into sophisticated configurations. Obtaining the desired shape and size requires meticulous control over the material's nucleation and growth. This synthesis method is particularly captivating for chemists. Bottom-up approaches, which initiate from individual atoms and molecules, resonate deeply with the principles of chemistry and molecular biology. Given that a significant portion of chemistry already revolves around manipulating

nanoscale entities or coordinating the self-assembly of molecules into more extensive structures, this methodology offers a natural progression for exploration and innovation. Bottom-up techniques present numerous advantages. They offer a wide range of preparation methods, facilitating meticulous control over scale dimensions, including at the atomic or molecular level. Moreover, they typically incur lower costs compared to top-down approaches [13, 14, 84–86]. Nonetheless, despite these benefits, realizing preprogrammed self-assembly of arbitrarily large systems with complexities similar to those observed in natural systems remains a formidable hurdle.

Preparation of nanomaterials can be classified into physical and chemical methods. The physical methods are based on subdivision of bulk metals, including pulverization or mechanical crushing of bulk metal, arc discharge between metal electrodes, etc. Metal nanoparticles thus produced are usually large in size and have a wide size distribution [46]. Several physical methods have been reported for the synthesis of nanosized particles. These include vapor condensation methods, spray pyrolysis, mechanical deformation, thermochemical decomposition of metal–organic precursors in flame reactor, and other aerosol processes named after the energy sources applied to provide the high temperature during gas-particle conversion [47, 48]. The chemical methods are grounded on the concept of reduction of metal ions or decomposition of precursors to form atoms, followed by aggregation of the atoms. Nanoparticles prepared by chemical methods usually have a narrow size distribution [46]. Increasing interest in chemical synthesis of nanoparticles is clearly indicated by the number of reports and reviews on this subject [49, 51–55]. However, it is notable that some methods can be considered as either chemical or physical routes depending on the media, precursors, and operating conditions such as milling.

The formation of metal nanoparticles by chemical methods can be carried out by reduction of metal ions with chemical reductants or decomposition of metal precursors with extra energy. The chemical reductants involve molecular hydrogen, alcohol, hydrazine (HA), $NaBH_4$, $LiAlH_4$, citrate, etc. Energy provided from the outside involves photoenergy (ultraviolet and visible light), γ-ray, electricity, thermal energy (heat), nonchemical energy, etc. In order to produce metal nanoparticles with a narrow size distribution, agents stabilizing colloidal dispersion of metal nanoparticles are of vital importance [46]. Various methods of the nanoparticle's synthesis can be classified based on the process media, including vapor, liquid, and solid-state processing routes, and combined method, such as vapor–solid–liquid approach [53].

Many of the properties associated with nanoparticles are directly related to the relatively higher energetic state of atoms and molecules at a surface when compared with those in the bulk. In many cases, the production of nanoparticles involves techniques to hinder the natural course of thermodynamics through the manipulation of kinetics. In other cases, it is possible to hinder the natural growth of phases through the use of dilution or via protection of surfaces using surface-active agents or by coating and encapsulation of nanoparticles in a glassy media such as those used for instance in the case of polymers [56].

1.4 Synthesis and Characterization of Gold Nanoparticles

The synthesis and characterization of Au NPs stand as an intriguing and essential domain within the realm of nanotechnology and materials science. Gold nanoparticles, celebrated for their distinct size-dependent properties, have been widely applied across diverse fields such as electronics, medicine, catalysis, and environmental science. This research endeavor involves the controlled creation of gold nanoparticles, often on a nanometer scale, and the subsequent detailed examination of their physical, chemical, and optical properties. Understanding how to synthesize these nanoparticles and precisely characterize their attributes is fundamental to harnessing their potential in

various technological advancements and innovations. In this paper, we delve into the intricacies of synthesizing and characterizing gold nanoparticles, shedding light on their diverse applications and the remarkable insights they offer into the nanoscale world of materials. Numerous methodologies have been employed for the fabrication of gold nanoparticles, encompassing techniques such as chemical, electrochemical, thermal, and sonochemical pathways. Synthesis of Au NPs by employing these methods is discussed below.

1.4.1 Chemical Methods of Synthesis

Synthesis of Au NPs by chemical reduction technique involves two steps. The primary step involves reducing the gold salt through the utilization of reducing agents like borohydrides, HA, amino boranes, hydroxyl amine, formaldehyde, and hydrogen peroxide and organic reducing molecules such as citric acid, oxalic acid, polyols, sugars, and acetylene. Electron-rich molecules such as metal sandwich complexes have also been used for the reduction of gold salts to produce Au NPs. The second step involves the stabilization of the synthesized Au NPs by various stabilizers such as trisodium citrate, sulfur-containing ligands such as thiolates, oxygen-based ligands, phosphorus-based ligands, nitrogen-based ligands including heterocyclic compounds, polymers, surfactants, dendrimers, etc. One of the well-known techniques for fabricating Au NPs was designed by Turkevisch in 1951 [57]. Turkevisch method involves the conventional chemical route by reducing gold salt ($HAuCl_4$) in aqueous sodium citrate solution. It involves adding sodium citrate to the boiling $HAuCl_4$ solution under vigorous stirring. Wine red Au NP solution is produced within few minutes of stirring with Au NP size of around 20 nm. Polte et al. [87] studied the mechanistic details of the Au NP formation using classical Turkevisch method. The study analyzed various aspects of Au NP formation, including their size, shape, and growth mechanisms, employing techniques such as SEM, HRTEM, UV-vis spectra, XANES, and SAXS. The findings and their interpretation are as follows. The nanoparticles produced in the study closely matched values reported in the literature for similar syntheses. The particles were predominantly spherical and nearly uniform in size, with a polydispersity of around 12% and a mean radius of 7.6 nm. The UV-vis spectra showed an absorbance maximum in the range of 520–550 nm, which is typical for the plasmon resonance of gold nanoparticles. During the synthesis, the peak maximum shifted slightly from about 540 nm to approximately 523 nm, indicating changes in particle size. The curve depicting the intensity at each peak position versus time demonstrated the typical time-dependent behavior, with a slow initial intensity increase followed by more rapid growth. However, the growth mechanism based on UV data remained controversial. Evolution of XANES spectra revealed an initially slow reduction process, followed by a significant decrease in Au(III) content after approximately 50 minutes, coinciding with the rapid escalation in the intensity of the Au NPs plasmon resonance detected via UV-Vis studies. The data suggested that a considerable portion of Au(III) species was being converted into metallic Au(0). SAXS analysis provided information on particle growth during the synthesis. The data indicated different phases of GNP formation. Initially, there was rapid nucleation, resulting in small particles with a mean radius of 2 nm and high polydispersity. Subsequently, particles grew by coalescence, followed by further growth through a diffusion-limited process. The final phase showed a rapid growth in particle size, accompanied by the near-complete consumption of Au(III) species. The study varied reaction temperature and the concentration of the gold precursor. Higher temperatures and increased precursor concentrations led to significantly faster Au NP formation, suggesting that the reduction of Au(III) is an activated chemical process with a reaction order greater than one. The experiments proposed a sequential process of Au NP formation that did not fully align with previously proposed mechanisms. It revealed rapid nucleation, followed by coalescence and

further precursor reduction contributing to particle growth. These findings challenged the classical theory of self-nucleation and highlighted the importance of coalescence processes in obtaining monodisperse GNPs. Varying the concentration of sodium borohydride produced the Au NPs of various morphologies such as nanospheres, nanowires, nanorods, and nanotriangles [88]. Frens in 1973 modified the Turkevisch method to produce Au NPs in size from 15 to 150 nm by changing the ratio of reducing agent and gold salt [89]. Several research teams have modified the Turkevich and Frens method to synthesize citrate-stabilized Au NPs with diverse sizes and diameters. For example, it was demonstrated by Kimling et al. that smaller-sized Au NPs are produced at higher concentration of citrate whereas lower concentration of citrate produced large-sized Au NPs by aggregation of small Au NPs [90]. Kumar et al. [91] investigated the mechanism behind the Turkevich–Frens method, illustrating the formation process of dicarboxy acetone (DCA) through the citrate oxidation, followed by the reduction of gold salt to Au atoms, which then assemble to form gold nanoparticles (Au NPs). The dicarboxyl acetone produced serves as a stabilizing agent, distinct from the role of citrate itself. Turkevisch method was further modified by various research groups to study the effect of varying the pH [92–95], reaction temperature, citrate concentration [96], and gold salt concentration [97] on Au NP shape, size distribution, and other characteristic properties. Utilizing ascorbic acid as a reducing agent in chemical reduction and an aqueous surfactant, cetyltrimethylammonium bromide (CTAB) as a shape director also resulted in the production of anisotropic Au NPs. The size and characteristics of gold nanoparticles (Au NPs) were found to be significantly affected by the alteration in the sequence of reagent addition. In a study by Jiménez et al. [98] the order of reagent addition was modified keeping factors such as the SC : Au ratio (13.6), temperature (100 °C), final volume (150 mL), and total reaction time (5 minutes) constant. The two methods were employed: (i) direct synthesis (SC was added to a hot $HAuCl_4$ solution) and (ii) inverse synthesis ($HAuCl_4$ solution was added to a boiling sodium citrate solution). A blue shift in the SPR peak, from 527.5 nm (direct synthesis) to 518 nm (inverse synthesis), indicating smaller Au NPs in the inverse method, was revealed by UV-vis spectra (Figure 1.3A). This shift was corroborated by TEM analysis (Figure 1.3B), which demonstrated a decrease in mean particle size and an improved size distribution, from 36.6 ± 6.8 nm (SD ~ 18%) for direct synthesis to 9.0 ± 1.2 nm (SD ~ 13%) for inverse synthesis. The same trend was observed for a lower SC : $HAuCl_4$ ratio (6.8), where a blue shift in the SPR peak from 522 nm (direct) to 519 nm (inverse) was observed, accompanied by a decrease in the absorbance maximum. Once again, TEM analysis confirmed a reduction in Au NP size and polydispersity, from 17.8 ± 2.5 nm (SD ~ 14%) for direct synthesis to 14.9 ± 1.5 nm (SD ~ 10%) for inverse synthesis. The addition of DCA to the reducing mixture had a notable impact on Au NP size and reaction rate. With a fixed SC : $HAuCl_4$ ratio (13.6), changing the SC : DCA ratios in the reducing mixture influenced reaction kinetics. A decrease in SPR peak from 523 to 519 nm was observed when increasing DCA content from 100 : 0 to 90 : 10 (SC : DCA), but it returned to 523 nm at a 50 : 50 ratio (Figure 1.3C). TEM analysis confirmed a correlation between SC : DCA ratio, final Au NP size, and monodispersity (Figure 1.3C). When using a 0 : 100 SC : DCA ratio, no particle formation was observed, likely due to the solution's pH of 3.7. This suggests that heating SC before adding Au^{3+} could induce SC oxidation. The role of pH in Au NP synthesis was also explored. A decrease in pH from 6.2 to 5.9 was observed when reducing SC content in the reducing mixture from a 100 : 0 to 90 : 10 SC : DCA ratio. However, the influence of SC : DCA ratio on reaction kinetics, SPR peak, and final Au NP size was more significant than pH changes. Adjusting the pH value from 5.1 to 6.2 resulted in a blue shift in the SPR peak and smaller Au NPs. The presence of DCA in the reaction mixture induced a decrease in NP size and an improvement in monodispersity, which was not attributed to pH changes. In conclusion, both the order of reagent addition and the addition of DCA influenced the size, shape, and reaction kinetics of Au NPs, indicating the complex interplay

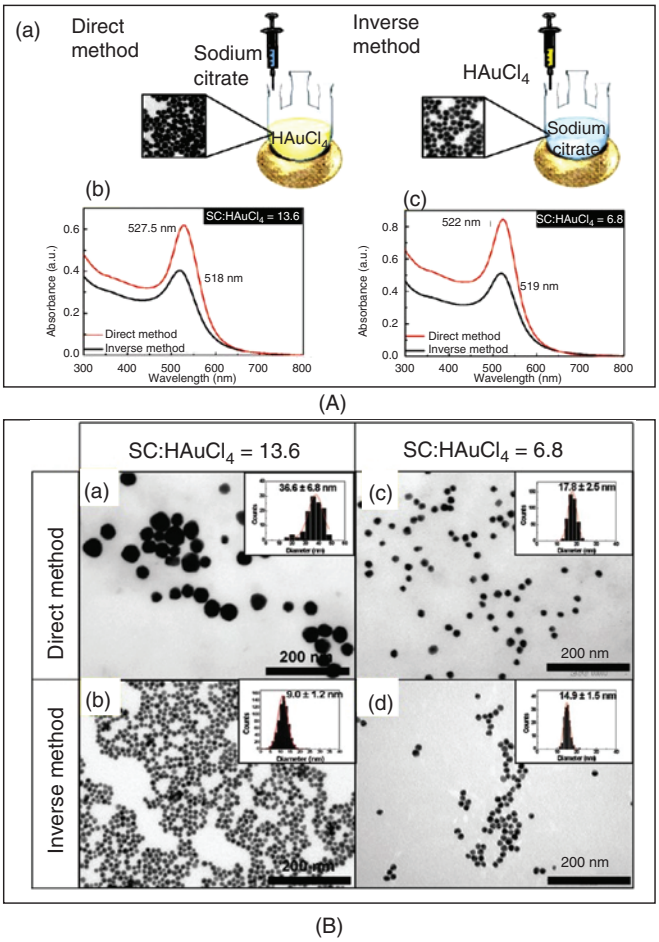

Figure 1.3 (A) Illustration of a comparison between the (a) direct and inverse sequences of reagent addition and the characterization of gold nanoparticles (Au NPs) through optical analysis (UV-vis spectroscopy). The synthesis was carried out at 100 °C for five minutes, with two sets of conditions: (b) 0.165 mM $HAuCl_4$ and an SC: $HAuCl_4$ ratio of 13.6 and (c) following the Turkevich conditions with 0.25 mM $HAuCl_4$ and an SC: $HAuCl_4$ ratio of 6.8. (B) The morphology of the synthesized gold nanoparticles (Au NPs) examined using transmission electron microscopy (TEM) at a temperature of 100 °C for five minutes. This characterization was performed under two different sets of conditions: (a and b) with 0.165 mM $HAuCl_4$ and an SC: $HAuCl_4$ ratio of 13.6, and (c and d) following the Turkevich conditions, which involved 0.25 mM $HAuCl_4$ and an SC: $HAuCl_4$ ratio of 6.8. The TEM images for both the direct and reverse sequences of reagent addition are presented. Additionally, the size distribution of the Au NPs is illustrated in the inset graphs within the TEM images. (C) Analysis of the gold nanoparticles (Au NPs) involved both optical assessment through UV-vis spectroscopy and morphological examination using transmission electron microscopy (TEM). These Au NPs were synthesized under conditions that included 0.165 mM of $HAuCl_4$ and an SC: $HAuCl_4$ ratio of 13.6, with the reaction temperature set at 100 °C. The study examined different ratios of the reducing mixture SC: DCA, specifically 100 : 0 (a and d), 90 : 10 (b and e), and 50 : 50 (c and f). The TEM images feature inset graphs that provide measurements of the size distribution of the Au NPs. Source: Reproduced with permission from Ojea-Jimenez et al. [98]/American Chemical Society.

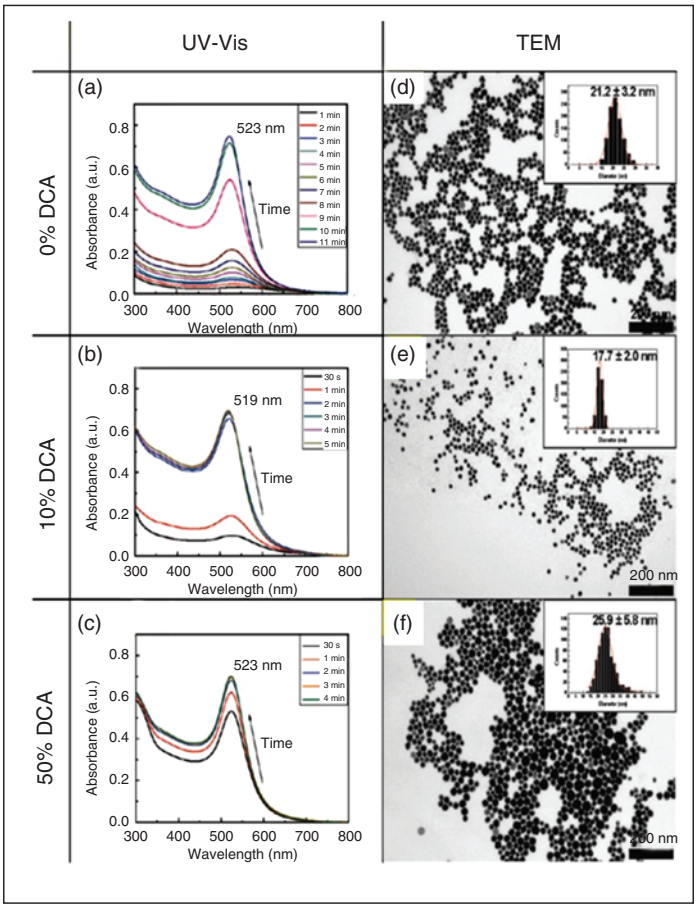

(C)

Figure 1.3 (*Continued*)

of these factors in the synthesis process. Due to the mild reducing ability of sodium citrate, Au NPs produced by Turkevisch method resulted in the production of Au NPs of bigger sizes, with diameters greater than 10 nm. The reducing ability of citrate ions was found to vary by changing the reaction medium, hence size of Au NPs can be tailored by changing the solvent polarity. In another study, Ojea-Jiménez et al. [99] reported that using D_2O as a solvent instead of water enhanced the reducing ability of citrate ions which resulted in the production of smaller-sized Au NPs of diameter of 5 nm. The synthesis of Au NPs was conducted at 100 °C under the same reaction conditions, but with varying amounts of D_2O in the solvent (% $D_2O = 0$, 50, and 100%). The growth of the particles was tracked through UV-Vis studies of the solutions, and the results discovered a blue-shift in the SPR band, shifting from 519 to 512.5 nm as % D_2O increased. This shift in the SPR band corresponds to changes in particle size, supported by a reduction in the hydrodynamic diameter from 15.4 to 9.7 nm and a decrease in negative surface charge from −43.0 to −33.9 mV. Transmission electron microscopy (TEM) and image analysis further confirmed that higher % D_2O led to a reduction in particle diameter. Using pure D_2O as the solvent resulted in the production of smaller Au NPs, measuring 5.3 ± 1.1 nm, in comparison to those produced in pure H_2O, which had a diameter of 9.0 ± 1.2 nm. It is noteworthy that this method could generate a small fraction of even smaller Au NPs, down to 2–3 nm, which could be isolated using standard separation techniques (detailed in the

Supporting Information), potentially yielding higher Au NP yields. Temperature and the presence of D_2O in the reaction were found to influence Au NP size. At lower temperatures (90 °C), reactions in D_2O proceeded more slowly, resulting in larger Au NPs compared to syntheses in H_2O at 90 °C or D_2O at 100 °C. This is consistent with observations that reducing the reaction temperatures resulted in the production of larger NPs. The study postulates a reaction mechanism for the reduction of Au(III) by sodium citrate, based on experimental evidence and existing literature. The mechanism involves two steps: a rapid ligand exchange with citrate to form an intermediate complex, followed by a slow rate-determining step involving a concerted decarboxylation and reduction of Au(III) species. The involvement of deuterium in D_2O affects the rate of this reaction, enhancing the reducing strength of the citrate molecule and influencing the fabrication of Au NPs. In conclusion, this research demonstrates that particle size can be regulated by altering the solvent system and provides insights into the intricate mechanism affected by the presence of deuterium in the solvent. It emphasizes the sensitivity of water-based systems, where hydrogen bonding interactions play a dominant role in all reaction steps. The citrate/aqueous synthesis method for Au NPs is widely used in the field of nanotechnology.

Another novel approach discovered by Brust and Schiffrin used tetraethylammonium bromide (TOAB) as a phase transfer agent to transfer $AuCl^{4-}$ from aqueous phase to the organic phase to synthesize thermally stable Au NPs employing $NaBH_4$ as a reductant in presence of dodecanthiol [100]. The reduction of the gold salt caused a transition in the color of the organic phase, shifting from orange to a rich brown hue, signifying the formation of both cuboctahedral and icosahedral gold nanoparticles (Au NPs). This approach demonstrated an easy and straightforward method for producing thiolate-stabilized gold nanoparticles (Au NPs) with good air stability and repeated dissolution and isolation without agglomeration. Further, this method produced small-sized (<5 nm) Au NPs with narrow size distribution and easy substitution and functionalization by different ligands. It was further shown that larger molar ratios of dodecane-thiol/$AuCl^{4-}$ produced smaller-sized Au NPs [101]. Further fast addition of $NaBH_4$ to cooled solutions produced smaller and mono-dispersed Au NPs. The reaction between thiol and Au NPs led to the oxidative addition of the S—H bond onto two Au atoms on the surface of the Au NP, leading to the creation of an S—Au bond and the elimination of an H_2 molecule through reductive elimination. Li et al. [102] employed Raman spectroscopy to demonstrate the formation of S—Au bonds on the surface of Au NPs, revealing that these bonds formed only after the addition of $NaBH_4$, thus elucidating the mechanism of Au NP formation. The study presented detailed spectroscopic investigations into the two-phase synthesis of metal nanoparticles (NPs), with a focus on the addition of thiol or ligands and $NaBH_4$ in the process. Raman spectroscopy revealed that no Au—S bonds were formed before the addition of $NaBH_4$, confirming that the metal precursor was not the commonly believed [M(I)SR]n-like polymer but rather the [TOA][MX_2] complex. 1H NMR spectra suggested the formation of inverse micelle structures involving TOAB (TOA), encapsulating water, and encapsulated metal ions. The proposed NP formation mechanism highlighted the role of inverse micelles, where Au NPs formed within micelles after $NaBH_4$ addition, and ligands later diffused through the TOA shell to form Au—S bonds at the interface. A reversed synthetic route successfully produced stable, ligand-protected ultrasmall Au NPs with better size control, and increasing stirring time led to larger NP formation. Additionally, the use of disulfide and organo-chalcogen ligands in the synthesis demonstrated the same principles, with the reversed route producing smaller, more monodisperse Au NPs. This study provides invaluable insights into the two-phase synthesis of metal nanoparticles, with implications for control and optimization in NP size and distribution.

Burst–Schiffrin method was further improved in 1995 by using methanol solution as a medium for Au NP synthesis in absence of phase transfer agent TAOB [103]. Since both gold salt and p-mercaptophenol are soluble in methanol, hence it acted as an excellent solvent for a single-phase

synthesis. This modified procedure proved to be advantageous since it avoided the incorporation of TAOB impurities in the synthesized Au NPs. Later all such solvents have been exploited for single-phase synthesis of Au NPs in which both $HAuCl_4$ and thiols are soluble such as methanol, ethanol, and water. Thus, a number of publications emerged on the single-phase synthesis of thiol-stabilized Au NPs [101, 104]. Brust et al. synthesized water soluble and biocompatible Au NPs stabilized with (1-mercaptoundec-11-yl) tetraethylene glycol of size less than 10 nm with hydrophilic tetra ethylene glycol (TEG) shell and hydrophobic alkanethiol core [105]. A variety of thiolate ligands such as alkane thiolates, arene thiolates, and other functionalized thiolates have been used for the synthesized of functionalized Au NPs [106–110]. Au NPs have also been synthesized by changing both gold salt precursors and reducing agents. Moores et al. documented the synthesis of phosphine-stabilized Au NPs using $[AuCl(SMe_2)]$ complex in place of $HAuCl_4$ and sodium naphthalene ($C_{10}H_8Na$) as a reductant [111]. The formation of Au NPs was confirmed through UV-Visible spectroscopy which revealed the emergence of SPR band around 580 nm. The presence of phosphine on the Au NP surface was confirmed by FTIR and TGA analysis. IR spectra gave the peaks corresponding to in plane and out-of-plane bending vibrations of aromatic C—H bonds (700 and 750 cm^{-1}), P—C bond vibrations (760 cm^{-1}) and characteristic aromatic C–L–C vibrations (1450 cm^{-1}). TGA showed the weight loss which revealed the presence of phosphine on surface of Au NPs. Both the techniques revealed the existence of phosphine ligands on Au NP surfaces even after several washings which indicated a strong coordination the phosphine ligands and Au NPs. TEM images showed the small average particle size of Au NPs of 5.7 nm ± 1.3 and 12.7 nm ± 3.7 nm. A single-step synthesis of phosphine-stabilized Au NPs has also been achieved by reducing Et_3PAuCl with 9-BBN employed as a reducing agent [112]. The coordination between the phosphine ligand and Au NPs was studied by NMR spectroscopic technique. The particle size was determined to be 1.4 ± 0.2 nm and 1.2 ± 0.2 nm for reaction carried out at 40 and 50 °C, respectively. Further the results illustrated that the core size of Au NPs decrease with increase in reaction temperature. Other examples of synthesis of Au NPs by phosphine derivatives include triphenyl phosphine [113], 1,1-binaphthyl-2,2-dithiol [114], calixarene phosphine [115, 116], and tetrakis-(hydroxymethyl)phosphonium chloride (THPC) [117] for applications such as proactive etching agents, optics, catalysis, bimetallic nano shell formation, respectively.

A variety of alkyl thiolate-functionalized gold nanoparticles have been synthesized using a modified single-phase method, where 9-borabicyclo[3.3.1]nonane (9-BBN) served as a mild reducing agent [118]. Nitrogen and oxygen ligands containing electronegative groups such as amine, carboxyl, phenolic, and carbonyl groups have also been used for stabilization of Au NPs [119–123]. Amines have been predominantly used for this purpose. For example, octadecyl amine-stabilized Au NPs have been synthesized by Crook et al. [120]. Ligands like 4-(*N*,*N*-dimethylamino) pyridine (DMAP) have been frequently used for stabilizing Au NPs for ligand substitution reactions and in heterogenous catalysis [124, 125]. DMAP-stabilized Au NPs are synthesized via a phase transfer process by adding aqueous DMAP solution to TOAB-stabilized Au NPs [126–129]. Among oxygen-containing ligands, phenolic and carboxyl derivatives are frequently employed stabilizers which include folic acid [130], *N*-2-hydroxyethylpiperazine-*N*-2-ethanesulphonic acid (HEPES) [131], and *N*-vinylpyrrolidone [132].

Au NPs have been functionalized by either direct Au NP synthesis or by ligand substitution reactions such as halide nucleophilic substitution [133], coupling reactions such as amidic coupling by employing amino termini [134], polymerization [135], nucleophilic addition reactions [136], and click functionalization. The weakness of Au-citrate bond enables it to be substituted or functionalized with stronger ligands such as thiolates. Such thiolate functionalized Au NPs have been synthesized by Mulvaney and Giersig from citrate-stabilized Au NPs by substituting citrate ligands with thiol ligands [137]. This strategy was later used by Mirkin et al. to synthesize

thiolate DNA functionalized Au NPs [138]. Functionalization of citrate-stabilized Au NPs with thiolated PEG was also carried out for use in in vivo computer tomography as a contrast agent [139]. Nitrile and amine-terminated dendrimer functionalized Au NPs have been synthesized by reaction between poly(propyleneimine) dendrionic thiols and citrate-stabilized Au NPs (19.5 nm) for drug delivery application [140]. Alkylthiolate ligands on Au NP surface have also been substituted by functionalized alkyl thiolate ligands by ligand substitution reaction by employing the corresponding functional thiols [141]. There are various reports where some other labile ligands on the Au NP surface have been substituted by thiol ligands [142–144]. However, ligand exchange reaction suffers some major drawbacks such as chances of incomplete ligand substitution and irreversible aggregation of the Au NPs. There is also a chance of incompatibility between new ligand and the initial medium in which Au NPs are already dispersed [145].

In summary, this section outlines several methods for synthesizing gold nanoparticles (Au NPs) using chemical reduction techniques. The synthesis process typically comprises two key steps: the reduction of gold salt and the stabilization of the resulting Au NPs. Various reducing agents, including borohydrides, HA, amino boranes, and organic molecules like citric acid, are utilized in the reduction step. The subsequent stabilization of Au NPs involves employing a diverse array of stabilizers such as trisodium citrate, sulfur-containing ligands, oxygen-based ligands, phosphorus-based ligands, nitrogen-based ligands, polymers, surfactants, and dendrimers. The Turkevich method, established in 1951, stands as a prominent technique for Au NP synthesis, involving the reduction of gold salt in an aqueous sodium citrate solution to yield wine-red Au NP solutions. Various modifications of this method by different research groups have been investigated to explore the impacts of factors like pH, reaction temperature, citrate concentration, and gold salt concentration on the size, shape, and distribution of Au NPs.

The section further explores the utilization of ascorbic acid as a reducing agent and CTAB as a shape-directing agent for the synthesis of anisotropic Au NPs. It highlights how the order of reagent addition and the introduction of DCA can impact the size, shape, and reaction kinetics of Au NPs. Another method, pioneered by Brust and Schiffrin, employs TOAB as a phase transfer agent to transfer $AuCl^{4-}$ ions from the aqueous phase to the organic phase, resulting in the production of thermally stable Au NPs. This Brust–Schiffrin approach has since been enhanced by using methanol as a medium for Au NP synthesis without the need for a phase transfer agent. Various ligands, such as alkyl thiolates, nitrogen and oxygen ligands, and phosphine derivatives, have been employed to stabilize and functionalize Au NPs. Ligand substitution reactions, including halide nucleophilic substitution, coupling reactions, polymerization, nucleophilic addition reactions, and click functionalization, have been utilized to functionalize Au NPs. The section underscores the importance of ligand exchange reactions while recognizing their limitations, such as incomplete ligand substitution and the potential for irreversible aggregation of Au NPs.

1.4.2 Electrochemical Method

The electrochemical method for the fabrication of transition metal NPs was first used by Reetz et al. [146, 147] employing tetra alkyl ammonium salts as stabilizer metal nanoclusters in nonaqueous medium. Electrochemical synthesis of Au NPs has been achieved using various quantities of surfactant, tetradodecylammonium bromide TTAB as stabilizer [148]. The particle size of the Au NPs varied with the amount of the TTAB surfactant, temperature, and current density used. The particle diameter decreased from 58.3 ± 12.6 to 10.6 ± 6.5 nm with increase in amount of the TTAB from 1 to 90 mg (Figure 1.4A). Thus, the particle size was found to be inversely proportional to the amount of the surfactant used. The Au particle diameter was found to vary directly with the current density. The particle diameter increased from 53.7 ± 17.2 to 12.2 ± 7.3 nm with an increase in the current

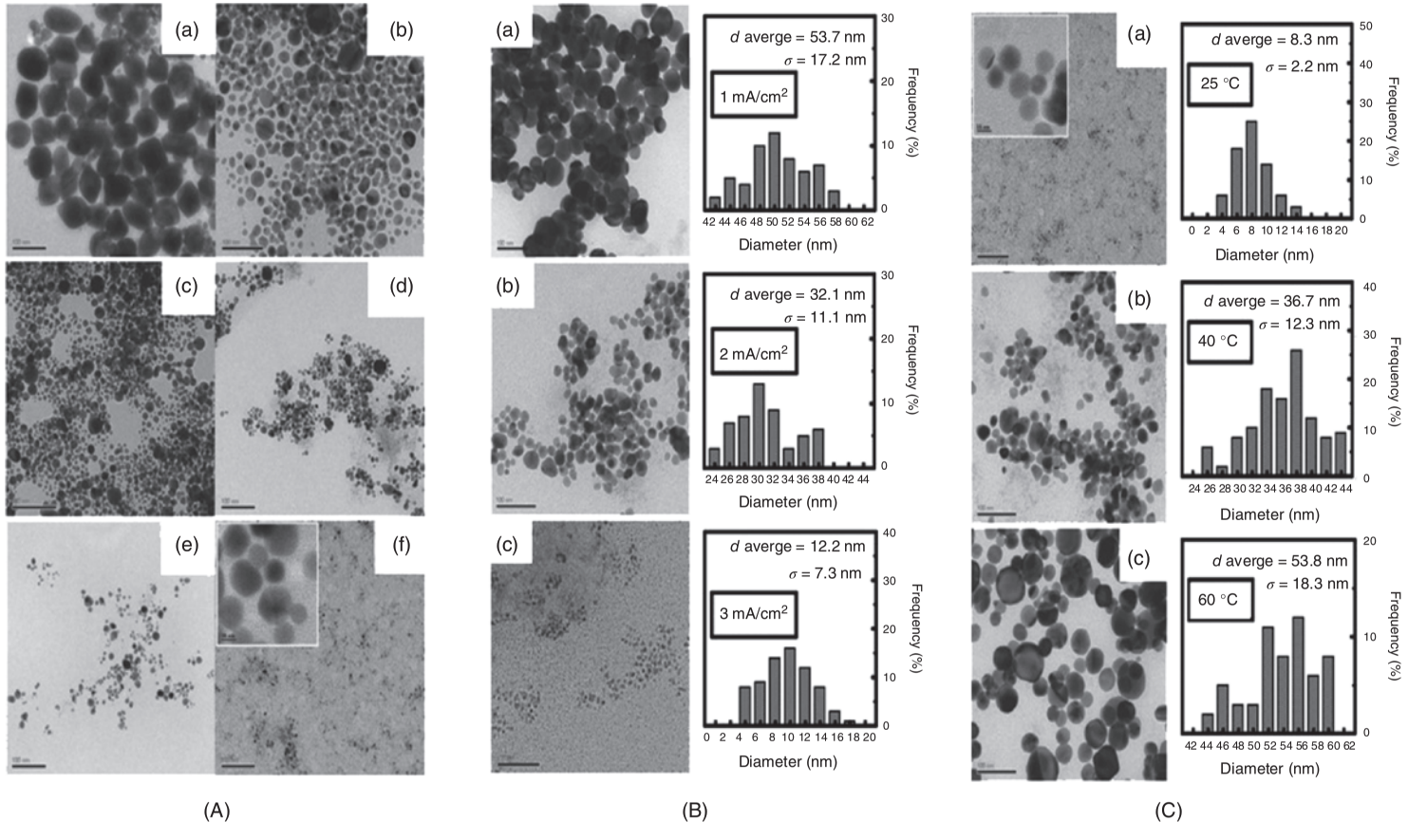

Figure 1.4 (A) Transmission electron microscope images of gold nanoparticles produced with varying quantities of TTAB surfactant, depicted as 1 mg (a), 10 mg (b), 30 mg (c), 50 mg (d), 70 mg (e), and 90 mg (f); the scale bar denotes a length of 100 nm. (B) Transmission electron microscopy images of gold nanoparticles generated under different current densities, specifically at 1 mA/cm^2 (a), 2 mA/cm^2 (b), and 3 mA/cm^2 (c), the scale bar indicates a size of 100 nm. (C) Transmission electron microscope pictures of gold nanoparticles produced under distinct growth temperatures, namely at 25 °C (a), 40 °C (b), and 60 °C (c); the scale bar denotes a size of 100 nm. Source: Reproduced with permission from Huang et al. [148]/IOP Publishing.

density from 1 to 3 mA/cm^2 (Figure 1.4B). The cathode was found to be strongly gold colored at the current density of 3 mA/cm^2. This decrease in particle size was also confirmed by blue shift in the SPR peak from 538 to 523 nm as the particle size decreased. Effect of varying growth temperature on the Au particle size was also studied for a constant current density and surfactant amount (30 mg, 2 mA/cm^2). Higher temperature resulted in heavy gold plating of the electrode. The particle size of Au NPs increased from 8.3 ± 2.2 to 53.8 ± 18.3 nm as the temperature raised from 25 to 60 °C (Figure 1.4C). Further UV-Visible spectroscopy revealed a red-shifting of the SPR peak from 521 to 538 nm with increase in particle diameter from 8.3 to 53.8 nm. Au NPs were synthesized by electrochemical deposition technique employing ITO film coated glass electrode using 0.1–1 mM $HAuCl_4$ in 0.5 M H_2SO_4 solution. Au NPs with size between 70 and 300 nm were produced under variable $HAuCl_4$ concentrations and deposition times [149]. Au NPs were found dispersed on the electrode surface with higher deposition time resulted in bigger Au NPs, whereas higher $HAuCl_4$ concentration resulted in larger concentration of Au NPs on the electrode surface. ITO-coated glass electrodes based Au NP formation by electrochemical method has been reported by various research groups [150–152]. High density and large surface area gold NP arrays were synthesized on a silicon substrate by electrochemical deposition technique using high overpotential. It was observed that high overpotential led to the fast nucleation and small particle size. Electrochemical deposition of Au NPs on *n*-doped silicon substrate by employing various electrochemical techniques with variable reaction parameters such as pH, temperatures, reagent concentration, deposition time, and reaction kinetics have been studied [153]. Of all the electrochemical methods, cyclic voltammetry was found to produce large-sized Au NPs due to electrodeposition taking place at the slower rate. Further for the similar reaction conditions such as same temperature and pH, the particle size was observed to be less in diffusion regime as compared to electrochemical deposition process. Various gold nanostructures were synthesized by one-step electrochemical deposition on GCE employing 5 mM $HAuCl_4$ solution [154]. The morphologies of Au NPs were controlled by changing the pH and temperature. For example, hierarchical waxberry-like Au NPs with high catalytic performance for oxygen reduction were produced at pH of 4 which also exhibited remarkable super hydrophobicity. The contact angle was found to increase with rise in temperature and deposition time. Electrochemical deposition of Au NPs was carried out in a solution containing thiosulfate and sulfite to study the nucleation and crystal growth of Au NPs on the GCE [155]. It was observed that electrodeposition for one second resulted in the production of uniform-sized Au NPs with diameters of 80 ± 5 nm. Coalescence of Au NPs was observed for 10 s, whereas large aggregates of Au NPs with diameters of 100–300 nm were obtained for 100 s of electrodeposition. Various research groups have reported the fabrication of Au NPs by the electrochemical method on a GCE [156–160]. A method known as substrate-enhanced electrolytic deposition has been used for the conversion of Au ions into Au NPs on CNTs supported on metal substrate which is having lower reduction potential than Au ions itself [161]. Here CNTs act as templates or cathode for deposition other than the reducing agents. Here size distribution of electrodeposited Au NP size on side walls of CNTs can be controlled by various parameters gold precursor concentration, nucleation potential, and deposition time. Since the particle size of the electrodeposited Au NPs on CNTs has bigger particle size usually between 50 and 500 nm, hence obtaining smaller Au NP with good dispersion is a challenge. This method produces Au NPs on CNTs, which act as a sensitive platform for biosensing applications, with signal intensity three times higher than nonmodified carbon paste electrodes [162]. Au NPs with cauliflower morphology with size of 200 nm have been electrodeposited on CNT-modified electrode, which exhibited good electrocatalytic activity for oxidation of dopamine, ascorbic acid, and uric acid [163]. Au NPs of different morphologies have been produced on a graphitic surface which in turn were produced by micromechanical cleavage of organic graphitic flakes on silicon wafer with SiO_2 insulating layer of 300 nm [164]. Room temperature resulted in production of 4 nm

thick dense cluster of Au on graphene surface [165]. Au polygons were obtained at 100 °C and irregular Au islands at 80 °C [166]. Gold dendrites were obtained as the substrate was cooled from 80 °C to room temperature [166]. As the temperature of the substrate reached above 200 °C, coalescence and growth resulted in the production of three dimensional and geometrical metal islands [166]. Au NPs with positive surface charge with a particle diameter of 2–6 nm have been self-assembled on graphene sheets functionalized with 1-pyrene butyric acid [63]. The synthesis was achieved by simple mixing of the aqueous dispersion of various components where electrostatic force acted as a driving force for Au NP formation. An amount of Au NPs assembled on functionalized graphene sheets could be easily modulated by changing the weight ratio of the various components. Further the functionalized graphene sheets exhibited the loading capacity on Au NPs up to 300 times more than its own weight. Glassy carbon electrode covered by this Au NP-G composite exhibited electrochemical stability and electrocatalytic ability. Furthermore, the Au NP-G composite-modified GC electrode acted as an efficient biosensor for electrochemical detection of uric acid with good sensitivity. Porous Au nanofoams have been prepared by electrochemical deposition of 0.1 M $HAuCl_4$ and 0–3 M NH_4Cl [167]. The deposition of Au took place on a Pt/Ti/Si electrode within the range of E = 0 to −8 V over the period of 15–120 seconds. The gold nanofoams had a pore size of 0.01–10 μm and was ascertained to be impurity free. It was observed that Au foam deposition was possible only when enough NH_4Cl was incorporated to the electrolytic solution as a hydrogen source. The Au nanofoam had a well-known nanoporous structure with promising sensing and electrocatalytic applications. Au nanorods with two different aspect rations have been prepared by electrochemical reduction technique using cationic surfactant as a soft template for shape-directed synthesis [168]. The synthesized Au nanorods had a mean diameter of 10 nm. The electrochemical method is found to be superior to other methods due to the use of modest equipment, low processing temperatures, low cost, and high purity.

In summary, the section discusses the electrochemical method for synthesizing transition metal nanoparticles (NPs), focusing on gold nanoparticles (Au NPs). The electrochemical method was initially utilized by Reetz et al., using tetraalkyl ammonium salts as stabilizers in a nonaqueous medium for metal nanoclusters. The synthesis of Au NPs through electrochemical methods involves varying parameters such as surfactant quantity, temperature, and current density. The particle size of Au NPs is found to be inversely proportional to the amount of the surfactant (TTAB) used, with smaller particles obtained at higher surfactant concentrations. Additionally, the current density and growth temperature are identified as factors influencing particle size. Higher current density and lower growth temperature lead to smaller Au NPs. The synthesis of Au NPs through electrochemical deposition on ITO film-coated glass electrodes is discussed, with variations in $HAuCl_4$ concentrations and deposition times resulting in Au NPs of different sizes.

Different research groups have reported the electrochemical deposition of Au NPs on various substrates, including silicon, silicon with CNTs, and graphitic surfaces. The morphologies of the Au NPs are controlled by adjusting pH, temperature, and deposition time. The text highlights the use of cyclic voltammetry, which produces larger-sized Au NPs due to slower electrodeposition rates. A method called substrate-enhanced electrolytic deposition is introduced, where Au ions are converted into Au NPs on CNTs supported on a metal substrate. The control over the size distribution of gold nanoparticles (Au NPs) electrodeposited onto carbon nanotubes (CNTs) can be achieved by manipulating factors like the concentration of the gold precursor, nucleation potential, and deposition time. This method is particularly useful for biosensing applications. The electrochemical deposition technique is praised for its simplicity, low processing temperatures, cost-effectiveness, and high purity in synthesizing Au NPs. Various morphologies, including cauliflower-like structures, dendrites, and nanofoams, are achieved through this method, demonstrating its versatility for different applications such as electrocatalysis and sensing. Overall, the

electrochemical method is presented as a superior technique due to its use of modest equipment and its potential for low-cost, high-purity synthesis of metal nanoparticles.

1.4.3 Polymer and Dendrimer-Mediated Synthesis

Various promising potential applications of gold nanoparticles such as photocatalysis, chemisorption, sensing, therapeutic, and magnetic device fabrication are dependent upon its size and morphology [26]. Controlling such features of the gold nanoparticles is a challenging and attractive with tremendous progress made in this direction. Several novel strategies have been developed for this purpose. To control the size and morphology of the Au NPs, various synthetic methods involve several chemical or biological entities have been employed for this purpose. It has been shown by various research studies, synthesis of Au NPs in the presence of surfactants can greatly affect the size shape, stability, and particle size distribution [18]. Employing polymeric stabilizers greatly enhances the long-term stability, improves the solubility, and provides amphiphilicity of Au NPs. Polymers also provide surface density, improve compatibility, and tailor the properties of Au NPs. Mention of polymer-stabilized Au NPs dates to 1718 in Helcher's treatise which report water soluble starch-stabilized Au NPs. However, nanotechnology has provided a rapid momentum for synthesizing polymer-stabilized Au NPs for use in various applications such as optics, catalysis, and biology. Two major techniques used for the fabrication of polymer-stabilized Au NPs are "grafting to" and "grafting from" techniques. Grafting from technique involves the attachment of polymer molecules on the Au NP surfaces in presence of radical initiators. This approach can be considered as a technique of functionalization of Au NPs. In contrast, the grafting-to method utilizes polymers containing sulfur, phosphorus, or nitrogen groups either at the terminus or within the polymer chain to stabilize gold nanoparticles (Au NPs). This route is synonymous with the Brust–Schiffrin process or ligand substitution method. Here the gold salt precursor is first mixed with functionalized polymer and latter reducing agent is added to obtain polymer-stabilized Au NPs. Various ligand polymers have been used for synthesized Au NPs such as thiolated PEG, polystyrene (PS), poly(*N*-isopropylacrylamide) (PNIPAM), poly(vinyl pyridine) (PVP), five-arm PEG-b-PCL star block copolymers and amine groups containing ligands such as poly(ethylenimine) (PEI), amine, and arsenic group containing poly(acryloylaminophenylarsonic acid) (PAAPHA), ionic polymers, poly(*N*-vinyl caprolactam) (PVCL) functionalized with oethyl-S-(1-methoxycarbonyl)ethyl dithiocarbonate, poly(*N*-vinyl caprolactam) (PVCL), and polymer ligands (DDT-PVAc and PTMP-PVAc) functionalized with thioether groups. Size of Au NPs can be regulated by varying the polymer/Au ratio, and the change in particle size can be easily detected by a change in intensity of SPR peak. Certain polymers serve dual roles as both stabilizers and reducing agents such as PS and PAAPHA. However, the problem with such reducing agents is that due to their weak reducing ability, Au NPs formed attain bigger particle sizes in comparison to those formed with strong reducing agents such as $NaBH_4$. Gold nanoparticles have also been fabricated using functionalized co-polymers. For example, thermoresponsive hybrid core–shell Au NP have been synthesized in situ using thiol and amino functionalized poly (nisopropylacrylamide) (NIPAM)-b-(glycidyl methacrylate) (GMA) (poly NIPAM-b-GMA) as template for stabilizing Au NPs inside polymer shells. Synthesis of Au NPs by ligand substitution reaction has a significant advantage in that the Au nano seeds synthesized by Turkevich or Brust method are nearly monodisperse which after ligand substitution reaction leads to the formation of monodispersed polymer-stabilized Au NPs. PEO-b-PS-b-P4VP-stabilized AuNPs were obtained by Azzam et al. by adding PEO-b-PS-b-P4VP to TOAB-stabilized Au NP solution in toluene with subsequent stirring for 24 hours. Various research groups have synthesized polymer-stabilized Au NPs by this technique. "Grafting to" technique employs polymer as templates for the stabilization of Au NPs as core–shell structures. A simple solution phase

synthesis was employed to reduce gold ions into Au NPs of controlled size and shape in presence of poly-(methylphenylphosphazene) (PMPP) of various concentrations which prevents the unlimited growth of the gold crystals under ambient temperature [169]. The stability of the polymer-mediated Au NPs can be further enhanced by encapsulation with block co polymers. For example, Xinjiao et al. documented the fabrication of Au NPs dimer systems using citric acid, which were stabilized in this state by further encapsulation within 154 block copolymers of polystyrene and poly (acrylic acid) [170]. Among various polymers, DNA is considered to be a good candidate for the stabilizing gold nanoparticles at various sizes and shapes due to its advanced features such as specificity, photochemical stability, and mechanical rigidity [171, 172]. Polymers have proved to be one of the best choices for the shape-directing synthesis and stability of gold nanoparticles [173, 174].

Dendrimers are synthetic macromolecules which are cauliflower shaped, highly branched with well-defined structure and composition [175, 176]. Dendrimers are used to stabilize Au NPs by various ways such as entrapping them into the macromolecular structure by the N, S, O, and P containing functional groups and by steric effects [177–181]. Such Au NPs are called as dendrimer-encapsulated Au NPs (Au-DENS). Au NPs are also stabilized by encapsulation by small dendrimer molecules at their surface boundaries which are known as dendrimer stabilized Au NPs. Au NPs can function as dendrimer cores, with coordinating ligands situated at the focal points of the dendrons to stabilize them. Such Au NP systems contain functional groups at the periphery of the dendrons, hence they are found to be useful for application as redox sensors [182, 183]. Dendrimer-encapsulated Au nanoparticles were first synthesized using polyamidoamine (PAMAM) as stabilizers by Crooks and Tomalia's research groups [184–186]. Since then, several dendrimers stabilized Au NPs of various types have been synthesized. Various factors which govern the synthesis of dendrimer-stabilized Au NPs such as dendrimer to Au Salt ratio [187–189] and type of functional groups in the dendrimer [190–193]. PEG dendrimer-stabilized Au NPs have been synthesized and stabilized by 1,2,3-triazole coordination by Click method [194]. In this method, Au NPs are either encapsulated by large dendrimer macromolecules or surrounded by small dendrimer molecules which are known as zeroth generation dendrimers. Au NPs have been synthesized using phosphorylcholine-functionalized dendrimers as stabilizers for use in biosensing applications due to good stability and controlled surface properties [195]. The inner structure of dendrimer-stabilized Au NPs has been investigated by Voelker's group using NICISS technique [191]. Cho et al. [196] reported the synthesis of four types of Newkome-type Dendron-stabilized Au NP (Figure 1.5A). The study encapsulates a comprehensive exploration of gold nanoparticles (AuNPs) conjugated with a variety of dendrons. It commences with the synthesis phase, which introduced four distinct dendron types, encompassing both two-directional dendrons with cystamine cores (G1—COOH and G2—COOH), a one-directional monothiol dendron (SH—G1—COOH), and a unique "di-anchored" dendron (TA—G1—COOH). The dendron conjugates, denoted as Au—G1—COOH, —G2—COOH, —SH—G1—COOH, and —TA—G1—COOH, were achieved through the amalgamation of dendron solutions with citrate-stabilized gold colloids. The characterization of these conjugates is delineated, featuring a multitude of analytical methods such as DLS (Figure 1.5B), UV-vis spectroscopy, XPS, and AFM (Figure 1.5C). These analyses unveiled crucial attributes, including optimal *z*-average sizes, minor redshifts in the SPR band, and highly uniform size distributions. The application of XPS further validated the presence of essential chemical functional groups on the AuNPs, while it became evident that steric effects wielded significant influence over the surface coverage of dendrons on the AuNPs. The stability studies constituted a pivotal aspect of the study, elucidating that the conjugates retained stability under conditions pertinent to biological contexts. These studies demonstrated the remarkable resilience of the conjugates across various media, including high-saline environments and a spectrum of pH values. Notably, the conjugates exhibited robustness even under highly acidic

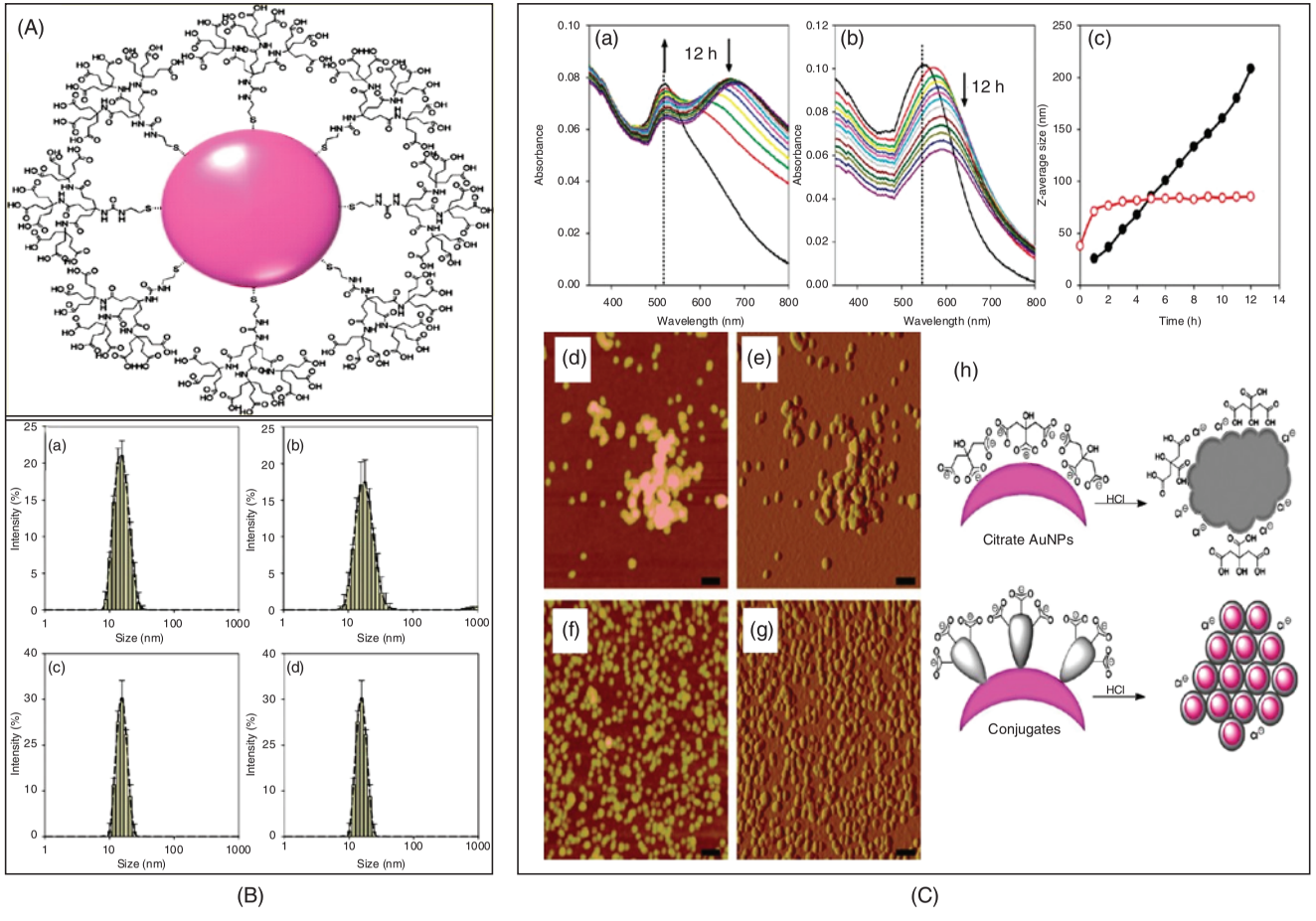

Figure 1.5 (A) Schematic representation of Newkome-type stabilized Au NPs. (B) DLS intensity-weighted size distributions of Au conjugates using NNLS: (a) Size profiles of Au-G1-COOH, (b) size profiles of Au-G2-COOH, (c) size profiles of Au-SH-G1-COOH, (d) size profiles of Au-TA-G1-COOH. (C) Time-dependent exploration of AuNPs in acidic environment (pH 3): (a) UV-vis absorbance patterns for citrate-stabilized AuNPs, (b) UV-vis absorbance patterns for Au-TA-G1-COOH with a notable 520 nm marker, (c) evolution of Z-average sizes over time for citrate-stabilized AuNPs and Au-TA-G1-COOH. Atomic force microscopy (AFM) imaging outcomes: (d) AFM height images of citrate-stabilized AuNPs, (e) AFM amplitude images of citrate-stabilized AuNPs, (f) AFM height images of Au-TA-G1-COOH, (g) AFM amplitude images of Au-TA-G1-COOH. Illustrating the mechanism of cluster formation: (h) Comparative schematic of cluster formation mechanism in citrate-capped AuNPs and AuNP-dendron conjugates under acidic conditions. Source: (a, b, c, h) Reproduced with permission from Cho et al. [196]/American Chemical Society.

conditions, with pH 3 causing minimal disruption. The revelation that chemical stability was governed by both dendron size (branch effect) and the S/Au ratio (Sulfur coverage effect) was underlined, with the latter emerging as the more prominent factor. Lastly, the paper addressed the issue of shelf life and explores the viability of lyophilization for semidry storage. Impressively, the conjugates proved to maintain stability over a minimum of six months under standard laboratory conditions. Furthermore, the preliminary foray into lyophilization hinted at the potential for extending their shelf life while retaining colloidal stability after resuspension.

In short, the section discusses the synthesis of Au NPs using polymer and dendrimer-mediated methods, exploring their potential applications across diverse fields such as optics, catalysis, and biology. The size and morphology of Au NPs are crucial for their functionalities, and the section delves into strategies for controlling these features. Polymeric stabilizers are highlighted for enhancing the long-term stability, solubility, and amphiphilicity of Au NPs. Two major synthesis techniques, "grafting to" and "grafting from," are discussed. The former involves using polymers with specific end groups to stabilize Au NPs, while the latter attaches polymer molecules to Au NP surfaces in the presence of radical initiators. Various ligand polymers, including thiolated PEG, polystyrene (PS), and poly(*N*-isopropylacrylamide) (PNIPAM), are employed to synthesize polymer-stabilized Au NPs. The size of Au NPs can be controlled by adjusting the polymer-to-gold ratio, and some polymers act as both stabilizers and reducing agents. Functionalized co-polymers, such as thermoresponsive hybrid core–shell Au NPs, are synthesized in situ using templates for stabilizing Au NPs inside polymer shells. Ligand substitution reactions are highlighted for their advantage in producing nearly monodisperse polymer-stabilized Au NPs.

The section also explores the use of block copolymers for enhancing the stability of polymer-mediated gold nanoparticles. DNA is recognized as a suitable candidate for stabilizing Au NPs due to its specificity, photochemical stability, and mechanical rigidity. Dendrimers, synthetic macromolecules with a highly branched and well-defined structure, are discussed as stabilizers for Au NPs. Different types of dendrimer-stabilized Au NPs, such as dendrimer-encapsulated Au NPs (Au-DENS) and dendrimer-stabilized Au NPs, are synthesized. Factors affecting the synthesis, including dendrimer-to-Au salt ratio and the type of functional groups in the dendrimer, are explored. The section concludes with a study by Cho et al., which investigates gold nanoparticles conjugated with various dendrons. The study introduces four distinct dendron types and discusses their synthesis, characterization, stability, and potential applications. The conjugates demonstrate resilience in various conditions, including high saline environments and different pH values, and exhibit stability over an extended period, even under lyophilization for semidry storage.

1.4.4 Photoreduction Method

The photoreduction process has demonstrated to be one of the most effective methods for synthesizing single-crystalline Au NPs [197]. Ultraviolet light spans between visible light and ionizing radiations and have the wavelength from 100 to 400 nm [198, 199]. UV light can be categorized into three groups, viz., UV-A having wavelength from 315 to 400 nm, UV-B with wavelength from 290 to 315 nm, and UV-C with wavelength between 100 and 290 nm [197]. In UV photochemical synthesis of Au NPs, the reducing agent may or may not facilitate the reduction of metal ions [200, 201]. In some cases, UV radiation is absorbed by the photosensitizer such as ketones, which produce free radicals by photolysis. These free radicals facilitate the reduction of metal ions into metal atoms. The metal atoms form metal cluster which subsequently grow to form metal nanoparticles [202, 203].

Shape-controlled synthesis of Au NPs by UV-irradiation technique was successfully achieved by Shengchun Yang et al. [204]. Size and shape-controlled synthesis of Au NPs by photochemical

technique was found to be more effective in presence of various macromolecules such as dendrimers and surfactants. UV radiation encourages the photochemical reduction of aqueous Au (111) solution, whereas macromolecules act as soft templates for the production of Au NPs, thereby providing the steric hindrance and preventing the agglomeration of the particles [205]. In most cases, the particle size decrease with increase in the degree of polymerization. Heparin-assisted synthesis of negatively charged functionalized gold nanoparticles was obtained using photochemical synthesis method and were used for the SERS [206]. Au NPs of the size of 80 nm were obtained by irradiation of chloroauric acid with highly energetic γ-radiations. These highly energetic radiations result in the fast nucleation of the metal ions thereby giving no or less time to control shape of the resulting nanoparticles. However, UV radiations being less energetic results in the formation of radicals with lifetime of the order of milliseconds, which results in reduction of the metal ions over longer time periods, hence, provides the opportunity to exert control over the particle morphology [207]. During photochemical synthesis, morphology of Au NPs can be regulated by various reaction parameters such as temperature, pH, precursor concentration, stabilizers, and reaction time [208, 209]. The influence of pH and reagents on the fabrication of Au NPs was studied by Rodriguez et al. using UV lamp (256 nm). The results demonstrated that basic solution (pH 9) resulted predominantly in the formation of nanospheres [209]. The UV-Vis studies revealed only one SPR band at 515 nm. Yet, in acidic solutions with pH levels of 3 or 5, nanorods were generated, exhibiting two SPR bands. Cheng et al. [210] similarly explored the impact of pH on Au NP morphology and reported findings consistent with those described earlier. The effect of pH on the size and morphology of Au NPs was also studied by Unal et al. using red cabbage extract as a reducing and a stabilizing agent under the influence of UV light source [211]. Anthocyanins, which are natural pigments and secondary metabolites found in RCE, are detailed as key components responsible for the pH-dependent color variations in the synthesized AuNPs. The synthesis process, depicted in Scheme (Figure 1.6A), is described as a step-by-step transformation involving anthocyanin-Au^{3+} complex formation, charge transfer, and the ultimate production of stable zero-valent AuNPs. Anthocyanins are highlighted as efficient photo-reductants. The results of AuNP characterization at pH 7.4 are then presented, demonstrating time-dependent Au formation, the transition to colloidal AuNPs, and their stable, spherical shape. The impact of RCE extract concentrations on AuNP formation is also discussed, with higher concentrations favoring stable AuNP synthesis, while lower concentrations lead to inadequate reduction. Furthermore, the influence of pH on AuNP formation is examined, showing that more stable and colloidal AuNPs are obtained at pH 11 compared to pH 2.5 (Figure 1.6B). The impact of using single or multiple reducing or stabilizing agents on AuNP formation is addressed, with anthocyanins from RCE acting efficiently as both reducing and stabilizing agents (Figure 1.6C). The colloidal stability of RCE AuNPs in different NaCl concentrations is highlighted, emphasizing their enhanced stability compared to commercial AuNPs. Finally, the RCE AuNPs are discussed as effective catalysts for the conversion of 4-nitrophenol to 4-aminophenol (4-NP to 4-AP) based on their catalytic performance. The findings suggest that RCE AuNPs could have potential applications in various scientific and biomedical fields due to their stability and catalytic capabilities. The morphology of Au NPs is also influenced by the concentration of the precursor [212]. In most of the Au NPs synthesis, $HAuCl_4$ is the most commonly employed gold precursor [205, 209, 213, 214]. Silver nitrate has also been used to produce anisotropic Au NPs, as silver ions directly contribute to the emergence of the longitudinal SPR peak in Au NP solutions. The impact of varying concentrations of $HAuCl_4$ and $AgNO_3$ on the morphology of Au NPs was investigated by Sanabria-Cala et al. [215] using UV light (256 nm) in presence of CTAB, a cationic surfactant. Their findings indicated that an increase in the concentration of $HAuCl_4$ led to the formation of spherical Au NPs, attributed to the constrained growth of CTAB micelles. Higher concentrations of silver nitrate favor the

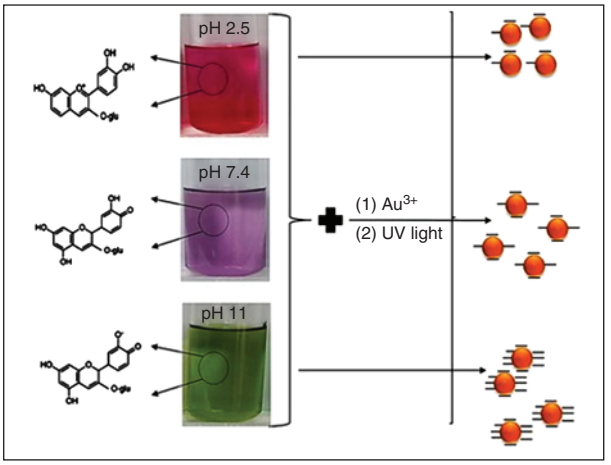

(A)

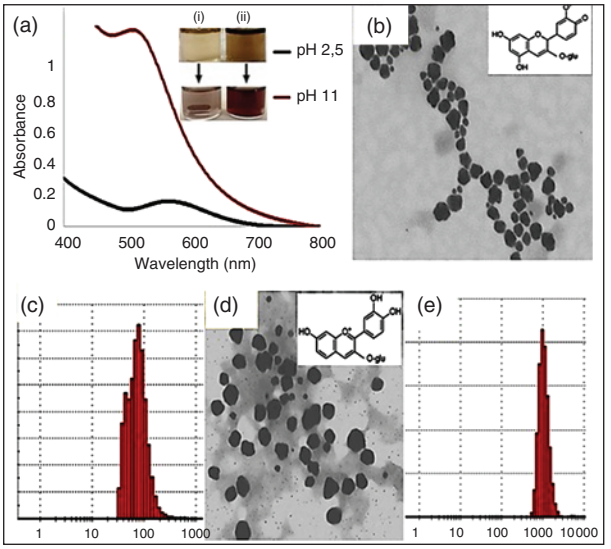

(B)

Figure 1.6 (A) Depiction of pH-dependent RCE Au NPs when exposed to UV irradiation. The color of RCE solutions, the electronic structure of anthocyanin, and the charge density on the surface of RCE Au NPs directly correlate with the reaction pHs. (B) Analysis of pH-dependent RCE Au NPs. (a) UV–Vis spectra of the Au NPs synthesized at pH 2.5 (depicted by the black line) and pH 11 (indicated by the red line). Inset in (a) Visual representation of the color of Au NP solutions at pH 2.5 (i) and pH 11 (ii). (b) Scanning electron microscopy (SEM) image of the Au NP formed at pH 11. Inset in (b) the molecular structure of anthocyanin carrying a negative charge. (c) Size distribution of the Au NP synthesized at pH 11. Similar characterization is performed for Au NPs formed at pH 2.5. (d) SEM image of the Au NPs. Inset in (d) the molecular structure of anthocyanin with a positive charge. (e) Size distribution of the Au NPs. (C) Analysis of the size and shape of Au NPs formed by varying reducing agents/capping agents (a) UV–Vis spectra showing Au NP absorption peaks. RCE alone: 537 nm (blue). Adding ascorbic acid to Au^{3+} shifted LSPR to 559 nm (red) and 547 nm (black) before and after RCE addition. (b) TEM image showing 27 nm Au NPs with RCE alone. (c) DLS spectra showing 70 nm effective diameter with RCE alone. (d) TEM image showing Au NPs size range (18–53 nm) with RCE added to Au^{3+} and ascorbic acid. (e) TEM image showing Au NPs size range (21–35 nm) with ascorbic acid added to Au^{3+} and RCE. (f) DLS spectra showing 185 nm effective diameter with RCE added to Au^{3+} and ascorbic acid. (g) DLS spectra showing 90 nm effective diameter with ascorbic acid added to Au^{3+} and RCE. Source: (a–c) Reproduced with permission from Unal et al. [211]/Elsevier.

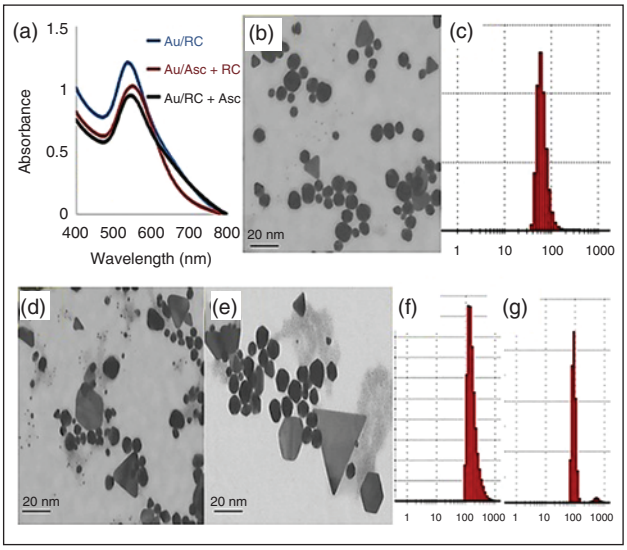

(C)

Figure 1.6 (*Continued*)

formation of anisotropic Au NPs. Numerous photochemical techniques for synthesizing Au NPs have utilized stabilizing agents including trisodium citrate, PVP, Triton X-100, citric acid, chitosan, and glycine [205, 213, 216–218]. Shiraishi et al. [219] investigated the influence of citric acid concentration on the morphology of Au NPs under UV radiation (254 nm). Higher concentration of citric acid produced smaller-sized Au NPs in higher yields which is indicated by the amplified intensity of the SPR peak around ~530 nm with increasing concentration of citric acid. Higher concentration of citric acid resulted in fast nucleation which subsequently led to the generation of tiny Au NPs. In some cases, formation of Au NPs was induced by UV radiations alone without the use of any chemical or biological reducing agent. For instance, Teixeira et al. fabricated Au NPs using UV light and polyethyleneimine (PEI) as the stabilizing agent without the use of any external reducing agent [217]. The influence of adjusting the concentration of $HAuCl_4$ (precursor) and PEI ([PEI] : [$HAuCl_4$] ratios of 5 : 1, 10 : 1, and 20 : 1) on the morphology of Au NPs was investigated. It was observed that Au NP formation did not occur in absence of PEI which indicated that it played a key role in the nucleation of Au atoms for the subsequent formation of Au NPs. Further increase in the ratio of PEI to precursor concentration led to the production of spherical Au NPs. Surfactants serve as commonly employed stabilizing agents, playing a pivotal role in the generation of Au NPs with diverse morphologies. Surfactants act as templates which regulate the growth the Au NPs and direct their shape and size [220]. Various types of surfactants have been used for this purpose such as anionic surfactant, e.g., SDS, SDBS, cationic surfactants such as CTAB, DTAB, and nonionic surfactants such as Tween X-80, Triton X-100, and hydrogenated castor oil (HCO). The nature of the surfactant and their structure also affects the NP size. For instance, the study by Shang et al. [221] systematically explored the influence of spacer length and hydrophobic chain length within gemini surfactants on the properties of synthesized gold nanoparticles. Gemini surfactants, specifically 16-s-16, were the focus of the investigation, varying the spacer length (s) through values of 3, 4, 6, 10, and 12. The research uncovered a fascinating interplay between these molecular parameters and the resulting nanoparticle properties. In the context of spacer length, initial observations from UV-Visible spectra of the $HAuCl_4$ solution revealed a charge transfer band at 222 nm and a moderate D–d transition band at 290 nm. However, after exposure to irradiation, a significant shift

occurred, with the D–d transition band moving to 320 nm. When Gemini surfactants were introduced to the $HAuCl_4$ solution, the quaternary amine groups within these molecules interacted with the negatively charged $AuCl_4$ ions, leading to the formation of turbid suspensions. Crucially, after 12 hours of irradiation, these suspensions transformed into transparent solutions with a distinct purple color, implying the successful generation of Au NPs. The UV-Visible bands of these NPs displayed a notable absorption peak at around 540 nm, characteristic of the gold plasmon band. Importantly, the spacer length played a pivotal role in determining the absorption peak's position. Longer spacer lengths led to a blue-shift in the wavelength. This trend was further corroborated through TEM and AFM characterization, which confirmed that particle size exhibited an inverse relationship with spacer length, decreasing from about 22 to 7 nm as spacer length increased. This intricate relationship between spacer length and nanoparticle properties unveiled the potential for fine-tuning gold nanoparticles according to specific design requirements. The study delved into the effect of hydrophobic chain length while maintaining a consistent spacer length. This analysis demonstrated that the size of synthesized gold nanoparticles increased with the extension of the hydrophobic chains, with a significant influence on the absorption wavelengths. When the chain length was increased from 16 to 18, the impact of the hydrophobic chain on nanoparticle properties became less pronounced. In particular, it led to a red-shift in the absorption wavelengths. This experimental exploration showcased the pivotal role that both spacer length and hydrophobic chain length play in modulating the properties of gold nanoparticles, offering a glimpse into the tailored design of these nanoparticles for various applications. The research extended to investigate the synthesis of gold nanoparticles using traditional surfactants, including anionic (SDBS, SDS), cationic (DTAB, CTAB), and nonionic (Triton X-100) surfactants. The choice of surfactant was revealed to significantly impact the size and properties of the generated Au NPs. In particular, cationic surfactants led to the production of smaller nanoparticles. While anionic and nonionic surfactants produced nanoparticles with different characteristics. The fundamental role of surfactants in mediating the production of Au NPs was evident, with their presence leading to transparent solutions with a distinct purple hue, in comparison to the formation of macro-scale gold particles in the absence of surfactants. The study also proposed a mechanism for the formation of Au NPs in the presence of cationic gemini surfactants. This mechanism hinged on the photolysis and reduction of $(Au^{III}Cl_4)$ ions dissociated from $HAuCl_4$. These ions were reduced to form Au metal, a process facilitated by the micelles formed by surfactants and their interaction with ions. Importantly, both spacer length and hydrophobic chain length influenced the aggregation of these micelles and the concentration of $(Au^{II}Cl_3)$ ions, resulting in varying nanoparticle sizes and absorption wavelengths.

In short, the section discusses the photoreduction method as an effective route for synthesizing single-crystalline gold nanoparticles (Au NPs). Ultraviolet (UV) light, spanning between visible light and ionizing radiations, is utilized for the UV photochemical synthesis of Au NPs. This method involves the reduction of metal ions, facilitated by UV radiation or photosensitizers like ketones that generate free radicals through photolysis, subsequently reducing metal ions to form metal clusters and nanoparticles. Shape-controlled fabrication of Au NPs through UV irradiation is demonstrated, with size and shape being effectively controlled in the presence of macromolecules such as dendrimers and surfactants. UV radiation encourages the photochemical reduction of aqueous Au solutions, while macromolecules act as soft templates, providing steric hindrance and preventing particle agglomeration. The effect of various parameters, like pH, temperature, precursor concentration, stabilizers, and reaction time, on the morphology of Au NPs during photochemical synthesis is explored. pH, in particular, is shown to affect the formation of nanospheres or nanorods, providing insights into the control of Au NP morphology.

The section presents a case study using red cabbage extract (RCE) as a reducing and stabilizing agent under UV light, resulting in the fabrication of stable, spherical Au NPs. The study investigates

the impact of RCE extract concentrations, pH, and the use of single or multiple reducing or stabilizing agents on Au NP formation, highlighting the stability and catalytic capabilities of RCE Au NPs. Furthermore, the fabrication of Au NPs using different precursors such as tetra chloroauric acid ($HAuCl_4$) and silver nitrate is discussed. Surfactants, including anionic (SDS, SDBS), cationic (CTAB, DTAB), and nonionic (Triton X-100) surfactants, are commonly used stabilizing agents that play a fundamental role in controlling Au NP growth, shape, and size. The study also investigates the influence of spacer length and hydrophobic chain length in gemini surfactants on the properties of synthesized Au NPs. Overall, the photoreduction method is presented as a versatile and controllable approach for synthesizing gold nanoparticles with tunable properties for various applications.

1.4.5 Using Reverse Micelles and Liposomes

Surfactants have been utilized to synthesize Au NPs within colloidal aggregates known as reverse micelles or water-in-oil (W/O) microemulsions [84, 222–225]. Reverse micelles are thermodynamically stable, transparent, and isotropic water in oil systems which are composed of water core or droplet dispersed in oil phase and stabilized by the surfactant molecules present at the interface of water and oil [226–230]. Water is confined in the inside polar core of the reverse micelles, which act as nanoreactors for the fabrication and growth of the Au NPs. The surfactant molecules present at the interface form a rigid or semirigid barriers that prevent the agglomeration of the Au NPs [231]. Further, the size of Au NPs is governed by the diameter of the reverse micellar water core [232]. Reverse micelles can be defined as nanoreactors that offer an optimal environment for the controlled nucleation and growth of nanostructures. Furthermore, the surfactant molecules provide the steric stabilization that prevents the Au NPs from aggregation. Different low molecular weight surfactants, including cetyl trimethyl ammonium bromide (CTAB), sodium dodecyl sulfonate (SDS), sodium bis(2-ethylhexyl) sulfosuccinate (AOT), Triton X-100, and others, can form reverse micelles to facilitate the creation of Au NPs with diverse sizes and shapes. Nanoparticles are prepared in reverse micelles using either a single microemulsion method or two microemulsion systems [233]. Single microemulsion method further includes energy triggering and microemulsion plus reactant technique [232]. In the energy-triggering approach, the introduction of a triggering agent into the microemulsion medium initiates the reaction. This activation of the medium sets off a cascade, resulting in the formation of nanoparticles. Pulse radiolysis and photolysis have been used as triggering agents for the formation of NPs [234]. In one microemulsion plus reactant method, one of the reactants such as gold salt is dispersed inside the aqueous cores of the microemulsion system, and the second reactant which usually acts as a precipitating agent (reducing agent such as $NaBH_4$) in the form of aqueous/nonaqueous or gas phase is introduced into the microemulsion medium. This microemulsion system can be prepared in an inverse manner with precipitating agent taken inside the aqueous cores of the microemulsions and the second gold salt fed from outside [232]. The reducing agent induces reduction of metal ions inside the aqueous cores of the microemulsion resulting in the formation of small nuclei which further aggregate to from NPs of specific size and shapes, which is governed by the size and shape of the reverse micelles. The whole process is diffusion driven since the second reactant diffusions into the water droplets of the microemulsions containing second reactant. In two microemulsion method, two separate microemulsion systems are prepared designated as ME-1 and ME-II. The aqueous phase of one of the microemulsions contain dissolved gold salt whereas second one contains reducing agent. The two microemulsions are then mixed under constant stirring during due to which Brownian motion of the reverse micelles leads to the intermicellar collusion and mixing of the micellar contents. Fusion and fission events occur during the micellar collusion

leading to the formation of temporal intermittent reverse micellar structures. The intermittent reverse micellar systems allow exchange of the reaction precursors inside the aqueous cores resulting in the occurrence of the chemical reduction of metal ions. After the chemical reduction, the intermittent reverse micellar structures then break to from reverse micelles containing metal atoms which aggregate to form metal nanoclusters. Metal nanoclusters then aggregate to form nuclei which grow further to form NPs. Employing reverse micelles for the synthesis of NPs suffers from a major drawback. During Au NP synthesis, surfactant is employed in large quantities which gets incorporated in Au NPs during separation step [145]. Since most of the surfactant molecules are biologically toxic in nature, which limits their use in biological applications. The single-step purification of microemulsion synthesized Au NPs has been done by Hollamby et al by inducing phase transition and subsequent separation [235]. The study explored the synthesis and purification of gold nanoparticles (Au-NPs) using a microemulsion system. The color change from yellow to ruby red observed upon mixing the microemulsion with $AuCl^{4-}$ was indicative of successful Au-NP formation. UV spectroscopy confirmed this transformation, showing the disappearance of the peak around 400 nm and the emergence of a strong absorbance band cantered at 525 nm. This change happened rapidly, with UV-vis stopped flow data revealing an initial decrease in absorbance followed by a rapid increase, reaching a maximum within 35 ± 3 ms. Phase separation was induced by adding equal volumes of water to the Au-NP-containing microemulsion, resulting in two coexisting phases: an octane-rich upper phase and a water-rich lower phase. Surprisingly, the Au-NPs partitioned strongly into the upper phase, as evidenced by the distinct color difference between the two phases (dark ruby red for the upper phase and light pink for the lower phase). UV-vis spectroscopy further quantified this concentration difference, revealing that sample contained twice the concentration of Au-NPs as the initial homogeneous sample, and 18 times that of the lower aqueous phase. The concentration calculations showed that approximately 82% of the mass of Au-NPs from the original microemulsion was partitioned into the top phase after separation. This strong partitioning and purification process allowed for the efficient separation and purification of the Au-NPs from any excess CTAB, the surfactant used. These purified Au-NPs could then be dried and redispersed in fresh octane. This preference of Au-NPs for the nonaqueous phase is somewhat unexpected, considering the typical behavior of CTAB to form stable bilayers on negatively charged surfaces. The mixed octane and butanol organic solvent in the upper phase appeared to disfavor CTAB bilayer formation, facilitating the hydrophobization of the Au-NP surface. Any residual Au-NPs in the lower phase might still be stabilized by a CTAB bilayer, but further investigation is required. TEM images confirmed that the purified Au-NPs retained their size and shape, consisting of a polymorphic collection of spheres, triangles, and short rods. These nanoparticles exhibited a wide length-scale range from approximately 100 to 400 Å. There are numerous studies on the Microemulsion synthesis of Au NPs for various applications [84, 222, 223, 236–239].

However, using co-polymer-based micelles offers several advantages over classical surfactant-based micelles. The critical micellar concentration (CMC) of co-polymers is small in comparison to surfactants. The also exhibit higher kinetic stability as compared to surfactants. Further size and shape of co-polymer-based micelles can be easily altered by varying the composition, architecture, and length of constituent blocks of a co-polymer. The stability of Au NPs formed inside co-polymer-based reverse micelles can be improved by raising the length of the coronal blocks [240, 241]. Gold NPs have been synthesized using various types of co-polymers such as poly(ethylene oxide)-poly(propylene oxide)-poly(ethylene oxide), (PEO-PPOPEO) [242–246], Poly(styrene) blockpoly(vinylpyridine) (PS-b-PVP) [247, 248], polymer micelle stabilized poly(styrene) block-poly(4-vinylpyridine)((PS-b-P4VP)4) [249], polystyrene-block-poly(2 vinylpyridine) [250], and poly(ethylene oxide)-poly(*n*-butyl acrylate) (PEO-PnBA) [251]. Gold NPs synthesized in block co-polymers have been used for various applications such as biosensing [246]

and catalysis [248, 252]. Gold NPs were synthesized by reducing the gold salt ($HAuCl_4$) in the polar cores of poly(styrene)-block-poly(2-vinylpyridine) (PS-*b*-P2VP) copolymer micelles by Moller et al. [253]. Three different reducing agents were used to reduce gold salt inside the microemulsions of different strengths such as HA, triethylsilane (TES), and potassium triethylborohydride (PTB). The size of the Au NPs was found to vary with the strength of the reducing agent used. The average diameter of the Au NPs formed was calculated to be 1.7, 2.6, and 8 nm using HA, TES, and PTB reductants, respectively. Rapid reduction of Au (III) ions occurred with HA and PTB, whereas TES proved to be milder reducing agent. DLS measurements demonstrated that incorporation of $HAuCl_4$ and reducing agents into PS-*b*-P2VP micelles caused the swelling of the resulting micelles. Gold dodecahedra and triangular nanoplates have been synthesized via one-step process reducing $HAuCl_4$ in presence of citric acid and Tetronic T904, an amphiphilic copolymer comprised of polyethylene oxide and propylene oxide units. Tetronic T904 co-polymer acted both reducing and stabilizing agent. TEM images showed the formation of dodecahedral Au NPs (85%) when using 0.5 mM $HAuCl_4$, 30 mM citric acid and 0.8 mM T904 and 1 mM HCl at 80 °C. The Au dodecahedra exhibited pentagonal symmetry the lateral size of 30 ± 4 nm and apex sizes of 19 ± 3 nm. The remaining 15% of the Au NP sample is composed of Au nameplates (Figure 1.7A). However, as the concentration of co-polymer was increased from 0.5 to 6 mM, the concentration of small triangular Au nanoplates increased in the sample. The product was found to contain 90% of Au nanoplates with an edge length of 40 nm. The remaining 10% included other shapes such as decahedra and octahedra (Figure 1.7B). The shape of the Au nanotriangles was found to evolve with time. After one hour of reaction, the sample mainly contained small Au NPs of undefined shapes. Spherical and polyhedral Au NPs were observed after six hours of reaction. Small triangular nanoplates with size of 15 nm were observed after 15 hours of reaction. As the reaction prolonged to 24 hours and then to 36 hours, a gradual improvement of size uniformity was observed with Au nanoplates of certain smaller-sized started disappearing whereas relatively larger Au nanotriangles became bigger (Figure 1.7C). The whole development suggested occurrence of Ostwald ripening and growth process. The synthesis of Au NPs inside co-polymers takes place in three steps [255]. First step involves the reduction of Au ions inside the crown ether like regions of the block co-polymers in solution. Second step involves the absorption of block co-polymers on the surface of Au NPs. Third step involves the growth of the smaller Au NPs stabilized by the polymer molecules. Various factors such as temperature, size, and shape of the reverse micelles and micellar environment are the main factors which govern the overall growth kinetic which lead to the Au NPs of specific morphologies [245, 256].

Liposomes are the supramolecular assemblies of amphiphilic liquids, which can be utilized as reverse micelles for the fabrication of Au NPs. A two-step approach for the synthesis of Au NPs inside liposomes has been performed by incorporating a reductant, $NaBH_4$ to a mixture of liposomes and $HAuCl_4$ [257]. In the first step, Au nanoparticles of 1 nm diameter were produced by employing an aqueous solution of 1,2-dipalmitoyl-sn-glycero-3-phosphothio-ethanol-phospholipid (PL). Subsequently, the size of Au NPs was increased from 1 to 5 nm through the interaction of PL with the Au NPs. Furthermore, it was determined that PL forms a double layer on the Au NP surfaces, and this interaction was facilitated by the thiol functionality of PL. Gold NPs have been synthesized inside glycerol incorporated nanosized liposomes of 1, 2-dioleoyl-sn-glycero-3-[phosphor-rac-(1-glycerol)] (DOPG) and 1-palmitoyl-2-hydroxy-sn-glycero-3-phosphocholine (lyso-PPC) in presence of a short-chain alkanethiol, 6-mercapto-1-hexanol (MCH) as the capping agent [258]. Effect of varying concentration of glycerol, reducing agent and capping agent on the size and morphology of Au NPs have been examined. Nanoliposomes were prepared using a combination of DOPG and lyso-PPC in the molar ratio of 88 : 12 with varying glycerol concentration (3-15% [v/v]). The authors initially explored the synthesis of Au NPs in glycerol. They observed the

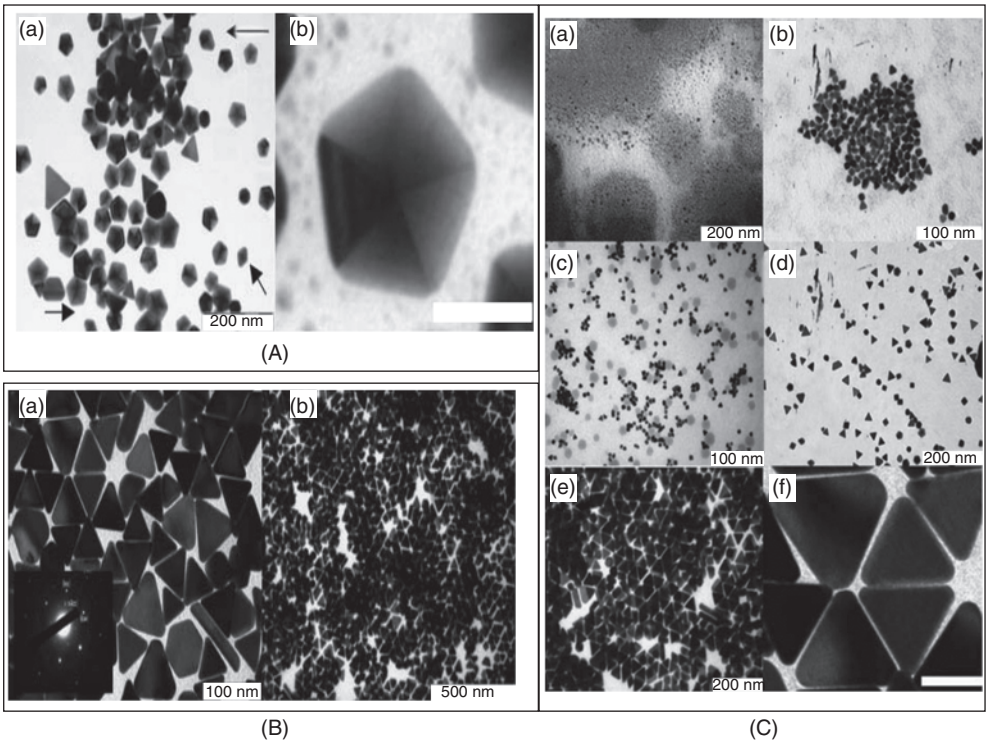

Figure 1.7 (A) Displays (a) transmission electron microscopy (TEM) images of Au decahedra that were synthesized at 80 °C in a solution containing 0.8 mM T904, 30 mM citric acid, 0.5 mM $HAuCl_4$, and 1 mM HCl. (b) The images reveal the fivefold twinned symmetry characteristic of decahedra. Notably, when the orientation of the decahedra to the electron beam changes, they exhibit a bipyramid geometry, as indicated by the arrows. The scale bar represents a length of 50 nm. (B) TEM images depict the ultrasmall Au nanoplates that were synthesized under the conditions of 80 °C, 6 mM T904, 12 mM citric acid, 0.5 mM $HAuCl_4$, and 3 mM HCl. Additionally, the inset in (a) shows the selected area electron diffraction (SAED) pattern, confirming the crystalline nature of the triangular nanoplates. (C) Provides a sequence of TEM images that illustrate the progressive formation of ultrasmall triangular nanoplates using the same conditions as in (A), captured at different time points: (a) 1 hour, (b) 6 hours, (c) 15 hours, (d) 24 hours, and (e) 36 hours. Furthermore, (f) presents a magnified view of the triangular nanoparticles. The scale bar in these images represents a length of 20 nm. Source: (a–c) Reproduced with permission from Goy-Lopez et al. [254]/Royal Society of Chemistry.

formation of relatively large and heterogeneous particles (10–50 nm) when chloroauric acid was mixed with glycerol in PBS solution at 25 °C in the absence of liposomes. However, when glycerol was incorporated into liposomes and a pH jump was applied, smaller and more homogeneous particles (5–10 nm) were obtained. This suggests the reduction of Au(III) to Au(0) was more effective when liposomes were used. Next, liposomes were introduced as nanoreactors for Au NP synthesis. The incorporation of glycerol within the liposome structure was expected to provide a semisolid reaction environment, favoring controlled nanoparticle formation. TEM images displayed the stages of the reduction reaction in the presence of glycerol-incorporated liposomal nanoreactors (Figure 1.8). Particles were observed both within the nanoreactors and in the surrounding solution after the elimination of the lipidic membrane. The authors then assessed the effect of glycerol concentration and the presence of a capping agent (6-mercapto-1-hexanol, MCH) on the particle size. They found that higher glycerol concentrations led to larger particles (7.7–6.4 nm), which indicated oxidation by-products of glycerol reacting with Au(III). However, the inclusion of MCH

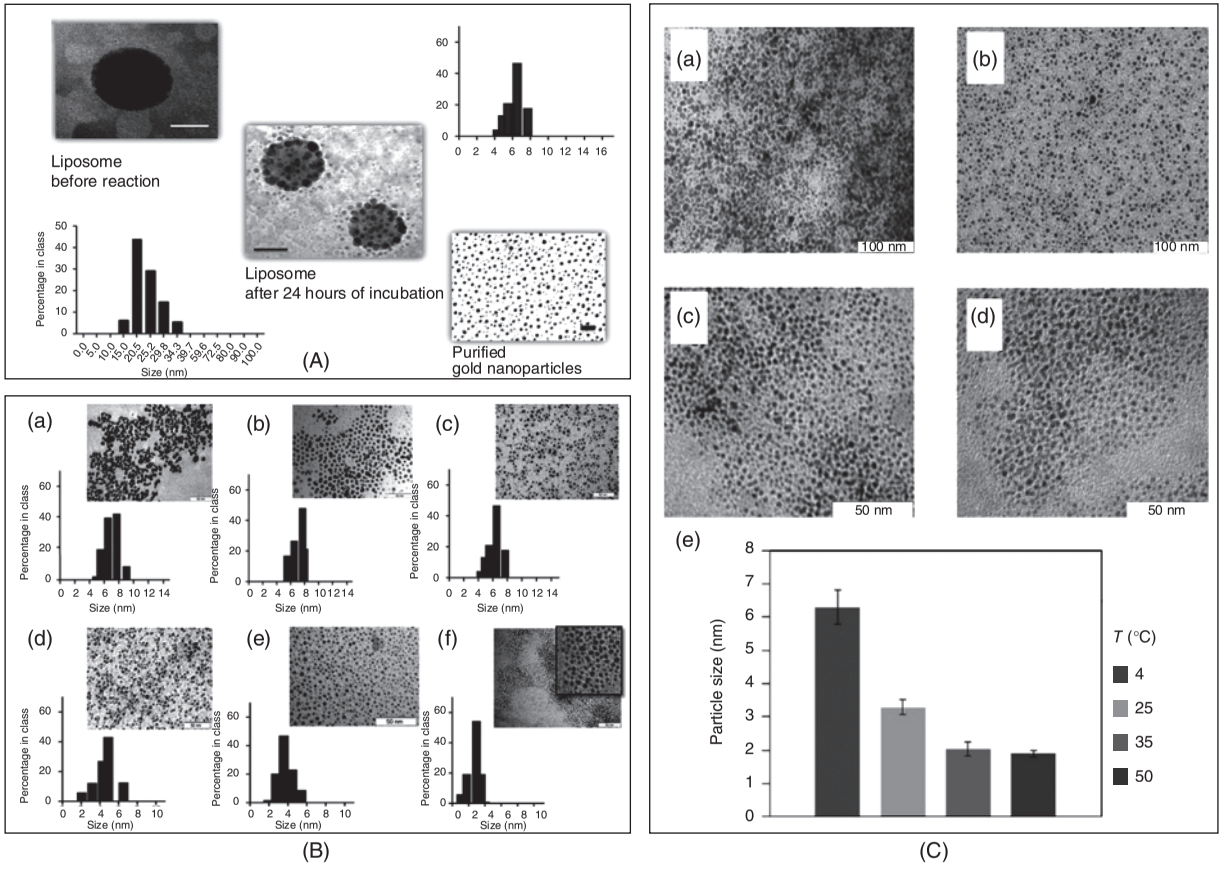

Figure 1.8 (A) Illustrates the progression of gold nanoparticle formation within liposomes containing 15% v/v glycerol. The images depict liposomes before the reaction (upper left), liposomes during the reaction (middle) (scale bars = 10 nm), and purified gold nanoparticles synthesized inside the nanoreactor (lower right, scale bar 20 nm). The graph in the lower left corner shows the size distribution of liposomes before the reaction (PI = 0.232), while the graph in the upper right corner displays the calculated nanoparticle size distribution using TEM. (B) The impact of capping agent and glycerol concentration is presented. The calculated particle size distribution and corresponding TEM images of particles are shown for two scenarios: (a–c) in liposomes without a capping agent (MCH) and (d–f) in the presence of MCH, with varying concentrations of glycerol (a, d) at 3%, (b, e) 10%, and (c, f) at 15%, after 24 hours of incubation at 25 °C. Scale bars in the images are 50 nm. (C) Demonstrates the influence of temperature on particle size and shape in glycerol (15% v/v)-incorporated liposomes with the capping agent MCH at different temperatures: (a) 4 °C, (b) 25 °C, (c) 35 °C, and (d) 50 °C after 24 hours of incubation. Additionally, graph (e) presents the calculated mean diameter of the particles ($n \geq 3$, scale bars = 20 nm). Source: (a–c) Reproduced with permission from Genc et al. [258]/American Chemical Society.

in liposomes resulted in a reduction in particle size (2.9–4.9 nm) due to the reducing effect of MCH (Figure 1.8B). The influence of temperature on particle properties was also investigated. Higher temperatures led to smaller particle sizes (1.9 nm at 50 °C compared to 6.3 nm at 4 °C) because of the increased reaction rate and rapid nucleation at elevated temperatures, leading to more efficient particle formation (Figure 1.8C). A quick one-step environmentally friendly synthesis of Au NPs has been performed by employing giant uni-lamellar vesicles (GUV) and ascorbic acid as a reductant [259]. Spherical Au NPs were formed at lower precursor concentrations, whereas nonspherical Au NPs were observed at higher precursor concentrations. Further GUVs were doped with cationic and anionic liquids to study the effect on Au NP size. The presence of anionic dopants led to the formation of larger Au NPs compared to cationic dopants.

In summary, this section explores the use of surfactants in synthesizing gold nanoparticles (Au NPs) within colloidal aggregates known as reverse micelles. Reverse micelles represent thermodynamically stable systems consisting of a water core dispersed within an oil phase, stabilized by surfactant molecules at the water/oil interface. The water core acts as nanoreactors for Au NP formation, with surfactants preventing NP aggregation by forming rigid or semi-rigid barriers. Various low molecular weight surfactants, such as CTAB, SDS, AOT, and Triton X-100, are employed to create reverse micelles for Au NP synthesis. Two methods, single microemulsion and two microemulsion systems, are discussed. Single microemulsion methods include energy-triggering and microemulsion-plus-reactant methods, utilizing triggering agents like pulse radiolysis or photolysis. Two microemulsion methods involve mixing separate microemulsion systems (ME-I and ME-II) to induce chemical reduction and NP formation.

A major drawback discussed is the incorporation of a large quantity of surfactant during Au NP synthesis, limiting biological applications due to the potential toxicity of surfactant molecules. A study by Hollamby et al. is mentioned, where a single-step purification method using phase transition and subsequent separation is employed to address this issue. The section then delves into the advantages of using co-polymer-based micelles over classical surfactant-based micelles. Co-polymers exhibit small CMCs, higher kinetic stability, and easy alteration of micelle size and shape by varying composition, architecture, and length. Various co-polymers, such as PEO-PPOPEO, PS-b-PVP, PS-b-P2VP, PEO-PnBA, have been used for synthesizing gold nanoparticles with applications in biosensing and catalysis. The use of liposomes, supramolecular assemblies of amphiphilic lipids, as reverse micelles for Au NP synthesis is also discussed. A two-step approach involves incorporating a reductant, $NaBH_4$, to a mixture of liposomes and $HAuCl_4$. The size and morphology of Au NPs can be manipulated by adjusting glycerol concentration, the choice of reducing agent, and the capping agent present within liposomes.

Overall, the section provides insights into diverse methods and techniques for synthesizing gold nanoparticles using surfactants, co-polymers, and liposomes, each with its advantages and applications.

1.4.6 Green Chemistry Methods

Though chemical methods of synthesis of NPs are most used due to good yield, but the toxic nature of the organic solvents and various organic/inorganic reducing agents limit their applications in biomedical areas [14, 84–86, 225]. Further chemical methods of synthesis make use of expensive stabilizing agents and other reagents. These and various other limitations of chemical methods of synthesis forced the researchers to work for the alternative green methods of synthesis which are eco-friendly as well as cost effective in nature [258, 260–262]. This endeavor for greener methods of synthesis gave rise to use of biological reducing agents and capping agents obtained from plants and animal sources. Hence, biological methods of synthesis became the focal point for synthesizing

nanoparticles. Biological methods use plant or plant extracts, plant-derived macromolecules such as polysaccharides, microbes, and enzymes for the synthesis of NPs [263–265].

Plants have been gaining major attention for the synthesis of Au NPs due to their wide availability and low cost. Plants contain phytochemicals with hydroxyl, carboxy, carbonyl groups, and various other macromolecules such as polysaccharides in natural abundance which easily reduce Au^{3+} to Au and finally stabilize the Au NPs as well [266, 267]. Further, the plant-mediated synthesis involves simple procedure of mixing the plant extract with $HAuCl_4$ and wait till color of the resulting mixture turns red/purple. Synthesis of Au NPs has been carried out by using various plants such as *Aloe vera* [268], *Azadirachta indica* [269], *Medicago sativa* [270], *Coriandrum sativum* [271], *Lemon grass* [272], *Terminalia catappa* [273], and *Pelargonium graveolens* [274]. Spherical Au NPs of 20 nm size have been synthesized by using *Croton caudatus Geisel* extract. The resulting Au NPs have been studied for antibacterial, antifungal, and anticancer activity [262]. *Simarouba glauca* plant extract has been used by N. Thangamania and N. Bhuvaneshwari for synthesizing Au NPs [275]. The size and morphology of Au NPs have been affected by varying leaf broth concentration. HRTEM images reflect the Au NPs of various sizes and morphologies. However, the Au NP size decreased with increase in the leaf broth concentration. Promising antimicrobial activity against a variety of microbial strains was observed in the resulting Au NPs. Gold nanoparticles were synthesized utilizing aqueous leaf extract from *Mentha longifolia* [260]. Characterization involved XRD, UV-visible studies, SEM, TEM, EDX, and FTIR spectroscopy. XRD analysis revealed the presence of pure phasic Au with high crystallinity. TEM images exhibited the formation of spherical Au NPs with an average particle size of 36.4 nm. These Au NPs demonstrated efficacy against human breast cancer cell lines. Najlaa S. Al-Radadi synthesized Au NPs with a particle size of 43.17 nm using *licorice* root extract [261]. Gold NPs have been synthesized by using gum Arabic obtained from plants [276–278]. Due to good water solubility and biocompatibility, chitosan which is a second most abundant natural polymer has been used to synthesize Au NPs [218, 279]. The resulting Au NPs have been stabilized by the amine groups as well as by steric effects.

The environmentally friendly synthesis of Au NPs using microbes has garnered significant attention in recent years. However, bacterial-mediated synthesis of NPs has its own advantages as well as disadvantages. The main advantage lies in the easy handling and genetic manipulation of the bacterial systems for NP synthesis. The lack of proper control over size and shape of NPs and inability of large-scale synthesis is the main challenge for the bacterial-mediated synthesis. Control over size, shape, and crystallinity can be accomplished by properly understanding the underlying molecular and genetic mechanism of the synthesis of NPs which is yet to be properly understood. Gold NPs have been fabricated utilizing four different microbes, viz., bacteria, fungi, actinomycetes, and yeasts. However, only a few species of bacteria are enabled to reduce metal ions to metal atoms. These bacteria reduce metal ions extracellularly and intracellularly. For example, Au NPs in the range of 5–25 nm have been prepared intracellularly using *Bacillus subtilis* by Beveridge and Murray. These bacteria reduce Au^{III} to Au atoms and finally to Au NPs inside the cell wall. Gold NPs of different morphologies such as spherical, cubical, and hexagonal with sizes in the range of 5–200 nm have been produced intracellularly by various sulfate-reducing bacteria [280, 281]. Numerous reports also exist regarding the extracellular synthesis of Au NPs [282–284]. For example, the synthesis of Au NPs has been accomplished using cell-free supernatant of *Paracoccus haeundaensis* BC74171T [282]. TEM micrographs and DLS revealed that the synthesized Au NPs were sphere shaped, with an average grain size of 20.93 ± 3.46 nm. The surface of Au NPs was found to be negatively charged as revealed by the zeta potential measurements which gave a surface potential of −4.26 mV. EDX spectrum displayed a strong peak at 2.15 keV corresponding to the elemental gold. The reaction rate enhanced with an increase in temperature as is evident by the emergence of the SPR peak at 534 nm at the temperature 60 °C. Below 60 °C, no SPR peak

was observed. The maximum peak intensity was recorded at 70 °C. Further, the peak intensity of the SPR peak was enhanced with an increase in incubation time which indicated the increase in number of Au NPs with time.

Since fungal mycelia can withstand higher pressures and agitation in bedchambers, hence they have been advantageously used for the fabrication of Au NPs as compared to microbial systems [285]. In recent years, a wide range of fungi has been recognized as potential candidates [286–289]. They also secrete numerous enzymes in large quantities, which act as bioreductants for the synthesis of Au NPs. Further, high metal tolerance and bioaccumulation capability of fungi makes them advantageous in Au NP synthesis as compared to bacteria and fungi. Further, large-scale synthesis of Au NPs is possible with fungi due to easy handling of biomass, downstream processing, and the ability to secrete large quantities of extracellular enzymes. Further, the Au NP size and morphology are controlled by various active biomolecules involved in energy metabolism of the cells like proteins such as ATPase, reducing sugars, glyceraldehyde-3-phosphate dehydrogenase, and binding proteins like 3-glucan. Like in bacteria, Au NPs can be fabricated both intracellularly and extracellularly using fungi. In intracellular synthesis, Au^{3+} ions are absorbed by the fungal cells and subsequently reduced by the biomolecules intracellularly, which result in the fabrication of Au NPs [290, 291]. The fungus *Verticillium* sp. has been utilized for the intracellular production of Au NPs. Gold nanoparticles displaying well-defined morphology and dimensions, measuring 20 nm in size, were detected on the cytoplasmic membrane of the fungal mycelium [292]. Ultrathin sections of the fungal mycelium when viewed TEM illustrated the presence of Au NPs exhibiting hexagonal, spherical, and triangular shapes on the cell wall. However, the Au NPs with quasi- hexagonal morphologies were observed on the cytoplasmic membrane. Spherical Au NPs with size of less than 10 nm were synthesized when Au (III) ions were added to the *Verticillium luteoalbum* and incubated at the pH of 3.0. However, the incubation at the higher pH of 5.0 led in the creation of Au NPs of triangular and hexagonal morphologies [293, 294]. In some cases, extracellular synthesis of Au NPs took place due to the significant extracellular production of bioenzymes, which acted as both reducing agents and capping agents simultaneously [294]. Shankar et al. employed an endophytic fungus, *Colletotrichum* sp., isolated from geranium plant leaves, for the rapid production of Au NPs [295]. Similarly, Au NPs have been produced extracellularly by using the fungus *Trichothecium* sp. to reduce Au (III) ions [296]. TEM images displayed the formation of highly polydisperse Au Nps which have a triangular, hexagonal, and rod like morphologies with size between 5 and 200 nm. It has been postulated that loosely bound proteins and enzymes secreted by the fungus is involved in the synthesis of Au NPs of various morphologies [296].

Numerous reports document the synthesis of Au NPs by yeasts. For example, bakers' yeast (*Saccharomyces cerevisiae*) has been employed to synthesize Au NPs. It was reported that aldehyde groups from the reducing sugars on the cell wall of the yeast reduce Au^{3+} ions to Au atoms and finally to Au NPs [55]. Gold NPs with spherical, triangular, and hexagonal morphologies with size less than 100 nm have been synthesized using *Yarrowia lipolytica* NCIM 3589, a tropical marine yeast. The Au NPs were found to be distributed mainly inside the cytoplasm of the yeast. Further, the reduction of Au^{3+} ions was observed to be pH dependent. Hexagonal and triangular Au nanocrystals were formed when the yeast cells were incubated at pH 2.0. At higher pH of 7.0 and 9.0, smaller Au NPs of the average grain size of 15 nm were produced [56]. Gold NPs of various morphologies have been synthesized using the yeast, *Magnusiomyces ingens* LH-F1. UV-Visible studies displayed a time-evolved SPR peak at 540 nm with little on no peak shifting with time. This unshifted SPR peak indicates the no significant agglomeration of Au NPs with time due to efficient capping by biomolecules of the yeast. Gold NPs were synthesized by employing the cell-free extract of *M. ingens* LH-F1 yeast [297]. The confirmation of Au NP formation was additionally validated

through UV-Visible spectroscopy, where a distinct SPR band was observed at around 540 nm. TEM images displayed the spherical and pseudospherical and anisotropic Au NPs with size less than 28 nm. The lower concentration ((25–50 mg/L) of cell-free extract led to the formation of Au NPs. of various morphologies such as triangular, hexagonal, and anisotropic structures. Whereas higher concentration (100–200 mg/L) produced mostly spherical Au NPs of smaller sizes.

In short, this section discusses the limitations of chemical methods for synthesizing nanoparticles (NPs), for instance, the utilization of hazardous organic solvents, expensive stabilizing agents, and reagents. Due to these drawbacks, researchers have explored alternative "green" methods of synthesis, particularly biological methods using reducing and capping agents derived from plants, microbes, and enzymes.

Plants, with their abundant phytochemicals and macromolecules like polysaccharides, are highlighted for their role in synthesizing gold nanoparticles (Au NPs). Various plants, such as *A. vera*, *Azadirachta indica*, *Medicago sativa*, and others, have been utilized for the eco-friendly and cost-effective synthesis of spherical Au NPs with different sizes. The resulting NPs have shown activities against bacteria, fungi, and cancer cells.

Microbes, including bacteria, fungi, actinomycetes, and yeasts, are investigated for their capacity to synthesize Au NPs. Bacterial synthesis is advantageous for easy handling and genetic manipulation, but challenges include controlling NP size and shape. Bacteria like *B. subtilis* and sulfate-reducing bacteria are discussed for their intracellular and extracellular synthesis of Au NPs.

Fungi are highlighted as potential players for Au NP biosynthesis because of their high tolerance to metals, bioaccumulation capability, and the ability to secrete large quantities of extracellular enzymes. Both intracellular and extracellular synthesis methods using fungi such as *Verticillium* sp. and *Colletotrichum* sp. are discussed. Fungal mycelia's ability to withstand higher pressures and agitation is noted as an advantage. Yeasts, including *Saccharomyces cerevisiae* and *Y. lipolytica*, are mentioned for their role in synthesizing Au NPs through reducing sugars on their cell walls. The pH dependence of Au NP synthesis by *Y. lipolytica* is highlighted.

Overall, the section emphasizes the shift toward green synthesis methods using biological entities for the production of Au NPs, offering eco-friendly and cost-effective alternatives to traditional chemical approaches. The specific examples provided showcase the potential applications of these synthesized NPs in various fields, including medicine and nanotechnology.

1.5 Synthesis and Characterization of Silver Nanoparticle

The synthesis and characterization of silver nanoparticles (AgNPs) represent a vibrant and essential area of nanotechnology research, offering numerous applications in diverse fields. Silver NPs are particularly intriguing because of their distinctive electronic, optical, and antibacterial characteristics. The process of synthesizing these nanoparticles involves reducing silver ions to nanoscale silver structures, and various methods, like chemical, physical, and biological approaches, are employed. Characterization techniques such as UV-Visible spectroscopy, TEM, SEM, XRD, and FTIR are crucial for understanding the size, shape, crystallinity, and surface characteristics of the synthesized AgNPs. The ability to precisely control the synthesis parameters and characterize the resulting NPs is pivotal for tailoring their properties to meet specific application requirements, ranging from medical and environmental uses to catalysis and electronics. This interdisciplinary field continues to advance, driven by the need for efficient and sustainable nanomaterials in various technological domains. Different methods for synthesizing silver nanoparticles can be categorized under the following subheadings.

1.5.1 Physical Approaches

Silver nanoparticles have been produced using physical methods such as the vaporization-condensation method and laser ablation process [298]. The evaporation–condensation method is conducted within a furnace tube under constant atmospheric pressure. The material is vaporized inside the furnace in presence of a carrier gas stream. However, this approach of synthesis of AgNPs has certain limitations such as large space occupied by the furnace, large power consumption, and long preheating time to achieve a stable operational temperature. However, the method has been modified by Jung et al. [299] to synthesize AgNPs by employing a tiny ceramic heater to generate a localized heating effect. The Ag metal source was heated on a heater, and the Ag vapors were conveyed by the carrier gas. Due to the rapid cooling of the aerosol generator in comparison to the conventional furnace tube furnace, the Ag vapors were transformed into Ag nanoparticles. The geometric mean diameter of the Ag particles, as well as the particle concentration, was observed to be directly proportional to the temperature of the heater surface and increased from 6.2 to 21.5 nm. Silver NPs were fabricated by Raffi et al. [300] by inert gas condensation method. The influence of diverse experimental parameters, including evaporation temperature and pressure of the inert gas on the size and morphology of AgNPs, was studied. Low evaporation temperature and inert gas pressure led to in the production of smaller AgNPs. With the evaporation temperature of 1123 K, the size of the Ag nanoparticles rose from 9 to 24 nm with an elevation in inert gas pressure from 0.5 to 100 Torr. Similarly, for the same inert gas pressure (e.g., 5 Torr), the particle size increased from 14 ± 2 to 20 ± 2 nm. Spherical AgNPs with particle size of 50, 90, and 130 nm have been synthesized by Harra et al. by evaporation–condensation technique [301]. Silver NPs have been produced via laser ablation of the bulk materials. Laser ablation synthesis of AgNPs can be traced to the year 2000 when Mafune et al. [302] synthesized AgNPs by laser ablation in aqueous solution of dodecyl sulfate (SDS). The effect of the SDS concentration and laser power on the average particle size of AgNPs has been studied. The average particle diameter decreased from 16.2 ± 4.0 to 11.7 ± 5.3 nm with increased in SDS concentration from 0.003 to 0.05 M, respectively. However, the average particle diameter increased from 7.9 ± 3.3 nm to 12.8 ± 4.1 nm with rise in the laser power from 40 to 70 mJ/pulse, respectively. Recently AgNPs have been fabricated using Nd : YAG laser by laser ablation method [303]. PLA has been focused on 99.9% pure Ag plate in water medium. The laser shots resulted in the production of AgNPs. The production of AgNPs was verified through UV-Visible spectroscopy, showing an SPR peak around 450 nm. Silver NPs have been created by Rafique et al. [304] in a single-step green method using two different lasers in de ionized water medium. Here the effect of laser type on the size and morphology of AgNPs has been studied. TEM images displayed the production of AgNPs with spherical shapes with size in between 10 and 30 nm using CW diode laser, whereas pulsed Nd : YAG laser resulted in the formation of monodispersed AgNPs with size between 4 and 14 nm. Further, the bandgap was found to be vary inversely to the Ag NP size. The bandgap values obtained for extrapolation of UV-Visible spectroscopy data were observed to be 2.47 eV for AgNPs synthesized by CW laser and 2.67 eV for AgNPs synthesized by pulsed laser. Although the physical methods produce AgNPs with high yield and high purity without using environmentally hazardous chemicals and production of toxic by-products, but the control over nanoparticle size and agglomeration is a great challenge. Further, the physical methods use complex equipment which have high-power consumption and requires long durations for nanoparticle synthesis.

1.5.2 Chemical Approach

Chemical methods of synthesis are found to be more convenient, efficient, and easy to handle. Chemical methods of synthesis involve the reduction of silver salts by suitable reducing agents

to synthesize Ag nanostructures with high productivity and at a very minimal cost. The chemical fabrication of AgNPs involves three components, viz., silver precursor, reducing agent, and capping agent. The size and morphology of AgNPs are governed by the dual stage, nucleation, and growth. Even the formation of primary nuclei is regulated by different reaction parameters like pH, precursor concentration, temperature, nature of reducing, and capping agent. [305–307]. The reduction of silver salts can be accomplished using a variety of inorganic and organic reducing agents which include metal complexes, block co-polymers, and biological macromolecules [85, 86, 266, 306–313]. Silver salts get reduced by receiving electron from reducing agents with the result Ag is obtained in a zerovalent state. The Ag atoms then agglomerate and grow by undergoing nucleation and growth to form colloidal Ag of variable sizes and shapes. The strength of the reducing agent greatly affects the size and morphology of AgNPs. For example, strong reductants like $NaBH_4$ yield small and monodisperse AgNPs with low stability [86]. However, weak reductants result in the production of bigger AgNPs due to slower reduction rate. Further weaker reducing agents provide enough time to control shape and size distribution of AgNPs [314]. The most critical aspect of Ag NP synthesis is the stabilization of the dispersive AgNPs [315, 316]. In order to achieve stabilization of AgNPs, various capping agents have been used such as polymers like PEG, PVP, PMMA, PMAA, biopolymers like cellulose, chitosan, and various other macromolecules like oleylamine gluconic acid [316–320]. Stabilization of AgNPs by stabilizing agents can be accomplished through either electrostatic or steric repulsions. Some capping agents provide steric stabilization to AgNPs by imparting negative charge to the NP surface such as halides, citrate, carboxylates, and polyoxoanions. Whereas few capping agents impart positive charge to the Ag NP surface such as branched PEI, etc. There are some macromolecules which impart steric stabilization to Ag NP solutions such an organic polymers and alkyl ammonium cations. Such bulky groups on the Ag NP surface undergo steric repulsion and impart stabilization to the Ag NP solution. For instance dodecanthiol capped AgNPs have been fabricated by Oliveira et al. which exhibit good stability in aqueous solutions [321]. Numerous reports have been documented on the synthesis of colloidal Ag using various stabilizing agents. Luo et al. [322] investigated the impact of PEG on the growth of Ag nanoparticles in the absence of other chemical agents. Here PEG acted both as a reducing agent and a stabilizing agent. The chain length of the glycol significantly influenced the formation of Ag nanoparticles. Ethylene glycol proved to be inactive in reducing Ag^+ ions even at high temperatures of 80 °C. However, AgNPs were effectively synthesized by using PEG 2000 under similar experimental conditions. With increase in polymer chain length of PEG, the rate at which Ag^+ ions are reduced to Ag nanoparticles increased significantly. The particle size enhanced from 10 to 80 nm with rise in reaction temperature. Silver nanoparticles have been fabricated using formaldehyde as a reductant and PVP as a stabilizer employing two different organic bases, triethyl amine and pyridine [323]. Triethyl amine being the more basic in nature resulted in the formation of AgNPs of larger sizes (20–30 nm). Whereas pyridine being less basic in nature as compared to triethyl amine produced smaller-sized AgNPs (10–20 nm). Monodisperse AgNPs have been produced using oleyl amine-paraffin system by Chen et al. [324]. It was reported that Ag NP synthesis occurred in three stages, viz., growth, incubation, and Ostwald ripening. This method used liquid paraffin as a solvent and Oleyl amine as a reductant and a capping agent. Colloidal silver nanoparticles with stability have been successfully synthesized by utilizing 2-(dimethylamino) ethanol (DMAE) as a reductant and PVP as a stabilizer [325]. The influence of the reducing agent and the dispersant on the particle size and morphology has been studied. Room temperature synthesis of AgNPs was achieved by this method. The AgNPs obtained were small and displayed uniform size distribution, with a diameter of less than 10 nm. Further, the Ag NP sample was found to be redispersible in water with good electroconductivity. Silver nanoparticles have also been conveniently prepared using low molecular weight compounds such as aldonic acid like

sodium gluconate as a dispersing agent instead of high molecular weight compounds such as PVP [326]. This method produced AgNPs with sizes less than 10 nm with good electrical conductivity. Aldonic acid, a low molecular weight compound, demonstrated efficacy as a stabilizing agent for the fabrication of dispersible Ag nanoparticles compared to high molecular weight compounds like PVP [326]. Further, this dispersing agent reduced the sintering temperature (150 °C) of AgNPs as compared to those prepared using other polymers such as PVP (200 °C). Ag nanoparticles have also been synthesized using the polyol method. In this method, silver salt is mixed with ethylene glycol in various rations and then heated. The stability of the AgNPs can be enhanced by using other polymeric stabilizers such as PVP. For instance, AgNPs have been produced by Kim et al. using polyol method [327]. Two distinct synthetic methods have been employed to produce Ag nanoparticles, aiming to investigate the influence of reaction parameters on particle size and morphology. In the first method called precursor solution method, silver nitrate was dissolved in ethylene glycol along with PVP (Mw = 10,000). The mixture was then refluxed at the temperature of 100–150 °C with heating rate of 1–7.5 °C/minute. Once the reaction was complete, AgNPs were extracted from the solution by centrifugation. In the second method called as injecting precursor method, first PVP was dissolved in ethylene glycol and heated to achieve the desired reaction temperature. Next aqueous solution of silver nitrate (40%) was injected into the hot mixture of PVP-ethylene glycol solution maintained at reaction temperature. Later, the AgNPs were recovered by centrifugation. Silver nanoplates and nanobelts have been prepared by refluxing suspension of silver nano seeds of average diameter of 3.5 nm [328]. The silver nano seeds were in turn synthesized by reducing $AgNO_3$ with $NaBH_4$ in presence of sodium citrate and PVP. The Ag nano seeds exhibited as sharp SPR peak at 400 nm. After refluxing the silver nanosuspension, four distinct SPR peaks emerged which were located at 330, 525, 855, and 1190 nm. The emergence of these SPR peaks reflected the transformation of Ag nano seeds into different morphologies. It was observed that Ag nano seeds transformed into triangular nanoplates (95%) and nanobelts or nanowires (5%). The silver nanoplates self-assembled into monolayered structures on TEM grid. The ED revealed each nanoplate to be a single crystal and the hexagonal symmetry of the patterned spots indicated two triangular faces of each nanoplate were bound by {111] faces. The nanowires were separated from the nanoplates by ultracentrifugation. Such Ag nanowires were found to have a diameter of 9 nm with wire length of 25 μm. Single crystal Ag nanocubes have been obtained by Im et al. by a typical polyol method by reducing $AgNO_3$ with ethylene glycol (EG) in presence of PVP [329]. The change in morphology of the twinned Ag nanocrystals was induced by addition of hydrochloric acid in minute quantities along with nitric acid formed *in situ* of the reaction. At lower concentration of nitric acid, a mixture of silver nanocubes, tetrahedrons, and nanowires were obtained after 25 hours of the reaction when 0.125 mM of HCl was used. This mixture of morphologies resulted due to incomplete itching of Ag-twinned seeds. Monodisperse Ag nanocubes with an edge length of 130 nm were formed after 26 hours exclusively when concentration of HNO_3 was increased to 0.25 mM. However, a totally different morphology of Ag nanostructures comprising of Ag nanowires and irregular particles was obtained with further increase in concentration of HCl to 0.37 mM (Figure 1.9A). The Ag nanocubes synthesis was scaled up by increasing the volume of the solutions by five times. The SEM images of the Ag NP sample obtained from the scale-up synthesis displayed the formation of Ag nanocubes exclusively with average edge length of 125 nm (Figure 1.9B). XRD pattern displayed the occurrence of (200) peak with abnormal intensity. The formation of single crystal Ag nanocubes with sharp edges and corners is observed in TEM image. The inset of the figure provides the EDS pattern of the AgNPs which also confirm the formation of single Ag nanocrystals. The polyol method was also used by Tao et al. to synthesize polyhedral Ag nanocrystals by reducing silver salt in diol solvent in presence of PVP as a stabilizer and

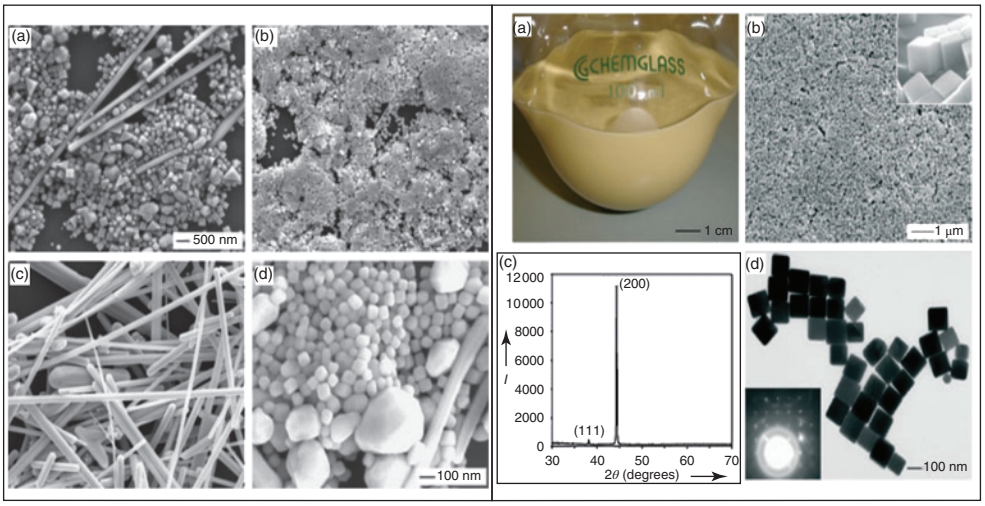

Figure 1.9 (A) Scanning electron microscopy (SEM) images depict silver nanoparticles synthesized under various concentrations of HCl, with a scale bar of 500 nm for each: (a) at 0.125 mm, (b) at 0.25 mm, and (c) at 0.375 mm. The reaction mixture consisted of $AgNO_3$ (23.5 mm) and PVP (36.7 mm, calculated in terms of the repeating unit), and the synthesis process involved heating in an oil bath maintained at 1408C. In (d), silver nanoparticles were produced using the same conditions as before, except that HNO_3 (0.25 mm) was used instead of HCl (0.25 mm). (B) (a) Image of the reaction mixture in a scaled-up (five times larger) synthesis. (b) Representative SEM pictures of the silver nanocubes produced in their as-synthesized state. The inset provides a closer view of the SEM image, highlighting the well-defined sharp corners and edges of these nanocubes. (c) XRD pattern obtained from the same batch of silver nanocubes. (d) TEM image displaying the silver nanocubes, with the inset showing an electron diffraction pattern recorded by aiming the electron beam perpendicularly at the (100) facet of a silver nanocube. Source: (a, b) Reproduced with permission from Im et al. [329]/John Wiley & Sons.

shape-controlling agent [330]. A variety of Ag nanocrystal shapes have been obtained such as cubes (80 nm) and truncated cubes (120 nm), cuboctahedra (150–200 nm), octahedra (250–300 nm), and truncated octahedra (200–250 nm), etc. (Figure 1.10A). Silver nano bars (aspect ratio; 2.7) and nano rice have been synthesized by Wiley et al. by polyol method by varying the concentration of bromide ions [331]. The nano bars were anisotropic with length of 146 nm and width of 56 nm. Silver nano bars have sharp edges and corners and are single crystals bounded by (100) facets. The edges and corners were latter rounded and transformed into single crystal nano rice by storing the Ag nano bars in 5% aqueous solution of PVP at room temperature for one week (Figure 1.10B). Both the types of Ag nanostructures exhibited two SPR peaks in visible and near IR regions. In case of both Ag nanobars and nano rice, the position of longitudinal SPR peaks red-shifted with increase in the aspect ratio, whereas not much change in position of transverse SPR was noticed (Figure 1.10C). Silver nanocubes, Ag bi pyramids, and Ag nanowires have been synthesized by the same group, i.e., Wiley et al. by a polyol process with PVP and $Ag NO_3$ in the molar ratio of 1.5. Silver nanocubes, right bipyramids, and nanowires were produced by the subsequent addition of Cl^-, Br^-, polyethyleneimine and Fe^{3+} ions to the PVP solution [332]. Single crystal Ag was grown into truncated cubes or sharp cubes by the addition of chloride ions which depended upon the kinetics of the reaction. Addition of NaCl as a Cl^- ions source produced truncated Ag nanocubes after 26 hours of the reaction, however, replacement of NaCl with HCl produced sharp Ag nanocubes. The 75 nm truncated Ag nanocubes exhibited dipolar SPR at 440 nm with two small shoulders associated with the main SPR suggested the occurrence of small amount of anisotropy. However, the 90 nm sized

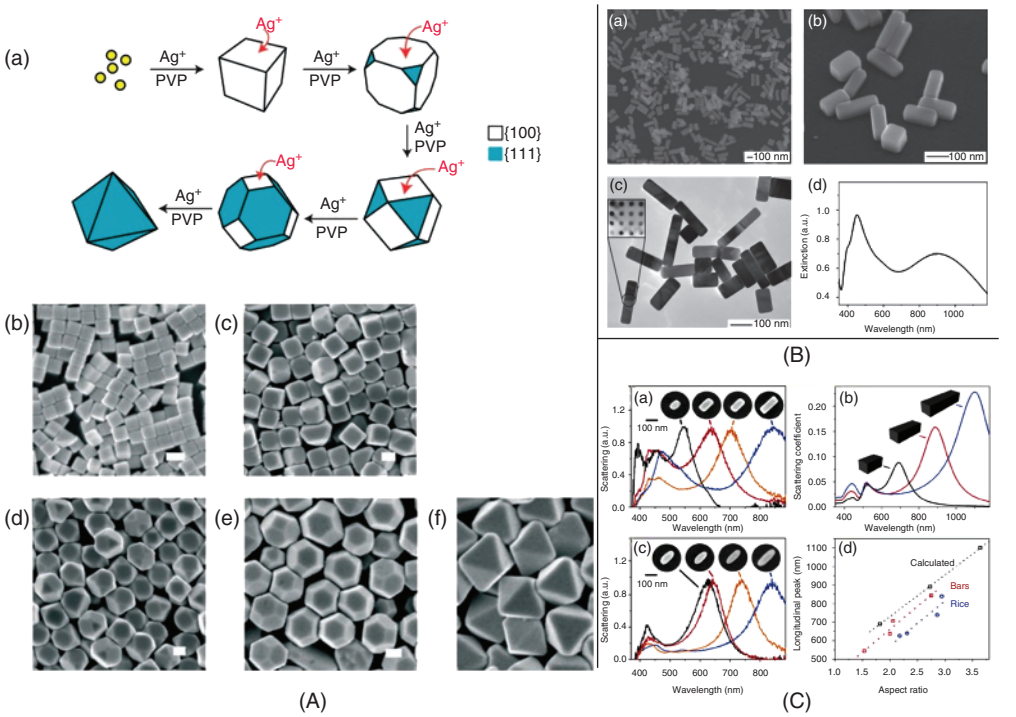

Figure 1.10 (A) By prolonging the polyol reaction for a specific duration, it is possible to achieve a high yield of various polyhedral shapes that are enclosed by {100} and {111} facets. (a) An illustration of the nucleation and growth process, where silver consistently accumulates on the {100} facet, eventually forming a fully {111}-enclosed octahedron. (b–f) Scanning electron microscope (SEM) pictures showing cubes, truncated cubes, cuboctahedra, truncated octahedra, and octahedra, in that order (scale bar: 100 nm). Source: Adapted from Ref. [330] with permission. Copyright (2006) John Wiley & Sons. (B) (a) Scanning electron microscope (SEM) image of silver nanobars. (b) SEM image of the same sample tilted at a 45° angle. (c) Transmission electron microscope (TEM) image of the silver nanobars, with the inset displaying a convergent beam electron diffraction pattern, confirming that the nanobars are single crystals enclosed by (100) facets. (d) The visible and near-infrared (vis-NIR) extinction spectrum of the nanobars exhibits a transverse plasmon resonance in the visible range and a longitudinal resonance in the near-infrared region. (C) (a) SEM images of individual nanobars along with their corresponding normalized scattering spectra. The longitudinal plasmon peak of the nanobars shifts toward longer wavelengths as the aspect ratio increases. (b) Scattering spectra of nanobars with lengths of 100, 150, and 200 nm, while maintaining a width of 55 nm and a height of 50 nm, calculated using discrete dipole approximation (DDA). (c) SEM images of individual nanorice and their corresponding normalized scattering spectra. (d) A plot illustrating the relationship between the longitudinal plasmon peak position and the aspect ratio. Both nanobars and nanorice exhibit redshifts in their peaks as their lengths increase, but, on average, the nanobar peaks are shifted 80 nm more towards longer wavelengths compared to nanorice. Source: (a) Reproduced with permission from Wiley et al. [331]/John Wiley & Sons, (b, c) Reproduced with permission from Wiley et al. [332]/American Chemical Society.

sharp Ag nanocubes exhibited a sharp dipolar SPR at 500 nm. Using NaBr in place of NaCl resulted in the formation of single twin crystals. These single twin seeds latter grew to form right bi pyramids with two different sizes of 75 and 150 nm. The most intense dipole SPR of 75 nm bipyramids exhibited a red-shifting of 100 nm from sharp Ag nanocubes. With increase in size of Ag nano bi pyramids, there was a shift in peak intensity from 530 to 742 nm due to enhanced charge separation and energy loss in 150 nm sized bi pyramids as compared to 75 nm sized bi pyramids. Silver nanowires have been produced from multiple twinned Ag seeds by preventing the etching either by running reaction under argon atmosphere or in presence of Fe (II) or Fe (III) in the molar ratio

of Ag : Fe = 11,000. Multiple twinned Ag nano seeds produced initially by the addition of both iron (II) acetylacetonate ($Fe(acac)_2$) and Cl^- grew into nanorods of 20 nm diameter and 150 nm length which latter rapidly grew into Ag nanowires of micrometer length after 60 minutes of the reaction. UV-Visible spectrum showed the occurrence of SPR peak at 400 nm for multiple twinned dodecahedral Ag nano seeds which shifted to 470 nm as the nano seeds transformed into Ag nanorods. But as the nanorods transformed into nanowires, the extinction band broadened further, but the most intense SPR peak blue shifted to 382 nm. Silver nano prisms have been synthesized by Metraux and Martin by chemical reduction by employing sodium borohydride and sodium citrate as reducing agents in presence of PVP and H_2O_2 [333]. The production of nano prisms was confirmed spectroscopically by occurrence of in plane dipole surface plasmon band. A large red-shifting in bands has been observed with increase $NaBH_4$ concentration. This red-shifting in the SPR bands has been ascribed to the increase in edge lengths and tip sharpness of the Ag nano prisms. The edge length of the nano prisms enhanced from 31 ± 7 to 39 ± 8 nm with rise in $NaBH_4$ concentration from 0.3 to 0.8 mM. Multibranched Ag nanoflowers have been synthesized by Zaheer and Rafiuddin employing citric acid as a reducing and shape-directing agent [334]. Cong et al. [335] reported the formation of Y and K-shaped Ag nanostructures using a polyol method with PVP as a capping agent.

In brief, the section discusses the synthesis and characterization of AgNPs through chemical methods, emphasizing their convenience, efficiency, and cost-effectiveness. Chemical synthesis involves reducing silver salts using various agents, such as metal complexes, block co-polymers, and biological macromolecules. The size and morphology of AgNPs are controlled by nucleation and growth stages, influenced by parameters like precursor concentration, temperature, pH, and types of reducing and capping agents. Strong reducing agents like sodium borohydride produce small, monodisperse AgNPs, while weak reducing agents result in larger NPs with controlled size distribution. Stabilizing agents, including polymers and biopolymers, are crucial for achieving stability, and they impart either electrostatic or steric repulsions. The synthesis methods vary, employing chemicals like PEG, PVP, PMMA, and low-molecular-weight compounds such as aldonic acid or using polyol methods. The diverse morphologies obtained include nanocubes, nanoplates, nanowires, nanorods, nanoflowers, and nanoprisms, showcasing the versatility of chemical synthesis in tailoring Ag NP properties for specific applications.

The section discusses the synthesis and characterization of silver nanoparticles (AgNPs) through chemical methods, emphasizing their convenience, efficiency, and cost-effectiveness. Chemical synthesis involves reducing silver salts using various agents, such as metal complexes, block co-polymers, and biological macromolecules. The size and morphology of AgNPs are controlled by nucleation and growth stages, influenced by parameters like precursor concentration, temperature, pH, and types of reducing and capping agents. Strong reducing agents like sodium borohydride produce small, monodisperse AgNPs, while weak reducing agents result in larger NPs with controlled size distribution. Stabilizing agents, including polymers and biopolymers, are crucial for achieving stability, and they impart either electrostatic or steric repulsions. The synthesis methods vary, employing chemicals like PEG, PVP, PMMA, and low-molecular-weight compounds such as aldonic acid or using polyol methods. The diverse morphologies obtained include nanocubes, nanoplates, nanowires, nanorods, nanoflowers, and nanoprisms, showcasing the versatility of chemical synthesis in tailoring Ag NP properties for specific applications.

1.5.3 Photoinduced Reduction Synthesis of AgNPs

Due to the good versatility, high spatial resolution, and convenient handling, photoinduced reduction have been employed for the synthesis of silver nanoparticles with diverse sizes and

morphologies. This method enables the use of various mediums to synthesize AgNPs using this approach like polymers, emulsions, glasses, and surfactant micelles. Utilizing a photoinduced reduction method, Ag nanoparticles with a size of 8 nm were synthesized through the utilization of micro reactor capsules composed of poly(styrene sulfonate)/poly(allylamine hydrochloride) [336]. Moreover, conversion of spherical AgNPs to triangular Ag nanocrystals with edge length of 30–12 m has been achieved by photoinduced method [337]. Dual-beam illumination was employed to achieve shape conversion of AgNPs, utilizing citrate and poly styrene sulfonate as stabilizing agents.

In another study, monodispersed silver nanoparticles (AgNPs) with ligand coatings were rapidly synthesized by swiftly reducing Ag^+ ions through α-aminoalkyl radicals. These radicals originated from thioxanthone (TX) and its derivatives, including the 2-substituted thioxanthone series, TX—O—CH_2—COO— (TO) and TX—S—CH_2—COO— (TS), in their excited triplet state via hydrogen abstraction toward an aliphatic amine. The reduction of Ag^+ ions to the Ag^0 state was kinetically controlled by the substituent effect on thioxanthones. This control also led to the tuning of the quantum yield in the reaction [338]. The application of irradiation to the solution led to a change in the absorption spectra of the SPR in the range of 320–66 nm, which suggests an increase in the rate of Ag NP formation. Whereas the absorption spectra of the chromophore remained constant which indicates the regeneration process of thioxanthones. The formation of NPs was established by TEM, which displayed a marked difference in morphologies of AgNPs by reduction in solution of TX and those of TO and TS. Multimodal AgNPs have been obtained by TO, whereas monodispersed AgNPs of an average size of 4.8 ± 1 nm have been achieved with TS. Silver NP aggregates have been obtained using TX with smaller-sized AgNPs seen on the periphery of the Ag NP aggregates. All the structural variation has been corroborated with the development of SPR bands during irradiation. Silver nanoparticles (AgNPs) were successfully synthesized through the photoreduction of $AgNO_3$ using sodium citrate. Irradiation with a variety of light sources, including UV, white, blue, green, cyan, and orange, was used to accomplish photoreduction. The location and intensity of optical absorption bands changed as a result of the light source shift, and this was attributed to changes in the AgNPs' sizes and morphologies [339]. A simple UV photo activation method has been employed by Ghosh et al. to fabricate stabilized AgNPs in Trition X-100 solution [340]. The surfactant Triton X-100 not only acted as reducing and stabilizing agents but also growth controlling agent. Through a reduction in the system's diffusion/mass transfer coefficient, the surfactant managed the growth of Ag NP through a diffusion-controlled mechanism. The fabrication of AgNPs was ascribed to the autocatalytic growth mechanism. Ligands of the salt precursors profoundly affected the photochemical reduction efficiency owing to electron scavenging property, solubility, and stability. Synthesis of AgNPs was realized by UV light irradiation of an alkaline solution of silver nitrate ($AgNO_3$) and water-soluble chitosan derivative, carboxymethylated chitosan (CMCTS) at variable pH and $AgNO_3$ concentrations [341]. CMCTS served simultaneously both reducing and a stabilizing agent for the Ag NP synthesis. The particle size and particle density increase with increase in pH from 0.7 to 2.2. Further, the Ag NP size and particle size distribution increased remarkably with increase in pH up to 9.6. But solution with pH of 12.4 resulted in the creation of large-sized AgNPs with relatively limited size distribution (2–8 nm) which led to the strongest SPR peak at pH of 12.4. Likewise, the decrease in concentration of CMCTS from 0.5 to 0.1% caused the SPR peak's intensity to drop with corresponding red-shifting. Further decrease in concentration of CMCTS from 0.1 to 0.033% resulted in increase in SPR peak intensity with corresponding blue shifting. Change in concentration of CMC resulted in change in particle size of the AgNPs. Thus, it was speculated that higher concentration of CMCTS resulted in the formation of nucleation templates by coiling of the CMCTS chains which restrict the activity of Ag^+ ions and CMCTS. Fabrication of Ag nano colloids was realized by photo-induced reduction of gelatin-stabilized aqueous silver bromide using ascorbic acid as a

reducing agent [342]. The effect of the molar ratios of AgBr to ascorbic acid has been studied. The absorption peaks shifted to shorted wave lengths from 429 to 389 nm with rise in molar ratio from 1 : 1.5 to 1 : 9.0. This SPR absorption shift has been attributed to AgNPs' declining size. Further, the reaction time shortened from 90 to 5 minutes with increase in the reductant concentration. The effect of the radiation type on the efficiency of the reaction was also studied using various radiation sources viz., xenon flash, high-pressure mercury vapor and halogen lamps. The spectroscopic measurements have demonstrated that photoreduction of AgBr to AgNPs was most efficient while using radiation from the halogen lamp. Silver nanoparticles have been grown on the surface of cellulose fibers by surface activation of cellulose fiber surface and reduction of the silver nitrate [343]. The effect of the intensity of the UV radiation on the growth and concentration of AgNPs was investigated. It was discovered that the AgNPs' particle size increased from 56 to 85 nm with increase in the UV radiation intensity from 40 to 48 mW/cm^2. However, it has been perceived that size of the AgNPs is not much influenced by the change in $AgNO_3$ concentration. UV light source has been used to induce Ag NP formation and cross-linking of the PVP polymer from a solution of $AgNO_3$ and PVP [344]. The emergence of an SPR signal at 420 nm indicated the formation of AgNPs. With an increase in irradiation time, the SPR band strength increased, and its peak somewhat shifted to longer wavelengths. When the irradiation period was prolonged from 30 to 480 minutes, the particle size went from 2.5 to 3.45 nm. Highly reflective ultrathin films of Ag NP have been generated by on a glass slide by the photoinduced approach using silver precursor and free radical photo generator without adding any extra reductant [345]. The resulting Ag NP film was characterized by AFM and TEM. AFM displays the surface roughness of the films ranging from 7 to 100 nm. The production of spherical AgNPs with a diameter ranging from 2 to 10 nm was visible in TEM pictures. Additionally, green-reducing agents sourced from plant sources and microbial species have been used to facilitate photoinduced green synthesis of AgNPs [346–350].

In brief, this section explores the use of photoinduced reduction methods for synthesizing silver nanoparticles (AgNPs) with various sizes and morphologies. The versatility of this method allows for synthesis in different mediums, including polymers, emulsions, glasses, and surfactant micelles. Examples include the use of micro-reactor capsules, ligand-coated monodispersed AgNPs, and UV photoactivation methods. The photoinduced approach enables the rapid reduction of Ag^+ ions to Ag^0 state, leading to the formation of AgNPs with controlled morphologies. The influence of various parameters such as pH, concentration, and types of stabilizing agents is discussed, showcasing the tunability of this method for specific applications. The section also covers studies on the efficiency of different light sources and the use of green reducing agents derived from plant and microbial sources for environmentally friendly Ag NP synthesis.

1.5.4 Electrochemical Synthesis of Silver Nanoparticles

Electrochemical techniques have been utilized for the synthesis of silver nanoparticles (AgNPs), achieving excellent uniformity through the careful control of electrolysis parameters and manipulation of the electrolytic solution composition. In the study conducted by Johnas et al., AgNPs coated with polyphenyl pyrrole were synthesized using the electrochemical method at the liquid–liquid interface. *N*-phenyl pyrrole played a crucial role in facilitating the transfer of silver ions (Ag^+) from the aqueous phase to the organic phase, followed by a gradual transfer of electrons from the metal electrode to the Ag^+ ions, resulting in the formation of metal silver clusters. The confirmation of AgNPs formation was established through the observation of a SPR peak at 390 nm [351]. Monodisperse silver nanoparticles (AgNPs) within the size range of 1–18 nm were successfully synthesized using the electrochemical reduction method both inside and outside zeolite crystals. This was accomplished by using electrodes modified with ultrathin faujasite zeolite sheet

(CZFMEs-FAU) [352]. The zeolite film prevents the AgNPs from agglomeration during electrochemical reduction of the silver ions. The control of AgNPs' size was achieved by varying the degree of ion exchange in CZFMEs. A low degree of silver exchange yielded abundant AgNPs with a uniform diameter of 18 nm on the zeolite film surface through electrochemical reduction. A high exchange rate, involving Na^+ ions replacing Ag^+ ions, resulted in the formation of smaller AgNPs ranging from 1 to 2 nm. Intermediate exchange rates produced AgNPs with intermediate sizes, around 5 nm. Additionally, Ma et al. successfully synthesized spherical AgNPs with an average diameter of 20.6 nm through electrochemical reduction of Ag ions in the presence of PVP [353]. PVP has been employed to increase the rate of Ag NP formation and to reduce the rate of silver film deposition. Low molar ratios of PVP/Ag^+ did not produced any absorption peak in the UV-Visible region. As the molar ratio was increased to 50 : 1 a broad SPR absorption band could be observed around 420 nm. However, as the molar ratio was increased from 50 : 1 to 1000 : 1, a highly symmetrical SPR band was noticed. The occurrence of symmetrical SPR band confirmed the fabrication of AgNPs of small size and uniforms size distribution. The particle size was found to be influenced by the rotational speed of the working electrode. Low rotational speeds (500 and750 rpms) produce large-sized AgNPs with high degree of polydispersity. Smaller-sized AgNPs with narrow particle size distribution were produced as the rotational speed was increased (1000 and 1500 rpms). The absorption spectra exhibited a reduction in the intensity of the SPR absorption bands as the rotation speed of the electrode increased. This decline in band intensity was attributed to a decrease in particle size. The introduction of SDS into the solution led to the formation of even smaller silver nanoparticles (AgNPs) with a narrower distribution of the particle sizes [353]. Silver nanoparticles of approximately 20 nm in size were produced by electrochemical approach using potentiostatic and galvanostatic methods in ethanol solution [354]. A simple electrochemical set up has been employed by khaydarov et al. to synthesized AgNPs without the use of any stabilizing agent using two silver plates as cathode and anode [355]. The electrochemical process involved the oxidation dissolution of silver from the anode, resulting in the formation of Ag^+ ions. Subsequently, Ag^+ ions migrated from the anode to the cathode, where they underwent reduction to form zerovalent Ag atoms. These atoms then nucleated and grew to develop into silver nanoparticles (AgNPs). The stability and dispersibility of the AgNPs were improved by incorporating PVP as a protective agent. TEM images showed that spherical AgNPs with an average particle size of 7 nm were created, with a size range of 2–20 nm. The electrochemical synthesis of AgNPs was accomplished through potentiostatic electrolysis, utilizing an Ag anode [356]. The silver ions are reduced to the metallic silver and deposited on the electrode. DLS data show the formation of nanosized AgNPs with particle size between 14 and 79 nm. Electrochemical synthesis of AgNPs was also carried out using sodium polyacrylate (NaPA) as a stabilizer [357]. Silver nanoparticles up to the size of 10 nm have been obtained by this method. Silver nanoparticles have been obtained by electrochemical reduction method using sacrificial Ag silver anode as a silver ions source and rhamnolipid, RL as a stabilizer [358]. Investigations was conducted into the impact of temperature and stabilizer on the rate of Ag dissolution and cathodic reductive production of Ag-RL complex ions. It was found that the rate at which AgNPs formed increased in response to an increase in RL concentration. Also, the rate of anodic and cathodic currents increased up to 1.5 times with increase in temperature from 40 to 60 °C. UV–Visible spectra demonstrated an increase in optical density of the SPR peak with peak shifting toward shorter wavelengths with increase in the number of CVA cycles. TEM images showed the fabrication of spherical AgNPs with size in the range of 2–20 nm when the RL concentration was within 0.5–2 g/L in the temperature range of 40–60 °C. A decrease in Ag NP size was observed with increase in RL concentration inside the solution. However, increase in Ag NP size and particle size dispersion has been observed with increase in temperature of the solution.

To summarize, this section explores the utilization of electrochemical techniques to produce silver nanoparticles (AgNPs). The electrochemical approach offers precise control over electrolysis parameters and electrolytic solution composition, leading to homogeneous and controlled Ag NP formation. Various techniques, including liquid–liquid interfaces and zeolite film-modified electrodes, are discussed for achieving monodisperse AgNPs with controlled sizes. The role of stabilizing agents such as polyphenyl pyrrole, PVP, and rhamnolipid in the electrochemical synthesis is highlighted. The influence of factors like rotational speed and temperature on the grain size and distribution is investigated. Additionally, comparisons between potentiostatic and galvanostatic methods, as well as the impact of different stabilizers on the rate of Ag NP formation, are discussed. The findings indicate the versatility of electrochemical methods for tailoring the size and properties of AgNPs for various applications.

1.5.5 Microwave-Assisted Synthesis of Silver Nanoparticles

The microwave heating technique proves to be a convenient and promising approach for producing highly crystalline silver nanostructures characterized by variable sizes and a narrow size distribution [359]. This method features shorter reaction times and reduced energy consumption, leading to the formation of silver nanoparticles (AgNPs) with high yield and minimal agglomeration [359]. The synthesis of silver nanoparticles has been accomplished through a microwave-assisted approach, utilizing *Cyanthillium cinereum* (*C. cinereum*) both as a reductant and a capping agent [360]. This method can also reduce chemical waste by using environmental friendly reaction media [361]. The AgNPs obtained were crystalline in nature and spherical in shape with the average particle size of 19.25 ± 0.44 nm as revealed by RTEM images. The highly crystalline nature of AgNPs was evident from SAED pattern by displaying the bright spots in ordered concentric fashion. The creation of NPs at an $AgNO_3$ concentration of 1×10^{-3} M was indicated by the existence of an SPR signal at 418 nm. Microwave-assisted fabrication of AgNPs has been accomplished inside hybrid hydrogel (CGH) of carboxy methyl cellulose (CMC) and gelatine. CMC acted as a reducing agent and stabilizing agent in the CGH. The formation of AgNPs was confirmed by the appearance of SPR peak around 414 nm. Silver NPs were obtained at different pH and different concentrations of CMC as reductant and silver nitrate. Stable SPR peak at 414 nm was observed at pH of 12.0 and $AgNO_3$ concentration of 0.8 mM. TEM images revealed the production of uniform and spherical CGH-AgNPs with the mean particle diameter of 12 nm. EDX analysis displayed a spectral peak at 3 keV indicating the formation of pure silver [362]. Microwave-assisted fabrication of anisotropic AgNPs has been realized from the decomposition of silver oxalate using PVP as a reducing agent [363]. Time evolution of SPR spectra shows the appearance of a peak at 367 nm, which exhibits red-shifting with subsequent increase in peak intensity with time. The peak shifting occurs from 367 after 60 seconds to 422 nm after 75 seconds and then to 462 nm after 90 seconds of irradiation (Figure 1.11A). The fabrication of spherical AgNPs after 60 seconds of irradiation was confirmed by the HRTEM mages which show spherical AgNPs between 3 and 9 nm in size (Figure 1.11B). After 75 seconds of irradiation, HRTEM images display the fabrication of anisotropic AgNPs like rods, triangles, and other morphologies with the dimensions of 15–45 nm diameter and 20–70 nm length (Figure 1.11C). After 90 seconds of microwave irradiation, the formation of anisotropic AgNPs with size between 50 and 120 nm occurred which has been ascribed to the emergence of a broad peak around 569 nm due to longitudinal interaction. Microwave-assisted procedure has been used to create AgNPs using starch as a reductant and a stabilizing agent. The AgNPs obtained were pseudo-spherical in morphologies with a 12 nm average particle size [364]. Fabrication of AgNPs was carried out by polyol process under microwave irradiation conditions using silver nitrate as a metal salt precursor. The metal salt precursor was combined with ethylene glycol serving as a

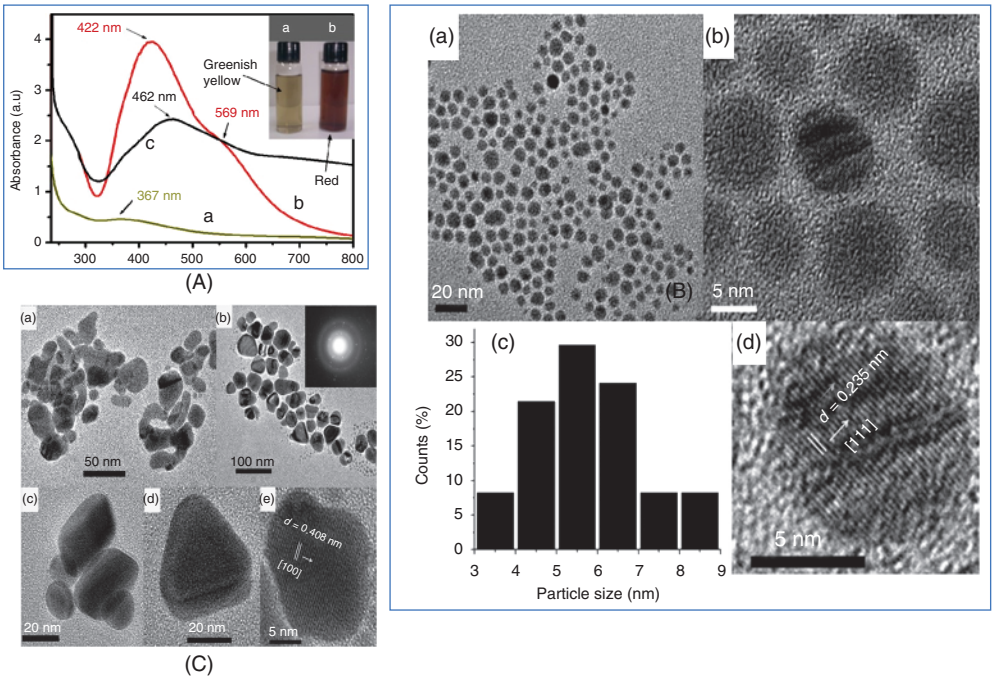

Figure 1.11 (A) UV-visible spectra of Ag nanoparticle colloids generated through microwave irradiation in ethylene glycol for different durations: (a) 60 seconds, (b) 75 seconds, and (c) 90 seconds. (B) High-resolution transmission electron microscopy (HRTEM) pictures of silver nanoparticles produced by subjecting silver oxalate to microwave exposure in ethylene glycol for 60 seconds, shown in (a) and (b). In (c), a size distribution histogram of these Ag nanoparticles is presented. (d) Depicts a detailed image of an Ag nanoparticle in the center of the (b) image, showing its lattice structure. (C) High-resolution transmission electron microscopy (HRTEM) pictures of silver nanoparticles created by exposing silver oxalate to microwave radiation in ethylene glycol for 75 seconds. Inset in (b) displays the selected area electron diffraction (SAED) pattern of one of the silver nanoparticles. Source: (a–c) Reproduced with permission from Navaladian et al. [363]/IOP Publishing.

reductant and PVP functioning as a capping agent under for 15 minutes at 150° in a microwave digestive system. The reaction yielded silver nanoparticles (AgNPs) of diverse shapes with discreet Ag nanorods of the size of 50 nm [365]. Similarly, AgNPs were obtained by microwave irradiation of the solution of $AgNO_3$ with sodium citrate as capping agent and formaldehyde acting as a reductant [366]. The range particle size of AgNPs varied with the concentration of all the three reactions components. As the concentration of silver nitrate was reduced, the particle size shrank, and the particle size distribution narrowed. As the concentration of sodium citrate increased, there was a corresponding decrease in the average particle size. Silver NPs of variable shapes Ag nanorods, nanowires, cubes, triangles and triangular bi pyramids have been fabricated by microwave polyol process utilizing ethylene glycol as a reducing agent in presence of $H_2[PtCl_6]$ and PVP [367]. PVP acted as a shape-directing agent and gets adsorbed on the [100] facet resulting in the production of Ag nanorods, nanowires, nanocubes, and triangular bipyramids. Ag nanostructures were obtained without PVP, but in the presence of Cl^- ions, the yields were lower. This indicates that chloride ions also play a role as shape directors, influencing the synthesis of Ag nanostructures with varying shapes. TEM pictures of the supernatant revealed the fabrication of nanorods/nanowires with length of 1 µm (yield 21%), Ag nanocubes (6%), Ag triangular bipyramids (4%), Ag nanoflowers (0.5%), and spherical Ag nanoparticles of average diameter of 60 nm (68%) (Figure 1.12A). However, a significant amount of Ag NP precipitate has been observed in the

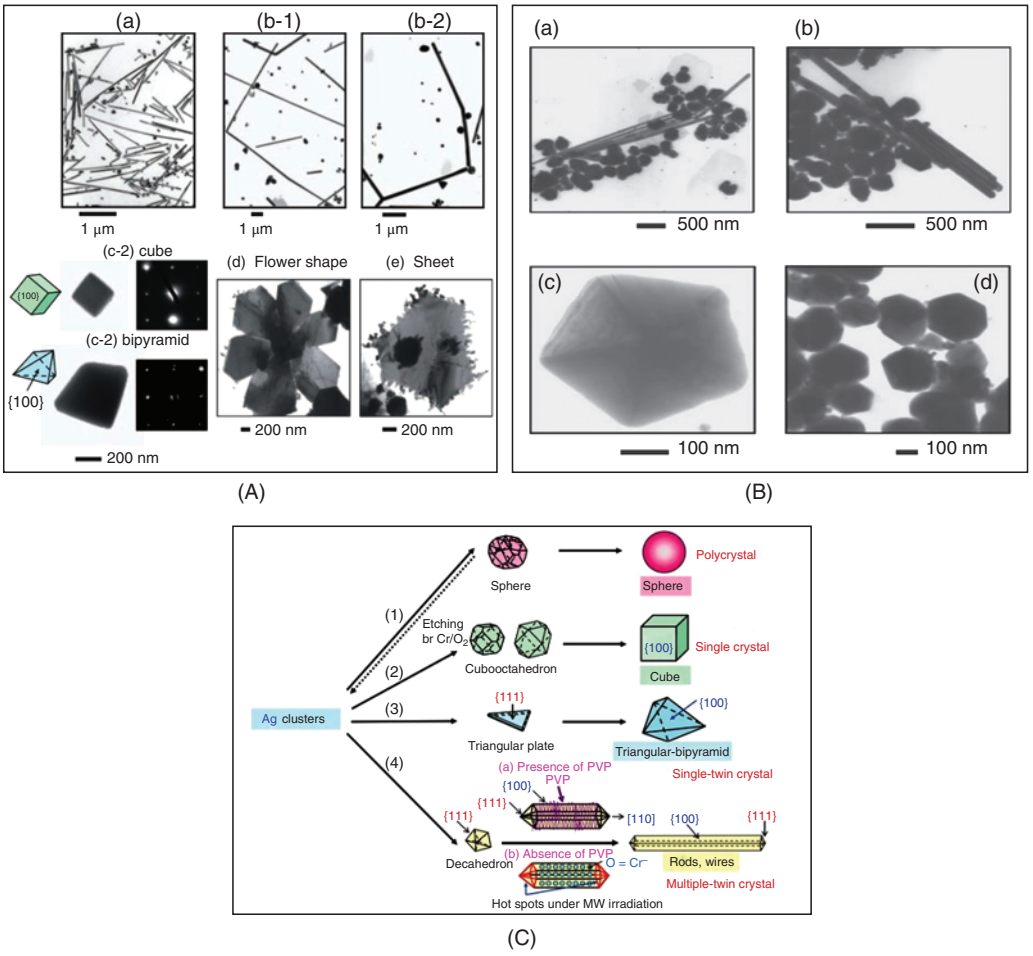

Figure 1.12 (A) Transmission electron microscopy images of silver nanostructures synthesized from surfactants using (a) $AgNO_3$ (46.5 mM)/$H_2[PtCl_6].6H_2O$ (115 mM)/PVP (264 mM)/EG and (b–e) $AgNO_3$ (46.5 mM)/$H_2[PtCl_6].6H_2O$ (115 mM)/EG Solutions. Illustration of selected area electron diffraction patterns for cube and bipyramid shapes in (c-1) and (c-2). (B) Transmission electron microscopy images of silver nanostructures derived from precipitates formed through the utilization of $AgNO_3$ (46.5 mM)/$H_2[PtCl_6].6H_2O$ (115 mM)/EG solutions. (C) Mechanism of silver nanostructure formation during microwave-assisted heating. Source: (a–c) Reproduced with permission from Tsuji et al. [367]/Oxford University Press.

absence of PVP. TEM pictures of the precipitate revealed the production of large-sized spherical Ag particles, 1-D wires and do decahedral silver structures (Figure 1.12B). The mechanistic steps of the growth of various Ag nanostructures are presented schematically in Figure 1.12C. A green chemistry approach utilizing microwave radiations was employed for the synthesis of silver nanoparticles (AgNPs). Amino acids like L-lysine and L-arginine served as reducing agents, while water-soluble starch acted as a capping agent. Starch-capped AgNPs self-assembled to form multilayered mirror-like films on the glass surface [368]. Highly monodispersed AgNPs have been fabricated by microwave irradiation of ethanolic solution of $AgNO_3$ using PVP as a stabilizer [369]. The confirmation of silver nanoparticles (AgNPs) formation was established through the emergence of a SPR peak at 416 nm. Stable and polycrystalline AgNPs with particle size of 10 ± 5 nm of were obtained after 5 seconds of microwave irradiation. Sodium alginate was used as a reducer and stabilizer in the microwave irradiation process to create silver nanoparticles [370]. The impact

of reaction parameters, including the concentration of sodium alginate, sodium nitrate, pH, and irradiation time, was examined. XRD studies revealed the presence of face-centered cubic silver in pure phase. UV visible spectroscopic studies revealed the SPR peak at 417 nm and the peak intensity increased with rise in concentration of sodium alginate from 0.1 to 0.5%. However, as the concentration of sodium alginate increased from 0.5 to 1.5%, the peak intensity reduced and shifted toward a longer wavelength, indicating the agglomeration of AgNPs and the creation of large-sized particles. Using 0.5% sodium alginate, and varying the concentration of silver nitrate, it was found that SPR peak intensity centered at 418 nm augmented with rise in concentration of the silver nitrate which indicated the fabrication of AgNPs in higher amounts at higher sodium nitrate concentrations. Further increase in irradiation times also resulted in an increase in SPR peak intensity at 418 nm with slight red-shifting to 427 nm which implied the increased rate of formation of AgNPs. At low pH, no reduction occurs as evidenced by the absence of SPR peak, whereas a band at 270 nm has been seen at pH 5 which corresponds to the presence of Ag^+ clusters. An elevation in pH led to the appearance of a new peak at 418 nm, indicating an augmented reduction rate of Ag^+ ions by sodium alginate due to more and more exposed carboxyl groups. TEM images revealed the development of fewer AgNPs at lower silver nitrate concentrations (0.8 mm/L). Nonetheless, the density and dispersibility of AgNPs increased as the $AgNO_3$ concentration was raised from 4 to 8 mm/L, while maintaining an average grain size of 12 nm at the higher $AgNO_3$ concentration. Average particles size also increased from 10 to 15 nm with increase in pH from 5 to 11. The average grain size of spherical AgNPs exhibited a decrease from 20 to 10 nm as the sodium alginate concentration increased from 0.1 to 0.5%. Numerous reports have been published on the microwave-assisted fabrication of AgNPs utilizing various reductants and stabilizers [371–376].

In brief, microwave heating methods provide a convenient and promising approach for the fabrication of highly crystalline AgNPs with variable sizes and narrow size distribution. This method, renowned for its abbreviated reaction times, diminished energy consumption, and minimized chemical waste, has been employed for the microwave-assisted synthesis of silver nanoparticles (AgNPs). Various reducing agents and stabilizers, such as *Cyanthillium cinereum*, carboxy methyl cellulose, gelatine, PVP, starch, ethylene glycol, amino acids (L-lysine and L-arginine), and sodium alginate, have been employed to achieve controlled Ag NP formation with specific morphologies. The microwave-assisted method proves to be versatile, offering a green and efficient synthesis route for tailored silver nanostructures with diverse applications.

1.5.6 Bio Fabrication of Silver Nanoparticles

In recent times, eco-friendly synthetic methods utilizing reductants sourced from biological entities like microbes and plant extracts have emerged as a practical substitute for traditional chemical synthesis routes in the creation of silver nanoparticles (AgNPs) [377–379]. The eco-friendly synthesis of AgNPs has become a practical substitute for physicochemical synthesis methods, primarily due to the elimination of toxic chemicals and solvents, as well as the nonproduction of hazardous by-products [380, 381].

Microorganisms like bacteria and fungi have been used for remediation of the toxic metal ion pollutants from the toxic environments [382, 383]. These microorganisms facilitate the reduction of toxic metal ions to metal nanoparticles. Synthesis of AgNPs by microbes involve both intracellular as well as extracellular syntheses. Intracellular synthesis involves use of intracellular components as reducers as well as stabilizers [384].

1.5.6.1 AgNPs Synthesized Using Bacteria

Bacteria have demonstrated significant efficacy as bio-factories for the synthesis of silver nanoparticles (AgNPs), occurring both intracellularly and extracellularly. Certain bacterial strains with

silver resistance have been found to accumulate silver on their cell wall, reaching up to 25% of their dry weight [385]. The bacterial strain resistant to silver, specifically *Pseudomonas stutzeri AG259*, was first utilized for the synthesis of silver nanoparticles (AgNPs) through the cultivation of the bacteria in a concentrated silver nitrate solution. The resultant AgNPs, averaging 200 nm in size, were noted for their accumulation inside bacterial cell wall [386]. Spherical silver nanoparticles (AgNPs) with sizes ranging from 5 to 15 nm were produced through the utilization of silver-resistant *Bacillus* species [387]. The silver nanoparticles (AgNPs) accumulated within the periplasmic space of the bacterial cells. Furthermore, successful extracellular synthesis of AgNPs was achieved by employing the *actinomycete* strain *Streptomyces glaucus* 71 MD [388]. TEM images unveiled the creation of spherical silver nanoparticles (AgNPs) with an average size measuring 13 nm. Large-scale production of AgNPs has been achieved by using *Proteus mirabilis PTCC 1710*. Extracellular synthesis of silver nanoparticles ranging in size from 5 to 25 nm was achieved using cultural supernatants derived from *Escherichia coli* ATCC 8739, *B. subtilis* ATCC 6633, and *Streptococcus thermophilus* ESh1 [389]. The rapid synthesis of silver nanoparticles (AgNPs) has been accomplished using supernatants of *Klebsiella pneumonia, E. coli, Enterobacter cloacae* [390], and *Bacillus megaterium* [391]. The rapid biosynthesis of silver nanoparticles (AgNPs) has been accomplished using the S-27 strain, *Bacillus flexus* family [392]. Upon adding the cultural supernatant to the silver nitrate solution, rapid color change yellow to brown was observed. The brown colored solution showed the SPR peak at 420 nm. AFM and FE-SEM images displayed anisotropic AgNPs (spherical and triangular) with average size of 12 and 61 nm. Both intracellular and extracellular syntheses of AgNPs have been achieved the bacterial strain *Proteus mirabilis* PTCC 1710 [393]. The AgNPs displayed SPR peak at 400–410 nm. TEM images revealed the generation of spherical silver nanoparticles (AgNPs) within the size range of 10–20 nm. Extracellular biosynthesis of AgNPs has been reported by Das et al. using CS11 strain of *Bacillus* sp. obtained from heavy the soil contaminated with heavy metals [394]. The silver nanoparticles were seen after 24 hours of interaction between $AgNO_3$ and bacteria at room temperature. The presence of silver nanoparticles (AgNPs) was spectroscopically confirmed through the appearance of a surface plasmon resonance (SPR) peak at 450 nm. The nanoparticles exhibited a spherical shape of the sizes of 42 and 92 nm. Silver nanoparticles (AgNPs) were synthesized using *Bacillus cereus* isolated from contaminated soil [395]. Optimization of the experimental conditions was done using central composite design. Optimized values of temperature (48.5 °C), inoculum size (8.7 mL), silver nitrate concentration (1 mM), and pH (9) were employed for fabrication of AgNPs. The synthesis yielded the spherical silver nanoparticles (AgNPs) with a size in the range of 5–7 nm. Spherical AgNPs with diameter of 40–50 nm have been synthesized using cultural supernatant from *Lactobacillus plantarum*. While numerous studies have been conducted on the synthesis of silver nanoparticles (AgNPs) utilizing various bacteria, a notable limitation of this approach is the relatively slow synthesis rate, and a restricted range of sizes and shapes has been achieved.

1.5.6.2 AgNPs Synthesized Using Fungi

Good metal tolerance and bioaccumulation ability of fungi have made them a good candidate for the biosynthesis of metal nanoparticles [396]. Also, fungi are much more convenient to handle inside the laboratories and secrete enzymes as reductant in larger quantities as compared to bacteria. These features enable fungi to produce metal nanoparticles at higher rates and in large quantities [397]. Further simplicity in handling of fungi has made them a good eco-friendly candidate for the green synthesis of NPs. The extracellular synthesis of AgNPs was first reported by Mukherjee et al. by exposing fungus *verticillium* to silver nitrate [398]. The Ag NP formation took place on mycelial surface due the reduction of the Ag^+ ions by the carboxylate ions of the enzymes secreted by the fungal cell. The silver atoms then underwent nucleation and growth to form AgNPs.

Silver NPs with the size of 25 ± 12 nm have been produced. Fast extracellular biogenesis of silver nanoparticles (AgNPs) has been documented employing fungus *Aspergillus fumigatus*, and NPs were formed within minutes of the reaction. The generated AgNPs had a spherical shape and ranged in size from 5 to 25 nm [399]. Naqvi et al. employed the fungus *Aspergillus flavus* to produce AgNPs by extracellular mycosynthesis, combining silver nitrate with the fungus's culture filtrate. Silver NPs in the size range of 5–30 nm have been obtained with the SPR peak around 400 nm [400]. The fungus y *Fusarium solani* (USM-3799) have been used by Ignle et al. for synthesizing AgNPs by mixing the 1 mM silver nitrate with fungal cell filtrate [401]. The development of an SPR peak at 420 nm optically identified the production of AgNPs. The presence of biomolecules like proteins as stabilizing agents on the Ag NP surface was ascertained by FTIR analysis. The formation of spherical AgNPs with an average grain size of 16.23 nm in the size range of 5–35 nm was shown by the TEM pictures. Synthesis of AgNPs has been achieved by Syed et al. by employing the thermophilic fungus *Humicola* sp. [402]. The synthesis was conducted by combining the suspension of fungal mycelia with the 100 mL of silver nitrate at the temperature of at 50 °C by maintaining the reaction pH at 9. The fabrication of AgNPs was monitored spectroscopically by measuring the absorption of the reaction mixture. SPR absorption peak around 415 nm has been identified. Ag NP formation was identified by a yellow to brown color shift in the reaction mixture. TEM pictures displayed spherical AgNPs with fcc symmetry and sizes ranging from 5 to 25 nm. The presence of protein molecules on the surface of silver nanoparticles (AgNPs), acting as stabilizing agents, has been verified through FTIR spectroscopy. The FTIR analysis revealed two bands at around 1644 and 1523 cm^{-1}, known as amide I and II bands. These bands are caused by the stretching vibrations of the amide linkages at —C=O (amide I) and —N—H (amide II). Rapid biosynthesis of AgNPs has been accomplished by the bio reduction of 1 mM $AgNO_3$ with different concentrations of hot water extract of basidiocarps, *Pleurotus cornucopiae var. citrinopileatus. P. cornucopiae* [403]. After the reaction mixture was incubated for 72 hours, the color of the mixture changed from yellow to yellowish brown, indicating the synthesis of AgNPs. AgNPs were identified by an SPR peak at about 450 nm in UV-visible spectroscopy. The presence of polysaccharides and proteins as reducing and capping agents has been confirmed by FTIR spectroscopically, and the FTIR spectrum of the Ag NP sample displays various peaks at 3304, 2200, 2066, 1969, 1636, 1261, 1094, and 611 cm^{-1}, which represent the absorptions corresponding to stretching and bending vibrations of the various functional groups of various biomolecules responsible form reduction and subsequent stabilization of AgNPs. The generation of spherical silver nanoparticles (AgNPs) has been corroborated through HRTEM, revealing sizes ranging between 20 and 30 nm. Silver NPs have been synthesizing by *Pleurotus ostreatus*, a tree oyster mushroom [404]. The color of the reaction mixture changed from pale yellow to dark brown after the mushroom aqueous extract and 1 mM silver nitrate were incubated, confirming the production of AgNPs. TEM images revealed the creation of spherical AgNPs with an average size of 28 nm. Numerous reports exist on the synthesis of AgNPs using various fungi, both intra and extracellularly [405–411]. Various yeast strains have also been explored for the synthesis of silver nanoparticles (AgNPs) with promising outcomes [397, 412, 413].

1.5.6.3 AgNPs Synthesized Using Actinomycetes, Algae, and Viruses

Like fungi biosynthesis of AgNPs has been achieved using actimycetes both intracellularly as well as extracellularly [414–420]. Synthesis of AgNPs has been carried out by the cell wall enzymes which reduced Ag^+ ions to Ag seeds which finally grow to produce using marine actinobacteria, *Streptomyces* sp *LK3b* [415]. Silver NPs exhibited SPR peak 420 nm, and XRD studies showed intense Bragg reflections corresponding to the fcc structure of nano silver. TEM and AFM micrographs displayed the formation of spherical silver nanoparticles (AgNPs) with an average grain size of 5 nm. The mechanistic examination disclosed the involvement of enzymes, such as

NADH-dependent nitrate reductase, in the reduction of Ag^+ ions to metallic Ag via an electron transfer mechanism. Biological synthesis of silver nanoparticles (AgNPs) has been carried out employing *Streptomyces antimycoticus L,* a strain of endophytes isolated from the leaves of *Mentha longifolia L* [421]. Confirmation of successful biosynthesis of silver (Ag) was ascertained through XRD, TEM, DLS, and UV-Visible studies. Utilizing these techniques, it was verified that spherical silver nanoparticles (AgNPs) were formed with sizes ranging from 13 to 40 nm. The stability of AgNPs was confirmed by carrying out the optical absorption measurement using UV-Visible spectroscopy. The UV-Visible spectrum proved the remarkable stability of silver nanoparticles (AgNPs) as evidenced by the presence of the SPR peak at 415 nm, which remained intact for nearly one month. Additionally, silver nanoparticles (AgNPs) were determined to possess a negative surface charge of −19.2 mV, as indicated by the zeta potential analysis. Green synthesis of AgNPs was achieved using cultural filtrate extracts of two endosymbiotic actinomycete strains, 192ANMG (F2) and 17ANMG (F7) isolated from *Crella cyathophora*, a marine sponge [422]. The colloidal and surface stability of AgNPs was checked by DLS and zeta potential measurements. Dynamic light scattering (DLS) demonstrated an increase in the hydrodynamic diameter of the particles upon the addition of the cultural filtrate to the silver nitrate solution, indicating the reduction of silver nitrate by the extract to form silver nanoparticles (AgNPs). The zeta potential measurements of the Ag NP samples indicated values of −24.6 and −25 mV for *Streptomyces* sp. 192ANMG (F2) and *Streptomyces* sp. 17ANMG (F7), respectively. TEM measurements revealed the formation of spherical AgNPs with average particle size of $\sim 8.66 \pm 2$ nm in case of *Streptomyces* sp. 192ANMG (F2) and nonspherical AgNPs with average particle size of 35 ± 2 nm in case of *Streptomyces* sp. 17ANMG (F7). The hexagonal structure of silver (Ag) in silver nanoparticles (AgNPs) was revealed through SAED analysis. Numerous reports have been published on the synthesis of AgNPs employing actinomycetes [423–427].

Certain investigations have indicated that the synthesis of silver nanoparticles (AgNPs) can be achieved through some of the aquatic microorganisms like algae. Such aquatic microorganisms have shown the tendency not only to accumulate Ag ions but also to synthesize the AgNPs. For example, Ag nanoplates have been fabricated at room temperature by the extract of *Chlorella vulgaris*, a unicellular green alga [428]. Initially, the algal extract, appearing as a light-yellow liquid, underwent a color change to pinkish red upon contact with a 1 mM $AgNO_3$ solution for 12 hours at room temperature. This color transformation was attributed to the SPR of Ag nanocrystals in the visible region. UV–vis spectroscopy revealed three distinct plasmon bands at approximately 465, 392, and 347 nm for the synthesized Ag nanocrystals (Figure 1.13a). TEM analysis unveiled the presence of circular, rod-like, and triangular Ag nanocrystals in the synthesized sample. Triangular particles, along with some circular particles, displayed uniform contrast, suggesting they were single-crystalline nanoplates (Figure 1.13b). FESEM imaging confirmed the platelike morphology, with rod-like particles identified as Ag nanoplates standing perpendicularly on the TEM grid. The Ag nanoplates exhibited an average diameter of 44 nm, with a standard deviation of 6 nm. The average thickness, estimated from the width of rod-like particles, was 20 ± 4 nm. High-resolution TEM images demonstrated the single crystallinity of the nanoplates, supported by electron diffraction patterns showing a sixfold symmetry indicative of {111} faces (Figure 1.13c). The diffraction spots' *d*-spacings corresponded to the {422}, {220}, and {422} planes, consistent with previous observations on Ag or Au nanocrystals (Figure 1.13d). The synthesis mechanism was attributed to active species in the algal extract, primarily identified as algal proteins (aP). Modifications made to algal proteins indicated that tyrosine (Tyr) residues played a role in reducing silver ions, while carboxyl groups in aspartic acid (Asp) and/or glutamic acid (Glu) residues contributed to the anisotropic growth of silver nanocrystals, resulting in the formation of nanoplates. Further experiments separated the algal proteins into low- and high-molecular-weight fractions. The high-molecular-weight fraction

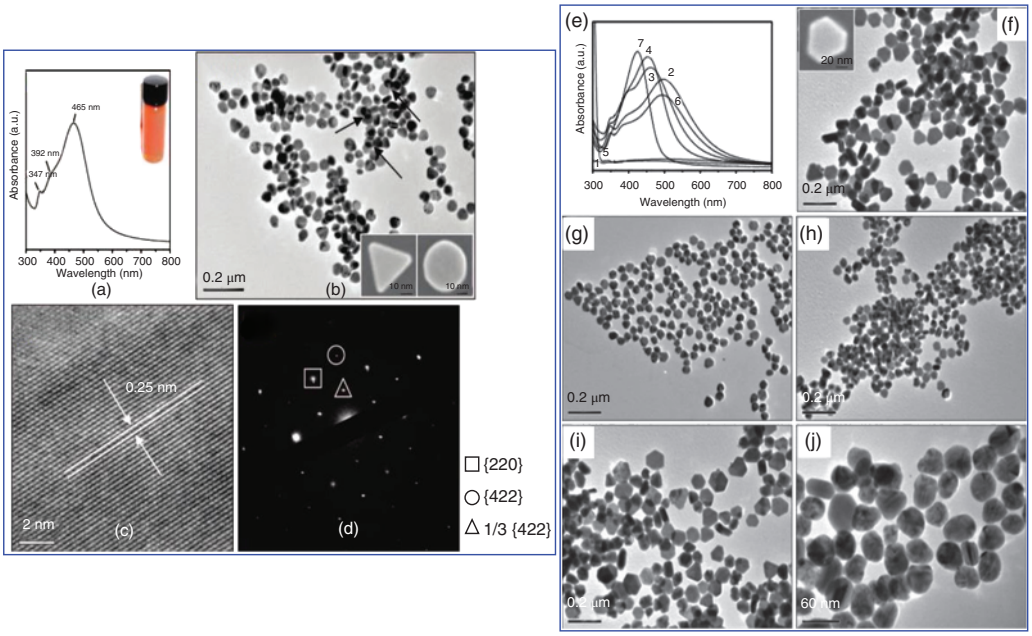

Figure 1.13 (a) UV–visible spectrum of Ag nanocrystals produced through the reduction of an aqueous Ag ion solution using the algal extract. The inset displays a digital image of the resultant Ag colloidal solution. (b) Representative transmission electron microscopy (TEM) image of the synthesized Ag nanocrystals, with arrows indicating areas where flat particles have overlapped. The inset features characteristic field emission scanning electron microscopy (FESEM) images portraying circular and triangular Ag nanocrystals exhibiting a planar structure. (c) High-resolution TEM (HRTEM) image captured from the vertex of an isolated Ag nanoplate. (d) Selected area electron diffraction (SAED) pattern of an Ag nanoplate, with spots enclosed in a box, a circle, and a triangle corresponding to {220}, {422}, and 1/3{422} reflections, respectively. (e) UV–visible spectra of Ag nanocrystals obtained under varied reaction conditions. Curves 1–7 were generated by adding 1 mL of 10 mM $AgNO_3$ to 9 mL of (curve 1) the low-molecular-weight fraction of the algal extract; (curve 2) the high-molecular-weight fraction of the algal extract (aP); (curve 3) heat-denatured aP; (curve 4) urea-denatured aP; (curve 5) NAI-modified aP; (curve 6) deacetylated NAI-modified aP; and (curve 7) amine-modified aP, respectively. The pH of all solutions was adjusted to 7.0. (f–j) Exemplary transmission electron microscopy (TEM) images of Ag nanocrystals prepared under conditions described in curves 2, 3, 4, 6, and 7, respectively. The inset in (b) displays a typical field emission scanning electron microscopy (FESEM) image of the truncated triangular plate, confirming the planar structure. Source: Reproduced with permission from Xie et al. [428]/American Chemical Society.

(aP) demonstrated significant absorption in the UV–vis spectrum, indicative of Ag nanoplate formation (Figure 1.13e). TEM analysis of Ag nanocrystals formed in the aP solution revealed mainly truncated triangular plates (Figure 1.13f–j). Heat-denatured and urea-denatured aP solutions exhibited similar UV–vis spectra and TEM images, suggesting that protein conformation did not significantly affect Ag nanoplate formation. The red- or blue-shifting of SPR peaks in denatured protein solutions correlated with the size of the formed nanoplates, indicating a direct relationship between protein conformation and nanoplate dimensions. The research findings led to the conclusion that algal proteins, particularly those containing tyrosine (Tyr) and carboxyl groups, played a vital role in both the reduction of silver ions (Ag ions) and the regulated growth of silver nanoplates. The mechanism involved a specific interaction between protein molecules and Ag ions, resulting in anisotropic growth and the fabrication of planar Ag nanostructures. The work opens avenues for understanding the active amino acid residues in protein molecules accountable for Ag ion reduction and nanoplate growth.

As the silver nitrate solution was brought in contact with algal extract, pinkish red colloidal suspension was obtained due to the SPR phenomenon exhibited by the A marine alga, *Caulerpa racemose* have been employed by Kathriaven et al. for the synthesis of AgNPs [429]. XRD studies revealed the fabrication of pure and crystalline face-centered cubic silver. The morphology of silver nanoparticles was observed to be both spherical and triangular, and the average particle size was determined to be 10 nm. Similarly, *Sargassum wightii*, a marine algae, has been discovered to extracellularly produce silver nanoparticles (AgNPs) [430]. Various other reports are there for the fabrication of AgNPs by various algal species [431–438].

In summary, this section delves into the potential of various microorganisms, including bacteria, fungi, actinomycetes, algae, and even viruses, to serve as efficient bio-factories for the environmentally friendly synthesis of silver nanoparticles (AgNPs). Bacteria, such as *Pseudomonas stutzeri* and *Proteus mirabilis*, demonstrate both intracellular and extracellular synthesis capabilities, producing AgNPs with varying sizes and distributions. Fungi, like *Verticillium*, *Aspergillus*, and *Fusarium solani*, exhibit metal tolerance and bioaccumulation abilities, offering a convenient and eco-friendly approach for Ag NP synthesis. Actinomycetes, algae, and even viruses also contribute to the green synthesis, providing a diverse range of potential biofabrication sources for tailored silver nanostructures. The section emphasizes the advantages of these biological methods, such as higher synthesis rates, large-scale production, and eco-friendly processes.

1.5.6.4 Mechanisms of the Fungal-Mediated Synthesis of AgNPs

Components present in the cell wall, such as proteins, enzymes, and other biomolecules, have been identified to play a crucial role in the synthesis of silver nanoparticles (AgNPs). These biomolecules facilitate the reduction of Ag^+ ions into Ag atoms, initiating nucleation and subsequent growth to fabricate silver nanoparticles (AgNPs). The AgNPs formed are then stabilized by proteins, peptides, and other biomolecular components. A number of reports have discussed the mechanistic details of the fungal-mediated synthesis of AgNPs. As an illustration, Duran et al. have connected cell wall polymers and other biomolecules like quinones, anthraquinones, and naphthoquinones to the production of silver nanoparticles (AgNPs) using *Fusarium oxysporum*. These biomolecules have been demonstrated to function as electron shuttles, transferring electrons to Ag^+ ions and reducing them to Ag atoms [439]. Mukherjee et al. have put forward a reasonable mechanistic detail for the synthesis of silver nanoparticles (AgNPs) by *Trichoderma asperellum* analyzing the FTIR spectroscopic peaks of the AgNPs and fungal cell-free extrate. As per the findings, it has been suggested that fungal extract contain protein molecules containing S-H bonds like cysteine, which plays a pivotal role for the reduction of silver ions. Cysteine has been found to undergo dehydrogenation and de-electronation in presence of Ag^+ ions which itself get reduced to Ag ions [440]. However, difference in the mechanistic details has been reported by several groups for extracellular and intracellular synthesis of AgNPs. In the process of extracellular synthesis, proteins, and enzymes released by fungal cells have been documented to play a pivotal role in the reduction of Ag^+ ions to Ag atoms, ultimately leading to the formation of silver nanoparticles (AgNPs) [441]. Whereas, in intracellular synthesis, synthesis of AgNPs occurs inside the cytoplasm and vesicles of the fungal cell which are then expelled out of the fungal cell by exocytosis [442].

1.5.7 Plant-Mediated Synthesis of Silver Nanoparticles

The realm of nanotechnology has experienced a significant shift in nanoparticle synthesis, with an increasing focus on green and sustainable methods. Notably, the plant-mediated fabrication of AgNPs emerges as an environmentally friendly and biocompatible approach. Plants, equipped with numerous bioactive compounds, serve as potent reservoirs for both reducing and stabilizing

agents in the metallic nanoparticle synthesis. This section delves into the captivating domain of plant-mediated synthesis, investigating the underlying mechanisms, benefits, and the varied applications of AgNPs generated through this eco-friendly chemistry approach. The green synthesis of AgNPs using whole plant or plan components is discussed below.

Plant extracts or various parts of plants have been employed in the synthesis of silver nanoparticles (AgNPs). The synthesis process involves utilizing plant extracts, serving the dual function of both reducing and stabilizing agents. Various plant species ranging from angiosperms to algae have been used for this purpose [443–447]. The first article on the synthesis of AgNPs has been documented by Gardea-Torresdey et al. using sprouts of *Alfa alfa* plant [448]. The roots of the plant absorbed Ag from the agar medium and transported to shoots where silver atoms agglomerated to form silver nanostructures. The AgNPs were arranged in one-dimensional array with size ranging from 2 to 20 nm. The fabrication of silver nanoparticles (AgNPs) has been effectively accomplished using Geranium (*P. graveolens*) leaf extract [449]. Upon adding the extract to aqueous $AgNO_3$ solution, spherical and crystalline AgNPs have been produced, with an average particle size between 16 and 40 nm. Silver nanoparticles were synthesized using *Capsicum annuum L.* extract [450]. The effect of reaction time and $AgNO_3$ concentration on the Ag NP size and morphology has been investigated. The silver nanoparticles (AgNPs) exhibited a spherical morphology, with the particle size increasing from 10 ± 2 nm at 5 hours to 25 ± 3 nm at 9 hours and further to 40 ± 5 nm at 13 hours [450]. Silver NPs were synthesized using *Apiin* extract obtained from henna plant [451]. In just two minutes of combining *Apiin* extract with silver nitrate, there was a noticeable increase in the intensity of the SPR peak, which was observed at 456 nm. TEM images reveal the development of quasi-spherical silver nanoparticles (AgNPs) with an average particle size of 39 nm. Silver nanoparticles (AgNPs) with a quasi-spherical morphology and a size range of 10–30 nm were effectively synthesized by employing the aqueous leaf extract of the *Chenopodium album* plant [452]. Silver NPs have been synthesized using the leaf extract of *Aesculus hippocastanum* plant [453]. The nanoparticles (NPs) exhibited a spherical shape with a size of 50 ± 5 nm. Furthermore, these NPs were characterized by a negative zeta potential value of −29.1 mV. Block and Rod like Ag nanostructures have been synthesized with sizes of 40, 50, and 57 nm have been synthesized by Vinodhini et al. by employing the leaf extracts of *Tabernaemontana divaricate, Basella alba,* and *Allium fistulosum*, respectively [454]. The obtained silver nanoparticles (AgNPs) demonstrated remarkable antimicrobial, antidiabetic, and antioxidant activities. Numerous studies have been published on the green synthesis of AgNPs utilizing plant leaf extracts, resulting in various sizes and shapes [455–464].

Ethanolic extracts of some medicinal plants have been used for synthesizing AgNPs [465]. The morphological attributes of silver nanoparticles (AgNPs) were assessed using TEM, DLS, and AFM. The AFM images displayed the development of spherical silver nanoparticles (AgNPs) with smooth surfaces. DLS studies revealed the mean diameter of AgNPs as 90.87 nm and PDI = 0.119 (*Gelsemium sempervirens*), 112.2 nm and PDI = 0.131 (*Thuja occidentalis*), 111.3 nm and PDI = 0.221 (*Phytolacca decandra*), and 122.8 nm and PDI = 0.281 (*Hydrastis canadensis*). The zeta potential values of −15.6, −16.8, −18.2, and −18.9 mV have been reported. Fruit extract of *Malus domestica* has been used by Roy et al. for synthesizing AgNPs of average diameter of 20 nm [466]. Rhizome extract of *Acorus calamus* has been exploited for the synthesis of spherical AgNPs with average diameter of 31.86 nm. Velmurugan et al. employed peanut shell extract for the production of silver nanoparticles (AgNPs) that exhibited spherical and oval shapes, with a size range between 10 and 50 nm. *Nyctanthes arbortristis* flower extract (ethanol) has been utilized to synthesize spherical and oval AgNPs that range in size from 5 to 20 nm. The extract's reducing capability was confirmed by the emergence of a brown color in the reaction mixture, along with the detection of the SPR peak at 440 nm [467]. The existence of lattice fringes observed in the

HRTEM images indicated the crystalline nature of the synthesized silver nanoparticles (AgNPs). Furthermore, the protective capping effect of phytochemicals present in the ethanolic extract was confirmed by the appearance of absorption peaks in the infrared (IR) spectrum of the Ag NP sample at 3430 cm^{-1} (–OH)), 2917 cm^{-1}, and 2848 cm^{-1} (alkanes), 1696 cm^{-1} (carbonyl), 1435 cm^{-1} (geminal methyl), and 1044 cm^{-1} (aliphatic amines). However, the FTIR spectrum of the extract only displays the characteristic IR bands of hydroxyl (3220–3250 cm), alkanes (715, 2895, and 2960 cm^{-1}), C=C of benzene (1627 cm^{-1}), aromatic amines (1374 cm^{-1}) and aliphatic amine (1040 and 1053 cm^{-1}). The existence of biomolecules on the surface of silver nanoparticles (AgNPs) was validated through thermogravimetric analysis/differential thermal analysis (TGA/DTA) analysis of the Ag NP sample which revealed the significant weight loss of about 70% corresponding to the degradation of bioactive compounds from the NP surfaces at high temperatures. Bark extract of *Butea monosperma* has been used to fabricate AgNPs [468]. Upon mixing the extract with aqueous $AgNO_{3,}$ the mixture turned reddish brown in color which demonstrated the fabrication of AgNPs. The brown colored solution also displayed SPR at 424 nm. TEM images revealed the presence of spherical silver nanoparticles (AgNPs) with an average size of 35 nm. High crystallinity of AgNPs was evident from the occurrence of lattice fringes in HRTEM images. The phase purity of AgNPs was ascertained by EDX-X-ray analysis which displayed a sharp absorption peak at 3 keV corresponding to pure Ag. The IR peak at 1758 cm^{-1} corresponding to C=O absorption was found to be present in IR spectrum of the bark extract but absent in the Ag NP sample. Thus, it has been attributed that carboxylic acid group plays a pivotal role in the conversion of Ag^{+} to Ag^{0}. The rapid one-step synthesis of silver nanoparticles (AgNPs) was accomplished by reducing $AgNO_3$ with the hot water extract obtained from *Citrus sinensis* (sweet orange) peels [469]. The color of the reaction mixture turned from yellow to brown with SPR peak observed a round 420 nm. The intensity of the SPR peak increased with temperature and at maximum intensity was reported at 40 °C. Further increase in temperature up to 60 °C resulted in decrease in intensity of the SPR band. Further pH changes were also found to affect the intensity of SPR peaks. Low pH ranges (pH 3–5) of the reaction medium resulted in low-intensity SPR peaks which indicated the acidic medium hinders the formation of AgNPs. The absorption intensity of SPR peak increased with increase in pH till pH 9 at which maximum intensity has been reported [469]. SPR intensity decreased with further increase in pH above 9. Tea extract (*Camellia sinensis*) resulted in rapid synthesis of AgNPs in a short time of one minute [470]. Particle shape was found to be spherical in AFM images with particle size of 3.9 ± 1.6 nm. The TGA of the pure green extract and AgNPs was carried out between 25 °C and 900 °C under nitrogen atmosphere. The TGA plots of the produced silver nanoparticles (AgNPs) displayed weight losses, with the initial loss (3.4–4.9%) observed at 130 °C, corresponding to the removal of adsorbed water molecules from the surfaces of the AgNPs. The subsequent weight loss (11.4–16.9%) detected in the temperature range of 130–150 °C was attributed to the thermal degradation of adsorbed phytochemicals from the surfaces of the silver nanoparticles (AgNPs). The weight loss (~8.9–10%) observed at 900 °C was a result of the thermal destruction of resistant aromatic compounds present in the green tea extract, which became adsorbed on the surfaces of the silver nanoparticles (AgNPs). Numerous reports have been published for the fabrication of AgNPs using various plant parts [471–477]. Besides the plant extracts, Pant-based polymers have been used to synthesize AgNPs and their derivatives like starch, polysaccharide, guargum, cellulose, hemicellulose D-glucuronic acid, arabinoxylan, and lignin [266, 478–485].

To summarize, the section discusses the transformative shift in nanotechnology toward green and sustainable approaches, focusing on the plant-mediated synthesis of silver nanoparticles (AgNPs). Harnessing the diverse bioactive compounds present in plants, this environmentally friendly method explores the mechanisms, advantages, and versatile applications of AgNPs. The synthesis of AgNPs employing plant extracts as both reducing and stabilizing agents is explored,

encompassing a wide array of plant species ranging from angiosperms to algae. Key examples include the use of *Alfalfa* sprouts, *Geranium* leaves, *Capsicum annuum* L., and various other plants, each resulting in unique nanoparticle characteristics. The section highlights the role of different plant parts, such as leaves, fruits, rhizomes, and even bark, in Ag NP synthesis. Noteworthy examples include the use of *Malus domestica* fruit extract, *Acorus calamus* rhizome extract, and *Butea monosperma* bark extract. The diverse sources contribute to the broad spectrum of sizes and shapes of AgNPs, expanding the possibilities for applications. Additionally, the utilization of ethanolic extracts from medicinal plants showcases the synthesis of AgNPs with specific morphological features. The use of extracts from *G. sempervirens*, *T. occidentalis*, *P. decandra*, and *H. canadensis* results in well-defined spherical AgNPs with smooth surfaces. Furthermore, the section explores the rapid synthesis of AgNPs using hot water extracts, such as those from *Citrus sinensis* peels and *Camellia sinensis* tea. The impact of factors such as temperature and pH on the synthesis process is discussed, emphasizing the one-minute synthesis achieved with tea extract. The synthesis of AgNPs is not limited to plant extracts alone, as the section notes the successful use of plant-based polymers and derivatives like starch, polysaccharide, guargum, cellulose, hemicellulose D-glucuronic acid, arabinoxylan, and lignin. These materials contribute to the diverse and eco-friendly arsenal of methods for producing silver nanoparticles.

In brief, the plant-mediated fabrication of AgNPs emerges as a promising avenue, demonstrating not only the feasibility of green and sustainable practices but also providing a rich variety of nanoparticle characteristics for a multitude of applications across different fields.

1.6 Synthesis of Magnetic Nanoparticles

The fabrication of MNPs with diverse characteristics has garnered significant attention, leading to the exploration of various synthesis methods [486–493]. This section will discuss the different approaches employed to generate shaped, controlled, and stable MNPs with various dimensions and morphologies. Among the numerous techniques, the co-precipitation method stands out as the most widely adopted for MNP synthesis. This method has proven effective in producing MNPs with controlled morphologies and magnetic properties. The co-precipitation process involves adding a base to an aqueous salt solution under an inert atmosphere, either at room temperature or at elevated synthesis temperatures [494]. The ensuing steps in the co-precipitation synthesis of MNPs are outlined below.

$$Fe^{2+} + 2Fe^{3+} + 8OH^- \rightarrow Fe(OH)_2$$

$$+2Fe(OH)_3 \rightarrow Fe_3O_4 + 4\,H_2O$$

In this approach, the size and shape of MNPs are influenced by several factors, including the type of metal salts employed, such as sulfates, chlorides, nitrates, perchlorates, the ratio of ferrous to ferric ions, reaction media temperature, pH, ionic strength, stirring rate of the reaction mixture, and the rate of dropwise base addition [495–497]. As an example, the fabrication of Fe_3O_4 NPs involved the hydrolysis of ferrous and ferric salts (sulfates and chlorides) with varying molar ratios, utilizing 1,6 hexane diamine as a base [498]. The choice of ferrous to ferric salts ratio was identified as a critical factor influencing the mechanism of Fe_3O_4 formation. Specifically, the use of ferrous salts alone led to the production of larger-sized MNPs, while employing both ferrous and ferric salts resulted in finer-sized MNPs. Moreover, the mean particle diameter increased from 9 to 37 nm with an elevated molar ratio of ferrous ions concerning the total iron ions in solution. The observed variation in particle size was attributed to distinct reaction mechanisms associated with metal salts of different valences [499, 500]. For instance, the formation of MNPs using ferrous ions alone occurs

through the dehydration reaction of ferrous hydroxide and ferric oxyhydroxide [499, 500]. Fe_3O_4 synthesis was also achieved via a co-precipitation reaction of ferrous and ferric chlorides without the use of surfactants [501]. The resulting magnetite nanoparticles exhibited an average diameter of 10 nm with a limited size distribution. Subsequently, these magnetite nanoparticles were converted into γ-Fe_3O_4 through direct aerial oxidation.

The microemulsion method has been utilized for the fabrication of MNPs, presenting advantages over alternative techniques by allowing superior control over particle size and morphology. Particle size and shape are also influenced by the type and structure of the surfactant utilized. Pilant et al. utilized microemulsions with ferrous dodecyl sulfate and a micellar solution to synthesize nanoscale MNPs, adjusting the concentration and temperature (25–50 °C) to control particle size. MNPs with an average particle size in the range of 3.7–11.6 nm were achieved, with saturation magnetization decreasing as particle size increased due to nonlinear structure changes at the interface [502]. Lopez et al. utilized the microemulsion method with Brij-97 surfactant to synthesize magnetic iron oxide nanoparticles (MIONPs) with a size range of 2–8 nm [503]. Results indicate that the microemulsion method, employing inverse micelles, facilitates the formation of water nanodroplets within an organic compound, functioning as nanoreactors to regulate particle size. These nanodroplets are surrounded by a surfactant coat that manages their size and separates them from the organic compound. By using a nonionic surfactant (Brij-97) and cyclohexane as the organic phase, microemulsions are created in the cyclohexane/Brij-97/water ternary system at low water concentrations across a broad range of Brij-97 concentrations. The synthesis process involves blending two microemulsions, M(I) and M(II), at 65 °C. M(I) consists of cyclohexane/Brij-97/aqueous iron salt solution, while M(II) is similar but lacks salts in the aqueous solution and contains a 20% larger volume of cyclohexylamine. An acidic medium is used to prevent Fe^{2+} oxidation, and an alkaline medium is employed for iron salt precipitation. After aging and cooling, the resulting precipitate is washed and dried, yielding different samples (A, B, C, D, E), each associated with varying x values in the microemulsions. X-ray diffraction patterns reveal a gradual broadening of peaks from sample A to E, indicating a reduction in particle size. The diffractograms are in line with γ-Fe_2O_3. TEM micrographs display particle aggregates with a noticeable size reduction from sample A to E. Magnetic measurements demonstrate alterations in the zero-field-cooled (ZFC) and field-cooled (FC) data, suggesting variations in the average blocking temperature (⟨TB⟩) and broadening of the size distribution with increasing particle size. Magnetization versus field curves at room temperature show a decline in maximum magnetization values from A to E, aligning with the observed reduction in magnetic particle volumes from TEM and X-ray fits. The use of stable microemulsions at elevated temperatures is revealed as an advancement in the synthesis of IONPs compared to the conventional room temperature microemulsion approach. The study emphasizes the capability to regulate the final particle size through simple adjustments in the synthesis procedure.

Magnetic iron oxide NPs were synthesized in bicontinuous microemulsions composed of dodecyltrimethylammonium bromide and didodecyldimethylammonium bromide (3,2 weight ratio) [487]. The results indicate that, consistent with a prior study, a system composed of DTAB/DDAB (3/2, w/w) mixture, MMA as the oleic phase, and an aqueous solution of $FeCl_3 \cdot 6H_2O$ and $FeCl_2 \cdot 4H_2O$ in a 3/2 molar ratio at an overall concentration of 0.75 M can form a microemulsion region at 80 °C. This region suggests a transition from reverse microemulsions to bicontinuous microemulsions as the system moves from the MMA-(DTAB/DDAB) side to the central zone of the diagram. Electrical conductivity measurements indicate a transition from low conductivity (up to ∼15% aqueous solution) corresponding to reverse microemulsions to higher conductivities (from ∼20 wt% aqueous solution) associated with bicontinuous microemulsions. The transition region from reverse to bicontinuous microemulsions is estimated to occur between 15 and 20 wt% aqueous solutions. Selected microemulsion compositions were used for precipitation reactions,

resulting in black powder products, indicative of magnetite formation. The yield of these reactions, calculated as 1.4–1.6 g of dried solids per 100 g of the total mixture, significantly exceeds the theoretical yield calculated from reported reverse microemulsion recipes. STEM micrographs reveal small-diameter particles (6.9–7.9 nm) with a relatively narrow size distribution when precipitation reactions are conducted in bicontinuous microemulsions. The diameters of these particles align with the channels in bicontinuous microemulsions, acting as nanoreactors to limit particle growth. Increasing surfactant concentration correlates with a reduction in particle size. X-ray diffraction patterns indicate the presence of magnetite or a mixture of magnetite–maghemite in the particles. Room temperature magnetization curves exhibit superparamagnetic behavior, consistent with essentially single domains in magnetic particles below 10 nm. The magnetization values decrease slightly with decreasing surfactant concentration, revealing a direct relationship between magnetization and particle size. Overall, the study demonstrates the advantage of bicontinuous over reverse microemulsions in terms of yield and control over particle size during the synthesis of MNPs. The magnetization behavior is consistent with previous findings and supports the notion that crystallinity influences the magnetic properties of the nanoparticles.

Microemulsions composed of CTAB surfactant were employed for the synthesis of MIONPs [504]. The size and morphology of ME-MIONs were characterized using TEM, highlighting their nearly spherical shape and a size range of 7–10 nm. Some agglomeration was observed, likely owing to the high surface energy of the nanoparticles. The oxidation of iron oxide is found to depend strongly on experimental factors such as temperature, reaction environment, and surface conditions. XRD results indicate that the obtained particles are likely composed of magnetite (Fe_3O_4), maghemite (γ-Fe_2O_3), or a combination of both, reflecting variations in crystal structure based on different experimental conditions. TEM-derived particle size values align with those obtained from XRD analysis, confirming the consistency of the results. The XRD patterns of ME 1-MION and ME 2-MION appear quite similar after calcination at 450 °C, suggesting a common spinel crystal structure. However, differences emerge after drying at 70 °C, making it challenging to definitively determine whether the nanoparticles consist of magnetite or maghemite. The broad diffraction peaks indicate a very small original particle size, in line with similar findings reported in the literature. The particle size, as determined from XRD analysis of samples dried at 70 °C, is measured at 9.2 nm for ME 1-MION and 7.8 nm for ME 2-MION. These findings highlight the influence of drying conditions on the ultimate particle size and crystalline structure of ME-MIONs.

Lakshman et al. also utilized a CTAB-based microemulsion to synthesize MIONs with sizes of 7–10 nm and a resulting surface area of 142 $m^2 g^{-1}$ [505]. Vidal et al. synthesized maghemite NPs through a one-pot microemulsion route using oleyl amine as a precipitating agent [506]. DLS measurements were conducted to investigate the size of microemulsion nanodroplets. The results indicate that stable microemulsions are formed above 50 °C, with instability issues arising below this temperature due to nanodroplet coalescence. The nanodroplet size increases as the temperature decreases, attributed to better hydration of the surfactant's hydrophilic part, leading to phase inversion. TEM and DLS were employed to examine the size distribution of particles obtained with oleylamine. The nanoparticles exhibited a size range of 8.2 ± 0.6 and 7.8 ± 0.5 nm for oleylamine-coated and oleic acid-coated nanoparticles, respectively. Upon washing and redispersion in heptane, the average sizes increased to 10.6 ± 0.7 and 9.6 ± 0.7 nm for oleylamine and oleic acid-coated particles, respectively. TEM micrographs of washed particles synthesized with cyclohexylamine revealed irregularly shaped particles with a broad size distribution, prone to aggregation. XRD patterns indicated that uncoated particles correspond to crystalline maghemite, and coated particles exhibited similar core structures. FTIR spectroscopy ascertained the presence of oleic acid and oleylamine on coated particles. Low wavenumber regions in mid-infrared (MIR) and far-infrared (FIR) spectra suggested absorption bands consistent with

maghemite nanoparticles. Thermogravimetric analysis (TGA) revealed mass losses for water, organic shell, and solvent residues. Coated particles showed similar mass-loss profiles, with oleic acid-coated particles having 4.2% and 45.0% mass loss for water and the organic shell, respectively. Oleylamine-coated particles displayed 4.4% mass loss for water and 45.4% for the organic shell. Magnetization studies indicated that size reduction and surfactant adsorption contributed to the reduction in magnetization. Oleylamine-coated particles exhibited a slightly lower magnetization than oleic acid-coated particles, suggesting differences in charge donation at the particle surface. Overall, the study provides detailed insights into the synthesis and characterization of magnetic IONPs, considering various surfactants and solvents, offering valuable information for potential applications. Numerous reports are available on the microemulsion synthesis of MNPs and their alloys [507–512].

The polyol process was utilized to produce MNPs. In this procedure, the liquid polyol served as the solvent for the metallic precursor, acting as both the reducing agent and, in certain instances, a complexing agent for metallic cations. The metal precursor's solubility in the polyol could vary. The solution underwent stirring and heating to a specific temperature, reaching the polyol's boiling point for less reducible metals. For metals with low reducibility, precise control of precipitation kinetics resulted in nonagglomerated metal particles with well-defined shapes and sizes. Improved regulation of the average size of metal particles was attained by incorporating foreign particles through seeding the reactive medium (heterogeneous nucleation). This separation of nucleation and growth steps led to the formation of uniform particles. A one-spot polyol process, as employed by Abbas et al., was utilized for synthesizing high magnetization magnetite nanoparticles [513]. The size of MNPs varied with changes in reaction parameters like temperature, time, and the ratio of polyol to metal precursor, yielding sizes of 32.3 and 9.2 nm. Exceptionally high magnetization values of 85.87 emu/g at 300K and 91.7 emu/g at 5K, with low coercivity, were observed. Superparamagnetic iron oxide MNPs were synthesized through a polyol process involving stepwise phase transformation using sodium acetate as a hydrolyzing agent [514]. The iron salt precursor underwent a sol–gel process, transforming into amorphous ferrihydrite, which, upon heating, transitioned to crystalline FeO(OH) with lepidocrocite (γ-FeO(OH)) phase, further reduced to Fe_3O_4. Varying the concentration of sodium acetate influenced the crystallinity and cluster size of iron oxide NPs. The cluster size increased from 143 to 338 nm with a rise in sodium acetate concentration from 0.9 to 1.8 mol% and then decreased with further increases (3.6%, 7%, and 10%) (Figure 1.14A). Particle size also varied with changes in the molar ratios of $FeCl_3$ and H_2O, decreasing from 104 to 11 nm with a drop in the molar ratio from 0.10 : 5 to 0.02 : 5. A rise in the molar ratio to 0.20 : 5 resulted in a particle size of 98 nm (Figure 1.14B). XRD studies indicated a decrease in diffraction peak intensity with decreasing molar ratios of $FeCl_3$ and H_2O. XRD investigations revealed a reduction in the intensity of diffraction peaks as the molar ratio of $FeCl_3$ to H_2O decreased from 0.10 : 5 to 0.02 : 5 (Figure 1.14C). This reduction in peak intensity corresponded to a decrease in crystallinity associated with the diminishing particle size of Fe_3O_4 NPs. Iacovita et al. employed a high-temperature polyol process for the fabrication of IOMNPs [515]. This synthesis was conducted under elevated temperature and pressure, resulting in ferromagnetic IOMNPs with a remarkable saturation magnetization of 83 emu/g at room temperature. The polyol method has been widely utilized for synthesizing MNPs with diverse compositions [516–522]. In addition to the discussed methods, MNPs have been produced through various other techniques, such as sonochemical [523–529], sol gel [530–532] and solvothermal method [533–537].

In short, this section discusses the production of MNPs and various synthesis methods to achieve controlled characteristics. The co-precipitation method is highlighted as widely adopted, involving the addition of a base to an aqueous salt solution under an inert atmosphere. Factors influencing the size and shape of MNPs include metal salts, their ratios, reaction media temperature, pH,

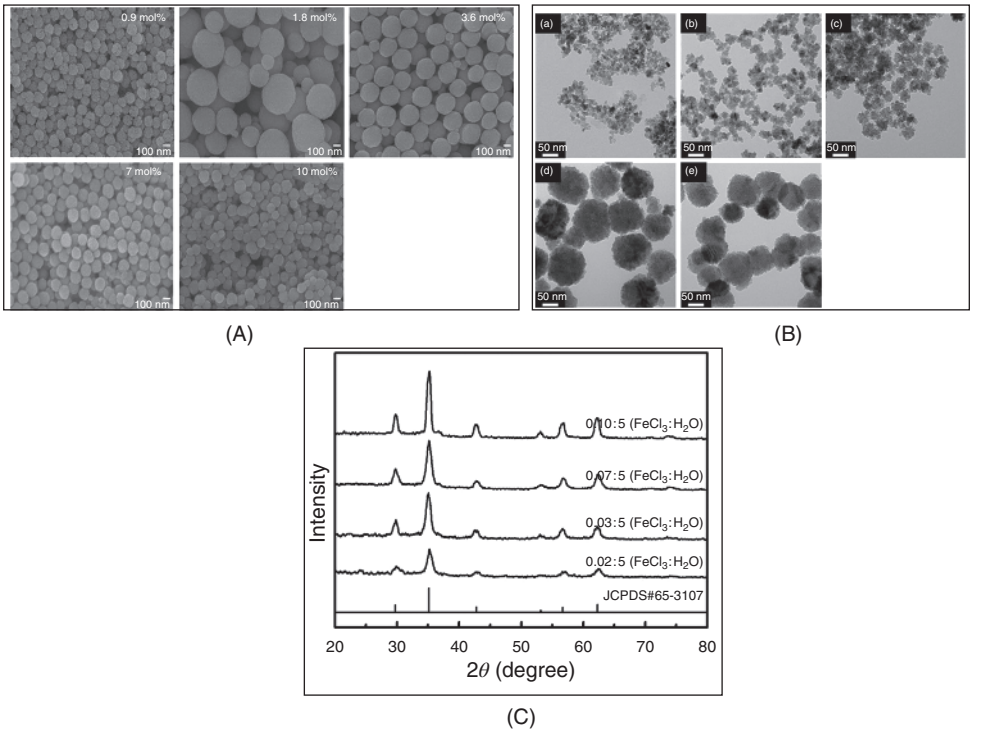

Figure 1.14 (A) Displays scanning electron microscopy (SEM) visuals of the Fe_3O_4 nanoparticles created using varying concentrations of NaOAc. In (B), transmission electron microscopy (TEM) images exhibit the Fe_3O_4 particles synthesized in accordance with different molar ratios of $FeCl_3$ and H_2O: (a) 0.02 : 5, (b) 0.03 : 5, (c) 0.07 : 5, (d) 0.10 : 5, (e) 0.20 : 5. Furthermore, (C) showcases the X-ray diffraction patterns of the synthesized Fe_3O_4 nanoparticles with distinct molar ratios of $FeCl_3$ and H_2O. Source: (a–c) Reproduced with permission from Oh et al. [514]/Elsevier.

ionic strength, stirring rate, and base addition rate. The microemulsion method is explored for MNP synthesis, offering advantages in size and morphology control. Different surfactants lead to varied results, and stable microemulsions at elevated temperatures are deemed advantageous. Bicontinuous microemulsions are presented as superior in yield and particle size control compared to reverse microemulsions. The polyol process is employed, utilizing liquid polyol as a solvent and reducing agent for metallic precursors. Precise control over parameters yields uniform particles. The one-spot polyol process produces high-magnetization magnetite nanoparticles, while stepwise phase transformation using sodium acetate results in superparamagnetic iron oxide MNPs with varying cluster and particle sizes. The high-temperature polyol process is utilized for ferromagnetic iron oxide MNPs with significant saturation magnetization. The section concludes by mentioning other synthesis techniques, such as sonochemical, sol–gel, and solvothermal methods, highlighting the diverse approaches to MNP production.

1.7 Synthesis of Classical Quantum Dots

Classical QDs refer to nanoscale particles made of semiconducting material, typically characterized by diameters in the range of a few nanometers [31]. The quantum confinement effects in these QDs lead to a widening of the band gap [32]. As a result, the state of unbound charge carriers within

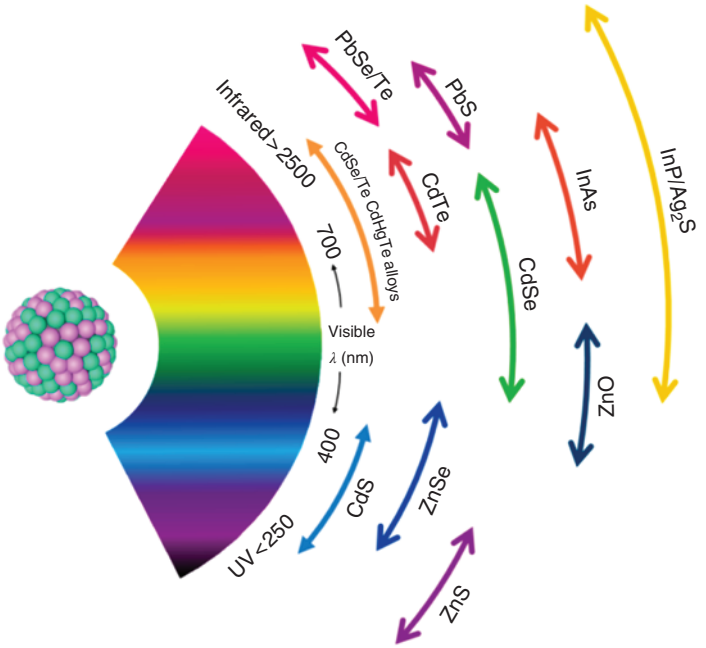

Figure 1.15 Illustrates core materials of representative quantum dots (QDs), scaled based on their emission wavelength and superimposed onto the spectrum. Source: Reproduced with permission from Pu et al. [539]/American Chemical Society.

the quantum dot (QD) is quantized, and the arrangement of distinct energy states is linked to the dimensions of the QD. This feature enables the adjustment of the emission color of QDs by managing their size and composition [538]. By choosing an appropriate core material with a desired bandgap and fine-tuning the size of QDs, the emission wavelength can cover the visible, ultraviolet (UV), and near-infrared (NIR) regions [539] (Figure 1.15). In comparison to organic dyes, QDs display similar quantum yields, yet they boast extinction coefficients 10–50 times greater, markedly reduced photobleaching rates, and fluorescence that is 10–20 times brighter. Additionally, they exhibit 100–200 times enhanced photostability [540]. Currently, CdSe and CdTe QDs are widely favored, showcasing attractive optical properties within the visible spectrum ranging from 400 to 700 nm [541–543]. Furthermore, QDs with NIR emission characteristics, including CuInSe, Ag_2S, and PbS QDs, have garnered interest for their benefits in *in vivo* animal imaging studies where NIR light is advantageous [544–546] Recently, there has also been interest in perovskite QDs because of their possible use in extremely effective photoelectric devices [547]. Indeed, recent literature has used the terms "carbon QDs" or "graphene QDs" to describe various carbon-based nanoparticles [548]. Upon further investigation, it becomes apparent that several of these particles display features more closely associated with fluorescent organic dots. In this article, the focus is on QDs composed of semiconductor nanocrystals. Several colloidal methods have been used to synthesize QDs, which are discussed briefly below.

1.7.1 Organometallic Methods of Synthesis of Quantum Dots

Conventional techniques for producing QDs typically entail injecting semiconductor precursors into appropriate organic solvents through a hot injection method. As an illustration, Murray et al. conducted the synthesis of CdSe QDs by injecting a liquid mixture of Cd precursor ($Cd(CH_3)_2$)

and Se metal in tri-*n*-octylphosphine (TOP) into heated trioctylphosphine oxide (TOPO) [51]. The TOPO solvent functions as a stabilizing agent, enabling the reaction to occur at elevated temperatures around 320 °C. Through precise control of the reaction temperature, a range of QDs with sizes spanning from 1.5 to 11.5 nm was successfully produced. However, the cadmium precursor, $Cd(CH_3)_2$, employed in this process proved to be highly toxic, rendering it impractical for large-scale synthetic applications. To address this issue, Peng et al. later substituted this toxic cadmium precursor with a less harmful reagent, CdO, aiming for a more environmentally friendly synthesis of CdTe, CdSe, and CdS QDs [55]. This method has the potential to generate additional QDs with reasonably high yields. Subsequent syntheses can be carried out at comparatively lower temperatures (250–300 °C) with consistent and reproducible outcomes. Deng et al. further streamlined the quantum dot synthesis process by developing Zinc-blend CdSe. They achieved this by substituting coordinating solvents such as TOP/TOPE with more economical and environmentally friendly options like paraffin liquid and oleic acid [549]. Nanocrystals of CdSe, with sizes that can be adjusted within the range of 2–5 nm and distinct UV-Visible peaks, were successfully produced. The hot injection method, with precise selection of synthetic parameters, has been applied to synthesize various QDs, including lead sulfide (PbS) [54, 550], lead selenide, PbSe [54], Indian phosphide InP [551], silver sulfide Ag_2S [552], and silver selenide Ag_2Se [553]. Size-controlled synthesis of fluorescent perovskite QDs has also been achieved by hot injection method [554, 555].

While injection-based reaction techniques yield QDs with desirable physical and chemical attributes, challenges in regulating post-injection reaction temperatures have led to reproducibility issues. In response to this challenge, various noninjection methods have been introduced for large-scale QD production. For instance, Efrima et al. developed a straightforward and adaptable low-temperature approach for synthesizing high-quality metal sulfide QDs by heating metal xanthate in hexadecylamine solvent [556]. The process was conducted at a moderate temperature range of 50–150 °C, generating metal sulfide QDs even at a low reaction temperature of 70 °C. Nevertheless, the QD size was manipulated by adjusting both the reaction temperature (ranging from 50 °C to 150 °C) and the concentration of metal xanthate. Elevated metal xanthate concentration led to the fabrication of smaller particles, attributed to rapid nucleation following the principles of La Mer behavior [557]. Liu et al. reported the low-temperature synthesis of PbS QDs using non injection approach [558]. The impact of various synthetic reaction parameters on the development of PbS QDs has been examined. The reactions were conducted within the temperature range of 30–120 °C, utilizing octadecane as the solvent. Lead oxide (PbO) and lead acetate served as the lead sources, while bis(trimethylsilyl)sulfide ((TMS)2S), thioacetamide (TAA), and elemental sulfur (S) were employed as sulfur sources. Different acids, such as oleic acid (OA), were explored as stabilizing agents. Optimal quality PbS QDs were reported when using (TMS)2S and OA. The reactions yielded QDs with a narrow bandwidth as small as 100 nm. These QDs displayed emissions spanning from 700 to 900 nm, dependent on factors such as reaction temperature, growth periods, acid-to-lead ratio, and the feed molar ratio of lead to sulfur. Du et al. synthesized monodisperse and single-crystalline Ag_2S QDs using a strategy involving a single-source precursor (Ag(DDTC)), resulting in single-crystalline Ag_2S QDs with a size of approximately 10 nm [559]. The reaction scheme for the synthesis of Ag_2S QDs by this method is shown schematically in Figure 1.16A. The synthetic procedure involved the heating of a mixture containing Ag (DDTC), oleic acid (OA), octadecylamine (ODA), and 1-octadecane (ODE), followed by precipitation, washing, and drying. The selection of capping ligands and solvents played a pivotal role in achieving uniform Ag_2S QDs. Adjusting the solution composition allowed for the tuning of QD size and size distribution. The Ag_2S QDs in the monoclinic phase exhibited near-infrared (NIR) emission at 1058 nm, indicating their potential for mitigating autofluorescence in bioimaging. X-ray diffraction (XRD)

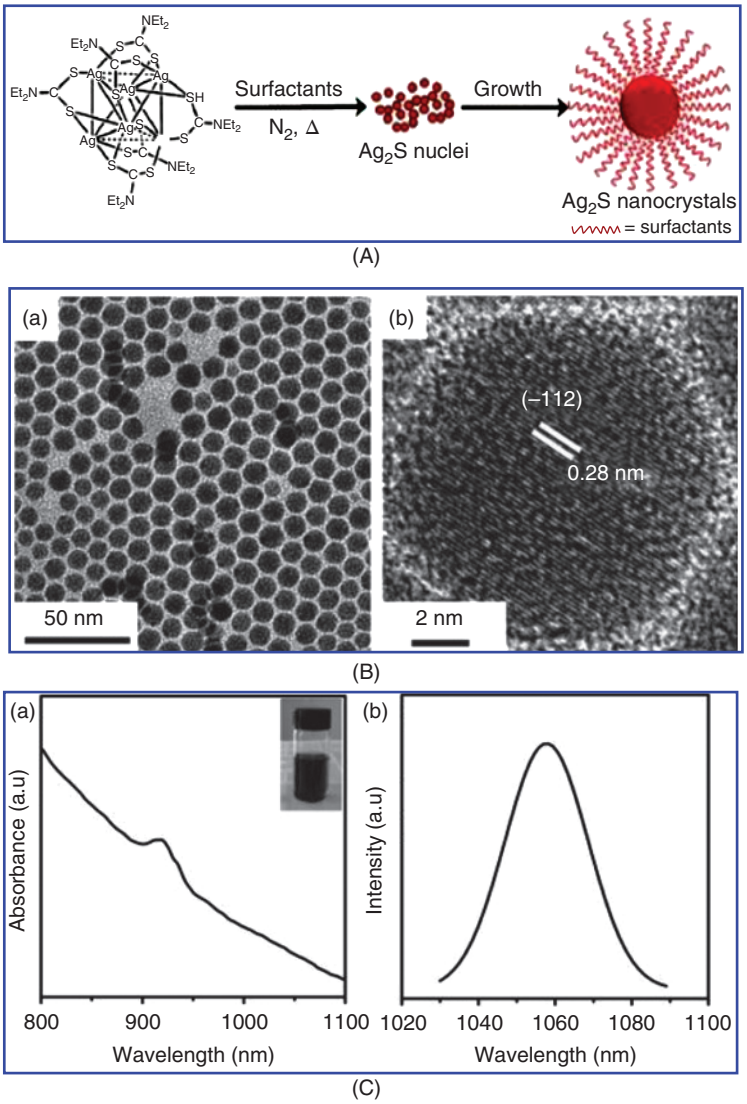

Figure 1.16 (A) Illustrates the process of synthesizing near-infrared (NIR) Ag_2S quantum dots (QDs) from a single-source precursor, Ag (DDTC). (B) Displays transmission electron microscopy (TEM) images, including (a) an overall view of Ag_2S QDs and (b) a high-resolution TEM (HRTEM) image focusing on a single Ag_2S QD. (C) Presents (a) the NIR absorption spectrum of the obtained Ag_2S QDs, with an inset showing the dispersion of Ag_2S in cyclohexane and (b) the NIR fluorescence emission spectrum of Ag_2S QDs at room temperature, excited at λex = 785 nm. Source: (a–c) Reproduced with permission from Du et al. [559]/American Chemical Society.

patterns validated the monoclinic nature of the Ag_2S nanocrystals, and TEM images portrayed well-dispersed QDs with a two-dimensional ordered arrangement. The TEM images illustrated the Ag_2S QDs to be uniformly sized, of an average size of 10.2 ± 0.4 nm. (Figure 1.16B). The single crystallinity of the QDS was confirmed by HRTEM images which interplanar distance of ~0.28 nm which corresponds to (112) facets of monoclinic Ag_2S (Figure 1.16B). Whereas NIR-UV-Visible spectrum showed a discreet and lowest energy absorption peak at 920 nm (Figure 1.16C). The NIR photoluminescence spectrum of the Ag_2S QDs, excited with a 785 nm laser diode, exhibited

a symmetric emission peak at 1058 nm with a small full-width at half-maximum (FWHM), indicating a narrow size distribution (Figure 1.16C). The quantum yield of the QDs was not examined in this study. The results suggest that the as-prepared Ag_2S QDs have potential as nontoxic alternatives for in vivo bioimaging, offering a unique optical window for tissue penetration. Further investigations may explore the incorporation of a core–shell structure to enhance quantum yield and photostability.

1.7.2 Aqueous Synthesis of QDS Using Chemical and Biological Methods

While organometallic methods for synthesizing QDs provide advantages such as high crystallinity, a narrow particle size distribution, and a high fluorescence quantum yield, they have limitations in biomedical applications. Organometallic QDs exhibit low water solubility, necessitating additional phase transfer steps to enhance their stability and dispersibility in water. Moreover, the organometallic synthesis process involves the use of various harmful solvents, posing environmental concerns. To address these limitations, water, a more environmentally friendly solvent, has been employed for QD synthesis. Aqueous-phase synthesis of QDs offers several benefits, including the use of water-soluble ligands as stabilizers for biomedical applications and lower reaction temperatures typically below 100 °C. The fabrication of QDs in an aqueous phase was initially documented by Henglein [560] in 1982 and Brus et al. [561] in 1983, where CdS QDs were synthesized. Vossemeyer et al. successfully produced monodisperse CdS QDs utilizing 1-thioglycerol as a stabilizer, and $Cd(C1O_4)$ $6H_2O$ and H_2S as reactant precursors. The size of the CdS QDs ranged from 13–19 Angstroms. Rogach et al. [562] described the aqueous phase synthesis of thiol-stabilized CdTe QDs with commendable luminescence properties using 2-mercaptoethanol and 1-thioglycerol as stabilizers. The synthesis involved adding NaHTe solutions to $Cd(C1O_4)2\text{-}6H_2O$ solutions in a nitrogen atmosphere at pH 9.2 in the presence of stabilizers. The size of the QDs was adjusted by regulating the initial concentrations of NaHTe precursor, temperature, and the type of stabilizer. The CdTe QDs exhibited fluorescence properties attributed to the 1s–1s electronic transition. High-quality CdZnS and Cu-doped CdZnS QDs were synthesized by Yakoubi et al. [563] using aqueous phase synthesis with 3-mercaptopropionic acid (MPA) or *N*-acetylcysteine (NAC) as capping agents. Initially, nearly monodisperse Cu:CdZnS QDs were produced in an aqueous solution, utilizing (MPA as a capping ligand. Subsequently, Cu:CdZnS/ZnS core/shell QDs were prepared by carefully depositing ZnS onto preformed Cu:CdZnS nanocrystals through the addition of Zn^{2+} and S^{2-} precursors and the ligand at 100 °C. The synthesis of host CdZnS QDs involved injecting an aqueous solution of Na_2S into a mixture of cationic Cd^{2+}, Zn^{2+}, and the ligand at basic pH, followed by heating at 100 °C. Optimal conditions for obtaining high-quality CdZnS QDs included a $Cd^{2+} + Zn^{2+}$ concentration of 5 mM and a $(Cd^{2+} + Zn^{2+})/S^{2-}$ molar ratio of 1/1. The CdZnS QDs displayed photoluminescence quantum yields (PL QYs) up to 7%, with variations in precursor concentrations or molar ratios affecting the PL efficiency. Different Cd and Zn precursors were explored, and $CdBr_2$ and $ZnBr_2$ resulted in the best PL QY (5%) for CdZnS QDs. The pH of the Cd^{2+}-Zn^{2+}-MPA precursor solution influenced the QDs' properties, with pH 8 yielding the highest PL QY (5%). The formation of alloyed $Cd_xZn_{1-x}S$ QDs was evidenced by continuous shifts in absorption and PL spectra, indicating the incorporation of wider bandgap ZnS with narrower bandgap CdS (Figure 1.17A). However, attempts at certain compositions like $Cd_{0.1}Zn_{0.9}S$ and $Cd_{0.8}Zn_{0.2}S$ failed to produce fluorescent nanocrystals. Cu-doped CdZnS QDs were synthesized by adding $CuCl_2$ to the reaction mixture. The PL emission redshifted upon Cu^{2+} doping, and the optimal doping concentration was found to be 0.5%. The Cd/Zn ratio influenced the emission wavelength, with higher Cd concentrations leading to a red-shift. The synthesis was versatile,

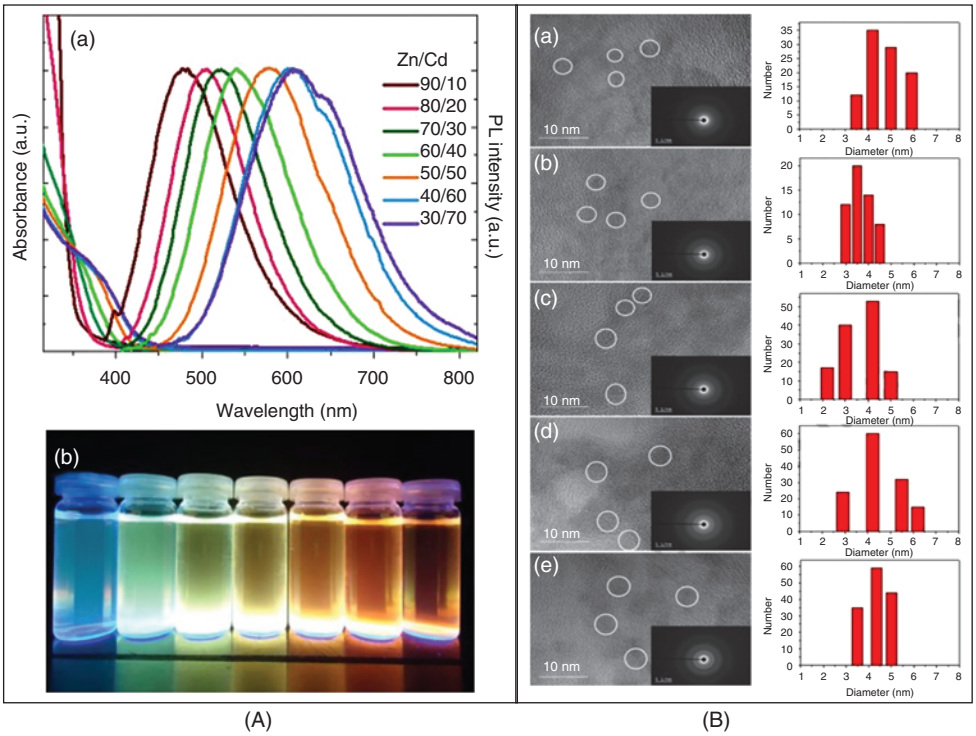

Figure 1.17 (A) Shows (a) UV-visible absorption and photoluminescence (PL) spectra of Cu-doped $Cd_xZn_{1-x}S$ quantum dots (QDs). Additionally, (b) presents a photographic representation of aqueous dispersions of Cu: $Cd_xZn_{1-x}S$ QDs under UV light irradiation, with variations in x from 0.1 to 0.7 and an excitation wavelength of 350 nm. Moving to (B), it includes high-resolution transmission electron microscopy (HR-TEM) images, selected area electron diffraction (SAED) patterns, and size distributions of Cu-doped QDs for different compositions: (a) $Cd_{0.2}Zn_{0.8}S$, (b) $Cd_{0.3}Zn_{0.7}S$, (c) $Cd_{0.4}Zn_{0.6}S$, (d) $Cd_{0.5}Zn_{0.5}S$, and (e) $Cd_{0.6}Zn_{0.4}S$. Source: (a, b) Reproduced with permission from Yakoubi et al. [563]/Elsevier.

allowing the use of different water-soluble thiol ligands. Among those tested, *N*-acetylcysteine (NAC), MPA, and glutathione (GSH) provided the highest PL QYs (27, 9, and 3%, respectively). To enhance stability and optical performance, Cu:CdZnS/ZnS core/shell QDs were prepared. The ZnS shell was grown using the successive ion layer adsorption and reaction (SILAR) technique, resulting in a significant increase in PL QY (from 9 to 42%). Further coating beyond five monolayers of ZnS led to aggregation and decreased PL intensity. Excited-state lifetime decays of Cu-doped CdZnS QDs indicated triexponential decays, with lifetimes ranging from 0.46 to 1.55 µs. The addition of a ZnS shell increased the average PL lifetime, indicating efficient surface passivation. The hydrodynamic diameters of Cu:CdZnS and Cu:CdZnS/ZnS QDs in a phosphate buffer solution (pH 7.4) were 7.3 ± 1.2 and 9.2 ± 1.5 nm, respectively (Figure 1.17B). Both QDs exhibited stability over ten days, with a slight increase in diameter and a reduction in PL intensity. The dots were stable over a range of pH (7–12), with a slight decrease in PL QY at pH 6 and rapid decay below pH 4. Photostability testing demonstrated that the QDs retained their PL QY even after prolonged UV-light exposure. In summary, a synthetic approach was developed that allowed for the fabrication of stable and highly luminescent Cu:CdZnS and Cu:CdZnS/ZnS QDs, holding promise for various applications, including biological labeling and tumor detection. Further tuning the particle size with different stoichiometric ratios of Cd/Zn precursors in CdZnS QDs allowed for the adjustment of photoluminescence properties across the entire visible spectrum. Aqueous phase synthesis

of QDs has been further extend to microwave [564], hydrothermal [565], ultrasonic [56, 566, 567], and microemulsion methods [568–570] of synthesis. For instance microwave-aided synthesis of water-dispersable CdTe/CdS/ZnS CSS QDs was reported by He et al. [571]. As synthesized QDS exhibited high photoluminescence quantum yield (40–80%) and excellent photostability. The size of these core shell shell (CSS) QDs was found to be around 4.5 nm. A one-pot aqueous phase microwave synthesis of CdTe QDs has been reported by employing Na_2TeO_3 as tellurium (Te) source and MPA as a stabilizing agent [572]. The QDs were produced in a brief reaction time of 10–14 minutes and achieved 40–60% emission in 550–640 nm wavelength range. These CdTe QDs were spherical in size with a mean diameter of 3 nm. By controlling the reaction temperature, various sizes of CdTe QDs with tuneable UV-Visible/PL emissions were produced. Several reports are available for the aqueous phase synthesis of QDs by employing various chemical methods of synthesis [573–580]. However, due to toxicity issues with heavy metal QDs, efforts have been on to synthesize greener QDs based on nontoxic elements like ZnO [581], ZnS [582], ZnSe [583] in aqueous phase which emit in the blue range. In the past decade, there has been a growing interest in synthesized near-infrared fluorescent QDs for in vivo imaging applications. Example of such QDs is Ag_2S QDs, which has been synthesized by several research groups [584–588].

Apart from the aqueous phase methods, QDs of various types have also been synthesized by utilizing the bio machinery or biocomponents derived from the various living things especially microorganisms such as bacteria and fungi [589]. In the intracellular synthesis, the precursors such as metal and sulfide ions enter the cell through the transmembrane and the synthesis is carried out by the intracellular enzymes present inside the cytoplasm. Whereas in extracellular synthesis, formation of QDs takes place due to the enzymes secreted by the cell to the outside medium and hence the synthesis occurs either on the cell membrane or inside the medium. Various QDs have been synthesized by this approach such as ZnS QDs [590, 591], CdS QDs [592–596], PbS QDs [597, 598], CdSe QDS [599, 600], Ag_2S QDs [601, 602], Ag_2Se QDs [603], and SnO_2 QDs [604].

In brief, this section discusses the synthesis of classical QDs, which are nanoscale particles of semiconducting material. These QDs exhibit quantum confinement effects, resulting in a quantized state of free charge carriers and tunable emission colors based on size and composition control. The advantages of QDs over organic dyes include larger extinction coefficients, reduced photobleaching rates, and brighter fluorescence. CdSe and CdTe QDs are popular in the visible spectrum, while CuInSe, PbS, and Ag2S QDs with near-infrared (NIR) emission properties have gained attention for in vivo imaging. Perovskite QDs are also explored for efficient photoelectric devices.

The synthesis methods are discussed, starting with organometallic approaches involving hot injection methods. Various examples, including CdSe QDs, are presented, and efforts to substitute toxic precursors with environmentally friendly alternatives are highlighted. Aqueous synthesis methods are then introduced to address limitations in organometallic approaches, focusing on water-soluble ligands for biomedical applications. Examples include CdS, CdTe, and CdZnS QDs synthesized in aqueous phases. The section also touches on alternative synthesis methods such as microwave, hydrothermal, ultrasonic, and microemulsion techniques.

The versatility of aqueous phase synthesis is demonstrated in the synthesis of stable and luminescent Cu:CdZnS and Cu:CdZnS/ZnS QDs, showing promise for applications like biological labeling and tumor detection. The discussion extends to near-infrared fluorescent QDs for in vivo imaging, particularly Ag_2S QDs. Additionally, the section explores the use of biological components for QD synthesis, involving microorganisms like bacteria and fungi. Both intracellular and extracellular synthesis approaches are discussed, highlighting the synthesis of various QDs, including ZnS, CdS, PbS, CdSe, Ag_2S, Ag_2Se, and SnO_2 QDs.

1.8 Synthesis of Carbon-Based Nanomaterials

Intensive research has focused on exploring the remarkable attributes of carbon nanomaterials, including fullerenes, carbon nanotubes, and graphene. These materials exhibit exceptional properties, such as outstanding electrical and thermal characteristics, high mechanical strength, making them suitable for diverse applications ranging from water treatment, hydrogen storage, optoelectronics, sensing, to controlled drug delivery. Additionally, their utilization as protective agents in various engineering products underscores their significance. In the biomedical field, these carbon nanomaterials have demonstrated promising results. This section presents a brief summary of the synthetic methods used to fabricate various types of carbon-based nanomaterials, such as carbon nanotubes, fullerenes, and graphene.

1.8.1 Synthesis of Carbon Nanotubes (CNTs)

Carbon nanotubes (CNTs) is a versatile carbon allotrope comprised of rolled up sheets of graphene [605]. Carbon nanotubes (CNTs) are found in two primary forms: single-walled carbon nanotubes (SWCNTs) and multiwalled carbon nanotubes (MWCNTs) [606]. SWCNTs are composed of a single layer of carbon atoms and have a diameter of around 3 nm [607], while MWCNTs are composed of two or more layers and have a diameter in the range of 7–100 nm [608]. Both types of CNTs can reach lengths up to 1 mm. Their extensive applications in the fields of sensors, electronics, mechanics, chemistry, and biology are attributed to their remarkable tensile strength, Young's modulus, and twisting properties compared to metals like steel and iron [609]. Various synthesis methods, including laser ablation, arc discharge, chemical vapor deposition (CVD), and plasma-enhanced CVD, have been employed to produce CNTs.

1.8.1.1 Plasma-Based Synthesis

Plasma-based synthesis stands out as a cutting-edge and versatile approach for the production of CNTs, offering unique advantages in terms of precision and control over the synthesis process [610]. Leveraging the fundamental principles of plasma physics, this method harnesses the energy of a high-temperature plasma to induce the growth of CNTs from carbon-containing precursors. The intricate interplay of reactive species in the plasma environment allows for the tailoring of CNT characteristics, including size, structure, and purity.

The techniques used in plasma-based synthesis of CNTs are discussed briefly below.

Arc Discharge Method Arc discharge technique was first used by Iijima to synthesize CNTS who observed MWCNTs in the sooth of graphite electrodes [611]. This technique involves the production of plasma between the two graphite electrodes, which finally results in the production of good-quality CNTs [612]. The anode of the setup is usually filled with carbon precursor and a catalyst (Fe, Co, etc.), whereas cathode is composed of pure graphite. The two electrodes are then mounted at a pot difference of 20 V and are kept at 1–2 mm distance. The electrodes are enclosed in a setup, which is filled with inert gas at very low pressures. As the arc is triggered between the electrodes, plasma is produced which is usually composed of carbon, catalyst vapors, and inert gas. During the process, CNTs get deposited on the graphite cathode and at the same time anode gets consumed. This method produces fine CNTs with fewer defects [613, 614]. The yield and quality of CNTs can be optimized by varying the reaction parameters such as type of the catalyst, inert gas type, inert gas pressure, electrode distance, and arc current density. For instance, using hydrogen in the growth region results in the production of highly crystalline MWCNTs [615–618]. Single-walled

CNTS are usually synthesized in the presence of catalytic material such as Gd, Ni, Fe, Co, Pt, Pd, and Ag or mixtures of metal catalysts such as Ni, Co, and Fe with different components such as Co-Ru, Co-Pt, Ni-Y, and Co-Ni [619, 620]. Multiwalled CNTs have usually been synthesized without the presence of a catalyst [621–623]. The mass production of SWCNTs has been achieved by employing Ni-Y bimetallic catalyst in helium ambient gas [624]. Various reports are available for the synthesis of CNTs using arc discharge method [624–626].

Laser Ablation Method Laser ablation method is the second method, which has been used to synthesize CNTs. For instance, synthesis of SWCNTs in high yields (70%) was achieved by Thess et al. in 1996 using Ni and Co as a catalyst at 1200 °C [627]. These CNTs were uniform in diameter and self-organized in the shape of ropes with each rope composed of 100–500 NTs. In this method, the reaction usually takes place inside quartz tube furnace. Graphitic material embedded with a catalyst is placed inside the quartz tube and heated by the pulsed laser due to which the material converts into vapor form. The pressure is maintained constant during the heating by employing the inert gases. Metal catalyst NPs formed in the graphitic vapor during pulsed heating catalyze the growth of CNTs [628]. This method is employed to produce mostly SWCNTs [629].

Chemical Vapor Deposition (CVD) The main problems associated with the plasma methods is low yield, high reaction temperature, and several purification process for obtaining pure CNTs. To overcome these limitations, chemical vapor deposition (CVD) method has been devised in 1996 for the large-scale production of CNTs [630]. Infect, arc method, and laser ablation methods are superior to CVD to produce more crystalline CNTs, but CVD has a special advantage of producing CNTs in bulk quantities and in high yields. In this method, the carbon substrate materials such as fullerene are placed inside an oven and heated to the temperature of 700–900 °C [631]. During the heating process, carbon-bearing gases such as methane, acetylene, and ethylene are added to the reaction chamber. During heating, the carbon-based materials are converted into atomic form, which interacts with the substrate and forms CNTs. The heating can be accomplished by either using energy from heater coil or plasma. CVD results in the production of CNTs in yields greater than 90% and high percentage purity. Based on catalyst location, CVD can be further classified into supported CVD [632] and floating catalyst CVD (FC-CVD) [633, 634]. In the former method, catalyst is first prepared and reduced before the synthesis of SWCNTs. This method is complicated due to interaction between catalyst and support. However, in latter method, catalyst and SWCTs synthesis occurs in the gaseous environment, thereby making it more scalable and a single-step process. Further, FC-CVD results in the production of SWCNTs with high purity. The morphology and chirality of the NCTs can be tuned by proper selection of the catalyst [635]. For instance, using bimetallic catalyst material results in the production of SWCNTs with narrow chirality [636]. The carbon source in CVD can be either in liquid phase or in solid phase. In CVD process using liquid hydrocarbon as a carbon source such as benzene and alcohol, the liquid carbon source is heated in a flask and purged by an inert gas, which carries the vapors hydrocarbon vapors into the reaction zone where decomposition and further reaction result in the production of CNTs [38]. In CVD using solid carbon source, the hydrocarbon material that may be a low volatile material such as camphor, naphthalene, and ferrocene is placed at a low-temperature zone of a reaction chamber, where it is vaporized and carried toward the high-temperature reaction zone loaded with the catalyst. The catalyst used in CVD may also be used either in solid, liquid, or gas form. The catalyst can be either placed inside the reactor or fed from outside. The catalyst can either be placed in the hot zone to catalyze the growth of CNTs or catalyst is subjected to pyrolysis at suitable temperatures which liberates the metal NPs in situ. The MNPs then catalyze the growth of the CNTs. This method is flexible compared to other methods like arc discharge or laser ablation method in the sense that

plenty of hydrocarbon sources in any of the three states can be used as substrates. It also permits the growth of CNTs in a variety of forms like powders and films owing to the lower growth temperatures (550–1000 °C), and CVD offers better control over the growth parameters. This approach has been utilized to cultivate carbon nanotubes (CNTs) tailored for specific applications [607, 637–643].

Plasma-Enhanced Chemical Vapor Deposition (PECVD) The thermal CVD method described above has a disadvantage of operating at moderately higher temperature, which are quite unbearable for certain substances to withstand without decomposition. Therefor an alternative method known as plasma-enhanced chemical vapor deposition (PECVD) method has been designed which operates at lower temperatures, room temperature in some cases for the deposition of CNTs [644]. In this method, a high voltage is applied between the two electrodes in a reaction chamber, which results in the production of the electric discharge. The substrate is put on the electrodes and the reactant gas is flushed through the chamber to deposit a uniform film [645]. The substrate is itself loaded with transition metal catalysts such as Fe, Ni, and Co by thermal CVD or sputtering technique. The electric discharge results in the production of fine metal particles which then catalyze the growth of CNTs from the carbon gas source such as CH4, C_2H_2, C_2H_4, C_2H_6, and CO, which is fed to the reaction chamber during the discharge [646]. The type of the catalyst affects the morphological features of the CNTS such as diameter, wall thickness by controlling the growth rate. For instance, aligned MWCNTs of the diameter of 15 nm have been produced by using Ni as a catalyst. This method operates in different modes like radio frequency (RF) mode known as RF-PECVD, diffusion current mode, DC-PECVD, microwave, MW-PECVD, and hot filament-PECVD. Hot filament-PECVD uses thermal energy for the generation of plasma and has successfully produced CNTs. DC-PECVD resulted in the production of mostly vertically aligned CNTs. For instance, Teo et al. also produced vertically aligned CNTs by DC-PECVD using n+ doped Si (100) substrate [647]. Here the substrate was biased at −600 V which initiated a DC glow plasma discharge. The CNTs were grown vertically by electric field in the plasma sheath. The transmission electron micrograph in Figure 1.18A illustrates a typical carbon nanotube (CN) grown via direct current plasma-enhanced chemical vapor deposition (dc PECVD). The presence of Ni catalysts at the tip of all CNs suggests favorable conditions for the tip-growth diffusion mechanism during deposition. The CNs exhibited well-crystallized graphene walls, numbering between 20 and 40, indicative of excellent conductivity along their axis. Electrical conductivity measurements revealed a room temperature bulk resistivity comparable to multiwall carbon nanotubes produced by arc discharge, emphasizing their potential utility. Graphitic bamboo-like fringes were observed along the length of the CN, consistent with findings from other PECVD studies. Upon the termination of growth and cooling of the catalyst, disordered carbon was expelled, resulting in mostly hollow, tubular structures, even for CNs with large diameters (300 nm). Examining the nucleation of multiple and single isolated CNs, it was observed that a 7 nm thick Ni film patterned into a 100 nm wide line yielded multiple CNs, while an array of 100 nm wide square dots produced more uniform, single CNs. The critical size for deterministic single CN nucleation was found to be 300 nm. A statistical study on the effect of catalyst dot size revealed that only at 100 nm were single CNs deterministically obtained. Beyond 300 nm, the average number of CNs per catalyst dot increased linearly with dot size, indicating some degree of control over CN number by adjusting dot dimensions (Figure 1.18B). To achieve good structural uniformity, single isolated CNs were grown, exhibiting tight distributions in diameter and height. The observed CN diameter was slightly smaller than the catalyst dot size, and a statistical approach revealed good uniformity. Field emission measurements on individual, isolated CNs showed similar Fowler–Nordheim characteristics and emission currents, confirming the uniformity of emission properties. The statistical predictions for field enhancement factor uniformity were validated by electrical measurements, demonstrating

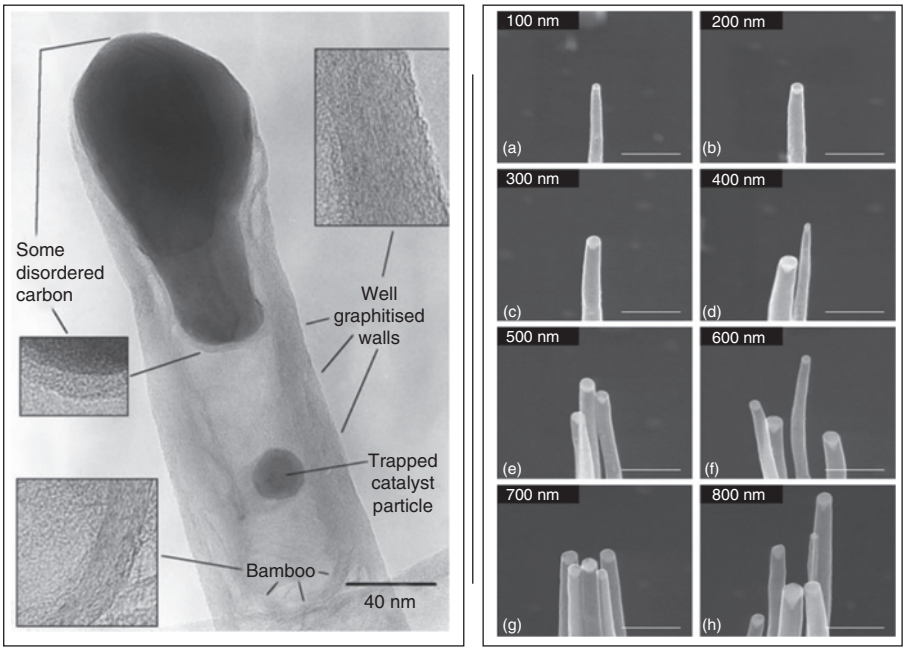

Figure 1.18 (A) Presents a transmission electron micrograph of a carbon nanotube (CN) grown via dc plasma-enhanced chemical vapor deposition (PECVD). The accompanying insets are magnified by 2.5×. In (A), high-resolution images of the CN heads nucleated from Ni dots, ranging in width from (a) 100 to (h) 800 nm, are displayed. The scale bar, 400 nm in length, and a sample tilt of 40° provide context for the images. Source: (a, b) Reproduced with permission from Teo et al. [647]/IOP Publishing.

the reproducibility and reliability of the deposition process. Boskovic et al. synthesized CN fibers (CNFs) at three different temperatures including room temperature using RF-PECVD using Ni powder as a catalyst and methane or methane/hydrogen as a carbon source [648]. TEM images revealed the spaghetti morphology of CNFs with CNF growth and diameter quite independent on substrate temperature. HRTEM reveals the Ni catalyst located at the tip of the CNF. Vertically aligned CNTs were synthesized by Hussain et al on $TiN/SiO_2/Si$ substrate and Ni as a catalyst using RF-PECVD [649]. SEM/XPS studies revealed that the surface of CNTs covered with ultra-thin layer of PANI. PECVD is widely used for the growth of CNTs for various applications. PECVD has been used to grow CNTs for various applications [650–659].

To summarize, this section discusses the synthesis of CNTs, a versatile carbon allotrope with applications across diverse fields such as sensors, electronics, mechanics, chemistry, and biology. Two main forms of CNTs are SWCNTs and MWCNTs, differing in the number of layers and diameter. The focus is on plasma-based synthesis methods for CNTs, offering precision and control over the synthesis process. The following techniques are explored:

Arc discharge method. This method involves the production of plasma between two graphite electrodes, leading to the deposition of high-quality CNTs. It utilizes carbon precursors and catalysts, and the parameters like catalyst type, inert gas, pressure, and electrode distance influence the yield and quality of CNTs.

Laser ablation method. In this method, a pulsed laser is used to heat graphitic material embedded with a catalyst inside a quartz tube furnace. The metal catalyst nanoparticles formed catalyze the growth of CNTs. This method is primarily employed for the synthesis of SWCNTs.

Chemical vapor deposition (CVD). CVD is introduced as a method to overcome limitations associated with plasma methods, offering large-scale production of CNTs. Carbon substrate materials are heated in an oven, and carbon-bearing gases are added, leading to the formation of CNTs. The catalyst's location classifies CVD into supported CVD and floating catalyst CVD, with the latter offering scalable and single-step processes.

Plasma enhanced chemical vapor deposition (PECVD). PECVD operates at lower temperatures compared to traditional CVD, making it suitable for substances that cannot withstand high temperatures. The method utilizes electric discharge and transition metal catalysts to deposit uniform CNT films. PECVD operates in different modes like RF, diffusion current, DC, microwave, and hot filament, each with specific advantages and applications. The discussion includes specific examples, such as the use of Ni-Y bimetallic catalyst for mass production of SWCNTs, the production of vertically aligned CNTs by DC-PECVD, and the use of PECVD for various applications.

In short, plasma-based synthesis methods offer a range of techniques to produce CNTs with controlled characteristics, enabling their application in diverse fields.

1.8.2 Synthesis of Graphene

The synthesis of graphene can be broadly categorized into three approaches that are discussed below.

1.8.2.1 Exfoliation: Mechanical and Liquid-Phase Exfoliation

Exfoliation methods involve the separation of the individual graphene sheets from the high-quality graphitic carbon using mechanical or chemical energy. The graphene sheets in graphitic carbon of which it is made of are bound together by weak van der Waals forces of attraction. Exfoliation involves the breaking of these weak bonds by chemical or mechanical energy to separate the graphene sheets. The first report of the synthesis of graphene by this method involved intercalation of the pure graphitic sheets with potassium metal and then exfoliation in ethanol to from dispersion of graphene sheets [660]. The sonication of the graphene suspension resulted in the production of graphene scrolls of the thickness of 40 ± 15 layers. Graphene scrolls tough several graphene layers thick provided the idea that it is possible practically to separate graphene sheets of few layers of thickness known as FLG from graphitic carbon. The production of few layer graphene (FLG) and single-layer graphene (SLG) was first reported by Novoselov et al. [661] who produced stable monocrystalline graphitic films with a few atom thickness by mechanical exfoliation of pyrolytic graphite. This process produced graphene proved to be reliable and fast, hence garnered the attention of the research community [662, 663]. Single and few layers of graphene were produced by Shukla et al. [664] using the exfoliation method by bonding the bulk graphite to the borosilicate glass and then subjected to exfoliation to get single or multilayers of graphene on the substrate. Mechanical exfoliation has resulted in the production of graphene sheets of variable thickness using various carbon sources such as natural graphite [665], highly ordered pyrolytic graphite (HOPG) [666, 667], and monocrystal graphite [668]. Although mechanical exfoliation produces high-quality graphene, but this method suffers from the main disadvantage of giving low yield and insufficient control over the number of graphene layers needed for a particular application [669]. A little different approach was used by exfoliation in the liquid phase. Liquid-phase exfoliation can produce high-quality graphene directly from graphite [670–672]. This method increases the interplanar spacing between graphitic layers by either intercalation of metal atoms or large-sized molecules or by chemical oxidation [673]. Mostly sonication of the graphite in liquid solvent exfoliates it into graphene of monolayer to few layers thickness [673–676]. The size of graphene flakes

as well as the number of graphene sheets can be altered by changing the sonication parameters such as sonication time, frequency, and sonication power [674, 676]. The yield and stability of the product graphene is affected by the type of the liquid solvent [677]. The proficiency of the solvent for graphite exfoliation in turn depends upon the surface tension of the solvent. Solvents demonstrating superior performance are those that effectively overcome the van der Waals interactions between graphene layers. For this reason, solvents with surface tension values from 40 to 50 mJ/m^2 are considered as better exfoliating solvents. Water is one of the good solvents used for exfoliation [678]. Some additional chemical species have been used which when added to the solvent such as water enhance the exfoliation by reducing the surface energy. Various solvents such as cyclohexanone, benzylamine, dimethyl sulfoxide (DMSO), dimethyl formamide (DMF), and tetramethyl urea have been employed for the exfoliation of the graphite exfoliation [679–683]. For instance, graphene dispersion with concentration up to 0.01 mg/mL was produced by Hernandz et al. [677] by exfoliation of graphite in *N*-methyl-pyrrolidone solvent. The yield was initially 1% which was further improved up to 12% by further processing. Liquid-phase exfoliation method has the advantage of large-scale production of graphene. Single to few layers graphene was produced by Lotya et al. [684] by dispersing graphite in sodium dodecylbenzene sulfonate (SDBS) followed by sonication. A comprehensive study on the dispersion, exfoliation, and characterization of graphene flakes has been carried out. The optimization of dispersion conditions was a crucial step in the process. The absorption coefficient (R) was determined, providing insights into the concentration of dispersed graphite. The study revealed empirical relationships, such as $CG = 0.01 \times CG,i$, shedding light on the concentration dynamics during centrifugation. The surfactant concentration (CSDBS) and graphite concentration (CG,i) were varied to optimize the dispersion conditions, leading to concentrations comparable to those achieved in surfactant-stabilized nanotube dispersions. The evidence of exfoliation was thoroughly examined through TEM analysis, revealing various types of graphene flakes, including monolayers, few-layer graphene, and larger disordered flakes (Figure 1.19A). TEM images reflected the presence of flakes with 40% flakes containing less than five layers and 3% flakes composed of monolayers of graphene. These graphene layers were found to be free of defects. TEM and HRTEM images of graphene flakes are shown in Figure 1.19B. The ability to recycle sediment for improved exfoliation was a notable finding, indicating the potential for enhancing the overall yield of graphene. Dispersion stability, characterized by the zeta potential, suggested effective electrostatic repulsion between surfactant-coated graphene flakes. The temporal stability of dispersions was investigated, revealing a biexponential sedimentation behavior. The proposed stabilization mechanism, based on DLVO theory, indicated a potential energy barrier opposing aggregation, contributing to the stability of surfactant-coated graphene sheets. The study extended to the fabrication of graphene films through vacuum filtration. SEM and optical images demonstrated the morphology of the films, emphasizing the presence of large and small graphene flakes. The characterization of flake quality through FTIR, Raman spectroscopy, and X-ray photoelectron spectroscopy indicated low levels of defects and oxidation, showcasing the high quality of the produced graphene flakes. The optical and electrical properties of the films were explored, with transparency and sheet resistance measurements indicating the potential application of these films. The deposition of individual graphene flakes onto surfaces, such as mica, was achieved, offering opportunities for further characterization and applications. The study provides valuable insights into the dispersion, exfoliation, and characterization of graphene flakes, paving the way for potential applications in various fields, including electronics and materials science. The comprehensive approach to understanding the underlying mechanisms and optimizing conditions contributes to the advancement of graphene research. Both single layer and FLG has been produced by exfoliation method using various modifications for a variety of applications [685–689].

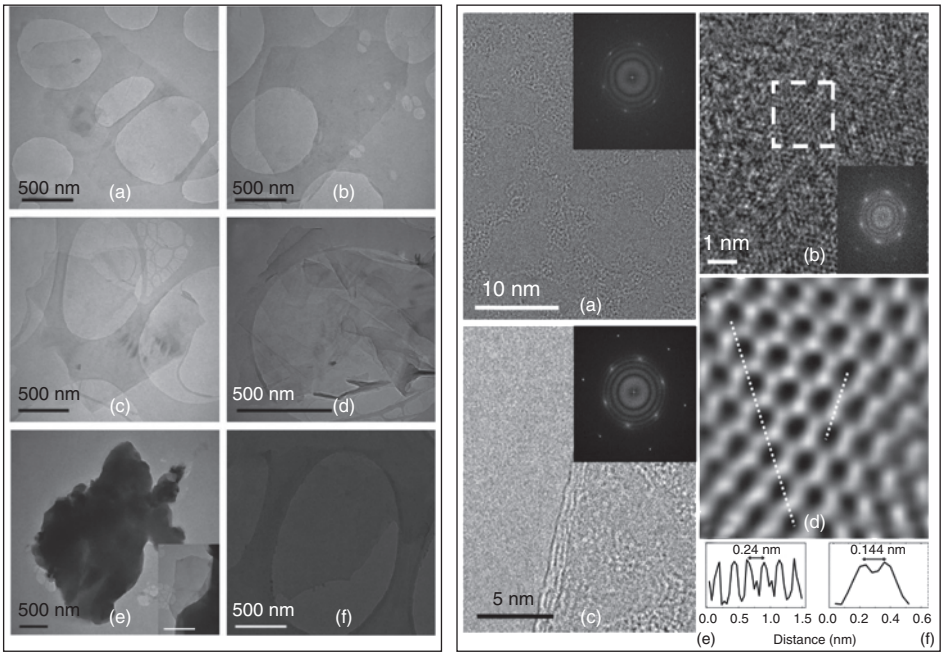

Figure 1.19 (A) Displays chosen TEM illustrations of flakes produced through surfactant processing. (a) Illustrates a monolayer, albeit with a small square debris piece near its left-hand edge. (b) Represents a bilayer, (c) a trilayer, and (d) a disordered multilayer. (e) Depicts an exceptionally large flake, with an inset offering a close-up of an edge displaying a small multilayer graphene flake protrusion. Additionally, (f) exhibits a monolayer from a sample prepared through sediment recycling. Moving to (B); it showcases high-resolution TEM images of surfactant-exfoliated graphene flakes. (a) Presents a HRTEM image of a segment of a graphene monolayer, accompanied by an inset of a fast Fourier transform equivalent to an electron diffraction pattern of the image. (b) Features a HRTEM image of a segment of a trilayer, also with an inset of a Fast Fourier transform. (c) Displays a HRTEM image of part of a graphene monolayer, along with an inset of a fast Fourier transform of the region enclosed by the white square. The scale bar in all images is 1 nm. Additionally, (d) provides a filtered image of part of the region in the white square. Lastly, (e) presents intensity analysis along the left white dashed line, revealing a hexagon width of 2.4 Å, while (f) shows intensity analysis along the right white dashed line, indicating a C—C bond length of 1.44 Å. Source: Reproduced with permission from Lotya et al. [684]/American Chemical Society.

In short, this section, the focus is on exfoliation methods for the synthesis of graphene, which involve separating individual graphene sheets from high-quality graphitic carbon using mechanical or chemical energy. Graphene sheets within graphitic carbon are held together by weak van der Waals forces, and exfoliation entails breaking these weak bonds through chemical or mechanical means to isolate the graphene sheets.

The initial report on graphene synthesis through exfoliation involved intercalating pure graphitic sheets with potassium metal, followed by exfoliation in ethanol to form a dispersion of graphene sheets. Subsequent sonication of the graphene suspension resulted in the production of graphene scrolls of approximately 40 ± 15 layers. This method provided the insight that separating graphene sheets of few layers, known as FLG, from graphitic carbon is practically feasible. The production of FLG and single-layer graphene (SLG) was pioneered by Novoselov et al., who mechanically exfoliated pyrolytic graphite to produce stable monocrystalline graphitic films with a few atom thickness. This method proved to be reliable and fast, gaining attention from the research community.

Mechanical exfoliation has been achieved using various carbon sources, such as natural graphite, HOPG, and monocrystal graphite. However, while this method produces high-quality graphene, it suffers from the main disadvantage of low yield and insufficient control over the number of graphene layers needed for particular applications. An alternative approach is liquid-phase exfoliation, which can produce high-quality graphene directly from graphite. This method increases the interplanar spacing between graphitic layers through intercalation or chemical oxidation. Sonication of graphite in liquid solvents, such as water or other organic solvents, exfoliates it into graphene sheets of monolayer to few layers in thickness. The size and number of graphene flakes can be controlled by adjusting sonication parameters, and the proficiency of the solvent depends on its surface tension.

Liquid-phase exfoliation offers the advantage of large-scale production of graphene. Various solvents, including *N*-methyl-pyrrolidone, cyclohexanone, benzylamine, dimethyl sulfoxide (DMSO), dimethyl formamide (DMF), and tetramethyl urea, have been employed for exfoliation. Notably, water has been identified as a good solvent for exfoliation. A comprehensive study on the dispersion, exfoliation, and characterization of graphene flakes has been conducted. The optimization of dispersion conditions was crucial, and the study revealed empirical relationships and stabilization mechanisms contributing to the stability of surfactant-coated graphene sheets. The ability to recycle sediment for improved exfoliation and the fabrication of graphene films through vacuum filtration were notable findings.

In summary, exfoliation methods, whether mechanical or liquid phase, offer pathways for the large-scale fabrication of graphene with controlled characteristics. These methods have found applications across various fields and the comprehensive studies provide valuable insights for advancing graphene research and applications in fields such as electronics and materials science. Both single-layer and few-layer graphene have been successfully produced through exfoliation methods with modifications tailored for specific applications.

1.8.2.2 Chemical Vapor Deposition (CVD)

This is a bottom-up approach in which organic molecules in either solid (camphor, polymers, and sucrose), liquid (benzene, hexane, ethanol, and turpentine oil), or gas (methane, ethane, and ethyne) phase are decomposed at high temperatures in without the presence of oxygen and the carbon atoms are self-assembled to yield graphene structures. This method produces graphene with fewer layers with large surface areas and long-range order. CVD offers flexibility over the choice of the carbon precursors. The formation of graphene layers is catalyzed by the presence of mostly transitional metals such as Ni, Cu, Co, Au, Pt, Pd, Ru, Ir, Re, and Rh. Depending upon the substrate material used, growth mechanism is a multistep process which involves such as decomposition, adsorption, dehydrogenation, diffusion, nucleation, segregation, and precipitation. The use of copper (Cu) as a catalyst is prevalent in the synthesis of graphene due to its low solubility for carbon, making it a widely adopted choice and offering effective control over the number of layers in the resulting graphene. For instance, synthesis of graphene has been achieved by Zhang et al. [690] by employing water less cleaning method of Cu foils. Here the contaminated Cu foils were first annealed at high temperatures, and the oxidized surface layer was removed during the cooling step. Next the diluted methane, Ar, and H_2 were then introduced into the chamber for the growth of graphene layers. It was revealed that annealing of Cu foils in the absence of He resulted in the production of defect-free multilayer graphene. The large-scale fabrication of 3D graphene with high electrical conductivity and a high specific area has been achieved by Mint et al. [691] using 3D Ni nanowire foam as a catalyst at lower temperatures (670 °C). Different types of catalysts and carbon precursors have been used for the growth of single to multilayer graphene for

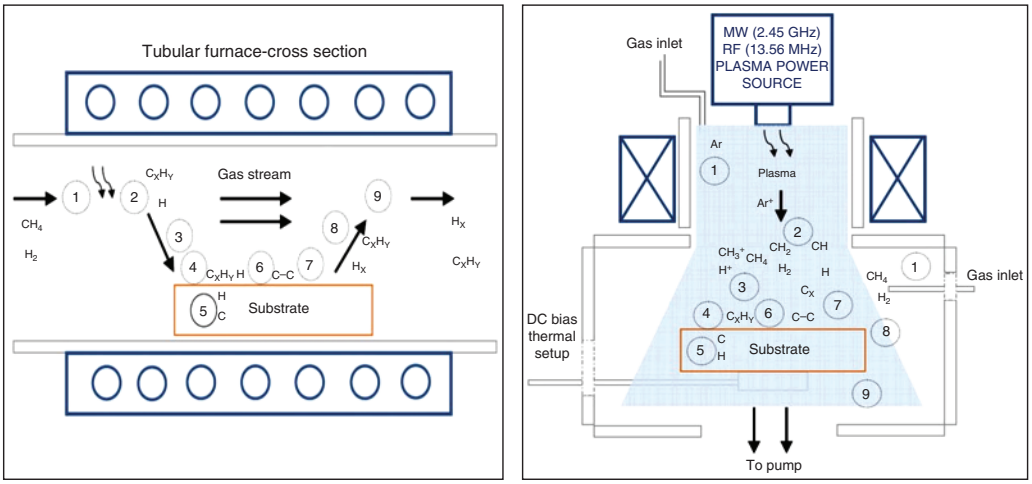

Figure 1.20 Illustrates schematic diagrams of (a) thermal CVD and (b) plasma-assisted CVD processes, specifically applied to graphene synthesis from CH_4/H_2 mixtures. Source: Reproduced with permission from Muñoz et al. [697]/John Wiley & Sons.

various applications. Researchers have also shown interest in plasma-assisted synthesis (PACVD) of graphene. The first report of the synthesis of single to multilayer graphene by PACVD dates to 2004 using radiofrequency PACVD [692, 693]. Graphene was synthesized on a variety of substrates without any catalyst deposition or surface preparation. The subnanometer thickness graphene sheets were produced from a mixture of CH_4 and H_2 at a total pressure of 12 Pa and a power of 900 W with a substrate temperature of around 680 °C. Due to simplicity of this process, it drew the interest of the scientific community worldwide to produce graphene with some modifications [694–696]. Schematic representation of the production of graphene by thermal CVD and plasma CVD is shown in Figure 1.20. The process involves several key steps: (i) Transportation of reactants through forced convection, (ii) thermal activation (in the case of (a)) or plasma activation (in the case of (b)), (iii) prevention of homogeneous gas reaction with particles and powder production in graphene synthesis, achieved by controlling kinetic parameters (P, T, *n*), (iv) transportation of reactants through gas diffusion originating from the main gas stream and traversing the boundary layer, (v) adsorption of reactants on the surface of the substrate, (vi) dissolution and bulk diffusion of species based on substrate solubility and physical properties. This step involves thermal activation-mediated-surface processes, encompassing chemical decomposition (catalytic), reaction, surface migration to attachment sites (such as atomic-level steps), incorporation, and other heterogeneous surface reactions, ultimately leading to film growth, (vii) desorption of by-products from the surface, (viii) transportation of by-products through diffusion in the boundary layer and back to the main gas stream, and (ix) forced convection-driven transportation of by-products away from the deposition region. CVD method has been used to prepare single to multilayer graphene for a variety of applications [698–701].

In short, this section discusses the CVD method, a bottom-up approach for synthesizing graphene. In CVD, organic molecules in solid, liquid, or gas phases, such as camphor, polymers, sucrose, benzene, hexane, ethanol, methane, ethane, and ethyne, are decomposed at high temperatures in the absence of oxygen. The carbon atoms then self-assemble to form graphene structures. This approach allows to produce graphene with fewer layers, large surface areas, and long-range order.

CVD offers flexibility in choosing carbon precursors, and the formation of graphene layers is catalyzed by transitional metals like Ni, Cu, Co, Au, Pt, Pd, Ru, Ir, Re, and Rh. Copper (Cu) is widely used as a catalyst due to its low solubility of carbon, enabling precise control over the number of graphene layers. For example, Zhang et al. achieved the synthesis of defect-free multilayer graphene by annealing Cu foils in the absence of helium. Large-scale production of 3D graphene with high electrical conductivity and specific area was achieved using 3D Ni nanowire foam as a catalyst at lower temperatures. Various catalysts and carbon precursors have been explored for growing single to multilayer graphene for diverse applications. Researchers have also explored plasma-assisted synthesis (PACVD) of graphene, with the first report dating back to 2004 using radiofrequency PACVD. Graphene was synthesized on various substrates without catalyst deposition or surface preparation. The process involves transporting reactants through forced convection, thermal or plasma activation, preventing homogeneous gas reactions, adsorption on the substrate surface, dissolution and bulk diffusion of species, desorption of by-products, and transportation of by-products away from the deposition region.CVD has been extensively used for preparing single to multilayer graphene for various applications, showcasing its versatility and potential in graphene synthesis.

1.8.2.3 Laser-Induced Synthesis

Laser-based synthesis has a special advantage of simple and efficient localized energy delivery [702]. The desired number of graphene sheets can be obtained by changing the parameters such as laser power, pulse width, and scanning rate [703]. Laser-induced processing of graphene has been achieved by techniques such as pulsed laser deposition, laser exfoliation, laser-induced CVD, and laser writing [704–707]. This method involves creating localized heating of a substrate or catalyst, either in a vacuum or a gas atmosphere, to facilitate the direct deposition or patterning of graphene. The regions of laser irradiation achieve the desired temperature instantly. The rapid temperature rise due to rapid heating rate decomposes the carbon source at a fast rate [708]. The forward movement of laser spots on the substrate lets local temperatures to drop which allows the diffusion of additional carbon atoms on the catalyst surface which results in the formation of graphene layers. Graphene layers have been fabricated on Ni foils using laser-induced CVD by irradiating the Ni foils with laser radiations in CH_4/H_2 atmosphere [709]. The control of the laser scan rate has been employed to manage the number of graphene layers. Jiang et al. successfully achieved the formation of few-layer graphene on Ni plated using laser-induced CVD in a CH_4/H_2 atmosphere under ambient conditions [710]. The quantity of graphene layers has been controlled by tuning the laser power and scan speed. There are various reports of the formation of high-quality FLG by laser-induced CVD. The fabrication of FLG on Ni films has been achieved by Wang et al. [711] using pulsed laser ablation of the graphite target at 650 °C. The thickness of the graphene films, correlating with the number of graphene layers, was regulated by adjusting the ablation time. Several metal films have been explored for the generation of few-layer graphene through the pulsed laser ablation technique. The number of graphene layers was influenced by the cooling rate and energy of the pulsed laser [709, 710]. The formation of high-quality graphene has been achieved by direct laser writing on various types of substrates, which has proved to be a low cost and simple method [712]. For instance, direct laser wring of graphene patterns on various insulating substrates such as glass, Si/SiO_2 has been achieved by Xiong et al. [712] using femtosecond laser under ambient conditions. Graphene patterns such as spirals, texts, electric circuits, and line arrays have been drawn using this technique. Laser synthesis has been used to synthesize graphene for various applications [713–717].

In short, this section explores laser-based synthesis as a method for graphene production, emphasizing its advantage of providing simple and efficient localized energy delivery. Laser

parameters such as power, pulse width, and scanning rate can be adjusted to control the number of graphene sheets obtained. Various techniques, including pulsed laser deposition, laser-induced CVD, laser exfoliation, and laser writing, have been employed for laser-induced processing of graphene. Laser-induced CVD involves the localized heating of a substrate or catalyst, either in a gas atmosphere or vacuum, for direct deposition or patterning of graphene. The rapid temperature rise, facilitated by the laser, decomposes the carbon source quickly, and the local temperature drop during laser movement allows the diffusion of additional carbon atoms on the catalyst surface, resulting in the fabrication of graphene layers. Control over the laser scan rate allows for the manipulation of the number of graphene layers.

Research has demonstrated the production of graphene layers on Ni foils through laser-induced CVD in a CH_4/H_2 atmosphere. The number of layers was regulated by manipulating the laser scan rate. Additionally, few-layer graphene formation on Ni-plated substrates was accomplished using laser-induced CVD under ambient conditions, with control over the number of layers achieved through adjustments in laser power and scan speed. Pulsed laser ablation methods were also employed for generating high-quality few-layer graphene on diverse metal films. The thickness of the graphene films, corresponding to the number of layers, is controlled by changing the ablation time, cooling rate, and laser energy. Direct laser writing on different substrates, such as glass and Si/SiO_2, has emerged as a low-cost and simple method for producing graphene patterns. For example, femtosecond lasers have been employed for ambient condition direct laser writing, creating graphene patterns like spirals, texts, electric circuits, and line arrays. Laser synthesis of graphene has found applications in various fields, highlighting its versatility and potential for practical use.

1.9 Conclusion and Future Perspective

The synthesis methods discussed, spanning from gold nanoparticles to graphene, showcase the versatility and innovation within nanomaterial fabrication. The synthesis of gold nanoparticles employs diverse methods, including chemical reduction, citrate reduction, and green synthesis using plant extracts. These methods yield nanoparticles with unique properties suitable for various applications such as medicine, catalysis, and sensing. Future perspectives may involve refining green synthesis approaches, exploring new reducing agents, and expanding applications in targeted drug delivery and diagnostics.

Like gold nanoparticles, silver nanoparticles are synthesized through chemical and green methods. The antibacterial and antiviral properties of silver nanoparticles make them valuable in medical applications. Future directions could focus on optimizing synthesis for specific medical uses, addressing toxicity concerns, and exploring broader applications in water purification and consumer products.

MNPs find applications in medicine, particularly in targeted drug delivery and imaging. Synthesis methods include co-precipitation, thermal decomposition, and microemulsion. Future perspectives involve enhancing biocompatibility, improving magnetic properties, and advancing functionalization for precise biomedical applications.

QDs offer unique optical properties with applications in imaging and sensing. Synthesis methods include colloidal synthesis and organometallic synthesis. Future research may emphasize improving quantum dot stability, reducing toxicity, and expanding their applications in fields like solar cells and bioimaging.

Carbon nanotubes exhibit remarkable properties, leading to applications in various fields. Synthesis methods include arc discharge, laser ablation, CVD, and plasma-enhanced CVD.

Future perspectives may involve scalability improvements, optimization for specific applications, and exploration of novel catalysts and precursors.

Graphene synthesis employs exfoliation methods, CVD, and laser-based approaches. Techniques like liquid-phase exfoliation and CVD offer scalable production. Future directions may include further optimization of CVD for large-scale applications, exploring new exfoliation methods, and advancing applications in electronics, materials science, and energy storage.

In conclusion, the future of nanomaterial synthesis lies in refining existing methods, exploring novel approaches, and expanding applications in diverse fields. The continuous advancement in nanomaterial synthesis contributes to the development of innovative technologies with far-reaching implications in medicine, electronics, and environmental science.

References

1 Bhushan B 2017 Introduction to Nanotechnology *Springer Handbook of Nanotechnology* Springer Handbooks ed B Bhushan (Berlin, Heidelberg: Springer) pp 1–19.

2 Nasrollahzadeh M, Sajadi S M, Sajjadi M and Issaabadi Z 2019 An Introduction to Nanotechnology Interface Science and Technology *An Introduction to Green Nanotechnology*, vol 28, ed M Nasrollahzadeh, S M Sajadi, M Sajjadi, Z Issaabadi and M Atarod (Elsevier) pp 1–27.

3 Roco M C 2011 The long view of nanotechnology development: the National Nanotechnology Initiative at 10 years *J. Nanopart. Res.* 13 427–45.

4 Litter M I and Ahmad A 2023 The World of Nanotechnology *Industrial Applications of Nanoparticles* (CRC Press) pp 1–15.

5 Nikulainen T and Palmberg C 2010 Transferring science-based technologies to industry – does nanotechnology make a difference? *Technovation* 30 3–11.

6 Toumey C 2010 Tracing and Disputing the Story of Nanotechnology *International Handbook on Regulating Nanotechnologies* (Edward Elgar Publishing).

7 Feynman R P 1992 There's plenty of room at the bottom [data storage] *J. Microelectromech. Syst.* 1 60–6.

8 Junk A and Riess F 2006 From an idea to a vision: there's plenty of room at the bottom *Am. J. Phys.* 74 825–30.

9 Singh N B, Susan M A B H and Chaudhary R G 2023 *Emerging Nanomaterials and Their Impact on Society in the 21st Century* (Materials Research Forum LLC).

10 Dvorsky R, Svoboda L and Bednář J 2022 *Nanoparticles' Preparation, Properties, Interactions and Self-Organization* (Cham: Springer International Publishing).

11 Vaseashta A and Dimova-Malinovska D 2005 Nanostructured and nanoscale devices, sensors and detectors *Sci. Technol. Adv. Mater.* 6 312–8.

12 Chansoriya T, Khilwani B and Ansari A S 2023 Nanoparticle-Based Drug Delivery System for Beginners *Interaction of Nanomaterials With Living Cells* ed F A Sheikh, S Majeed and M A Beigh (Singapore: Springer Nature) pp 557–80.

13 Wani I A 2021 Recent advances in biogenic silver nanoparticles & nanocomposite based plasmonic-colorimetric and electrochemical sensors *ECS J. Solid State Sci. Technol.* 10 047003.

14 Wani I A and Ahmad T 2013 Size and shape dependant antifungal activity of gold nanoparticles: a case study of Candida *Colloids Surf. B Biointerfaces* 101 162–70.

15 Moeinzadeh S and Jabbari E 2017 Nanoparticles and Their Applications *Springer Handbook of Nanotechnology* Springer Handbooks ed B Bhushan (Berlin, Heidelberg: Springer) pp 335–61.

16 Sousa A A, Schuck P and Hassan S A 2021 Biomolecular interactions of ultrasmall metallic nanoparticles and nanoclusters *Nanoscale Adv.* 3 2995–3027.

17 Moore J S 1997 Shape-persistent molecular architectures of nanoscale dimension *Acc. Chem. Res.* 30 402–13.

18 Loos J 2005 The art of SPM: scanning probe microscopy in materials science *Adv. Mater.* 17 1821–33.

19 Singh V, Yadav P and Mishra V 2020 Recent Advances on Classification, Properties, Synthesis, and Characterization of Nanomaterials *Green Synthesis of Nanomaterials for Bioenergy Applications* ed M Srivastava, V K Gupta, P K Mishra and N Srivastava (John Wiley & Sons, Ltd) pp 83–97.

20 Saleh T A 2020 Nanomaterials: classification, properties, and environmental toxicities *Environ. Technol. Innov.* 20 101067.

21 Sudha P N, Sangeetha K, Vijayalakshmi K and Barhoum A 2018 Nanomaterials History, Classification, Unique Properties, Production and Market *Emerging Applications of Nanoparticles and Architecture Nanostructures* Micro and Nano Technologies ed A Barhoum and A S H Makhlouf (Elsevier) pp 341–84.

22 Dazon C, Fierro V, Celzard A and Witschger O 2020 Identification of nanomaterials by the volume specific surface area (VSSA) criterion: application to powder mixes *Nanoscale Adv.* 2 4908–17.

23 Ghosh C K 2015 Quantum Effect on Properties of Nanomaterials *Introduction to Nano: Basics to Nanoscience and Nanotechnology* Engineering Materials ed A Sengupta and C K Sarkar (Berlin, Heidelberg: Springer) pp 73–111.

24 Roduner E 2006 Size matters: why nanomaterials are different *Chem. Soc. Rev.* 35 583–92.

25 Rotello V 2004 *Nanoparticles: Building Blocks for Nanotechnology* (Springer Science & Business Media).

26 Ghosh Chaudhuri R and Paria S 2012 Core/shell nanoparticles: classes, properties, synthesis mechanisms, characterization, and applications *Chem. Rev.* 112 2373–433.

27 Baig N, Kammakakam I and Falath W 2021 Nanomaterials: a review of synthesis methods, properties, recent progress, and challenges *Mater. Adv.* 2 1821–71.

28 Kumar Sharma R, Bandichhor R, Mishra V, Sharma S, Yadav S, Mehta S, Arora B, Rana P, Dutta S and Solanki K 2023 Advanced metal oxide-based nanocatalysts for the oxidative synthesis of fine chemicals *Mater. Adv.* 4 1795–830.

29 Polarz S and Smarsly B 2002 Nanoporous materials *J. Nanosci. Nanotechnol.* 2 581–612.

30 Notario B, Pinto J and Rodriguez-Perez M A 2016 Nanoporous polymeric materials: a new class of materials with enhanced properties *Prog. Mater. Sci.* 78–79 93–139.

31 Alivisatos A P 1996 Semiconductor clusters, nanocrystals, and quantum dots *Science* 271 933–7.

32 Baskoutas S and Terzis A F 2006 Size-dependent band gap of colloidal quantum dots *J. Appl. Phys.* 99 013708.

33 Aavani F, Khorshidi S and Karkhaneh A 2019 A concise review on drug-loaded electrospun nanofibres as promising wound dressings *J. Med. Eng. Technol.* 43 38–47.

34 Delehanty J B, Medintz I L, Pons T, Brunel F M, Dawson P E and Mattoussi H 2006 Self-assembled quantum dot– peptide bioconjugates for selective intracellular delivery *Bioconjug. Chem.* 17 920–7.

35 Akbarzadeh A, Samiei M and Davaran S 2012 Magnetic nanoparticles: preparation, physical properties, and applications in biomedicine *Nanoscale Res. Lett.* 7 1–13.

36 Rizwan M, Shoukat A, Ayub A, Razzaq B and Tahir M B 2021 Types and Classification of Nanomaterials *Synthesis, Characterization, Hazards and Safety* Micro and Nano Technologies ed M B Tahir, M Sagir and A M Asiri (Elsevier) pp 31–54.

37 Sannino D 2021 Types and Classification of Nanomaterials *Nanotechnology: Trends and Future Applications* ed M B Tahir, M Rafique and M Sagir (Singapore: Springer) pp 15–38.

38 Rao N, Singh R and Bashambu L 2021 Carbon-based nanomaterials: synthesis and prospective applications *Mater. Today Proc.* 44 608–14.

39 Jamkhande P G, Ghule N W, Bamer A H and Kalaskar M G 2019 Metal nanoparticles synthesis: an overview on methods of preparation, advantages and disadvantages, and applications *J. Drug Deliv. Sci. Technol.* 53 101174.

40 Chavali M S and Nikolova M P 2019 Metal oxide nanoparticles and their applications in nanotechnology *SN Appl. Sci.* 1 607.

41 Chauhan R, Kumar A, Tripathi R and Kumar A 2021 Advancing of Zinc Oxide Nanoparticles for Cosmetic Applications *Handbook of Consumer Nanoproducts* ed S Mallakpour and C M Hussain (Singapore: Springer) pp 1–16.

42 Haas K-H 2021 Application of Metal Oxide Nanoparticles and Their Economic Impact *Metal Oxide Nanoparticles* ed O Diwald and T Berger (John Wiley & Sons, Ltd) pp 29–65.

43 Al-Amin M, Sarker S, Mumu H and Gafur M 2021 Fabrication methods and fracture behaviour of zirconia toughened alumina (ZTA) nano composite ceramic: a review *Mater. Today Proc.*

44 Duntu S H, Agyapong J, Ahmad I, Islam M and Boakye-Yiadom S 2022 Combined effect of low ZrO_2 content and carbon nanostructures on mechanical and wear properties of hot-pressed Al_2O_3/ZrO_2 hybrid nanocomposites *Ceram. Int.* 48 34803–16.

45 Terna A D, Elemike E E, Mbonu J I, Osafile O E and Ezeani R O 2021 The future of semiconductors nanoparticles: synthesis, properties and applications *Mater. Sci. Eng. B* 272 115363.

46 Yacobi B G 2003 Types of Semiconductors *Semiconductor Materials: An Introduction to Basic Principles* Microdevices (Boston, MA: Springer) pp 135–70.

47 Thambidurai M, Muthukumarasamy N, Agilan S, Murugan N, Vasantha S, Balasundaraprabhu R and Senthil T S 2010 Strong quantum confinement effect in nanocrystalline CdS *J. Mater. Sci.* 45 3254–8.

48 Liu J, Nie Y, Xue W, Wu L, Jin H, Jin G, Zhai Z and Fu C 2020 Size effects on structural and optical properties of tin oxide quantum dots with enhanced quantum confinement *J. Mater. Res. Technol.* 9 8020–8.

49 Sumanth Kumar D, Jai Kumar B and Mahesh H M 2018 Quantum Nanostructures (QDs): An Overview *Synthesis of Inorganic Nanomaterials* Micro and Nano Technologies ed S M Bhagyaraj, O S Oluwafemi, N Kalarikkal and S Thomas (Woodhead Publishing) pp 59–88.

50 Unser S, Bruzas I, He J and Sagle L 2015 Localized surface plasmon resonance biosensing: current challenges and approaches *Sensors* 15 15684–716.

51 Cb M, Norris D J and Bawendi M G 1993 Synthesis and characterization of nearly monodisperse CdE (E = sulfur, selenium, tellurium) semiconductor nanocrystallites *J. Am. Chem. Soc.* 115 8706–15.

52 Pattantyus-Abraham A G, Kramer I J, Barkhouse A R, Wang X, Konstantatos G, Debnath R, Levina L, Raabe I, Nazeeruddin M K, Grätzel M and Sargent E H 2010 Depleted-heterojunction colloidal quantum dot solar cells *ACS Nano* 4 3374–80.

53 Kumar D S, Kumar B J and Mahesh H M 2016 Optical properties of colloidal aqueous synthesized 3 mercaptopropionic acid stabilized CdS quantum dots *AIP Conf. Proc.* 1728 020162.

54 Li H, Chen D, Li L, Tang F, Zhang L and Ren J 2010 Size-and shape-controlled synthesis of PbSe and PbS nanocrystals via a facile method *CrystEngComm* 12 1127–33.

55 Peng Z A and Peng X 2001 Formation of high-quality CdTe, CdSe, and CdS nanocrystals using CdO as precursor *J. Am. Chem. Soc.* 123 183–4.

56 Rosiles-Perez C, Serrano-Estrada M A, Sidhik S, Alatorre-Ordaz A, Torres-Castro A, Vallejo M A, Jiménez-González A E and López-Luke T 2020 Synthesis of high quality PbS colloidal quantum dots by ultrasonic bath as photosensitizers in a TiO_2 solar cell *J. Solid State Chem.* 292 121720.

57 Turkevich J, Stevenson P C and Hillier J 1951 A study of the nucleation and growth processes in the synthesis of colloidal gold *Discuss. Faraday Soc.* 11 55–75.

58 Amendola V, Pilot R, Frasconi M, Maragò O M and Iatì M A 2017 Surface plasmon resonance in gold nanoparticles: a review *J. Phys. Condens. Matter* 29 203002.

59 Hutter E and Fendler J H 2004 Exploitation of localized surface plasmon resonance *Adv. Mater.* 16 1685–706.

60 Louis C and Pluchery O 2012 *Gold Nanoparticles for Physics, Chemistry and Biology* (World Scientific).

61 Lohse S E and Murphy C J 2013 The quest for shape control: a history of gold nanorod synthesis *Chem. Mater.* 25 1250–61.

62 Giasuddin A, Jhuma K and Haq A M 2013 Use of gold nanoparticles in diagnostics, surgery and medicine: a review *Bangladesh J. Med. Biochem.* 5 56–60.

63 Hong W, Bai H, Xu Y, Yao Z, Gu Z and Shi G 2010 Preparation of gold nanoparticle/graphene composites with controlled weight contents and their application in biosensors *J. Phys. Chem. C* 114 1822–6.

64 Akbari Nakhjavani S, Afsharan H, Khalilzadeh B, Ghahremani M H, Carrara S and Omidi Y 2019 Gold and silver bio/nano-hybrids-based electrochemical immunosensor for ultrasensitive detection of carcinoembryonic antigen *Biosens. Bioelectron.* 141 111439.

65 Anker J N, Hall W P, Lyandres O, Shah N C, Zhao J and Van Duyne R P 2010 Biosensing with plasmonic nanosensors *Nanosci. Technol. Collect. Rev. Nat. J.* 308–19.

66 Tamiya E 2016 Nano-materials for LSPR and electrochemical biosensors *Nanomed. Nanotechnol. Biol. Med.* 2 450.

67 McMillan B G, Berlouis L E A, Cruickshank F R, Pugh D and Brevet P-F 2005 Transverse and longitudinal surface plasmon resonances of a hexagonal array of gold nanorods embedded in an alumina matrix *Appl. Phys. Lett.* 86 211912.

68 Ghosh S K and Pal T 2007 Interparticle coupling effect on the surface plasmon resonance of gold nanoparticles: from theory to applications *Chem. Rev.* 107 4797–862.

69 El-Brolossy T A, Abdallah T, Mohamed M B, Abdallah S, Easawi K, Negm S and Talaat H 2008 Shape and size dependence of the surface plasmon resonance of gold nanoparticles studied by photoacoustic technique *Eur. Phys. J. Spec. Top.* 153 361–4.

70 Eustis S and El-Sayed M A 2006 Why gold nanoparticles are more precious than pretty gold: noble metal surface plasmon resonance and its enhancement of the radiative and nonradiative properties of nanocrystals of different shapes *Chem. Soc. Rev.* 35 209–17.

71 Ren Y, Qi H, Chen Q, Wang S and Ruan L 2017 Localized surface plasmon resonance of nanotriangle dimers at different relative positions *J. Quant. Spectrosc. Radiat. Transf.* 199 45–51.

72 Klar T, Perner M, Grosse S, von Plessen G, Spirkl W and Feldmann J 1998 Surface-plasmon resonances in single metallic nanoparticles *Phys. Rev. Lett.* 80 4249–52.

73 Pathak N K and Sharma R P 2016 Study of broadband tunable properties of surface plasmon resonances of noble metal nanoparticles using Mie scattering theory: plasmonic perovskite interaction *Plasmonics* 11 713–9.

74 Xu H and Käll M 2002 Modeling the optical response of nanoparticle-based surface plasmon resonance sensors *Sensors Actuators B Chem.* 87 244–9.

75 Lopatynskyi A M, Lopatynska O G, Guo L J and Chegel V I 2011 Localized surface plasmon resonance biosensor – part I: theoretical study of sensitivity – extended Mie approach *IEEE Sensors J.* 11 361–9.

76 Duque J S, Blandón J S and Riascos H 2017 Localized plasmon resonance in metal nanoparticles using Mie theory *J. Phys. Conf. Ser.* 850 012017.

77 Abid N, Khan A M, Shujait S, Chaudhary K, Ikram M, Imran M, Haider J, Khan M, Khan Q and Maqbool M 2022 Synthesis of nanomaterials using various top-down and bottom-up approaches, influencing factors, advantages, and disadvantages: a review *Adv. Colloid Interf. Sci.* 300 102597.

78 Bloch K, Pardesi K, Satriano C and Ghosh S 2021 Bacteriogenic platinum nanoparticles for application in nanomedicine *Front. Chem.* 9 624344.

79 Cruz J N 2023 *Nanobiomaterials: Perspectives for Medical Applications in the Diagnosis and Treatment of Diseases* (Materials Research Forum LLC).

80 Amabilino D B 2016 *Supramolecular Chemistry at Surfaces* (Royal Society of Chemistry).

81 Ahmed M 2020 Nanomaterial Synthesis *Polymer Science and Nanotechnology* ed R Narain (Elsevier) pp 361–99.

82 Wang Y, Pan J-A, Wu H and Talapin D V 2019 Direct wavelength-selective optical and electron-beam lithography of functional inorganic nanomaterials *ACS Nano* 13 13917–31.

83 Wang Y, Fedin I, Zhang H and Talapin D V 2017 Direct optical lithography of functional inorganic nanomaterials *Science* 357 385–8.

84 Ahmad T, Wani I A, Ahmed J and Al-Hartomy O A 2014 Effect of gold ion concentration on size and properties of gold nanoparticles in TritonX-100 based inverse microemulsions *Appl. Nanosci.* 4 491–8.

85 Wani I A, Ganguly A, Ahmed J and Ahmad T 2011 Silver nanoparticles: ultrasonic wave assisted synthesis, optical characterization and surface area studies *Mater. Lett.* 65 520–2.

86 Wani I A, Khatoon S, Ganguly A, Ahmed J, Ganguli A K and Ahmad T 2010 Silver nanoparticles: large scale solvothermal synthesis and optical properties *Mater. Res. Bull.* 45 1033–8.

87 Polte J, Ahner T T, Delissen F, Sokolov S, Emmerling F, Thünemann A F and Kraehnert R 2010 Mechanism of gold nanoparticle formation in the classical citrate synthesis method derived from coupled in situ XANES and SAXS evaluation *J. Am. Chem. Soc.* 132 1296–301.

88 Grzelczak M, Pérez-Juste J, Mulvaney P and Liz-Marzán L M 2008 Shape control in gold nanoparticle synthesis *Chem. Soc. Rev.* 37 1783–91.

89 Frens G 1973 Controlled nucleation for the regulation of the particle size in monodisperse gold suspensions *Nat. Phys. Sci.* 241 20–2.

90 Kimling J, Maier M, Okenve B, Kotaidis V, Ballot H and Plech A 2006 Turkevich method for gold nanoparticle synthesis revisited *J. Phys. Chem. B* 110 15700–7.

91 Kumar S, Gandhi K S and Kumar R 2007 Modeling of formation of gold nanoparticles by citrate method *Ind. Eng. Chem. Res.* 46 3128–36.

92 Li C, Li D, Wan G, Xu J and Hou W 2011 Facile synthesis of concentrated gold nanoparticles with low size-distribution in water: temperature and pH controls *Nanoscale Res. Lett.* 6 440.

93 Rahman M R, Saleh F S, Okajima T and Ohsaka T 2011 pH dependence of the size and crystallographic orientation of the gold nanoparticles prepared by seed-mediated growth *Langmuir* 27 5126–35.

94 Xia H, Bai S, Hartmann J and Wang D 2010 Synthesis of monodisperse quasi-spherical gold nanoparticles in water via silver(I)-assisted citrate reduction *Langmuir* 26 3585–9.

95 Patungwasa W and Hodak J H 2008 pH tunable morphology of the gold nanoparticles produced by citrate reduction *Mater. Chem. Phys.* 108 45–54.

96 Volkert A A, Subramaniam V and Haes A J 2011 Implications of citrate concentration during the seeded growth synthesis of gold nanoparticles *Chem. Commun.* 47 478–80.

97 Zabetakis K, Ghann W E, Kumar S and Daniel M-C 2012 Effect of high gold salt concentrations on the size and polydispersity of gold nanoparticles prepared by an extended Turkevich–Frens method *Gold Bull.* 45 203–11.

98 Ojea-Jiménez I, Bastús N G and Puntes V 2011 Influence of the sequence of the reagents addition in the citrate-mediated synthesis of gold nanoparticles *J. Phys. Chem. C* 115 15752–7.

99 Ojea-Jiménez I, Romero F M, Bastús N G and Puntes V 2010 Small gold nanoparticles synthesized with sodium citrate and heavy water: insights into the reaction mechanism *J. Phys. Chem. C* 114 1800–4.

100 Brust M, Walker M, Bethell D, Schiffrin D J and Whyman R 1994 Synthesis of thiol-derivatised gold nanoparticles in a two-phase liquid–liquid system *J. Chem. Soc. Chem. Commun.* 0 801–2.

101 Hostetler M J, Green S J, Stokes J J and Murray R W 1996 Monolayers in three dimensions: synthesis and electrochemistry of ω-functionalized alkanethiolate-stabilized gold cluster compounds *J. Am. Chem. Soc.* 118 4212–3.

102 Li Y, Zaluzhna O, Xu B, Gao Y, Modest J M and Tong Y J 2011 Mechanistic insights into the Brust-Schiffrin two-phase synthesis of organo-chalcogenate-protected metal nanoparticles *J. Am. Chem. Soc.* 133 2092–5.

103 Brust M, Fink J, Bethell D, Schiffrin D J and Kiely C 1995 Synthesis and reactions of functionalised gold nanoparticles *J. Chem. Soc. Chem. Commun.* 16 1655–6.

104 Templeton A C, Wuelfing W P and Murray R W 2000 Monolayer-protected cluster molecules *Acc. Chem. Res.* 33 27–36.

105 Kanaras A G, Kamounah F S, Schaumburg K, Kiely C J and Brust M 2002 Thioalkylated tetraethylene glycol: a new ligand for water soluble monolayer protected gold clusters *Chem. Commun.* 20 2294–5.

106 Di Pasqua A J, Mishler R E, Ship Y-L, Dabrowiak J C and Asefa T 2009 Preparation of antibody-conjugated gold nanoparticles *Mater. Lett.* 63 1876–9.

107 Leontowich A F G, Calver C F, Dasog M and Scott R W J 2010 Surface properties of water-soluble glycine-cysteamine-protected gold clusters *Langmuir* 26 1285–90.

108 Busby M, Chiorboli C and Scandola F 2006 Relaxation dynamics and transient behavior of small arenethiol passivated gold nanoparticles *J. Phys. Chem. B* 110 6020–6.

109 Gupta R K, Srinivasan M P and Dharmarajan R 2011 Synthesis of short chain thiol capped gold nanoparticles, their stabilization and immobilization on silicon surface *Colloids Surf. A Physicochem. Eng. Asp.* 390 149–56.

110 Pattabi R M and Pattabi M 2009 Synthesis and characterization of thiosalicylic acid stabilized gold nanoparticles *Spectrochim. Acta A Mol. Biomol. Spectrosc.* 74 195–9.

111 Moores A, Goettmann F, Sanchez C and Floch P L 2004 Phosphinine stabilised gold nanoparticles; synthesis and immobilisation on mesoporous materials *Chem. Commun.* 24 2842–3.

112 Shem P M, Sardar R and Shumaker-Parry J S 2009 One-step synthesis of phosphine-stabilized gold nanoparticles using the mild reducing agent 9-BBN *Langmuir* 25 13279–83.

113 Pettibone J M and Hudgens J W 2011 Gold cluster formation with phosphine ligands: etching as a size-selective synthetic pathway for small clusters *ACS Nano* 5 2989–3002.

114 Gautier C, Taras R, Gladiali S and Bürgi T 2008 Chiral 1, 1′-binaphthyl-2, 2′-dithiol-stabilized gold clusters: size separation and optical activity in the UV–vis *Chirality Pharmacol. Biol. Chem. Consequences Mol. Asymmetry* 20 486–93.

115 De Silva N, Ha J-M, Solovyov A, Nigra M M, Ogino I, Yeh S W, Durkin K A and Katz A 2010 A bioinspired approach for controlling accessibility in calix [4] arene-bound metal cluster catalysts *Nat. Chem.* 2 1062–8.

116 Ha J-M, Solovyov A and Katz A 2009 Synthesis and characterization of accessible metal surfaces in calixarene-bound gold nanoparticles *Langmuir* 25 10548–53.
117 Villa A, Wang D, Su D, Veith G M and Prati L 2010 Using supported Au nanoparticles as starting material for preparing uniform Au/Pd bimetallic catalysts *Phys. Chem. Chem. Phys.* 12 2183–9.
118 Sardar R and Shumaker-Parry J S 2009 9-BBN induced synthesis of nearly monodisperse ω-functionalized alkylthiol stabilized gold nanoparticles *Chem. Mater.* 21 1167–9.
119 Xu C, Sun L, Kepley L J, Crooks R M and Ricco A J 1993 Molecular interactions between organized, surface-confined monolayers and vapor-phase probe molecules. 6. In-situ FT-IR external reflectance spectroscopy of monolayer adsorption and reaction chemistry *Anal. Chem.* 65 2102–7.
120 Kumar A, Mandal S, Selvakannan P R, Pasricha R, Mandale A B and Sastry M 2003 Investigation into the interaction between surface-bound alkylamines and gold nanoparticles *Langmuir* 19 6277–82.
121 Porta F, Krpetić Ž, Prati L, Gaiassi A and Scarì G 2008 Gold-ligand interaction studies of water-soluble aminoalcohol capped gold nanoparticles by NMR *Langmuir* 24 7061–4.
122 Wangoo N, Suri C R and Shekhawat G 2008 Interaction of gold nanoparticles with protein: a spectroscopic study to monitor protein conformational changes *Appl. Phys. Lett.* 92 133104.
123 Wangoo N, Bhasin K K, Mehta S K and Suri C R 2008 Synthesis and capping of water-dispersed gold nanoparticles by an amino acid: bioconjugation and binding studies *J. Colloid Interface Sci.* 323 247–54.
124 Griffin F and Fitzmaurice D 2007 Preparation and thermally promoted ripening of water-soluble gold nanoparticles stabilized by weakly physisorbed ligands *Langmuir* 23 10262–71.
125 Gittins D I and Caruso F 2001 Spontaneous phase transfer of nanoparticulate metals from organic to aqueous media *Angew. Chem. Int. Ed.* 40 3001–4.
126 Yu A, Liang Z, Cho J and Caruso F 2003 Nanostructured electrochemical sensor based on dense gold nanoparticle films *Nano Lett.* 3 1203–7.
127 Gandubert V J and Lennox R B 2005 Assessment of 4-(Dimethylamino)pyridine as a capping agent for gold nanoparticles *Langmuir* 21 6532–9.
128 Barlow B C and Burgess I J 2007 Electrochemical evaluation of 4-(Dimethylamino)pyridine adsorption on polycrystalline gold *Langmuir* 23 1555–63.
129 Lange H, Maultzsch J, Meng W, Mollenhauer D, Paulus B, Peica N, Schlecht S and Thomsen C 2011 Adsorption behavior of 4-Methoxypyridine on gold nanoparticles *Langmuir* 27 7258–64.
130 Li G, Li D, Zhang L, Zhai J and Wang E 2009 One-step synthesis of folic acid protected gold nanoparticles and their receptor-mediated intracellular uptake *Chem. Eur. J.* 15 9868–73.
131 Jena B K and Raj C R 2007 Synthesis of flower-like gold nanoparticles and their electrocatalytic activity towards the oxidation of methanol and the reduction of oxygen *Langmuir* 23 4064–70.
132 Yavuz M S, Li W and Xia Y 2009 Facile synthesis of gold icosahedra in an aqueous solution by reacting HAuCl4 with *N*-vinyl pyrrolidone *Chem. Eur. J.* 15 13181–7.
133 Shon Y-S and Choo H 2003 Organic reactions of monolayer-protected metal nanoparticles *Comptes Rendus Chim.* 6 1009–18.
134 Geng M, Zhang Y, Huang Q, Zhang B, Li Q, Li W and Li J 2010 Functionalization of C60 with gold nanoparticles *Carbon* 48 3570–4.
135 Demartini A, Alloisio M, Cuniberti C, Dellepiane G, Jadhav S A, Thea S, Giorgetti E, Gellini C and Muniz-Miranda M 2009 Polydiacetylene-functionalized noble metal nanocages *J. Phys. Chem. C* 113 19475–81.

136 Jadhav S A 2012 Functional self-assembled monolayers (SAMs) of organic compounds on gold nanoparticles *J. Mater. Chem.* 22 5894–9.

137 Giersig M and Mulvaney P 2002 Preparation of ordered colloid monolayers by electrophoretic deposition *Langmuir* 9(12) 3408–13.

138 Giljohann D A, Seferos D S, Daniel W L, Massich M D, Patel P C and Mirkin C A 2010 Gold nanoparticles for biology and medicine *Angew. Chem. Int. Ed. Engl.* 49 3280–94.

139 Kim D, Park S, Lee J H, Jeong Y Y and Jon S 2007 Antibiofouling polymer-coated gold nanoparticles as a contrast agent for in vivo X-ray computed tomography imaging *J. Am. Chem. Soc.* 129 7661–5.

140 Daniel M-C, Grow M E, Pan H, Bednarek M, Ghann W E, Zabetakis K and Cornish J 2011 Gold nanoparticle-cored poly(propyleneimine) dendrimers as a new platform for multifunctional drug delivery systems *New J. Chem.* 35 2366–74.

141 Templeton A C, Hostetler M J, Kraft C T and Murray R W 1998 Reactivity of monolayer-protected gold cluster molecules: steric effects *J. Am. Chem. Soc.* 120 1906–11.

142 Milette J, Toader V, Reven L and Lennox R B 2011 Tuning the miscibility of gold nanoparticles dispersed in liquid crystals via the thiol-for-DMAP reaction *J. Mater. Chem.* 21 9043–50.

143 Rucareanu S, Maccarini M, Shepherd J L and Lennox R B 2008 Polymer-capped gold nanoparticles by ligand-exchange reactions *J. Mater. Chem.* 18 5830–4.

144 Rucareanu S, Gandubert V J and Lennox R B 2006 4-(*N*,*N*-dimethylamino) pyridine-protected Au nanoparticles: versatile precursors for water- and organic-soluble gold nanoparticles *Chem. Mater.* 18 4674–80.

145 Zhao P, Li N and Astruc D 2013 State of the art in gold nanoparticle synthesis *Coord. Chem. Rev.* 257 638–65.

146 Reetz M T, Helbig W, Quaiser S A, Stimming U, Breuer N and Vogel R 1995 Visualization of surfactants on nanostructured palladium clusters by a combination of STM and high-resolution TEM *Science* 267 367–9.

147 Reetz M T and Helbig W 1994 Size-selective synthesis of nanostructured transition metal clusters *J. Am. Chem. Soc.* 116 7401–2.

148 Huang C-J, Chiu P-H, Wang Y-H, Chen K-L, Linn J-J and Yang C-F 2006 Electrochemically controlling the size of gold nanoparticles *J. Electrochem. Soc.* 153 D193.

149 Dai X and Compton R G 2006 Direct electrodeposition of gold nanoparticles onto indium tin oxide film coated glass: application to the detection of arsenic(III) *Anal. Sci. Int. J. Jpn. Soc. Anal. Chem.* 22 567–70.

150 Angerstein-Kozlowska H, Conway B E, Hamelin A and Stoicoviciu L 1987 Elementary steps of electrochemical oxidation of single-crystal planes of Au Part II. A chemical and structural basis of oxidation of the (111) plane *J. Electroanal. Chem. Interfacial Electrochem.* 228 429–53.

151 Sheridan E, Hjelm J and Forster R J 2007 Electrodeposition of gold nanoparticles on fluorine-doped tin oxide: control of particle density and size distribution *J. Electroanal. Chem.* 608 1–7.

152 Aziz M A, Patra S and Yang H 2008 A facile method of achieving low surface coverage of Au nanoparticles on an indium tin oxide electrode and its application to protein detection *Chem. Commun.* 38 4607–9.

153 Gamero M and Alonso C 2010 Deposition of nanostructurated gold on *n*-doped silicon substrate by different electrochemical methods *J. Appl. Electrochem.* 40 175.

154 Zhang H, Xu J-J and Chen H-Y 2008 Shape-controlled gold nanoarchitectures: synthesis, superhydrophobicity, and electrocatalytic properties *J. Phys. Chem. C* 112 13886–92.

155 Sobri S and Roy S 2008 Nucleation studies of gold on carbon electrodes *J. Eng. Sci. Technol.* 3 62–70.

156 Othman S H, El-Deab M S, Okajima T and Ohsaka T 2009 Novel procedure for the fabrication of gold nanostructures enriched in Au (1 1 0) facet orientation *Electrochem. Commun.* 11 1273–6.

157 Arihara K, Ariga T, Takashima N, Arihara K, Okajima T, Kitamura F, Tokuda K and Ohsaka T 2003 Multiple voltammetric waves for reductive desorption of cysteine and 4-mercaptobenzoic acid monolayers self-assembled on gold substrates *Phys. Chem. Chem. Phys.* 5 3758–61.

158 Zhou Y-G, Rees N V, Pillay J, Tshikhudo R, Vilakazi S and Compton R G 2011 Gold nanoparticles show electroactivity: counting and sorting nanoparticles upon impact with electrodes *Chem. Commun.* 48 224–6.

159 Zhou Y, Zheng X, Wu L, Zhi J and Xu M 2011 An easy method for manufacture of gold nanoparticles on a glassy carbon surface *J. Mater. Sci.* 46 1139–42.

160 Komsiyska L and Staikov G 2008 Electrocrystallization of Au nanoparticles on glassy carbon from $HClO_4$ solution containing $[AuCl4]^-$ *Electrochim. Acta* 54 168–72.

161 Qu L and Dai L 2005 Substrate-enhanced electroless deposition of metal nanoparticles on carbon nanotubes *J. Am. Chem. Soc.* 127 10806–7.

162 Hung V W-S and Kerman K 2011 Gold electrodeposition on carbon nanotubes for the enhanced electrochemical detection of homocysteine *Electrochem. Commun.* 13 328–30.

163 Afraz A, Rafati A A and Najafi M 2014 Optimization of modified carbon paste electrode with multiwalled carbon nanotube/ionic liquid/cauliflower-like gold nanostructures for simultaneous determination of ascorbic acid, dopamine and uric acid *Mater. Sci. Eng. C* 44 58–68.

164 Qiu C, Zhou H, Cao B, Sun L and Yu T 2013 Raman spectroscopy of morphology-controlled deposition of Au on graphene *Carbon* 59 487–94.

165 Lee J, Shim S, Kim B and Shin H S 2011 Surface-enhanced Raman scattering of single-and few-layer graphene by the deposition of gold nanoparticles *Chem. Eur. J.* 17 2381–7.

166 Wayman C M and Darby T P 1975 Nucleation and growth of gold films on graphite: II. The effect of substrate temperature *J. Cryst. Growth* 28 53–67.

167 Cherevko S and Chung C-H 2011 Direct electrodeposition of nanoporous gold with controlled multimodal pore size distribution *Electrochem. Commun.* 13 16–9.

168 Yu C S-S, Lee C-L and Wang C R C 1997 Gold nanorods: electrochemical synthesis and optical properties *J. Phys. Chem. B* 101 6661–4.

169 Walker C H, St. John J V and Wisian-Neilson P 2001 Synthesis and size control of gold nanoparticles stabilized by poly (methylphenylphosphazene) *J. Am. Chem. Soc.* 123 3846–7.

170 Wang X, Li G, Chen T, Yang M, Zhang Z, Wu T and Chen H 2008 Polymer-encapsulated gold-nanoparticle dimers: facile preparation and catalytical application in guided growth of dimeric ZnO-nanowires *Nano Lett.* 8 2643–7.

171 Giljohann D A, Seferos D S, Patel P C, Millstone J E, Rosi N L and Mirkin C A 2007 Oligonucleotide loading determines cellular uptake of DNA-modified gold nanoparticles *Nano Lett.* 7 3818–21.

172 Wang Z, Kanaras A G, Bates A D, Cosstick R and Brust M 2004 Enzymatic DNA processing on gold nanoparticles *J. Mater. Chem.* 14 578–80.

173 Guo S, Wang L and Wang E 2007 Templateless, surfactantless, simple electrochemical route to rapid synthesis of diameter-controlled 3D flowerlike gold microstructure with "clean" surface *Chem. Commun.* 44 3163–5.

174 Shan J and Tenhu H 2007 Recent advances in polymer protected gold nanoparticles: synthesis, properties and applications *Chem. Commun.* 110(10) 4580–98.

175 Newkome G R and Shreiner C 2010 Dendrimers derived from 1→ 3 branching motifs *Chem. Rev.* 110(10) 6338–442.

176 Caminade A-M, Turrin C-O, Laurent R, Ouali A and Delavaux-Nicot B 2011 *Dendrimers: Towards Catalytic, Material and Biomedical Uses* (John Wiley & Sons).

177 Esumi K, Miyamoto K and Yoshimura T 2002 Comparison of PAMAM–Au and PPI–Au nanocomposites and their catalytic activity for reduction of 4-nitrophenol *J. Colloid Interface Sci.* 254 402–5.

178 Esumi K, Houdatsu H and Yoshimura T 2004 Antioxidant action by gold- Pamam dendrimer nanocomposites *Langmuir* 20 2536–8.

179 Endo T, Yoshimura T and Esumi K 2005 Synthesis and catalytic activity of gold–silver binary nanoparticles stabilized by PAMAM dendrimer *J. Colloid Interface Sci.* 286 602–9.

180 Kim T H, Choi H S, Go B R and Kim J 2010 Modification of a glassy carbon surface with amine-terminated dendrimers and its application to electrocatalytic hydrazine oxidation *Electrochem. Commun.* 12 788–91.

181 Yancey D F, Carino E V and Crooks R M 2010 Electrochemical synthesis and electrocatalytic properties of Au@ Pt dendrimer-encapsulated nanoparticles *J. Am. Chem. Soc.* 132 10988–9.

182 Daniel M-C, Ruiz J, Nlate S, Blais J-C and Astruc D 2003 Nanoscopic assemblies between supramolecular redox active metallodendrons and gold nanoparticles: synthesis, characterization, and selective recognition of $H_2PO_4^-$, HSO_4^-, and adenosine-5′-triphosphate (ATP^{2-}) anions *J. Am. Chem. Soc.* 125 2617–28.

183 Kaewtong C, Jiang G, Ponnapati R, Pulpoka B and Advincula R 2010 Redox nanoreactor dendrimer boxes: in situ hybrid gold nanoparticles via terthiophene and carbazole peripheral dendrimer oxidation *Soft Matter* 6 5316–9.

184 Balogh L, Valluzzi R, Laverdure K S, Gido S P, Hagnauer G L and Tomalia D A 1999 Formation of silver and gold dendrimer nanocomposites *J. Nanopart. Res.* 1 353–68.

185 Garcia M E, Baker L A and Crooks R M 1999 Preparation and characterization of dendrimer-gold colloid nanocomposites *Anal. Chem.* 71 256–8.

186 Chechik V and Crooks R M 1999 Monolayers of thiol-terminated dendrimers on the surface of planar and colloidal gold *Langmuir* 15 6364–9.

187 Shan Y, Luo T, Peng C, Sheng R, Cao A, Cao X, Shen M, Guo R, Tomás H and Shi X 2012 Gene delivery using dendrimer-entrapped gold nanoparticles as nonviral vectors *Biomaterials* 33 3025–35.

188 Peng C, Zheng L, Chen Q, Shen M, Guo R, Wang H, Cao X, Zhang G and Shi X 2012 PEGylated dendrimer-entrapped gold nanoparticles for in vivo blood pool and tumor imaging by computed tomography *Biomaterials* 33 1107–19.

189 Kim Y-G, Oh S-K and Crooks R M 2004 Preparation and characterization of 1-2 nm dendrimer-encapsulated gold nanoparticles having very narrow size distributions *Chem. Mater.* 16 167–72.

190 Love C S, Chechik V, Smith D K and Brennan C 2004 Dendron-stabilised gold nanoparticles: generation dependence of core size and thermal stability *J. Mater. Chem.* 14 919–23.

191 Hoffman L W, Andersson G G, Sharma A, Clarke S R and Voelcker N H 2011 New insights into the structure of PAMAM dendrimer/gold nanoparticle nanocomposites *Langmuir* 27 6759–67.

192 Frasconi M, Tortolini C, Botre F and Mazzei F 2010 Multifunctional Au nanoparticle dendrimer-based surface plasmon resonance biosensor and its application for improved insulin detection *Anal. Chem.* 82 7335–42.

193 Namazi H and Fard A M P 2011 Preparation of gold nanoparticles in the presence of citric acid-based dendrimers containing periphery hydroxyl groups *Mater. Chem. Phys.* 129 189–94.

194 Boisselier E, Diallo A K, Salmon L, Ornelas C, Ruiz J and Astruc D 2010 Encapsulation and stabilization of gold nanoparticles with "click" polyethyleneglycol dendrimers *J. Am. Chem. Soc.* 132 2729–42.

195 Jia L, Lv L-P, Xu J-P and Ji J 2011 Phosphorylcholine functionalized dendrimers for the formation of highly stable and reactive gold nanoparticles and their glucose conjugation for biosensing *J. Nanopart. Res.* 13 4075–83.

196 Cho T J, Zangmeister R A, MacCuspie R I, Patri A K and Hackley V A 2011 Newkome-type dendron-stabilized gold nanoparticles: synthesis, reactivity, and stability *Chem. Mater.* 23 2665–76.

197 Jara N, Milán N S, Rahman A, Mouheb L, Boffito D C, Jeffryes C and Dahoumane S A 2021 Photochemical synthesis of gold and silver nanoparticles – a review *Molecules* 26 4585.

198 Lin S K and Cheng W T 2020 Fabrication and characterization of colloidal silver nanoparticle via photochemical synthesis *Mater. Lett.* 261 127077.

199 Eftekhari-Kenzerki Z, Fardid R and Behzad-Behbahani A 2019 Impact of silver nanoparticles on the ultraviolet radiation direct and bystander effects on TK6 cell line *J. Med. Phys.* 44 118.

200 McTiernan C D, Alarcon E I, Hallett-Tapley G L, Murillo-Lopez J, Arratia-Perez R, Netto-Ferreira J C and Scaiano J C 2014 Electron transfer from the benzophenone triplet excited state directs the photochemical synthesis of gold nanoparticles *Photochem. Photobiol. Sci.* 13 149–53.

201 Valandro S R, Poli A L, Neumann M G and Schmitt C C 2019 Photochemical synthesis of Ag and Au nanoparticles using a thioxanthone substituted chitosan as simultaneous photoinitiator and stabilizer *J. Braz. Chem. Soc.* 30 2642–9.

202 Marin M L, McGilvray K L and Scaiano J C 2008 Photochemical strategies for the synthesis of gold nanoparticles from Au(III) and Au(I) using photoinduced free radical generation *J. Am. Chem. Soc.* 130 16572–84.

203 Yuan M, Li Y-B, Guo J, Zhong R-B, Wang L-P and Zhang F 2018 Solvent effects on gold nanoparticle formation from photochemical reduction of Au(III) by UV irradiation *Nucl. Sci. Tech.* 29 158.

204 Zhou Y, Wang C Y, Zhu Y R and Chen Z Y 1999 A novel ultraviolet irradiation technique for shape-controlled synthesis of gold nanoparticles at room temperature *Chem. Mater.* 11 2310–2.

205 Sau T K, Pal A, Jana N R, Wang Z L and Pal T 2001 Size controlled synthesis of gold nanoparticles using photochemically prepared seed particles *J. Nanopart. Res.* 3 257–61.

206 del Pilar R-T M, Díaz-Torres L A and Romero-Servin S 2014 Heparin assisted photochemical synthesis of gold nanoparticles and their performance as SERS substrates *Int. J. Mol. Sci.* 15 19239–52.

207 Grzelczak M and Liz-Marzán L M 2014 The relevance of light in the formation of colloidal metal nanoparticles *Chem. Soc. Rev.* 43 2089–97.

208 Mukha I, Khodko A, Vityuk N, Severynovska O, Pivovarenko V, Kachalova N, Smirnova N and Eremenko A 2020 Light-driven formation of gold/tryptophan nanoparticles *Appl. Nanosci.* 10 2827–33.

209 Rodríguez G C, Gauthier G H, Ladeira L O, Cala J S and Cataño D L 2017 Effect of pH and chloroauric acid concentration on the geometry of gold nanoparticles obtained by photochemical synthesis *J. Phys. Conf. Ser.* 935 (IOP Publishing) 012027.

210 Cheng J, Ge L, Xiong B and He Y 2011 Investigation of pH effect on gold nanorod synthesis *J. Chin. Chem. Soc.* 58 822–7.

211 Unal I S, Demirbas A, Onal I, Ildiz N and Ocsoy I 2020 One step preparation of stable gold nanoparticle using red cabbage extracts under UV light and its catalytic activity *J. Photochem. Photobiol. B* 204 111800.

212 Scaiano J C, Billone P, Gonzalez C M, Marett L, Marin M L, McGilvray K L and Yuan N 2009 Photochemical routes to silver and gold nanoparticles *Pure Appl. Chem.* 81 635–47.

213 Rodríguez-Torres M d P, Díaz-Torres L A, Salas P, Rodríguez-González C and Olmos-López M 2014 UV photochemical synthesis of heparin-coated gold nanoparticles *Gold Bull.* 47 21–31.

214 Bianchi P, Petit G and Monbaliu J-C M 2020 Scalable and robust photochemical flow process towards small spherical gold nanoparticles *React. Chem. Eng.* 5 1224–36.

215 Sanabria-Calaa J A, Conde-Rodrígueza G R, Gauthiera G H, Ladeirab L O, Laverde-Catañoa D A, Peña-Ballesterosa D Y and Merchan-Arenasc D 2018 Gold nanoparticles formation mechanism by photochemical synthesis *Chem. Eng.* 64 https://doi.org/10.3303/CET1864068.

216 Hamaguchi K, Kawasaki H and Arakawa R 2010 Photochemical synthesis of glycine-stabilized gold nanoparticles and its heavy-metal-induced aggregation behavior *Colloids Surf. A Physicochem. Eng. Asp.* 367 167–73.

217 Teixeira P R, Santos M S, Silva A L G, Báo S N, Azevedo R B, Sales M J A and Paterno L G 2016 Photochemically-assisted synthesis of non-toxic and biocompatible gold nanoparticles *Colloids Surf. B Biointerfaces* 148 317–23.

218 Boufi S, Vilar M R, Ferraria A M and do Rego A M B 2013 In situ photochemical generation of silver and gold nanoparticles on chitosan *Colloids Surf. A Physicochem. Eng. Asp.* 439 151–8.

219 Shiraishi Y, Tanaka H, Sakamoto H, Ichikawa S and Hirai T 2017 Photoreductive synthesis of monodispersed Au nanoparticles with citric acid as reductant and surface stabilizing reagent *RSC Adv.* 7 6187–92.

220 Huang Y and Kim D-H 2012 Light-controlled synthesis of gold nanoparticles using a rigid, photoresponsive surfactant *Nanoscale* 4 6312–7.

221 Shang Y, Min C, Hu J, Wang T, Liu H and Hu Y 2013 Synthesis of gold nanoparticles by reduction of HAuCl4 under UV irradiation *Solid State Sci.* 15 17–23.

222 Manna A, Imae T, Yogo T, Aoi K and Okazaki M 2002 Synthesis of gold nanoparticles in a Winsor II type microemulsion and their characterization *J. Colloid Interface Sci.* 256 297–303.

223 Note C, Kosmella S and Koetz J 2006 Poly (ethyleneimine) as reducing and stabilizing agent for the formation of gold nanoparticles in w/o microemulsions *Colloids Surf. A Physicochem. Eng. Asp.* 290 150–6.

224 Mihaly M, Fleancu M C, Olteanu N L, Bojin D, Meghea A and Enachescu M 2012 Synthesis of gold nanoparticles by microemulsion assisted photoreduction method *Comptes Rendus Chim.* 15 1012–21.

225 Ahmad T, Wani I A, Manzoor N, Ahmed J, Kalam A and Al-Shihri A S 2014 Structural characterization, antifungal activity and optical properties of gold nanoparticles prepared by reverse micelles *Adv. Sci. Lett.* 20 1631–6.

226 Pileni M P 1989 *Structure and Reactivity in Reverse Micelles* (Elsevier).

227 Pileni M P 1993 Reverse micelles as microreactors *J. Phys. Chem.* 97 6961–73.

228 Uskoković V and Drofenik M 2005 Synthesis of materials within reverse micelles *Surf. Rev. Lett.* 12 239–77.

229 Luisi P L, Giomini M, Pileni M and Robinson B H 1988 Reverse micelles as hosts for proteins and small molecules *Biochim. Biophys. Acta BBA-Rev. Biomembr.* 947 209–46.

230 Wu M-L, Chen D-H and Huang T-C 2001 Synthesis of Au/Pd bimetallic nanoparticles in reverse micelles *Langmuir* 17 3877–83.

231 Murphy C J, Sau T K, Gole A and Orendorff C J 2005 Surfactant-directed synthesis and optical properties of one-dimensional plasmonic metallic nanostructures *MRS Bull.* 30 349–55.

232 Malik M A, Wani M Y and Hashim M A 2012 Microemulsion method: a novel route to synthesize organic and inorganic nanomaterials: 1st nano update *Arab. J. Chem.* 5 397–417.

233 López-Quintela M A, Tojo C, Blanco M C, Rio L G and Leis J R 2004 Microemulsion dynamics and reactions in microemulsions *Curr. Opin. Colloid Interface Sci.* 9 264–78.

234 Kurihara K, Kizling J, Stenius P and Fendler J H 1983 Laser and pulse radiolytically induced colloidal gold formation in water and in water-in-oil microemulsions *J. Am. Chem. Soc.* 105 2574–9.

235 Hollamby M J, Eastoe J, Chemelli A, Glatter O, Rogers S, Heenan R K and Grillo I 2010 Separation and purification of nanoparticles in a single step *Langmuir* 26 6989–94.

236 Hernandez J, Solla-Gullón J and Herrero E 2004 Gold nanoparticles synthesized in a water-in-oil microemulsion: electrochemical characterization and effect of the surface structure on the oxygen reduction reaction *J. Electroanal. Chem.* 574 185–96.

237 Muralidharan G, Subramanian L, Nallamuthu S K, Santhanam V and Kumar S 2011 Effect of reagent addition rate and temperature on synthesis of gold nanoparticles in microemulsion route *Ind. Eng. Chem. Res.* 50 8786–91.

238 Porta F, Prati L, Rossi M and Scarı` G 2002 Synthesis of Au(0) nanoparticles from W/O microemulsions *Colloids Surf. A Physicochem. Eng. Asp.* 211 43–8.

239 Tianimoghadam S and Salabat A 2018 A microemulsion method for preparation of thiol-functionalized gold nanoparticles *Particuology* 37 33–6.

240 Fustin C-A, Colard C, Filali M, Guillet P, Duwez A-S, Meier M A, Schubert U S and Gohy J-F 2006 Tuning the hydrophilicity of gold nanoparticles templated in star block copolymers *Langmuir* 22 6690–5.

241 Riess G 2003 Micellization of block copolymers *Prog. Polym. Sci.* 28 1107–70.

242 Sakai T and Alexandridis P 2004 Single-step synthesis and stabilization of metal nanoparticles in aqueous pluronic block copolymer solutions at ambient temperature *Langmuir* 20 8426–30.

243 Bakshi M S, Kaura A, Bhandari P, Kaur G, Torigoe K and Esumi K 2006 Synthesis of colloidal gold nanoparticles of different morphologies in the presence of triblock polymer micelles *J. Nanosci. Nanotechnol.* 6 1405–10.

244 Chen S, Guo C, Hu G-H, Wang J, Ma J-H, Liang X-F, Zheng L and Liu H-Z 2006 Effect of hydrophobicity inside PEO- PPO- PEO block copolymer micelles on the stabilization of gold nanoparticles: experiments *Langmuir* 22 9704–11.

245 Khullar P, Mahal A, Singh V, Banipal T S, Kaur G and Bakshi M S 2010 How PEO-PPO-PEO triblock polymer micelles control the synthesis of gold nanoparticles: temperature and hydrophobic effects *Langmuir* 26 11363–71.

246 Liu J, Niu J, Yin L and Jiang F 2011 In situ encapsulation of laccase in nanofibers by electrospinning for development of enzyme biosensors for chlorophenol monitoring *Analyst* 136 4802–8.

247 Ali N and Park S-Y 2008 Micellar structures of poly (styrene-b-4-vinylpyridine) s in THF/toluene mixtures and their functionalization with gold *Langmuir* 24 9279–85.

248 Cuenya B R, Baeck S-H, Jaramillo T F and McFarland E W 2003 Size- and support-dependent electronic and catalytic properties of Au^0/Au^{3+} nanoparticles synthesized from block copolymer micelles *J. Am. Chem. Soc.* 125 12928–34.

249 Li J, Shi L, An Y, Li Y, Chen X and Dong H 2006 Reverse micelles of star-block copolymer as nanoreactors for preparation of gold nanoparticles *Polymer* 47 8480–7.

250 Spatz J P, Mößmer S and Möller M 1996 Mineralization of gold nanoparticles in a block copolymer microemulsion *Chem. Eur. J.* 2 1552–5.

251 Kim D H, Wei A and Won Y-Y 2012 Preparation of super-stable gold nanorods via encapsulation into block copolymer micelles *ACS Appl. Mater. Interfaces* 4 1872–7.

252 Jaramillo T F, Baeck S-H, Cuenya B R and McFarland E W 2003 Catalytic activity of supported Au nanoparticles deposited from block copolymer micelles *J. Am. Chem. Soc.* 125 7148–9.

253 Papp S, Kőrösi L, Gool B, Dederichs T, Mela P, Möller M and Dékány I 2009 Formation of gold nanoparticles in diblock copolymer micelles with various reducing agents: kinetic and thermodynamic studies *J. Therm. Anal. Calorim.* 101 865–72.

254 Goy-López S, Juárez J, Cambón A, Botana J, Pereiro M, Baldomir D, Taboada P and Mosquera V 2010 Block copolymer-regulated synthesis of gold nanocrystals with sharp tips and edges *J. Mater. Chem.* 20 6808–14.

255 Sakai T and Alexandridis P 2005 Mechanism of gold metal ion reduction, nanoparticle growth and size control in aqueous amphiphilic block copolymer solutions at ambient conditions *J. Phys. Chem. B* 109 7766–77.

256 Khullar P, Singh V, Mahal A, Kaur H, Singh V, Banipal T S, Kaur G and Bakshi M S 2011 Tuning the shape and size of gold nanoparticles with triblock polymer micelle structure transitions and environments *J. Phys. Chem. C* 115 10442–54.

257 He P and Urban M W 2005 Phospholipid-stabilized Au–nanoparticles *Biomacromolecules* 6 1224–5.

258 Genç R, Clergeaud G, Ortiz M and O'Sullivan C K 2011 Green synthesis of gold nanoparticles using glycerol-incorporated nanosized liposomes *Langmuir* 27 10894–900.

259 Sau T K, Urban A S, Dondapati S K, Fedoruk M, Horton M R, Rogach A L, Stefani F D, Rädler J O and Feldmann J 2009 Controlling loading and optical properties of gold nanoparticles on liposome membranes *Colloids Surf. A Physicochem. Eng. Asp.* 342 92–6.

260 Li S, Al-Misned F A, El-Serehy H A and Yang L 2021 Green synthesis of gold nanoparticles using aqueous extract of *Mentha Longifolia* leaf and investigation of its anti-human breast carcinoma properties in the in vitro condition *Arab. J. Chem.* 14 102931.

261 Al-Radadi N S 2021 Facile one-step green synthesis of gold nanoparticles (AuNp) using licorice root extract: antimicrobial and anticancer study against HepG2 cell line *Arab. J. Chem.* 14 102956.

262 Vijaya Kumar P, Kala M J S and Prakash K S 2019 Green synthesis of gold nanoparticles using *Croton Caudatus Geisel* leaf extract and their biological studies *Mater. Lett.* 236 19–22.

263 Ahmed R H and Mustafa D E 2020 Green synthesis of silver nanoparticles mediated by traditionally used medicinal plants in Sudan *Int. Nano Lett.* 10 1–14.

264 Arunachalam K D, Annamalai S K, Arunachalam A M and Kennedy S 2013 Green synthesis of crystalline silver nanoparticles using *Indigofera aspalathoides*-medicinal plant extract for wound healing applications *Asian J. Chem.* 25 S311.

265 Lakshmanan G, Sathiyaseelan A, Kalaichelvan P T and Murugesan K 2018 Plant-mediated synthesis of silver nanoparticles using fruit extract of *Cleome viscosa* L.: assessment of their antibacterial and anticancer activity *Karbala Int. J. Mod. Sci.* 4 61–8.

266 Vasquez R D, Apostol J G, De Leon J D, Mariano J D, Mirhan C M C, Pangan S S and Zamora E T 2016 Polysaccharide-mediated green synthesis of silver nanoparticles from *Sargassum siliquosum* JG Agardh: assessment of toxicity and hepatoprotective activity *OpenNano* 1 16–24.

267 Kulkarni A P, Srivastava A A and Zunjarrao R S 2012 Plant mediated synthesis of silver nanoparticles and their applications *Int J Pharm. Bio. Sci* 3 121–7.

268 Chandran S P, Chaudhary M, Pasricha R, Ahmad A and Sastry M 2006 Synthesis of gold nanotriangles and silver nanoparticles using Aloevera plant extract *Biotechnol. Prog.* 22 577–83.

269 Thirumurugan A, Jiflin G J, Rajagomathi G, Tomy N A, Ramachandran S and Jaiganesh R 2010 Biotechnological synthesis of gold nanoparticles of *Azadirachta indica* leaf extract *Int. J. Biol. Technol.* 1 75–7.

270 Keshavarzi M, Davoodi D, Pourseyedi S and Taghizadeh S 2018 The effects of three types of alfalfa plants (Medicago sativa) on the biosynthesis of gold nanoparticles: an insight into phytomining *Gold Bull.* 51 99–110.

271 Rao S V 2011 Picosecond nonlinear optical studies of gold nanoparticles synthesised using coriander leaves (*Coriandrum sativum*) *J. Mod. Opt.* 58 1024–9.

272 Shankar S S, Rai A, Ahmad A and Sastry M 2005 Controlling the optical properties of lemongrass extract synthesized gold nanotriangles and potential application in infrared-absorbing optical coatings *Chem. Mater.* 17 566–72.

273 Ankamwar B 2010 Biosynthesis of gold nanoparticles (green-gold) using leaf extract of *Terminalia catappa E-J. Chem.* 7 1334–9.

274 Elia P, Zach R, Hazan S, Kolusheva S, Porat Z and Zeiri Y 2014 Green synthesis of gold nanoparticles using plant extracts as reducing agents *Int. J. Nanomedicine* 9 4007–21.

275 Thangamani N and Bhuvaneshwari N 2019 Green synthesis of gold nanoparticles using *Simarouba glauca* leaf extract and their biological activity of micro-organism *Chem. Phys. Lett.* 732 136587.

276 Goia D and Matijević E 1999 Tailoring the particle size of monodispersed colloidal gold *Colloids Surf. A Physicochem. Eng. Asp.* 146 139–52.

277 Eskandari-Nojehdehi M, Jafarizadeh-Malmiri H and Jafarizad A 2018 Microwave accelerated green synthesis of gold nanoparticles using gum Arabic and their physico-chemical properties assessments *Z. Für Phys. Chem.* 232 325–43.

278 Jafarizad A, Safaee K and Ekinci D 2017 Green synthesis of gold nanoparticles using aqueous extracts of *Ziziphus Jujuba* and gum arabic *J. Clust. Sci.* 28 2765–77.

279 Shih C-M, Shieh Y-T and Twu Y-K 2009 Preparation of gold nanopowders and nanoparticles using chitosan suspensions *Carbohydr. Polym.* 78 309–15.

280 Valentina Y, Rather M Y and Yogamoorthi A 2019 Biosynthesis of gold nanoparticle using cell-free extract of clinical isolates *Staphylococcus Aureus* and *Escherichia coli Malays. J. Med. Biol. Res.* 6 107–16.

281 Sodaiezade H 2020 Gold bioaccumulation by filamentous soil cyanobacteria isolated from mouteh goldmine (Isfahan Province, Iran) *J. Phycol. Res.* 4 469–80.

282 Patil M P, Kang M, Niyonizigiye I, Singh A, Kim J-O, Seo Y B and Kim G-D 2019 Extracellular synthesis of gold nanoparticles using the marine bacterium *Paracoccus haeundaensis* BC74171T and evaluation of their antioxidant activity and antiproliferative effect on normal and cancer cell lines *Colloids Surf. B Biointerfaces* 183 110455.

283 Abdel-Kareem M M and Zohri A A 2018 Extracellular mycosynthesis of gold nanoparticles using *Trichoderma hamatum*: optimization, characterization and antimicrobial activity *Lett. Appl. Microbiol.* 67 465–75.

284 Camas M, Sazak Camas A and Kyeremeh K 2018 Extracellular synthesis and characterization of gold nanoparticles using *Mycobacterium* sp. BRS2A-AR2 isolated from the aerial roots of the Ghanaian mangrove plant, *Rhizophora racemosa Indian J. Microbiol.* 58 214–21.

285 Khalil A T, Ovais M, Iqbal J, Ali A, Ayaz M, Abbas M, Ahmad I and Devkota H P 2021 Microbes-mediated synthesis strategies of metal nanoparticles and their potential role in cancer therapeutics *Semin. Cancer Biol.* 86 693–705.

286 Syed B, Prasad N M and Satish S 2016 Endogenic mediated synthesis of gold nanoparticles bearing bactericidal activity *J. Microsc. Ultrastruct.* 4 162–6.

287 Molnár Z, Bódai V, Szakacs G, Erdélyi B, Fogarassy Z, Sáfrán G, Varga T, Kónya Z, Tóth-Szeles E, Szűcs R and Lagzi I 2018 Green synthesis of gold nanoparticles by thermophilic filamentous fungi *Sci. Rep.* 8 1–12.

288 Gholami-Shabani M, Shams-Ghahfarokhi M, Gholami-Shabani Z, Akbarzadeh A, Riazi G, Ajdari S, Amani A and Razzaghi-Abyaneh M 2015 Enzymatic synthesis of gold nanoparticles using sulfite reductase purified from *Escherichia coli*: a green eco-friendly approach *Process Biochem.* 50 1076–85.

289 Vágó A, Szakacs G, Sáfrán G, Horvath R, Pécz B and Lagzi I 2016 One-step green synthesis of gold nanoparticles by mesophilic filamentous fungi *Chem. Phys. Lett.* 645 1–4.

290 Du L, Xian L and Feng J-X 2011 Rapid extra-/intracellular biosynthesis of gold nanoparticles by the fungus *Penicillium* sp *J. Nanopart. Res.* 13 921–30.

291 Zhang X, He X, Wang K and Yang X 2011 Different active biomolecules involved in biosynthesis of gold nanoparticles by three fungus species *J. Biomed. Nanotechnol.* 7 245–54.

292 Mukherjee P, Ahmad A, Mandal D, Senapati S, Sainkar S R, Khan M I, Ramani R, Parischa R, Ajayakumar P V, Alam M, Sastry M and Kumar R 2001 Bioreduction of AuCl(4)(−) ions by the fungus, *Verticillium* sp. and surface trapping of the gold nanoparticles Formed D.M. and S.S. thank the Council of Scientific and Industrial Research (CSIR), Government of India, for financial assistance *Angew. Chem. Int. Ed. Engl.* 40 3585–8.

293 Gericke M and Pinches A 2006 Biological synthesis of metal nanoparticles *Hydrometallurgy* 83 132–40.

294 Gericke M and Pinches A 2006 Microbial production of gold nanoparticles *Gold Bull.* 39 22–8.

295 Shankar S S, Ahmad A, Pasricha R and Sastry M 2003 Bioreduction of chloroaurate ions by geranium leaves and its endophytic fungus yields gold nanoparticles of different shapes *J. Mater. Chem.* 13 1822–6.

296 Ahmad A, Senapati S, Khan M I, Kumar R and Sastry M 2005 Extra-/intracellular biosynthesis of gold nanoparticles by an alkalotolerant fungus, *Trichothecium* sp *J. Biomed. Nanotechnol.* 1 47–53.

297 Qu Y, You S, Zhang X, Pei X, Shen W, Li Z, Li S and Zhang Z 2018 Biosynthesis of gold nanoparticles using cell-free extracts of *Magnusiomyces ingens* LH-F1 for nitrophenols reduction *Bioprocess Biosyst. Eng.* 41 359–67.

298 Yaqoob A A, Umar K and Ibrahim M N M 2020 Silver nanoparticles: various methods of synthesis, size affecting factors and their potential applications–a review *Appl. Nanosci.* 10 1369–78.

299 Jung J H, Cheol O H, Soo Noh H, Ji J H and Soo Kim S 2006 Metal nanoparticle generation using a small ceramic heater with a local heating area *J. Aerosol Sci.* 37 1662–70.

300 Raffi M, Rumaiz A K, Hasan M M and Shah S I 2007 Studies of the growth parameters for silver nanoparticle synthesis by inert gas condensation *J. Mater. Res.* 22 3378–84.

301 Harra J, Mäkitalo J, Siikanen R, Virkki M, Genty G, Kobayashi T, Kauranen M and Mäkelä J M 2012 Size-controlled aerosol synthesis of silver nanoparticles for plasmonic materials *J. Nanopart. Res.* 14 870.

302 Fumitaka M, Kohno J, Takeda Y, Kondow T and Sawabe H 2000 Formation and size control of silver nanoparticles by laser ablation in aqueous solution *J. Phys. Chem. B* 104 9111–7.

303 Alhamid M Z, Hadi B S and Khumaeni A 2019 Synthesis of silver nanoparticles using laser ablation method utilizing Nd:YAG laser *AIP Conf. Proc.* 2202 020013.

304 Rafique M, Rafique M S, Kalsoom U, Afzal A, Butt S H and Usman A 2019 Laser ablation synthesis of silver nanoparticles in water and dependence on laser nature *Opt. Quant. Electron.* 51 179.

305 Chen S-F and Zhang H 2012 Aggregation kinetics of nanosilver in different water conditions *Adv. Nat. Sci. Nanosci. Nanotechnol.* 3 035006.

306 Dang T M D, Le T T T, Fribourg-Blanc E and Dang M C 2012 Influence of surfactant on the preparation of silver nanoparticles by polyol method *Adv. Nat. Sci. Nanosci. Nanotechnol.* 3 035004.

307 Patil R S, Kokate M R, Jambhale C L, Pawar S M, Han S H and Kolekar S S 2012 One-pot synthesis of PVA-capped silver nanoparticles their characterization and biomedical application *Adv. Nat. Sci. Nanosci. Nanotechnol.* 3 015013.

308 Dong P, Feng J, Zhang D, Li C, Shi Q and Xie X 2020 In situ synthesis of amply antimicrobial silver nanoparticle (AgNP) by polyzwitterionic copolymers bearing hydroxyl groups *React. Funct. Polym.* 153 104609.

309 Aadil K R, Pandey N, Mussatto S I and Jha H 2019 Green synthesis of silver nanoparticles using acacia lignin, their cytotoxicity, catalytic, metal ion sensing capability and antibacterial activity *J. Environ. Chem. Eng.* 7 103296.

310 Wani I A, Khatoon S, Ganguly A, Ahmed J and Ahmad T 2013 Structural characterization and antimicrobial properties of silver nanoparticles prepared by inverse microemulsion method *Colloids Surf. B Biointerfaces* 101 243–50.

311 Manna A, Imae T, Iida M and Hisamatsu N 2001 Formation of silver nanoparticles from a *N*-hexadecylethylenediamine silver nitrate complex *Langmuir* 17 6000–4.

312 Demchenko V, Riabov S, Sinelnikov S, Radchenko O, Kobylinskyi S and Rybalchenko N 2020 Novel approach to synthesis of silver nanoparticles in interpolyelectrolyte complexes based on pectin, chitosan, starch and their derivatives *Carbohydr. Polym.* 242 116431.

313 Huo H, Li Z, Tan T, Chen L, Ungar G, Hoogenboom R, Zhang Q and Liu F 2021 Asymmetric incorporation of silver nanoparticles in polymeric assemblies by coassembly of tadpole-like nanoparticles and amphiphilic block copolymers *Macromol. Rapid Commun.* 42 2100354.

314 Dong X, Ji X, Wu H, Zhao L, Li J and Yang W 2009 Shape control of silver nanoparticles by stepwise citrate reduction *J. Phys. Chem. C* 113 6573–6.

315 Hebeish A A, El-Rafie M H, Abdel-Mohdy F A, Abdel-Halim E S and Emam H E 2010 Carboxymethyl cellulose for green synthesis and stabilization of silver nanoparticles *Carbohydr. Polym.* 82 933–41.

316 Radziuk D, Skirtach A, Sukhorukov G, Shchukin D and Möhwald H 2007 Stabilization of silver nanoparticles by polyelectrolytes and poly (ethylene glycol) *Macromol. Rapid Commun.* 28 848–55.

317 Pillai Z S and Kamat P V 2004 What factors control the size and shape of silver nanoparticles in the citrate ion reduction method *J. Phys. Chem. B* 108 945–51.

318 Kassaee M Z, Mohammadkhani M, Akhavan A and Mohammadi R 2011 In situ formation of silver nanoparticles in PMMA via reduction of silver ions by butylated hydroxytoluene *Struct. Chem.* 22 11–5.

319 Kainourgios P, Tziveleka L-A, Kartsonakis I A, Ioannou E, Roussis V and Charitidis C A 2021 Silver nanoparticles grown on cross-linked poly (methacrylic acid) microspheres: synthesis, characterization, and antifungal activity evaluation *Chemosensors* 9 152.

320 Alavi M and Rai M 2019 Recent progress in nanoformulations of silver nanoparticles with cellulose, chitosan, and alginic acid biopolymers for antibacterial applications *Appl. Microbiol. Biotechnol.* 103 8669–76.

321 Oliveira M M, Ugarte D, Zanchet D and Zarbin A J G 2005 Influence of synthetic parameters on the size, structure, and stability of dodecanethiol-stabilized silver nanoparticles *J. Colloid Interface Sci.* 292 429–35.

322 Luo C, Zhang Y, Zeng X, Zeng Y and Wang Y 2005 The role of poly(ethylene glycol) in the formation of silver nanoparticles *J. Colloid Interface Sci.* 288 444–8.
323 Hsu S L-C and Wu R-T 2007 Synthesis of contamination-free silver nanoparticle suspensions for micro-interconnects *Mater. Lett.* 61 3719–22.
324 Chen M, Feng Y-G, Wang X, Li T-C, Zhang J-Y and Qian D-J 2007 Silver nanoparticles capped by oleylamine: formation, growth, and self-organization *Langmuir* 23 5296–304.
325 Natsuki J and Abe T 2011 Synthesis of pure colloidal silver nanoparticles with high electroconductivity for printed electronic circuits: the effect of amines on their formation in aqueous media *J. Colloid Interface Sci.* 359 19–23.
326 Natsuki J, Natsuki T and Abe T 2013 Low molecular weight compounds as effective dispersing agents in the formation of colloidal silver nanoparticles *J. Nanopart. Res.* 15 1483.
327 Kim D, Jeong S and Moon J 2006 Synthesis of silver nanoparticles using the polyol process and the influence of precursor injection *Nanotechnology* 17 4019–24.
328 Sun Y, Mayers B and Xia Y 2003 Transformation of silver nanospheres into nanobelts and triangular nanoplates through a thermal process *Nano Lett.* 3 675–9.
329 Im S H, Lee Y T, Wiley B and Xia Y 2005 Large-scale synthesis of silver nanocubes: the role of HCl in promoting cube perfection and monodispersity *Angew. Chem. Int. Ed.* 44 2154–7.
330 Tao A, Sinsermsuksakul P and Yang P 2006 Polyhedral silver nanocrystals with distinct scattering signatures *Angew. Chem. Int. Ed.* 45 4597–601.
331 Wiley B J, Chen Y, McLellan J M, Xiong Y, Li Z-Y, Ginger D and Xia Y 2007 Synthesis and optical properties of silver nanobars and nanorice *Nano Lett.* 7 1032–6.
332 Wiley B J, Im S H, Li Z-Y, McLellan J, Siekkinen A and Xia Y 2006 Maneuvering the surface plasmon resonance of silver nanostructures through shape-controlled synthesis *J. Phys. Chem. B* 110 15666–75.
333 Métraux G S and Mirkin C A 2005 Rapid thermal synthesis of silver nanoprisms with chemically tailorable thickness *Adv. Mater.* 17 412–5.
334 Zaheer Z and Rafiuddin 2011 Multi-branched flower-like silver nanoparticles: preparation and characterization *Colloids Surf. A Physicochem. Eng. Asp.* 384 427–31.
335 Cong F-Z, Wei H, Tian X-R and Xu H-X 2012 A facile synthesis of branched silver nanowire structures and its applications in surface-enhanced Raman scattering *Front. Phys.* 7 521–6.
336 Shchukin D G, Radtchenko I L and Sukhorukov G B 2003 Photoinduced reduction of silver inside microscale polyelectrolyte capsules *ChemPhysChem* 4 1101–3.
337 Jin R, Charles Cao Y, Hao E, Métraux G S, Schatz G C and Mirkin C A 2003 Controlling anisotropic nanoparticle growth through plasmon excitation *Nature* 425 487–90.
338 Malval J-P, Jin M, Balan L, Schneider R, Versace D-L, Chaumeil H, Defoin A and Soppera O 2010 Photoinduced size-controlled generation of silver nanoparticles coated with carboxylate-derivatized thioxanthones *J. Phys. Chem. C* 114 10396–402.
339 Sato-Berrú R, Redón R, Vázquez-Olmos A and Saniger J M 2009 Silver nanoparticles synthesized by direct photoreduction of metal salts. Application in surface-enhanced Raman spectroscopy *J. Raman Spectrosc.* 40 376–80.
340 Kumar Ghosh S, Kundu S, Mandal M, Nath S and Pal T 2003 Studies on the evolution of silver nanoparticles in micelle by UV-photoactivation *J. Nanopart. Res.* 5 577–87.
341 Huang L, Zhai M L, Long D W, Peng J, Xu L, Wu G Z, Li J Q and Wei G S 2008 UV-induced synthesis, characterization and formation mechanism of silver nanoparticles in alkalic carboxymethylated chitosan solution *J. Nanopart. Res.* 10 1193–202.
342 Król-Gracz A, Michalak E, Nowak P M and Dyonizy A 2011 Photo-induced chemical reduction of silver bromide to silver nanoparticles *Cent. Eur. J. Chem.* 9 982–9.

343 Omrani A A and Taghavinia N 2012 Photo-induced growth of silver nanoparticles using UV sensitivity of cellulose fibers *Appl. Surf. Sci.* 258 2373–7.

344 Rosa R M, Silva J C, Sanches I S and Henriques C 2017 Simultaneous photo-induced cross-linking and silver nanoparticle formation in a PVP electrospun wound dressing *Mater. Lett.* 207 145–8.

345 Caillosse E, Zaier M, Mezghani M, Hajjar-Garreau S, Vidal L, Lougnot D and Balan L 2020 Photo-induced self-assembly of silver nanoparticles for rapid generation of first and second surface mirrors *ACS Appl. Nano Mater.* 3 6531–40.

346 Kumar V, Gundampati R K, Singh D K, Bano D, Jagannadham M V and Hasan S H 2016 Photoinduced green synthesis of silver nanoparticles with highly effective antibacterial and hydrogen peroxide sensing properties *J. Photochem. Photobiol. B* 162 374–85.

347 Kumar V, Singh D K, Mohan S, Gundampati R K and Hasan S H 2017 Photoinduced green synthesis of silver nanoparticles using aqueous extract of *Physalis angulata* and its antibacterial and antioxidant activity *J. Environ. Chem. Eng.* 5 744–56.

348 Kumar V, Singh D K, Mohan S and Hasan S H 2016 Photo-induced biosynthesis of silver nanoparticles using aqueous extract of *Erigeron bonariensis* and its catalytic activity against acridine orange *J. Photochem. Photobiol. B* 155 39–50.

349 Liu J, Zhang X, Yu M, Li S and Zhang J 2012 Photoinduced silver nanoparticles/nanorings on plasmid DNA scaffolds *Small* 8 310–6.

350 Kumar V, Gundampati R K, Singh D K, Jagannadham M V, Sundar S and Hasan S H 2016 Photo-induced rapid biosynthesis of silver nanoparticle using aqueous extract of *Xanthium strumarium* and its antibacterial and antileishmanial activity *J. Ind. Eng. Chem.* 37 224–36.

351 Johans C, Clohessy J, Fantini S, Kontturi K and Cunnane V J 2002 Electrosynthesis of polyphenylpyrrole coated silver particles at a liquid–liquid interface *Electrochem. Commun.* 4 227–30.

352 Zhang Y, Chen F, Zhuang J, Tang Y, Wang D, Wang Y, Dong A and Ren N 2002 Synthesis of silver nanoparticles via electrochemical reduction on compact zeolite film modified electrodes *Chem. Commun.* 23 2814–5.

353 Ma H, Yin B, Wang S, Jiao Y, Pan W, Huang S, Chen S and Meng F 2004 Synthesis of silver and gold nanoparticles by a novel electrochemical method *ChemPhysChem* 5 68–75.

354 Starowicz M, Stypuła B and Banaś J 2006 Electrochemical synthesis of silver nanoparticles *Electrochem. Commun.* 8 227–30.

355 Khaydarov R A, Khaydarov R R, Gapurova O, Estrin Y and Scheper T 2009 Electrochemical method for the synthesis of silver nanoparticles *J. Nanopart. Res.* 11 1193–200.

356 Nasretdinova G R, Fazleeva R R, Mukhitova R K, Nizameev I R, Kadirov M K, Ziganshina A Y and Yanilkin V V 2015 Electrochemical synthesis of silver nanoparticles in solution *Electrochem. Commun.* 50 69–72.

357 Kuntyi O I, Kytsya A R, Mertsalo I P, Mazur A S, Zozula G I, Bazylyak L I and Topchak R V 2019 Electrochemical synthesis of silver nanoparticles by reversible current in solutions of sodium polyacrylate *Colloid Polym. Sci.* 297 689–95.

358 Kuntyi O, Mazur A, Kytsya A, Karpenko O, Bazylyak L, Mertsalo I, Pokynbroda T and Prokopalo A 2020 Electrochemical synthesis of silver nanoparticles in solutions of rhamnolipid *Micro Nano Lett.* 15 802–7.

359 Nadagouda M N, Speth T F and Varma R S 2011 Microwave-assisted green synthesis of silver nanostructures *Acc. Chem. Res.* 44 469–78.

360 Anjana V N, Joseph M, Francis S, Joseph A, Koshy E P and Mathew B 2021 Microwave assisted green synthesis of silver nanoparticles for optical, catalytic, biological and electrochemical applications *Artif. Cells Nanomedicine Biotechnol.* 49 438–49.

361 Polshettiwar V, Nadagouda M N and Varma R S 2009 Microwave-assisted chemistry: a rapid and sustainable route to synthesis of organics and nanomaterials *Aust. J. Chem.* 62 16–26.
362 Chen J, Wang J, Zhang X and Jin Y 2008 Microwave-assisted green synthesis of silver nanoparticles by carboxymethyl cellulose sodium and silver nitrate *Mater. Chem. Phys.* 108 421–4.
363 Navaladian S, Viswanathan B, Varadarajan T K and Viswanath R P 2008 Microwave-assisted rapid synthesis of anisotropic Ag nanoparticles by solid state transformation *Nanotechnology* 19 045603.
364 Sreeram K J, Nidhin M and Nair B U 2008 Microwave assisted template synthesis of silver nanoparticles *Bull. Mater. Sci.* 31 937–42.
365 Komarneni S, Li D, Newalkar B, Katsuki H and Bhalla A S 2002 Microwave- polyol process for Pt and Ag nanoparticles *Langmuir* 18 5959–62.
366 Yin H, Yamamoto T, Wada Y and Yanagida S 2004 Large-scale and size-controlled synthesis of silver nanoparticles under microwave irradiation *Mater. Chem. Phys.* 83 66–70.
367 Tsuji M, Matsumoto K, Jiang P, Matsuo R, Hikino S, Tang X-L and Kamarudin K S N 2008 The role of adsorption species in the formation of Ag nanostructures by a microwave-polyol route *Bull. Chem. Soc. Jpn.* 81 393–400.
368 Hu B, Wang S-B, Wang K, Zhang M and Yu S-H 2008 Microwave-assisted rapid facile "green" synthesis of uniform silver nanoparticles: self-assembly into multilayered films and their optical properties *J. Phys. Chem. C* 112 11169–74.
369 Pal A, Shah S and Devi S 2009 Microwave-assisted synthesis of silver nanoparticles using ethanol as a reducing agent *Mater. Chem. Phys.* 114 530–2.
370 Zhao X, Xia Y, Li Q, Ma X, Quan F, Geng C and Han Z 2014 Microwave-assisted synthesis of silver nanoparticles using sodium alginate and their antibacterial activity *Colloids Surf. A Physicochem. Eng. Asp.* 444 180–8.
371 Seku K, Gangapuram B R, Pejjai B, Kadimpati K K and Golla N 2018 Microwave-assisted synthesis of silver nanoparticles and their application in catalytic, antibacterial and antioxidant activities *J. Nanostructure Chem.* 8 179–88.
372 Khan A, El-Toni A M, Alrokayan S, Alsalhi M, Alhoshan M and Aldwayyan A S 2011 Microwave-assisted synthesis of silver nanoparticles using poly-*N*-isopropylacrylamide/acrylic acid microgel particles *Colloids Surf. A Physicochem. Eng. Asp.* 377 356–60.
373 Peng H, Yang A and Xiong J 2013 Green, microwave-assisted synthesis of silver nanoparticles using bamboo hemicelluloses and glucose in an aqueous medium *Carbohydr. Polym.* 91 348–55.
374 Adhikari L, Larm N E, Bhawawet N and Baker G A 2018 Rapid microwave-assisted synthesis of silver nanoparticles in a Halide-free deep eutectic solvent *ACS Sustain. Chem. Eng.* 6 5725–31.
375 Dzido G, Markowski P, Małachowska-Jutsz A, Prusik K and Jarzębski A B 2015 Rapid continuous microwave-assisted synthesis of silver nanoparticles to achieve very high productivity and full yield: from mechanistic study to optimal fabrication strategy *J. Nanopart. Res.* 17 27.
376 Barani H and Mahltig B 2022 Microwave-assisted synthesis of silver nanoparticles: effect of reaction temperature and precursor concentration on fluorescent property *J. Clust. Sci.* 33 101–11.
377 Kumar A, Vemula P K, Ajayan P M and John G 2008 Silver-nanoparticle-embedded antimicrobial paints based on vegetable oil *Nat. Mater.* 7 236–41.
378 Fayaz A M, Balaji K, Girilal M, Yadav R, Kalaichelvan P T and Venketesan R 2010 Biogenic synthesis of silver nanoparticles and their synergistic effect with antibiotics: a study against gram-positive and gram-negative bacteria *Nanomed. Nanotechnol. Biol. Med.* 6 103–9.

379 Ahmed S and Ikram S 2015 Silver nanoparticles: one pot green synthesis using *Terminalia arjuna* extract for biological application *J Nanomed Nanotechnol* 6 1–6.

380 Abou El-Nour K M, Eftaiha A, Al-Warthan A and Ammar R A 2010 Synthesis and applications of silver nanoparticles *Arab. J. Chem.* 3 135–40.

381 Lee S H and Jun B-H 2019 Silver nanoparticles: synthesis and application for nanomedicine *Int. J. Mol. Sci.* 20 865.

382 Klaus-Joerger T, Joerger R, Olsson E and Granqvist C-G 2001 Bacteria as workers in the living factory: metal-accumulating bacteria and their potential for materials science *Trends Biotechnol.* 19 15–20.

383 Arokiyaraj S, Vincent S, Saravanan M, Lee Y, Oh Y K and Kim K H 2017 Green synthesis of silver nanoparticles using *Rheum palmatum* root extract and their antibacterial activity against *Staphylococcus aureus* and *Pseudomonas aeruginosa Artif. Cells Nanomedicine Biotechnol.* 45 372–9.

384 Patra S, Mukherjee S, Barui A K, Ganguly A, Sreedhar B and Patra C R 2015 Green synthesis, characterization of gold and silver nanoparticles and their potential application for cancer therapeutics *Mater. Sci. Eng. C* 53 298–309.

385 Slawson R M, Trevors J T and Lee H 1992 Silver accumulation and resistance in *Pseudomonas stutzeri Arch. Microbiol.* 158 398–404.

386 Klaus T, Joerger R, Olsson E and Granqvist C-G 1999 Silver-based crystalline nanoparticles, microbially fabricated *Proc. Natl. Acad. Sci.* 96 13611–4.

387 Pugazhenthiran N, Anandan S, Kathiravan G, Udaya Prakash N K, Crawford S and Ashokkumar M 2009 Microbial synthesis of silver nanoparticles by *Bacillus* sp *J. Nanopart. Res.* 11 1811.

388 Tsibakhashvili N Y, Kirkesali E I, Pataraya D T, Gurielidze M A, Kalabegishvili T L, Gvarjaladze D N, Tsertsvadze G I, Frontasyeva M V, Zinicovscaia I I, Wakstein M S, Khakhanov S N, Shvindina N V and Shklover V Y 2011 Microbial synthesis of silver nanoparticles by *Streptomyces glaucus* and *Spirulina platensis Adv. Sci. Lett.* 4 3408–17.

389 El-Shanshoury A, E-R R, ElSilk S E and Ebeid M E 2011 Extracellular biosynthesis of silver nanoparticles using *Escherichia coli* ATCC 8739, *Bacillus subtilis* ATCC 6633, and *Streptococcus thermophilus* ESh1 and their antimicrobial activities *ISRN Nanotechnol.* 2011 1–7.

390 Shahverdi A R, Minaeian S, Shahverdi H R, Jamalifar H and Nohi A-A 2007 Rapid synthesis of silver nanoparticles using culture supernatants of Enterobacteria: a novel biological approach *Process Biochem.* 42 919–23.

391 Saravanan M, Vemu A K and Barik S K 2011 Rapid biosynthesis of silver nanoparticles from *Bacillus megaterium* (NCIM 2326) and their antibacterial activity on multi drug resistant clinical pathogens *Colloids Surf. B Biointerfaces* 88 325–31.

392 Priyadarshini S, Gopinath V, Priyadharsshini N M, MubarakAli D and Velusamy P 2013 Synthesis of anisotropic silver nanoparticles using novel strain, *Bacillus flexus* and its biomedical application *Colloids Surf. B Biointerfaces* 102 232–7.

393 Samadi N, Golkaran D, Eslamifar A, Jamalifar H, Fazeli M R and Mohseni F A 2009 Intra/extracellular biosynthesis of silver nanoparticles by an autochthonous strain of *Proteus mirabilis* isolated from photographic waste *J. Biomed. Nanotechnol.* 5 247–53.

394 Das V L, Thomas R, Varghese R T, Soniya E V, Mathew J and Radhakrishnan E K 2014 Extracellular synthesis of silver nanoparticles by the Bacillus strain CS 11 isolated from industrialized area *3 Biotech* 4 121–6.

395 Ibrahim S, Ahmad Z, Manzoor M Z, Mujahid M, Faheem Z and Adnan A 2021 Optimization for biogenic microbial synthesis of silver nanoparticles through response surface methodology, characterization, their antimicrobial, antioxidant, and catalytic potential *Sci. Rep.* 11 770.

396 Sastry M, Ahmad A, Islam Khan M and Kumar R 2003 Biosynthesis of metal nanoparticles using fungi and actinomycete *Curr. Sci.* 85 162–70.

397 Mandal D, Bolander M E, Mukhopadhyay D, Sarkar G and Mukherjee P 2006 The use of microorganisms for the formation of metal nanoparticles and their application *Appl. Microbiol. Biotechnol.* 69 485–92.

398 Mukherjee P, Ahmad A, Mandal D, Senapati S, Sainkar S R, Khan M I, Parishcha R, Ajaykumar P V, Alam M and Kumar R 2001 Fungus-mediated synthesis of silver nanoparticles and their immobilization in the mycelial matrix: a novel biological approach to nanoparticle synthesis *Nano Lett.* 1 515–9.

399 Bhainsa K C and D'souza S F 2006 Extracellular biosynthesis of silver nanoparticles using the fungus *Aspergillus fumigatus Colloids Surf. B Biointerfaces* 47 160–4.

400 Naqvi S Z H, Kiran U, Ali M I, Jamal A, Hameed A, Ahmed S and Ali N 2013 Combined efficacy of biologically synthesized silver nanoparticles and different antibiotics against multidrug-resistant bacteria *Int. J. Nanomedicine* 8 3187.

401 Ingle A, Rai M, Gade A and Bawaskar M 2009 *Fusarium solani*: a novel biological agent for the extracellular synthesis of silver nanoparticles *J. Nanopart. Res.* 11 2079.

402 Syed A, Saraswati S, Kundu G C and Ahmad A 2013 Biological synthesis of silver nanoparticles using the fungus *Humicola* sp. and evaluation of their cytoxicity using normal and cancer cell lines *Spectrochim. Acta - Part Mol. Biomol. Spectrosc.* 114 144–7.

403 Owaid M N, Raman J, Lakshmanan H, Al-Saeedi S S S, Sabaratnam V and Abed I A 2015 Mycosynthesis of silver nanoparticles by *Pleurotus cornucopiae* var. citrinopileatus and its inhibitory effects against Candida sp *Mater. Lett.* 153 186–90.

404 Al-Bahrani R, Raman J, Lakshmanan H, Hassan A A and Sabaratnam V 2017 Green synthesis of silver nanoparticles using tree oyster mushroom *Pleurotus ostreatus* and its inhibitory activity against pathogenic bacteria *Mater. Lett.* 186 21–5.

405 Vigneshwaran N, Ashtaputre N M, Varadarajan P V, Nachane R P, Paralikar K M and Balasubramanya R H 2007 Biological synthesis of silver nanoparticles using the fungus *Aspergillus flavus Mater. Lett.* 61 1413–8.

406 Mohammed Fayaz A, Balaji K, Kalaichelvan P T and Venkatesan R 2009 Fungal based synthesis of silver nanoparticles – an effect of temperature on the size of particles *Colloids Surf. B Biointerfaces* 74 123–6.

407 Feroze N, Arshad B, Younas M, Afridi M I, Saqib S and Ayaz A 2020 Fungal mediated synthesis of silver nanoparticles and evaluation of antibacterial activity *Microsc. Res. Tech.* 83 72–80.

408 Gudikandula K, Vadapally P and Singara Charya M A 2017 Biogenic synthesis of silver nanoparticles from white rot fungi: their characterization and antibacterial studies *OpenNano* 2 64–78.

409 Tyagi S, Tyagi P K, Gola D, Chauhan N and Bharti R K 2019 Extracellular synthesis of silver nanoparticles using entomopathogenic fungus: characterization and antibacterial potential *SN Appl. Sci.* 1 1545.

410 Elegbede J A, Lateef A, Azeez M A, Asafa T B, Yekeen T A, Oladipo I C, Adebayo E A, Beukes L S and Gueguim-Kana E B 2018 Fungal xylanases-mediated synthesis of silver nanoparticles for catalytic and biomedical applications *IET Nanobiotechnol.* 12 857–63.

411 Alavi M 2022 Bacteria and fungi as major bio-sources to fabricate silver nanoparticles with antibacterial activities *Expert Rev. Anti-Infect. Ther.* 20 897–906.

412 Apte M, Sambre D, Gaikawad S, Joshi S, Bankar A, Kumar A R and Zinjarde S 2013 Psychrotrophic yeast *Yarrowia lipolytica* NCYC 789 mediates the synthesis of antimicrobial silver nanoparticles via cell-associated melanin *AMB Express* 3 32.

413 Mourato A, Gadanho M, Lino A R and Tenreiro R 2011 Biosynthesis of crystalline silver and gold nanoparticles by extremophilic yeasts *Bioinorg. Chem. Appl.* 2011 546074.

414 Abdeen S, Geo S, Sukanya S, Praseetha P K and Dhanya R P 2014 Biosynthesis of silver nanoparticles from actinomycetes for therapeutic applications *Int. J. Nano Dimens.* 5 155–62.

415 Karthik L, Kumar G, Kirthi A V, Rahuman A A and Rao K B 2014 *Streptomyces* sp. LK3 mediated synthesis of silver nanoparticles and its biomedical application *Bioprocess Biosyst. Eng.* 37 261–7.

416 Golinska P, Wypij M, Ingle A P, Gupta I, Dahm H and Rai M 2014 Biogenic synthesis of metal nanoparticles from actinomycetes: biomedical applications and cytotoxicity *Appl. Microbiol. Biotechnol.* 98 8083–97.

417 Balagurunathan R, Radhakrishnan M, Rajendran R B and Velmurugan D 2011 Biosynthesis of gold nanoparticles by actinomycete Streptomyces viridogens strain HM10 *Indian J. Biochem. Biophys.* 48 331–5.

418 Chauhan R, Kumar A and Abraham J 2013 A biological approach to the synthesis of silver nanoparticles with *Streptomyces* sp JAR1 and its antimicrobial activity *Sci. Pharm.* 81 607.

419 Sukanya M K, Saju K A, Praseetha P K and Sakthivel G 2013 Therapeutic potential of biologically reduced silver nanoparticles from actinomycete cultures *J. Nanosci.* 2013 940719.

420 Prakasham R S, Buddana S K, Yannam S K and Guntuku G S 2012 Characterization of silver nanoparticles synthesized by using marine isolate *Streptomyces albidoflavus J. Microbiol. Biotechnol.* 22 614–21.

421 Salem S S, EL-Belely E F, Niedbała G, Alnoman M M, Hassan S E-D, Eid A M, Shaheen T I, Elkelish A and Fouda A 2020 Bactericidal and in-vitro cytotoxic efficacy of silver nanoparticles (Ag-NPs) fabricated by endophytic actinomycetes and their use as coating for the textile fabrics *Nanomaterials* 10 2082.

422 Hamed A A, Kabary H, Khedr M and Emam A N 2020 Antibiofilm, antimicrobial and cytotoxic activity of extracellular green-synthesized silver nanoparticles by two marine-derived actinomycete *RSC Adv.* 10 10361–7.

423 Sowani H, Mohite P, Munot H, Shouche Y, Bapat T, Kumar A R, Kulkarni M and Zinjarde S 2016 Green synthesis of gold and silver nanoparticles by an actinomycete *Gordonia amicalis* HS-11: mechanistic aspects and biological application *Process Biochem.* 51 374–83.

424 Subbaiya R, Saravanan M, Priya A R, Shankar K R, Selvam M, Ovais M, Balajee R and Barabadi H 2017 Biomimetic synthesis of silver nanoparticles from *Streptomyces atrovirens* and their potential anticancer activity against human breast cancer cells *IET Nanobiotechnol.* 11 965–72.

425 Abd-Elnaby H M, Abo-Elala G M, Abdel-Raouf U M and Hamed M M 2016 Antibacterial and anticancer activity of extracellular synthesized silver nanoparticles from marine *Streptomyces rochei* MHM13 *Egypt. J. Aquat. Res.* 42 301–12.

426 Mabrouk M, Elkhooly T A and Amer S K 2021 Actinomycete strain type determines the monodispersity and antibacterial properties of biogenically synthesized silver nanoparticles *J. Genet. Eng. Biotechnol.* 19 57.

427 Khan I, Anburajan P, Kumar G, Yoon J-J, Bahuguna A, de Moura A G L, Pugazhendhi A, Kim S-H and Kang S-C 2021 Comparative effect of silver nanoparticles (AgNPs) derived from actinomycetes and henna on biohydrogen production by *Clostridium beijerinckii* (KTCC1737) *Int. J. Energy Res.* 45 17269–78.

428 Xie J, Lee J Y, Wang D I and Ting Y P 2007 Silver nanoplates: from biological to biomimetic synthesis *ACS Nano* 1 429–39.

429 Kathiraven T, Sundaramanickam A, Shanmugam N and Balasubramanian T 2015 Green synthesis of silver nanoparticles using marine algae *Caulerpa racemosa* and their antibacterial activity against some human pathogens *Appl. Nanosci.* 5 499–504.

430 Govindaraju K, Kiruthiga V, Kumar V G and Singaravelu G 2009 Extracellular synthesis of silver nanoparticles by a marine alga, Sargassum wightii Grevilli and their antibacterial effects *J. Nanosci. Nanotechnol.* 9 5497–501.

431 Castro L, Blázquez M L, Muñoz J A, González F and Ballester A 2013 Biological synthesis of metallic nanoparticles using algae *IET Nanobiotechnol.* 7 109–16.

432 Prasad T N V K V, Kambala V S R and Naidu R 2013 Phyconanotechnology: synthesis of silver nanoparticles using brown marine algae *Cystophora moniliformis* and their characterisation *J. Appl. Phycol.* 25 177–82.

433 Sinha S N, Paul D, Halder N, Sengupta D and Patra S K 2015 Green synthesis of silver nanoparticles using fresh water green alga *Pithophora oedogonia* (Mont.) Wittrock and evaluation of their antibacterial activity *Appl. Nanosci.* 5 703–9.

434 Arya A, Mishra V and Chundawat T S 2019 Green synthesis of silver nanoparticles from green algae (*Botryococcus braunii*) and its catalytic behavior for the synthesis of benzimidazoles *Chem. Data Collect.* 20 100190.

435 Chugh D, Viswamalya V S and Das B 2021 Green synthesis of silver nanoparticles with algae and the importance of capping agents in the process *J. Genet. Eng. Biotechnol.* 19 126.

436 Aboelfetoh E F, El-Shenody R A and Ghobara M M 2017 Eco-friendly synthesis of silver nanoparticles using green algae (*Caulerpa serrulata*): reaction optimization, catalytic and antibacterial activities *Environ. Monit. Assess.* 189 349.

437 Acharya D, Satapathy S, Thathapudi J J, Somu P and Mishra G 2022 Biogenic synthesis of silver nanoparticles using marine algae *Cladophora glomerata* and evaluation of apoptotic effects in human colon cancer cells *Mater. Technol.* 37 569–80.

438 Danaei M, Motaghi M M, Naghmachi M, Amirmahani F and Moravej R 2021 Green synthesis of silver nanoparticles (AgNPs) by filamentous algae extract: comprehensive evaluation of antimicrobial and anti-biofilm effects against nosocomial pathogens *Biologia (Bratisl.)* 76 3057–69.

439 Durán N, Marcato P D, Alves O L, De Souza G I H and Esposito E 2005 Mechanistic aspects of biosynthesis of silver nanoparticles by several *Fusarium oxysporum* strains *J Nanobiotechnol* 3 1–7.

440 Mukherjee P, Roy M, Mandal B P, Dey G K, Mukherjee P K, Ghatak J, Tyagi A K and Kale S P 2008 Green synthesis of highly stabilized nanocrystalline silver particles by a non-pathogenic and agriculturally important fungus *T. asperellum Nanotechnology* 19 75103.

441 Ahmad A, Mukherjee P, Senapati S, Mandal D, Khan M I, Kumar R and Sastry M 2003 Extracellular biosynthesis of silver nanoparticles using the fungus *Fusarium oxysporum Colloids Surf. B Biointerfaces* 28 313–8.

442 Korbekandi H, Ashari Z, Iravani S and Abbasi S 2013 Optimization of biological synthesis of silver nanoparticles using *Fusarium oxysporum Iran. J. Pharm. Res. IJPR* 12 289.

443 Roopan S M, Madhumitha G, Rahuman A A, Kamaraj C, Bharathi A and Surendra T V 2013 Low-cost and eco-friendly phyto-synthesis of silver nanoparticles using *Cocos nucifera* coir extract and its larvicidal activity *Ind. Crop. Prod.* 43 631–5.

444 Mukunthan K S, Elumalai E K, Patel T N and Murty V R 2011 *Catharanthus roseus*: a natural source for the synthesis of silver nanoparticles *Asian Pac. J. Trop. Biomed.* 1 270.

445 Shukla V K, Singh R P and Pandey A C 2010 Black pepper assisted biomimetic synthesis of silver nanoparticles *J. Alloys Compd.* 507 L13–6.

446 Mondal N K, Chowdhury A, Dey U, Mukhopadhya P, Chatterjee S, Das K and Datta J K 2014 Green synthesis of silver nanoparticles and its application for mosquito control *Asian Pac. J. Trop. Dis.* 4 S204–10.

447 Anuj S A and Ishnava K B 2013 Plant mediated synthesis of silver nanoparticles by using dried stem powder of *Tinospora cordifolia*, its antibacterial activity and comparison with antibiotics *Int J Pharm. Bio. Sci* 4 849–63.

448 Gardea-Torresdey J L, Gomez E, Peralta-Videa J R, Parsons J G, Troiani H and Jose-Yacaman M 2003 *Alfalfa sprouts*: a natural source for the synthesis of silver nanoparticles *Langmuir* 19 1357–61.

449 Shankar S S, Ahmad A and Sastry M 2003 Geranium leaf assisted biosynthesis of silver nanoparticles *Biotechnol. Prog.* 19 1627–31.

450 Li S, Shen Y, Xie A, Yu X, Qiu L, Zhang L and Zhang Q 2007 Green synthesis of silver nanoparticles using *Capsicum annuum* L. extract *Green Chem.* 9 852–8.

451 Kasthuri J, Veerapandian S and Rajendiran N 2009 Biological synthesis of silver and gold nanoparticles using apiin as reducing agent *Colloids Surf. B Biointerfaces* 68 55–60.

452 Dwivedi A D and Gopal K 2010 Biosynthesis of silver and gold nanoparticles using *Chenopodium album* leaf extract *Colloids Surf. A Physicochem. Eng. Asp.* 369 27–33.

453 Küp F Ö, Çoşkunçay S and Duman F 2020 Biosynthesis of silver nanoparticles using leaf extract of *Aesculus hippocastanum* (horse chestnut): evaluation of their antibacterial, antioxidant and drug release system activities *Mater. Sci. Eng. C* 107 110207.

454 Vinodhini S, Vithiya B S M and Prasad T A A 2022 Green synthesis of silver nanoparticles by employing the *Allium fistulosum*, *Tabernaemontana divaricate* and *Basella alba* leaf extracts for antimicrobial applications *J. King Saud Univ. - Sci.* 34 101939.

455 Loo Y Y, Chieng B W, Nishibuchi M and Radu S 2012 Synthesis of silver nanoparticles by using tea leaf extract from *Camellia sinensis Int. J. Nanomedicine* 7 4263–7.

456 Krishnaraj C, Jagan E G, Rajasekar S, Selvakumar P, Kalaichelvan P T and Mohan N 2010 Synthesis of silver nanoparticles using *Acalypha indica* leaf extracts and its antibacterial activity against water borne pathogens *Colloids Surf. B Biointerfaces* 76 50–6.

457 Ahmed M J, Murtaza G, Mehmood A and Bhatti T M 2015 Green synthesis of silver nanoparticles using leaves extract of *Skimmia laureola*: characterization and antibacterial activity *Mater. Lett.* 153 10–3.

458 Sathyavathi R, Krishna M B, Rao S V, Saritha R and Rao D N 2010 Biosynthesis of silver nanoparticles using *Coriandrum sativum* leaf extract and their application in nonlinear optics *Adv. Sci. Lett.* 3 138–43.

459 Veerasamy R, Xin T Z, Gunasagaran S, Xiang T F W, Yang E F C, Jeyakumar N and Dhanaraj S A 2011 Biosynthesis of silver nanoparticles using mangosteen leaf extract and evaluation of their antimicrobial activities *J. Saudi Chem. Soc.* 15 113–20.

460 Yasir M, Singh J, Tripathi M K, Singh P and Shrivastava R 2017 Green synthesis of silver nanoparticles using leaf extract of common arrowhead houseplant and its anticandidal activity *Pharmacogn. Mag.* 13 S840–4.

461 Kumar V, Singh S, Srivastava B, Bhadouria R and Singh R 2019 Green synthesis of silver nanoparticles using leaf extract of *Holoptelea integrifolia* and preliminary investigation of its antioxidant, anti-inflammatory, antidiabetic and antibacterial activities *J. Environ. Chem. Eng.* 7 103094.

462 Singh R, Hano C, Nath G and Sharma B 2021 Green biosynthesis of silver nanoparticles using leaf extract of *Carissa carandas* L. and their antioxidant and antimicrobial activity against human pathogenic bacteria *Biomolecules* 11 299.

463 Azmi S N H, Al-Jassasi B M H, Al-Sawafi H M S, Al-Shukaili S H G, Rahman N and Nasir M 2021 Optimization for synthesis of silver nanoparticles through response surface methodology using leaf extract of *Boswellia sacra* and its application in antimicrobial activity *Environ. Monit. Assess.* 193 497.

464 Yassin M T, Mostafa A A-F, Al-Askar A A and Al-Otibi F O 2022 Facile green synthesis of silver nanoparticles using aqueous leaf extract of *Origanum majorana* with potential bioactivity against multidrug resistant bacterial strains *Crystals* 12 603.

465 Das S, Das J, Samadder A, Bhattacharyya S S, Das D and Khuda-Bukhsh A R 2013 Biosynthesized silver nanoparticles by ethanolic extracts of *Phytolacca decandra*, *Gelsemium sempervirens*, *Hydrastis canadensis* and *Thuja occidentalis* induce differential cytotoxicity through G2/M arrest in A375 cells *Colloids Surf. B Biointerfaces* 101 325–36.

466 Roy K, Sarkar C K and Ghosh C K 2014 Green synthesis of silver nanoparticles using fruit extract of *Malus domestica* and study of its antimicrobial activity *Dig. J. Nanomater. Biostruct.* 9 1137–47.

467 Gogoi N, Babu P J, Mahanta C and Bora U 2015 Green synthesis and characterization of silver nanoparticles using alcoholic flower extract of *Nyctanthes arbortristis* and in vitro investigation of their antibacterial and cytotoxic activities *Mater. Sci. Eng. C* 46 463–9.

468 Pattanayak S, Mollick M M R, Maity D, Chakraborty S, Dash S K, Chattopadhyay S, Roy S, Chattopadhyay D and Chakraborty M 2017 Butea monosperma bark extract mediated green synthesis of silver nanoparticles: characterization and biomedical applications *J. Saudi Chem. Soc.* 21 673–84.

469 Omran B A, Nassar H N, Fatthallah N A, Hamdy A, El-Shatoury E H and Sh E-G N 2018 Waste upcycling of *Citrus sinensis* peels as a green route for the synthesis of silver nanoparticles *Energy Sources Part Recovery Util. Environ. Eff.* 40 227–36.

470 Rolim W R, Pelegrino M T, de Araújo L B, Ferraz L S, Costa F N, Bernardes J S, Rodigues T, Brocchi M and Seabra A B 2019 Green tea extract mediated biogenic synthesis of silver nanoparticles: characterization, cytotoxicity evaluation and antibacterial activity *Appl. Surf. Sci.* 463 66–74.

471 Hasnain M S, Javed M N, Alam M S, Rishishwar P, Rishishwar S, Ali S, Nayak A K and Beg S 2019 Purple heart plant leaves extract-mediated silver nanoparticle synthesis: optimization by Box-Behnken design *Mater. Sci. Eng. C* 99 1105–14.

472 Dakshayani S S, Marulasiddeshwara M B, Kumar M N S, Golla R, Kumar P R, Devaraja S and Hosamani R 2019 Antimicrobial, anticoagulant and antiplatelet activities of green synthesized silver nanoparticles using Selaginella (Sanjeevini) plant extract *Int. J. Biol. Macromol.* 131 787–97.

473 Khabeeri O M, Al-Thabaiti S A and Khan Z 2020 *Citrus sinensis* peel waste assisted synthesis of AgNPs: effect of surfactant on the nucleation and morphology *SN Appl. Sci.* 2 2038.

474 Alsakhawy S A, Baghdadi H H, El-Shenawy M A and El-Hosseiny L S 2022 Antibacterial activity of silver nanoparticles phytosynthesized by citrus fruit peel extracts *BioNanoScience* 12 1106–15.

475 Manik U P, Nande A, Raut S and Dhoble S J 2020 Green synthesis of silver nanoparticles using plant leaf extraction of *Artocarpus heterophylus* and *Azadirachta indica Results Mater.* 6 100086.

476 Alharbi N S, Alsubhi N S and Felimban A I 2022 Green synthesis of silver nanoparticles using medicinal plants: characterization and application *J. Radiat. Res. Appl. Sci.* 15 109–24.

477 Aisida S O, Ugwu K, Akpa P A, Nwanya A C, Ejikeme P M, Botha S, Ahmad I, Maaza M and Ezema F I 2019 Biogenic synthesis and antibacterial activity of controlled silver nanoparticles using an extract of *Gongronema Latifolium Mater. Chem. Phys.* 237 121859.

478 Raghavendra G M, Jung J and Seo J 2016 Step-reduced synthesis of starch-silver nanoparticles *Int. J. Biol. Macromol.* 86 126–8.

479 Jung J, Raghavendra G M, Kim D and Seo J 2018 One-step synthesis of starch-silver nanoparticle solution and its application to antibacterial paper coating *Int. J. Biol. Macromol.* 107 2285–90.

480 Vanamudan A and Sudhakar P P 2016 Biopolymer capped silver nanoparticles with potential for multifaceted applications *Int. J. Biol. Macromol.* 86 262–8.

481 Maryan A S and Gorji M 2016 Synthesize of nano silver using cellulose or glucose as a reduction agent: the study of their antibacterial activity on polyurethan fibers *Bulg. Chem. Commun.* 47 151–5.

482 Chen G, Yan L, Wan X, Zhang Q and Wang Q 2019 In situ synthesis of silver nanoparticles on cellulose fibers using D-glucuronic acid and its antibacterial application *Materials* 12 3101.

483 Hong P, Liu Y, Peng W, Zhang J and Ruan R 2016 Green synthesis and stability evaluation of Ag nanoparticles using bamboo hemicellulose *Bioresources* 11 385–99.

484 Amin M, Iram F, Iqbal M S, Saeed M Z, Raza M and Alam S 2013 Arabinoxylan-mediated synthesis of gold and silver nanoparticles having exceptional high stability *Carbohydr. Polym.* 92 1896–900.

485 Hu S and Hsieh Y-L 2016 Silver nanoparticle synthesis using lignin as reducing and capping agents: a kinetic and mechanistic study *Int. J. Biol. Macromol.* 82 856–62.

486 Zhi J, Wang Y, Lu Y, Ma J and Luo G 2006 In situ preparation of magnetic chitosan/Fe_3O_4 composite nanoparticles in tiny pools of water-in-oil microemulsion *React. Funct. Polym.* 66 1552–8.

487 Loo A L, Pineda M G, Saade H, Treviño M E and López R G 2008 Synthesis of magnetic nanoparticles in bicontinuous microemulsions. Effect of surfactant concentration *J. Mater. Sci.* 43 3649–54.

488 Foroughi F, Hassanzadeh-Tabrizi S A and Amighian J 2015 Microemulsion synthesis and magnetic properties of hydroxyapatite-encapsulated nano $CoFe_2O_4$ *J. Magn. Magn. Mater.* 382 182–7.

489 Wang X, Zhang P, Gao J, Chen X and Yang H 2015 Facile synthesis and magnetic properties of Fe_3C/C nanoparticles via a sol–gel process *Dyes Pigments* 112 305–10.

490 Alagiri M, Ponnusamy S and Muthamizhchelvan C 2012 Synthesis and characterization of NiO nanoparticles by sol–gel method *J. Mater. Sci. Mater. Electron.* 23 728–32.

491 Atrak K, Ramazani A and Taghavi Fardood S 2018 A novel sol–gel synthesis and characterization of $MgFe_2O_4$@γ–Al_2O_3 magnetic nanoparticles using tragacanth gel and its application as a magnetically separable photocatalyst for degradation of organic dyes under visible light *J. Mater. Sci. Mater. Electron.* 29 6702–10.

492 Chen R, Wang W, Zhao X, Zhang Y, Wu S and Li F 2014 Rapid hydrothermal synthesis of magnetic $Co_xNi_{1-x}Fe_2O_4$ nanoparticles and their application on removal of Congo red *Chem. Eng. J.* 242 226–33.

493 Peng J, Hojamberdiev M, Xu Y, Cao B, Wang J and Wu H 2011 Hydrothermal synthesis and magnetic properties of gadolinium-doped $CoFe_2O_4$ nanoparticles *J. Magn. Magn. Mater.* 323 133–7.

494 Sun J, Zhou S, Hou P, Yang Y, Weng J, Li X and Li M 2007 Synthesis and characterization of biocompatible Fe_3O_4 nanoparticles *J. Biomed. Mater. Res. A* 80A 333–41.

495 Massart R and Cabuil V 1987 Effect of some parameters on the formation of colloidal magnetite in alkaline-medium-yield and particle-size control *J. Chim. Phys. Phys.-Chim. Biol.* 84 967–73.

496 Wu W, He Q and Jiang C 2008 Magnetic iron oxide nanoparticles: synthesis and surface functionalization strategies *Nanoscale Res. Lett.* 3 397.

497 Majidi S, Zeinali Sehrig F, Farkhani S M, Soleymani Goloujeh M and Akbarzadeh A 2016 Current methods for synthesis of magnetic nanoparticles *Artif. Cells Nanomedicine Biotechnol.* 44 722–34.

498 Iida H, Takayanagi K, Nakanishi T and Osaka T 2007 Synthesis of Fe_3O_4 nanoparticles with various sizes and magnetic properties by controlled hydrolysis *J. Colloid Interface Sci.* 314 274–80.

499 Refait P and Génin J-M R 1993 The oxidation of ferrous hydroxide in chloride-containing aqueous media and pourbaix diagrams of green rust one *Corros. Sci.* 34 797–819.

500 Olowe A A and Génin J M R 1991 The mechanism of oxidation of ferrous hydroxide in sulphated aqueous media: importance of the initial ratio of the reactants *Corros. Sci.* 32 965–84.

501 Kang Y S, Risbud S, Rabolt J F and Stroeve P 1996 Synthesis and characterization of nanometer-size Fe_3O_4 and γ-Fe_2O_3 particles *Chem. Mater.* 8 2209–11.

502 Feltin N and Pileni M P 1997 New technique for synthesizing iron ferrite magnetic nanosized particles *Langmuir* 13 3927–33.

503 López Pérez J A, López Quintela M A, Mira J, Rivas J and Charles S W 1997 Advances in the preparation of magnetic nanoparticles by the microemulsion method *J. Phys. Chem. B* 101 8045–7.

504 Okoli C, Boutonnet M, Mariey L, Järås S and Rajarao G 2011 Application of magnetic iron oxide nanoparticles prepared from microemulsions for protein purification *J. Chem. Technol. Biotechnol.* 86 1386–93.

505 Lakshmanan R, Okoli C, Boutonnet M, Järås S and Rajarao G K 2014 Microemulsion prepared magnetic nanoparticles for phosphate removal: time efficient studies *J. Environ. Chem. Eng.* 2 185–9.

506 Vidal-Vidal J, Rivas J and López-Quintela M A 2006 Synthesis of monodisperse maghemite nanoparticles by the microemulsion method *Colloids Surf. A Physicochem. Eng. Asp.* 288 44–51.

507 Vestal C R and Zhang Z J 2002 Synthesis of $CoCrFeO_4$ nanoparticles using microemulsion methods and size-dependent studies of their magnetic properties *Chem. Mater.* 14 3817–22.

508 Santra S, Tapec R, Theodoropoulou N, Dobson J, Hebard A and Tan W 2001 Synthesis and characterization of silica-coated iron oxide nanoparticles in microemulsion: the effect of nonionic surfactants *Langmuir* 17 2900–6.

509 Najafi A and Nematipour K 2017 Synthesis and magnetic properties evaluation of monosized FeCo alloy nanoparticles through microemulsion method *J. Supercond. Nov. Magn.* 30 2647–53.

510 Pillai V and Shah D O 1996 Synthesis of high-coercivity cobalt ferrite particles using water-in-oil microemulsions *J. Magn. Magn. Mater.* 163 243–8.

511 Asab G, Zereffa E A and Abdo Seghne T 2020 Synthesis of silica-coated Fe_3O_4 nanoparticles by microemulsion method: characterization and evaluation of antimicrobial activity *Int. J. Biomater.* 2020 e4783612.

512 Mollarasouli F, Zor E, Ozcelikay G and Ozkan S A 2021 Magnetic nanoparticles in developing electrochemical sensors for pharmaceutical and biomedical applications *Talanta* 226 122108.

513 Abbas M, Parvatheeswara Rao B, Naga S M, Takahashi M and Kim C 2013 Synthesis of high magnetization hydrophilic magnetite (Fe_3O_4) nanoparticles in single reaction – surfactantless polyol process *Ceram. Int.* 39 7605–11.

514 Oh A H, Park H-Y, Jung Y-G, Choi S-C and An G S 2020 Synthesis of Fe_3O_4 nanoparticles of various size via the polyol method *Ceram. Int.* 46 10723–8.

515 Iacovita C, Fizeşan I, Pop A, Scorus L, Dudric R, Stiufiuc G, Vedeanu N, Tetean R, Loghin F and Stiufiuc R 2020 In vitro intracellular hyperthermia of iron oxide magnetic nanoparticles, synthesized at high temperature by a polyol process *Pharmaceutics* 12 424.

516 Couto G G, Klein J J, Schreiner W H, Mosca D H, de Oliveira A J A and Zarbin A J G 2007 Nickel nanoparticles obtained by a modified polyol process: synthesis, characterization, and magnetic properties *J. Colloid Interface Sci.* 311 461–8.

517 Jeyadevan B, Shinoda K, Justin R J, Matsumoto T, Sato K, Takahashi H, Sato Y and Tohji K 2006 Polyol process for Fe-based hard(fct-FePt) and soft(FeCo) magnetic nanoparticles *IEEE Trans. Magn.* 42 3030–5.

518 Cheng C, Xu F and Gu H 2011 Facile synthesis and morphology evolution of magnetic iron oxide nanoparticles in different polyol processes *New J. Chem.* 35 1072–9.

519 Liu C, Wu X, Klemmer T, Shukla N, Yang X, Weller D, Roy A G, Tanase M and Laughlin D 2004 Polyol process synthesis of monodispersed FePt nanoparticles *J. Phys. Chem. B* 108 6121–3.

520 Julio Jimenez L F, Herrera Barros A and Caamaño De Ávila Z I 2019 Synthesis and characterization of $Fe_{55}Co_{45}$ magnetic nanoparticles by polyol and green chemistry method *Results Phys.* 15 102785.

521 Li D and Komarneni S 2006 Microwave-assisted polyol process for synthesis of Ni nanoparticles *J. Am. Ceram. Soc.* 89 1510–7.

522 Joseyphus R J, Shinoda K, Kodama D and Jeyadevan B 2010 Size controlled Fe nanoparticles through polyol process and their magnetic properties *Mater. Chem. Phys.* 123 487–93.

523 Wang Y, Nkurikiyimfura I and Pan Z 2015 Sonochemical synthesis of magnetic nanoparticles *Chem. Eng. Commun.* 202 616–21.

524 Hassanjani-Roshan A, Vaezi M R, Shokuhfar A and Rajabali Z 2011 Synthesis of iron oxide nanoparticles via sonochemical method and their characterization *Particuology* 9 95–9.

525 Hee Kim E, Sook Lee H, Kook Kwak B and Kim B-K 2005 Synthesis of ferrofluid with magnetic nanoparticles by sonochemical method for MRI contrast agent *J. Magn. Magn. Mater.* 289 328–30.

526 Dang F, Enomoto N, Hojo J and Enpuku K 2009 Sonochemical synthesis of monodispersed magnetite nanoparticles by using an ethanol–water mixed solvent *Ultrason. Sonochem.* 16 649–54.

527 Aliramaji S, Zamanian A and Sohrabijam Z 2015 Characterization and synthesis of magnetite nanoparticles by innovative sonochemical method *Procedia Mater. Sci.* 11 265–9.

528 Yadav V K, Ali D, Khan S H, Gnanamoorthy G, Choudhary N, Yadav K K, Thai V N, Hussain S A and Manhrdas S 2020 Synthesis and characterization of amorphous iron oxide nanoparticles by the sonochemical method and their application for the remediation of heavy metals from wastewater *Nanomaterials* 10 1551.

529 Bazzaz Dilmaghani A, Monajjemzadeh F, Afshar Mogaddam M R and Farajzadeh M A 2022 Sonochemical synthesis of deep eutectic solvent-coated magnetic nanoparticles and their application in magnetic dispersive micro solid phase extraction–dispersive liquid–liquid microextraction of polycyclic aromatic hydrocarbons from mascara *Microchem. J.* 181 107665.

530 Moradnia F, Taghavi Fardood S, Ramazani A, Min B, Joo S W and Varma R S 2021 Magnetic $Mg_{0.5}Zn_{0.5}FeMnO_4$ nanoparticles: green sol-gel synthesis, characterization, and photocatalytic applications *J. Clean. Prod.* 288 125632.

531 Jasrotia R, Singh V P, Sharma B, Verma A, Puri P, Sharma R and Singh M 2020 Sol-gel synthesized Ba-Nd-Cd-In nanohexaferrites for high frequency and microwave devices applications *J. Alloys Compd.* 830 154687.

532 Elayakumar K, Manikandan A, Dinesh A, Thanrasu K, Kanmani Raja K, Thilak Kumar R, Slimani Y, Jaganathan S K and Baykal A 2019 Enhanced magnetic property and antibacterial biomedical activity of Ce^{3+} doped $CuFe_2O_4$ spinel nanoparticles synthesized by sol-gel method *J. Magn. Magn. Mater.* 478 140–7.

533 Fotukian S M, Barati A, Soleymani M and Alizadeh A M 2020 Solvothermal synthesis of $CuFe_2O_4$ and Fe_3O_4 nanoparticles with high heating efficiency for magnetic hyperthermia application *J. Alloys Compd.* 816 152548.

534 Zhang H, Wu J-R, Wang X, Li X-S, Wu M-X, Liang F and Yang Y-W 2019 One-pot solvothermal synthesis of carboxylatopillar[5]arene-modified Fe_3O_4 magnetic nanoparticles for ultrafast separation of cationic dyes *Dyes Pigments* 162 512–6.

535 Kalam A, Al-Sehemi A G, Assiri M, Du G, Ahmad T, Ahmad I and Pannipara M 2018 Modified solvothermal synthesis of cobalt ferrite ($CoFe_2O_4$) magnetic nanoparticles photocatalysts for degradation of methylene blue with H_2O_2/visible light *Results Phys.* 8 1046–53.

536 Chen Y, Zhang J, Wang Z and Zhou Z 2019 Solvothermal synthesis of size-controlled monodispersed superparamagnetic iron oxide nanoparticles *Appl. Sci.* 9 5157.

537 Muthukumar K, Lakshmi D S, Acharya S D, Natarajan S, Mukherjee A and Bajaj H C 2018 Solvothermal synthesis of magnetic copper ferrite nano sheet and its antimicrobial studies *Mater. Chem. Phys.* 209 172–9.

538 Dai X, Deng Y, Peng X and Jin Y 2017 Quantum-dot light-emitting diodes for large-area displays: towards the dawn of commercialization *Adv. Mater.* 29 1607022.

539 Pu Y, Cai F, Wang D, Wang J-X and Chen J-F 2018 Colloidal synthesis of semiconductor quantum dots toward large-scale production: a review *Ind. Eng. Chem. Res.* 57 1790–802.

540 Gao X, Yang L, Petros J A, Marshall F F, Simons J W and Nie S 2005 In vivo molecular and cellular imaging with quantum dots *Curr. Opin. Biotechnol.* 16 63–72.

541 Mattoussi H, Mauro J M, Goldman E R, Anderson G P, Sundar V C, Mikulec F V and Bawendi M G 2000 Self-assembly of CdSe–ZnS quantum dot bioconjugates using an engineered recombinant protein *J. Am. Chem. Soc.* 122 12142–50.

542 Peng X, Manna L, Yang W, Wickham J, Scher E, Kadavanich A and Alivisatos A P 2000 Shape control of CdSe nanocrystals *Nature* 404 59–61.

543 Wu S, Dou J, Zhang J and Zhang S 2012 A simple and economical one-pot method to synthesize high-quality water soluble CdTe QDs *J. Mater. Chem.* 22 14573–8.

544 Jamieson T, Bakhshi R, Petrova D, Pocock R, Imani M and Seifalian A M 2007 Biological applications of quantum dots *Biomaterials* 28 4717–32.

545 Park J, Dvoracek C, Lee D K H, Galloway J F, Bhang D H C, Pomper P M G and Searson P P C 2011 CuInSe/ZnS core/shell NIR quantum dots for biomedical imaging *Small Weinh. Bergstr. Ger.* 7 3148.

546 Jiang P, Zhu C-N, Zhang Z-L, Tian Z-Q and Pang D-W 2012 Water-soluble Ag_2S quantum dots for near-infrared fluorescence imaging in vivo *Biomaterials* 33 5130–5.

547 Huang H, Susha A S, Kershaw S V, Hung T F and Rogach A L 2015 Control of emission color of high quantum yield $CH_3NH_3PbBr_3$ perovskite quantum dots by precipitation temperature *Adv. Sci.* 2 1500194.

548 Wang D, Liu J, Chen J-F and Dai L 2016 Surface functionalization of carbon dots with polyhedral oligomeric silsesquioxane (POSS) for multifunctional applications *Adv. Mater. Interfaces* 3 1500439.

549 Deng Z, Cao L, Tang F and Zou B 2005 A new route to zinc-blende CdSe nanocrystals: mechanism and synthesis *J. Phys. Chem. B* 109 16671–5.

550 Acharya K P, Khon E, O'Conner T, Nemitz I, Klinkova A, Khnayzer R S, Anzenbacher P and Zamkov M 2011 Heteroepitaxial growth of colloidal nanocrystals onto substrate films via hot-injection routes *ACS Nano* 5 4953–64.

551 Song W-S, Lee H-S, Lee J C, Jang D S, Choi Y, Choi M and Yang H 2013 Amine-derived synthetic approach to color-tunable InP/ZnS quantum dots with high fluorescent qualities *J. Nanopart. Res.* 15 1–10.

552 Jiang P, Tian Z-Q, Zhu C-N, Zhang Z-L and Pang D-W 2012 Emission-tunable near-infrared Ag_2S quantum dots *Chem. Mater.* 24 3–5.

553 Zhu C-N, Jiang P, Zhang Z-L, Zhu D-L, Tian Z-Q and Pang D-W 2013 Ag_2Se quantum dots with tunable emission in the second near-infrared window *ACS Appl. Mater. Interfaces* 5 1186–9.

554 Protesescu L, Yakunin S, Bodnarchuk M I, Krieg F, Caputo R, Hendon C H, Yang R X, Walsh A and Kovalenko M V 2015 Nanocrystals of cesium lead halide perovskites ($CsPbX_3$, X= Cl, Br, and I): novel optoelectronic materials showing bright emission with wide color gamut *Nano Lett.* 15 3692–6.

555 Wang A, Yan X, Zhang M, Sun S, Yang M, Shen W, Pan X, Wang P and Deng Z 2016 Controlled synthesis of lead-free and stable perovskite derivative Cs_2SnI_6 nanocrystals via a facile hot-injection process *Chem. Mater.* 28 8132–40.

556 Pradhan N and Efrima S 2003 Single-precursor, one-pot versatile synthesis under near ambient conditions of tunable, single and dual band fluorescing metal sulfide nanoparticles *J. Am. Chem. Soc.* 125 2050–1.

557 LaMer V K and Dinegar R H 1950 Theory, production and mechanism of formation of monodispersed hydrosols *J. Am. Chem. Soc.* 72 4847–54.

558 Liu T-Y, Li M, Ouyang J, Zaman M B, Wang R, Wu X, Yeh C-S, Lin Q, Yang B and Yu K 2009 Non-injection and low-temperature approach to colloidal photoluminescent PbS nanocrystals with narrow bandwidth *J. Phys. Chem. C* 113 2301–8.

559 Du Y, Xu B, Fu T, Cai M, Li F, Zhang Y and Wang Q 2010 Near-infrared photoluminescent Ag_2S quantum dots from a single source precursor *J. Am. Chem. Soc.* 132 1470–1.

560 Henglein A 2002 Photochemistry of colloidal cadmium sulfide. 2. Effects of adsorbed methyl viologen and of colloidal platinum *ACS Publ.* 86(13) 2291–3.

561 Rossetti R, Nakahara S and Brus L E 1983 Quantum size effects in the redox potentials, resonance Raman spectra, and electronic spectra of CdS crystallites in aqueous solution *J. Chem. Phys.* 79 1086–8.

562 Rogach A L, Katsikas L, Kornowski A, Su D, Eychmüller A and Weller H 1996 Synthesis and characterization of thiol-stabilized CdTe nanocrystals *Berichte Bunsenges. Für Phys. Chem.* 100 1772–8.

563 Yakoubi A, Chaabane T B, Aboulaich A, Mahiou R, Balan L, Medjahdi G and Schneider R 2016 Aqueous synthesis of Cu-doped CdZnS quantum dots with controlled and efficient photoluminescence *J. Lumin.* 175 193–202.

564 Thomas D, Lee H O, Santiago K C, Pelzer M, Kuti A, Treadwell L J and Bahoura M 2021 Europium doping of cadmium selenide (CdSe) quantum dots via rapid microwave synthesis for optoelectronic applications *Dalton Trans.* 51 264–73.

565 Darr J A, Zhang J, Makwana N M and Weng X 2017 Continuous hydrothermal synthesis of inorganic nanoparticles: applications and future directions *Chem. Rev.* 117 11125–238.

566 Ji W, Liu S, Zhang H, Wang R, Xie W and Zhang H 2017 Ultrasonic spray processed, highly efficient all-inorganic quantum-dot light-emitting diodes *ACS Photonics* 4 1271–8.

567 Katelnikovas A, Steponaviciute M, Ezerskyte E, Drabavicius A and Klimkevicius V 2022 Ultrasound-induced synthesis of all-inorganic lead perovskite quantum dots: fast, simple, and highly reproducible *Mater. Today Chem.* 26 101163.

568 Xue J, Li H, Liu J, Wang Y, Liu Y, Sun D, Wang W, Huang L and Tang J 2019 Facile synthesis of silver sulfide quantum dots by one pot reverse microemulsion under ambient temperature *Mater. Lett.* 242 143–6.

569 Manjunatha C, Hari Krishna R and Ashoka S 2021 Chapter 2 - Green Synthesis of Inorganic Nanoparticles Using Microemulsion Methods *Green Sustainable Process for Chemical and Environmental Engineering and Science* ed Inamuddin, R Boddula, M I Ahamed and A M Asiri (Elsevier) pp 41–67.

570 Tarkas H S, Marathe D M, Mahajan M S, Muntaser F, Patil M B, Tak S R and Sali J V 2017 Synthesis of tin monosulfide (SnS) nanoparticles using surfactant free microemulsion (SFME) with the single microemulsion scheme *Mater. Res. Express* 4 025018.

571 He Y, Lu H-T, Sai L-M, Su Y-Y, Hu M, Fan C-H, Huang W and Wang L-H 2008 Microwave synthesis of water-dispersed CdTe/CdS/ZnS core-shell-shell quantum dots with excellent photostability and biocompatibility *Adv. Mater.* 20 3416–21.

572 Duan J, Song L and Zhan J 2009 One-pot synthesis of highly luminescent CdTe quantum dots by microwave irradiation reduction and their Hg^{2+}-sensitive properties *Nano Res.* 2 61–8.

573 Wang L, Yin Y, Jain A and Zhou H S 2014 Aqueous phase synthesis of highly luminescent, nitrogen-doped carbon dots and their application as bioimaging agents *Langmuir* 30 14270–5.

574 Dai M-Q, Zheng W, Huang Z and Yung L-Y L 2012 Aqueous phase synthesis of widely tunable photoluminescence emission CdTe/CdS core/shell quantum dots under a totally ambient atmosphere *J. Mater. Chem.* 22 16336–45.

575 Borse V, Sadawana M and Srivastava R 2016 CdTe quantum dots: aqueous phase synthesis, stability studies and protein conjugation for development of biosensors *Nanophotonics VI* 9884 (SPIE) 245–56.

576 Qian H, Li L and Ren J 2005 One-step and rapid synthesis of high quality alloyed quantum dots (CdSe–CdS) in aqueous phase by microwave irradiation with controllable temperature *Mater. Res. Bull.* 40 1726–36.

577 Mrad M, Ben Chaabane T, Rinnert H, Lavinia B, Jasniewski J, Medjahdi G and Schneider R 2020 Aqueous synthesis for highly emissive 3-mercaptopropionic acid-capped AIZS quantum dots *Inorg. Chem.* 59 6220–31.

578 Xu Y, Hao J, Niu X, Qi S, Chen H, Wang K, Chen X and Yi T 2016 Seed-mediated growth approach for rapid synthesis of high-performance red-emitting CdTe quantum dots in aqueous phase and their application in detection of highly reactive oxygen species *Chem. Eng. J.* 299 201–8.

579 Su Q, Gan L and Yang X 2021 Achieving room temperature phosphorescence in aqueous phase through rigidifying the triplet state and information encryption *Appl. Surf. Sci.* 566 150726.

580 Tan J, Zhang J, Li W, Zhang L and Yue D 2016 Synthesis of amphiphilic carbon quantum dots with phosphorescence properties and their multifunctional applications *J. Mater. Chem. C* 4 10146–53.

581 Fu Y-S, Du X-W, Kulinich S A, Qiu J-S, Qin W-J, Li R, Sun J and Liu J 2007 Stable aqueous dispersion of ZnO quantum dots with strong blue emission via simple solution route *J. Am. Chem. Soc.* 129 16029–33.

582 Li H, Shih W Y and Shih W-H 2007 Non-heavy-metal ZnS quantum dots with bright blue photoluminescence by a one-step aqueous synthesis *Nanotechnology* 18 205604.

583 Zheng Y, Yang Z and Ying J Y 2007 Aqueous synthesis of glutathione-capped ZnSe and $Zn_{1-x}Cd_xSe$ alloyed quantum dots *Adv. Mater.* 19 1475–9.

584 Chen G, Tian F, Zhang Y, Zhang Y, Li C and Wang Q 2014 Tracking of transplanted human mesenchymal stem cells in living mice using near-infrared Ag_2S quantum dots *Adv. Funct. Mater.* 24 2481–8.

585 Yang H-Y, Zhao Y-W, Zhang Z-Y, Xiong H-M and Yu S-N 2013 One-pot synthesis of water-dispersible Ag_2S quantum dots with bright fluorescent emission in the second near-infrared window *Nanotechnology* 24 055706.

586 Wang C, Wang Y, Xu L, Zhang D, Liu M, Li X, Sun H, Lin Q and Yang B 2012 Facile aqueous-phase synthesis of biocompatible and fluorescent Ag_2S nanoclusters for bioimaging: tunable photoluminescence from red to near infrared *Small* 8 3137–42.

587 Ren Q, Ma Y, Zhang S, Ga L and Ai J 2021 One-step synthesis of water-soluble silver sulfide quantum dots and their application to bioimaging *ACS Omega* 6 6361–7.

588 Lu F, Ju W, Zhao N, Zhao T, Zhan C, Wang Q, Fan Q and Huang W 2020 Aqueous synthesis of PEGylated Ag_2S quantum dots and their in vivo tumor targeting behavior *Biochem. Biophys. Res. Commun.* 529 930–5.

589 Mustafa S M, Barzinjy A A, Hamad A H and Hamad S M 2022 Biosynthesis of quantum dots and their usage in solar cells: insight from the novel researches *Int. Nano Lett.* 12 139–51.

590 Labrenz M, Druschel G K, Thomsen-Ebert T, Gilbert B, Welch S A, Kemner K M, Logan G A, Summons R E, Stasio G D, Bond P L, Lai B, Kelly S D and Banfield J F 2000 Formation of sphalerite (ZnS) deposits in natural biofilms of sulfate-reducing bacteria *Science* 290 1744–7.

591 Bai H-J, Zhang Z-M and Gong J 2006 Biological synthesis of semiconductor zinc sulfide nanoparticles by immobilized *Rhodobacter sphaeroides Biotechnol. Lett.* 28 1135–9.

592 Prasad K and Jha A K 2010 Biosynthesis of CdS nanoparticles: an improved green and rapid procedure *J. Colloid Interface Sci.* 342 68–72.

593 Sweeney R Y, Mao C, Gao X, Burt J L, Belcher A M, Georgiou G and Iverson B L 2004 Bacterial biosynthesis of cadmium sulfide nanocrystals *Chem. Biol.* 11 1553–9.

594 Mi C, Wang Y, Zhang J, Huang H, Xu L, Wang S, Fang X, Fang J, Mao C and Xu S 2011 Biosynthesis and characterization of CdS quantum dots in genetically engineered *Escherichia coli J. Biotechnol.* 153 125–32.

595 Gallardo-Benavente C, Carrión O, Todd J D, Pieretti J C, Seabra A B, Durán N, Rubilar O, Pérez-Donoso J M and Quiroz A 2019 Biosynthesis of CdS quantum dots mediated by volatile sulfur compounds released by antarctic *Pseudomonas fragi Front. Microbiol.* 10 https://doi.org/10.3389/fmicb.2019.01866.

596 Qin Z, Yue Q, Liang Y, Zhang J, Zhou L, Hidalgo O B and Liu X 2018 Extracellular biosynthesis of biocompatible cadmium sulfide quantum dots using *Trametes versicolor J. Biotechnol.* 284 52–6.

597 Seshadri S, Saranya K and Kowshik M 2011 Green synthesis of lead sulfide nanoparticles by the lead resistant marine yeast, *Rhodosporidium diobovatum Biotechnol. Prog.* 27 1464–9.

598 Öcal N, Ceylan A and Duman F 2020 Intracellular biosynthesis of PbS quantum dots using *Pseudomonas aeruginosa* ATCC 27853: evaluation of antibacterial effects and DNA cleavage activities *World J. Microbiol. Biotechnol.* 36 147.

599 Kumar S A, Ansary A A, Ahmad A and Khan M I 2007 Extracellular biosynthesis of CdSe quantum dots by the fungus, *Fusarium oxysporum J. Biomed. Nanotechnol.* 3 190–4.

600 Cao K, Chen M-M, Chang F-Y, Cheng Y-Y, Tian L-J, Li F, Deng G-Z and Wu C 2020 The biosynthesis of cadmium selenide quantum dots by *Rhodotorula mucilaginosa* PA-1 for photocatalysis *Biochem. Eng. J.* 156 107497.

601 Suresh A K, Doktycz M J, Wang W, Moon J-W, Gu B, Meyer H M, Hensley D K, Allison D P, Phelps T J and Pelletier D A 2011 Monodispersed biocompatible silver sulfide nanoparticles: facile extracellular biosynthesis using the γ-proteobacterium, *Shewanella oneidensis Acta Biomater.* 7 4253–8.

602 Raouf Hosseini M and Nasiri Sarvi M 2015 Recent achievements in the microbial synthesis of semiconductor metal sulfide nanoparticles *Mater. Sci. Semicond. Process.* 40 293–301.

603 Liu J, Zheng D, Zhong L, Gong A, Wu S and Xie Z 2021 Biosynthesis of biocompatibility Ag_2Se quantum dots in *Saccharomyces cerevisiae* and its application *Biochem. Biophys. Res. Commun.* 544 60–4.

604 Fatimah I, Sahroni I, Muraza O and Doong R 2020 One-pot biosynthesis of SnO_2 quantum dots mediated by *Clitoria ternatea* flower extract for photocatalytic degradation of rhodamine B *J. Environ. Chem. Eng.* 8 103879.

605 Dai H 2002 Carbon nanotubes: opportunities and challenges *Surf. Sci.* 500 218–41.

606 Dineshkumar B, Krishnakumar K, Bhatt A R, Paul D, Cherian J, John A and Suresh S 2015 Single-walled and multi-walled carbon nanotubes based drug delivery system: cancer therapy: a review *Indian J. Cancer* 52 262.

607 Cassell A M, Raymakers J A, Kong J and Dai H 1999 Large scale CVD synthesis of single-walled carbon nanotubes *J. Phys. Chem. B* 103 6484–92.

608 Kukovecz Á, Kozma G and Kónya Z 2013 Multi-Walled Carbon Nanotubes *Springer Handbook of Nanomaterials* Springer Handbooks ed R Vajtai (Berlin, Heidelberg: Springer) pp 147–88.

609 Liew K M, Wong C H, He X Q, Tan M J and Meguid S A 2004 Nanomechanics of single and multiwalled carbon nanotubes *Phys. Rev. B* 69 115429.

610 Lim S, Luo Z, Shen Z and Lin J 2010 Plasma-assisted synthesis of carbon nanotubes *Nanoscale Res. Lett.* 5 1377.

611 Iijima S 1991 Helical microtubules of graphitic carbon *Nature* 354 56.

612 Arora N and Sharma N N 2014 Arc discharge synthesis of carbon nanotubes: comprehensive review *Diam. Relat. Mater.* 50 135–50.

613 Purohit R, Purohit K, Rana S, Rana R S and Patel V 2014 Carbon nanotubes and their growth methods *Procedia Mater. Sci.* 6 716–28.

614 Farhat S and Scott C D 2006 Review of the arc process modeling for fullerene and nanotube production *J. Nanosci. Nanotechnol.* 6 1189–210.

615 Ando Y 2010 Carbon nanotube: the inside story *J. Nanosci. Nanotechnol.* 10 3726–38.

616 Mohammad M I, Moosa A A, Potgieter J H and Ismael M K 2013 Carbon nanotubes synthesis via arc discharge with a Yttria catalyst *Int. Sch. Res. Not.* 2013 e785160.

617 Wang X K, Lin X W, Dravid V P, Ketterson J B and Chang R P H 1995 Carbon nanotubes synthesized in a hydrogen arc discharge *Appl. Phys. Lett.* 66 2430–2.

618 Rouf S A, Usman Z, Masood H T, Majeed A M, Sarwar M, Abbas W, Rouf S A, Usman Z, Masood H T, Majeed A M, Sarwar M and Abbas W 2021 *Synthesis and Purification of Carbon Nanotubes* (IntechOpen).

619 Roch A, Jost O, Schultrich B and Beyer E 2007 High-yield synthesis of single-walled carbon nanotubes with a pulsed arc-discharge technique *Phys. Status Solidi B* 244 3907–10.

620 Joseph Berkmans A, Jagannatham M, Rohit Reddy D and Haridoss P 2015 Synthesis of thin bundled single walled carbon nanotubes and nanohorn hybrids by arc discharge technique in open air atmosphere *Diam. Relat. Mater.* 55 12–5.

621 Zhao S, Hong R, Luo Z, Lu H and Yan B 2011 Carbon nanostructures production by AC arc discharge plasma process at atmospheric pressure *J. Nanomater.* 2011 14.

622 Parkansky N, Boxman R L, Alterkop B, Zontag I, Lereah Y and Barkay Z 2004 Single-pulse arc production of carbon nanotubes in ambient air *J. Phys. Appl. Phys.* 37 2715.

623 Tsai Y Y, Su J S, Su C Y and He W H 2009 Production of carbon nanotubes by single-pulse discharge in air *J. Mater. Process. Technol.* 209 4413–6.

624 Gang X, Shenli J, Jian X and Zongqian S 2007 Analysis of the carbon nano-structures formation in liquid arcing *Plasma Sci. Technol.* 9 770.

625 Corbella C, Portal S, Zolotukhin D B, Martinez L, Lin L, Kundrapu M N and Keidar M 2019 Pulsed anodic arc discharge for the synthesis of carbon nanomaterials *Plasma Sources Sci. Technol.* 28 045016.

626 Zhang D, Ye K, Yao Y, Liang F, Qu T, Ma W, Yang B, Dai Y and Watanabe T 2019 Controllable synthesis of carbon nanomaterials by direct current arc discharge from the inner wall of the chamber *Carbon* 142 278–84.

627 Thess A, Lee R, Nikolaev P, Dai H, Petit P, Robert J, Xu C, Lee Y H, Kim S G, Rinzler A G, Colbert D T, Scuseria G E, Tománek D, Fischer J E and Smalley R E 1996 Crystalline ropes of metallic carbon nanotubes *Science* 273 483–7.

628 Niu K-Y, Sun J, Yang J and Du X-W 2012 The synthesis of carbon nanotubes by pulsed-laser ablation of a nickel/carbon composite target in ethanol or ambient air *Sci. Adv. Mater.* 4 463–6.

629 Chrzanowska J, Hoffman J, Małolepszy A, Mazurkiewicz M, Kowalewski T A, Szymanski Z and Stobinski L 2015 Synthesis of carbon nanotubes by the laser ablation method: effect of laser wavelength *Phys. Status Solidi B* 252 1860–7.

630 Li W Z, Xie S S, Qian L X, Chang B H, Zou B S, Zhou W Y, Zhao R A and Wang G 1996 Large-scale synthesis of aligned carbon nanotubes *Science* 274 1701–3.

631 Rathinavel S, Priyadharshini K and Panda D 2021 A review on carbon nanotube: an overview of synthesis, properties, functionalization, characterization, and the application *Mater. Sci. Eng. B* 268 115095.

632 Kang J, Li J, Du X, Shi C, Zhao N and Nash P 2008 Synthesis of carbon nanotubes and carbon onions by CVD using a Ni/Y catalyst supported on copper *Mater. Sci. Eng. A* 475 136–40.

633 Ding E-X, Jiang H, Zhang Q, Tian Y, Laiho P, Hussain A, Liao Y, Wei N and Kauppinen E I 2017 Highly conductive and transparent single-walled carbon nanotube thin films from ethanol by floating catalyst chemical vapor deposition *Nanoscale* 9 17601–9.

634 Ahmad S, Liao Y, Hussain A, Zhang Q, Ding E-X, Jiang H and Kauppinen E I 2019 Systematic investigation of the catalyst composition effects on single-walled carbon nanotubes synthesis in floating-catalyst CVD *Carbon* 149 318–27.

635 Zhou W, Ding L and Liu J 2009 Role of catalysts in the surface synthesis of single-walled carbon nanotubes *Nano Res.* 2 593–8.

636 He M, Chernov A I, Obraztsova E D, Jiang H, Kauppinen E I and Lehtonen J 2013 Synergistic effects in FeCu bimetallic catalyst for low temperature growth of single-walled carbon nanotubes *Carbon* 52 590–4.

637 Escobar M, Moreno M S, Candal R J, Marchi M C, Caso A, Polosecki P I, Rubiolo G H and Goyanes S 2007 Synthesis of carbon nanotubes by CVD: effect of acetylene pressure on nanotubes characteristics *Appl. Surf. Sci.* 254 251–6.

638 Yang Y, Zhang H and Yan Y 2019 Synthesis of CNTs on stainless steel microfibrous composite by CVD: effect of synthesis condition on carbon nanotube growth and structure *Compos. Part B Eng.* 160 369–83.

639 Kuwana K and Saito K 2005 Modeling CVD synthesis of carbon nanotubes: nanoparticle formation from ferrocene *Carbon* 43 2088–95.

640 Allaedini G, Tasirin S M and Aminayi P 2015 Synthesis of CNTs via chemical vapor deposition of carbon dioxide as a carbon source in the presence of NiMgO *J. Alloys Compd.* 647 809–14.

641 Verma B, Sewani H and Balomajumder C 2020 Synthesis of carbon nanotubes via chemical vapor deposition: an advanced application in the management of electroplating effluent *Environ. Sci. Pollut. Res.* 27 14007–18.

642 Kumar U and Yadav B C 2019 Synthesis of carbon nanotubes by direct liquid injection chemical vapor deposition method and its relevance for developing an ultra-sensitive room temperature based CO_2 sensor *J. Taiwan Inst. Chem. Eng.* 96 652–63.

643 Wu S-L, Chen C-M, Kuo J-H and Wey M-Y 2020 Synthesis of carbon nanotubes with controllable diameter by chemical vapor deposition of methane using $Fe@Al_2O_3$ core–shell nanocomposites *Chem. Eng. Sci.* 217 115541.

644 Prasek J, Drbohlavova J, Chomoucka J, Hubalek J, Jasek O, Adam V and Kizek R 2011 Methods for carbon nanotubes synthesis – review *J. Mater. Chem.* 21 15872–84.

645 Meyyappan M, Delzeit L, Cassell A and Hash D 2003 Carbon nanotube growth by PECVD: a review *Plasma Sources Sci. Technol.* 12 205.

646 Chen M, Chen C-M and Chen C-F 2002 Preparation of high yield multi-walled carbon nanotubes by microwave plasma chemical vapor deposition at low temperature *J. Mater. Sci.* 37 3561–7.

647 Teo K B K, Lee S-B, Chhowalla M, Semet V, Binh V T, Groening O, Castignolles M, Loiseau A, Pirio G, Legagneux P, Pribat D, Hasko D G, Ahmed H, Amaratunga G A J and Milne W I 2003 Plasma enhanced chemical vapour deposition carbon nanotubes/nanofibres – how uniform do they grow *Nanotechnology* 14 204.

648 Boskovic B O, Stolojan V, Khan R U A, Haq S and Silva S R P 2002 Large-area synthesis of carbon nanofibres at room temperature *Nat. Mater.* 1 165–8.

649 Hussain S, Kovacevic E, Amade R, Berndt J, Pattyn C, Dias A, Boulmer-Leborgne C, Ammar M-R and Bertran-Serra E 2018 Plasma synthesis of polyaniline enrobed carbon nanotubes for electrochemical applications *Electrochim. Acta* 268 218–25.

650 Park D, Kim Y H and Lee J K 2003 Pretreatment of stainless steel substrate surface for the growth of carbon nanotubes by PECVD *J. Mater. Sci.* 38 4933–9.

651 Gangele A, Sharma C S and Pandey A K 2017 Synthesis of patterned vertically aligned carbon nanotubes by PECVD using different growth techniques: a review *J. Nanosci. Nanotechnol.* 17 2256–73.

652 Cui L, Chen J, Yang B, Sun D and Jiao T 2015 RF-PECVD synthesis of carbon nanowalls and their field emission properties *Appl. Surf. Sci.* 357 1–7.

653 Shoukat R and Khan M I 2017 Growth of nanotubes using IC-PECVD as benzene carbon carrier *Microsyst. Technol.* 23 5447–53.

654 Tailleur A, Achour A, Djouadi M A, Le Brizoual L, Gautron E and Tristant P 2012 PECVD low temperature synthesis of carbon nanotubes coated with aluminum nitride *Surf. Coat. Technol.* 211 18–23.

655 Park S, Gupta A P, Yeo S J, Jung J, Paik S H, Mativenga M, Kim S H, Shin J H, Ahn J S and Ryu J 2018 Carbon nanotube field emitters synthesized on metal alloy substrate by PECVD for customized compact field emission devices to be used in X-ray source applications *Nanomaterials* 8 378.

656 Yerlanuly Y, Christy D, Van Nong N, Kondo H, Alpysbayeva B, Nemkayeva R, Kadyr M, Ramazanov T, Gabdullin M, Batryshev D and Hori M 2020 Synthesis of carbon nanowalls on the surface of nanoporous alumina membranes by RI-PECVD method *Appl. Surf. Sci.* 523 146533.

657 Krishna A, Gecil Evangeline T, Aravinda L S, Sharath Kumar N, Niranjan Reddy K, Balashanmugam N and Mamilla R S 2020 Synthesis and thermal simulations of novel

encapsulated CNT multifunctional thin-film based nanomaterial of SiO_2-CNT and TiN-CNT by PVD and PECVD techniques for thermal applications *Diam. Relat. Mater.* 109 108029.

658 Sacco L N, van Ginkel H J and Vollebregt S 2022 Synthesis of Carbon nanofibers (CNFs) by PECVD using Ni catalyst printed by spark ablation *2022 IEEE 22nd International Conference on Nanotechnology (NANO)* pp 128–31.

659 Ankit K, Evangeline T G, Aravinda L S, Kumar N S, Sankar M R, Nagahanumaiah K, Reddy N and Balashanmugam N 2022 Encapsulation of CNT Films on Silicon Wafer by DLC Synthesized by PECVD for Application as a Thermal Interface Material *Advances in Micro and Nano Manufacturing and Surface Engineering: Proceedings of AIMTDR 2021* (Singapore: Springer Nature Singapore) pp 95–106.

660 Viculis L M, Mack J J and Kaner R B 2003 A chemical route to carbon nanoscrolls *Science* 299 1361–1.

661 Novoselov K S, Geim A K, Morozov S V, Jiang D, Zhang Y, Dubonos S V, Grigorieva I V and Firsov A A 2004 Electric field effect in atomically thin carbon films *Science* 306 666–9.

662 Datta S S, Strachan D R, Khamis S M and Johnson A T C 2008 Crystallographic etching of few-layer graphene *Nano Lett.* 8 1912–5.

663 Gass M H, Bangert U, Bleloch A L, Wang P, Nair R R and Geim A K 2008 Free-standing graphene at atomic resolution *Nat. Nanotechnol.* 3 676–81.

664 Shukla A, Kumar R, Mazher J and Balan A 2009 Graphene made easy: high quality, large-area samples *Solid State Commun.* 149 718–21.

665 Hiura H, Ebbesen T W, Fujita J, Tanigaki K and Takada T 1994 Role of sp^3 defect structures in graphite and carbon nanotubes *Nature* 367 148–51.

666 Lu X, Yu M, Huang H and Ruoff R S 1999 Tailoring graphite with the goal of achieving single sheets *Nanotechnology* 10 269.

667 Bernhardt T M, Kaiser B and Rademann K 1998 Formation of superperiodic patterns on highly oriented pyrolytic graphite by manipulation of nanosized graphite sheets with the STM tip *Surf. Sci.* 408 86–94.

668 Liu F 2021 Mechanical exfoliation of large area 2D materials from vdW crystals *Prog. Surf. Sci.* 96 100626.

669 Kumar R, Sahoo S, Joanni E, Singh R K, Tan W K, Kar K K and Matsuda A 2019 Recent progress in the synthesis of graphene and derived materials for next generation electrodes of high performance lithium ion batteries *Prog. Energy Combust. Sci.* 75 100786.

670 Jiang F, Yu Y, Feng A and Song L 2018 Effects of ammonia on graphene preparation via microwave assisted intercalation exfoliation method *Ceram. Int.* 44 12763–6.

671 Ma H, Shen Z, Yi M, Ben S, Liang S, Liu L, Zhang Y, Zhang X and Ma S 2017 Direct exfoliation of graphite in water with addition of ammonia solution *J. Colloid Interface Sci.* 503 68–75.

672 Parvez K, Yang S, Feng X and Müllen K 2015 Exfoliation of graphene via wet chemical routes *Synth. Met.* 210 123–32.

673 Guan Z, Shen X, Yu R, Wang Z and Chen L 2016 Chemical intercalation of solvated sodium ions in graphite *Electrochim. Acta* 222 1365–70.

674 Baig Z, Mamat O, Mustapha M, Mumtaz A, Munir K S and Sarfraz M 2018 Investigation of tip sonication effects on structural quality of graphene nanoplatelets (GNPs) for superior solvent dispersion *Ultrason. Sonochem.* 45 133–49.

675 Asgar H, Deen K M, Riaz U, Rahman Z U, Shah U H and Haider W 2018 Synthesis of graphene via ultra-sonic exfoliation of graphite oxide and its electrochemical characterization *Mater. Chem. Phys.* 206 7–11.

676 Bakhshandeh R and Shafiekhani A 2018 Ultrasonic waves and temperature effects on graphene structure fabricated by electrochemical exfoliation method *Mater. Chem. Phys.* 212 95–102.

677 Hernandez Y, Nicolosi V, Lotya M, Blighe F M, Sun Z, De S, McGovern I T, Holland B, Byrne M, Gun'Ko Y K, Boland J J, Niraj P, Duesberg G, Krishnamurthy S, Goodhue R, Hutchison J, Scardaci V, Ferrari A C and Coleman J N 2008 High-yield production of graphene by liquid-phase exfoliation of graphite *Nat. Nanotechnol.* 3 563–8.

678 Narayan R and Kim S O 2015 Surfactant mediated liquid phase exfoliation of graphene *Nano Converg.* 2 20.

679 Liu W W and Wang J N 2011 Direct exfoliation of graphene in organic solvents with addition of NaOH *Chem. Commun.* 47 6888–90.

680 Guardia L, Fernández-Merino M J, Paredes J I, Solís-Fernández P, Villar-Rodil S, Martínez-Alonso A and Tascón J M D 2011 High-throughput production of pristine graphene in an aqueous dispersion assisted by non-ionic surfactants *Carbon* 49 1653–62.

681 Haar S, El Gemayel M, Shin Y, Melinte G, Squillaci M A, Ersen O, Casiraghi C, Ciesielski A and Samorì P 2015 Enhancing the liquid-phase exfoliation of graphene in organic solvents upon addition of *n*-Octylbenzene *Sci. Rep.* 5 16684.

682 Xu Y, Cao H, Xue Y, Li B and Cai W 2018 Liquid-phase exfoliation of graphene: an overview on exfoliation media, techniques, and challenges *Nanomaterials* 8 942.

683 Arao Y, Mori F and Kubouchi M 2017 Efficient solvent systems for improving production of few-layer graphene in liquid phase exfoliation *Carbon* 118 18–24.

684 Lotya M, Hernandez Y, King P J, Smith R J, Nicolosi V, Karlsson L S, Blighe F M, De S, Wang Z, McGovern I T, Duesberg G S and Coleman J N 2009 Liquid phase production of graphene by exfoliation of graphite in surfactant/water solutions *J. Am. Chem. Soc.* 131 3611–20.

685 Wu Z-S, Ren W, Gao L, Zhao J, Chen Z, Liu B, Tang D, Yu B, Jiang C and Cheng H-M 2009 Synthesis of graphene sheets with high electrical conductivity and good thermal stability by hydrogen arc discharge exfoliation *ACS Nano* 3 411–7.

686 Wang G, Wang B, Park J, Wang Y, Sun B and Yao J 2009 Highly efficient and large-scale synthesis of graphene by electrolytic exfoliation *Carbon* 47 3242–6.

687 Ang P K, Wang S, Bao Q, Thong J T L and Loh K P 2009 High-throughput synthesis of graphene by intercalation–exfoliation of graphite oxide and study of ionic screening in graphene transistor *ACS Nano* 3 3587–94.

688 Pingale A D, Owhal A, Katarkar A S, Belgamwar S U and Rathore J S 2021 Facile synthesis of graphene by ultrasonic-assisted electrochemical exfoliation of graphite *Mater. Today Proc.* 44 467–72.

689 Liu F, Wang C, Sui X, Riaz M A, Xu M, Wei L and Chen Y 2019 Synthesis of graphene materials by electrochemical exfoliation: recent progress and future potential *Carbon Energy* 1 173–99.

690 Zhang Y H, Chen Z Y, Ge X M, Liang Y J, Hu S K, Sui Y P and Yu G H 2018 A waterless cleaning method of the Cu foil for CVD graphene growth *Mater. Lett.* 211 258–60.

691 Min B H, Kim D W, Kim K H, Choi H O, Jang S W and Jung H-T 2014 Bulk scale growth of CVD graphene on Ni nanowire foams for a highly dense and elastic 3D conducting electrode *Carbon* 80 446–52.

692 Wang J J, Zhu M Y, Outlaw R A, Zhao X, Manos D M, Holloway B C and Mammana V P 2004 Free-standing subnanometer graphite sheets *Appl. Phys. Lett.* 85 1265–7.

693 Wang J, Zhu M, Outlaw R A, Zhao X, Manos D M and Holloway B C 2004 Synthesis of carbon nanosheets by inductively coupled radio-frequency plasma enhanced chemical vapor deposition *Carbon* 42 2867–72.

694 Hiramatsu M, Shiji K, Amano H and Hori M 2004 Fabrication of vertically aligned carbon nanowalls using capacitively coupled plasma-enhanced chemical vapor deposition assisted by hydrogen radical injection *Appl. Phys. Lett.* 84 4708–10.

695 Zhu M, Wang J, Holloway B C, Outlaw R A, Zhao X, Hou K, Shutthanandan V and Manos D M 2007 A mechanism for carbon nanosheet formation *Carbon* 45 2229–34.

696 Wang C, Yang S, Wang Q, Wang Z and Zhang J 2008 Super-low friction and super-elastic hydrogenated carbon films originated from a unique fullerene-like nanostructure *Nanotechnology* 19 225709.

697 Muñoz R and Gómez-Aleixandre C 2013 Review of CVD synthesis of graphene *Chem. Vap. Depos.* 19 297–322.

698 Hussain A, Mehdi S M, Abbas N, Hussain M and Naqvi R A 2020 Synthesis of graphene from solid carbon sources: a focused review *Mater. Chem. Phys.* 248 122924.

699 Wang J, Ren Z, Hou Y, Yan X, Liu P, Zhang H, Zhang H and Guo J 2020 A review of graphene synthesis at low temperatures by CVD methods *New Carbon Mater.* 35 193–208.

700 Huet B and Raskin J-P 2018 Role of Cu foil in-situ annealing in controlling the size and thickness of CVD graphene domains *Carbon* 129 270–80.

701 Shin J H, Kim S H, Kwon S S and Park W I 2018 Direct CVD growth of graphene on three-dimensionally-shaped dielectric substrates *Carbon* 129 785–9.

702 Palneedi H, Park J H, Maurya D, Peddigari M, Hwang G-T, Annapureddy V, Kim J-W, Choi J-J, Hahn B-D, Priya S, Lee K J and Ryu J 2018 Laser irradiation of metal oxide films and nanostructures: applications and advances *Adv. Mater.* 30 1705148.

703 Zhao Y, Han Q, Cheng Z, Jiang L and Qu L 2017 Integrated graphene systems by laser irradiation for advanced devices *Nano Today* 12 14–30.

704 Kumar R, Singh R K, Singh D P, Joanni E, Yadav R M and Moshkalev S A 2017 Laser-assisted synthesis, reduction and micro-patterning of graphene: recent progress and applications *Coord. Chem. Rev.* 342 34–79.

705 Kumar R, Joanni E, Singh R K, da Silva E T S G, Savu R, Kubota L T and Moshkalev S A 2017 Direct laser writing of micro-supercapacitors on thick graphite oxide films and their electrochemical properties in different liquid inorganic electrolytes *J. Colloid Interface Sci.* 507 271–8.

706 Tseng S-F 2018 Picosecond laser micropatterning of graphene films for rapid heating chips *Appl. Surf. Sci.* 450 380–6.

707 Kasischke M, Subaşı E, Bock C, Pham D-V, Gurevich E L, Kunze U and Ostendorf A 2019 Femtosecond laser patterning of graphene electrodes for thin-film transistors *Appl. Surf. Sci.* 478 299–303.

708 Al-Nimr M A 1997 Heat transfer mechanisms during short-duration laser heating of thin metal films *Int. J. Thermophys.* 18 1257–68.

709 Jiang J, Lin Z, Ye X, Zhong M, Huang T and Zhu H 2014 Graphene synthesis by laser-assisted chemical vapor deposition on Ni plate and the effect of process parameters on uniform graphene growth *Thin Solid Films* 556 206–10.

710 Tu R, Liang Y, Zhang C, Li J, Zhang S, Yang M, Li Q, Goto T, Zhang L, Shi J, Li H, Ohmori H, Kosinova M and Basu B 2018 Fast synthesis of high-quality large-area graphene by laser CVD *Appl. Surf. Sci.* 445 204–10.

711 Wang K, Tai G, Wong K H, Lau S P and Guo W 2011 Ni induced few-layer graphene growth at low temperature by pulsed laser deposition *AIP Adv.* 1 022141.

712 Xiong W, Zhou Y S, Hou W J, Jiang L J, Gao Y, Fan L S, Jiang L, Silvain J F and Lu Y F 2014 Direct writing of graphene patterns on insulating substrates under ambient conditions *Sci. Rep.* 4 4892.

713 Mikheev K G, Zonov R G, Mogileva T N, Fateev A E and Mikheev G M 2021 Optical anisotropy of laser-induced graphene films *Opt. Laser Technol.* 141 107143.

714 Lee S, Toney M F, Ko W, Randel J C, Jung H J, Munakata K, Lu J, Geballe T H, Beasley M R, Sinclair R, Manoharan H C and Salleo A 2010 Laser-synthesized epitaxial graphene *ACS Nano* 4 7524–30.

715 Wei D, Mitchell J I, Tansarawiput C, Nam W, Qi M, Ye P D and Xu X 2013 Laser direct synthesis of graphene on quartz *Carbon* 53 374–9.

716 Rao C N R, Matte H S S R and Subrahmanyam K S 2013 Synthesis and selected properties of graphene and graphene mimics *Acc. Chem. Res.* 46 149–59.

717 Kumar N, Salehiyan R, Chauke V, Joseph Botlhoko O, Setshedi K, Scriba M, Masukume M and Sinha Ray S 2021 Top-down synthesis of graphene: a comprehensive review *FlatChem* 27 100224.